Multiscale Modeling Approach to Understand Active sites in Non-Conventional Catalyst Layers for Fuel Cell Applications

A Dissertation Presented for the
Doctor of Philosophy
Degree
The University of Tennessee, Knoxville

Diana Constanza Orozco-Gallo
December 2017

DEDICATION

Once, I had a dream of becoming a better version of myself. Today, I am grateful that life has rewarded me in the pursuit of my dreams. It has been a long journey full of hard work and sacrifices but also meaningful memories. Today, I can stand in front of a mirror and be proud of myself. Today, my work just begins.

This journey could not have been possible without many people in my life to whom I dedicate this work:

My beloved family—Maria, Jose, David, and Sebastian—who were there during this journey, supporting me in the distance and encouraging my dreams. They gave me inspiration, motivation, and fuel that allowed me to finish.

My boyfriend, Kirk, who helped me through the last mile of this journey, who cheered me up daily, and helped correct my grammar but most importantly, who inspires me to be better every day and to give my all in my work.

My tango family who gave me strength, relief, and help in the difficult times. They believe in my capabilities and have molded me into the confident person I am today.

ACKNOWLEDGEMENTS

This work would not have been possible without the help of several people:

My advisor, Dr. Thomas A. Zawodzinski, for being my mentor, believing in me, and granting me the opportunity to learn from him. I am thankful for his guidance and firm encouragement in the hardest moments and for the long, interesting, and meaningful discussions.

My committee members Dr. Steve Abel, Dr. Siris Laursen, and Dr. Haixuan Xu, for being part of the evaluation process and for their help and suggestions at different stages of this research.

Dr. Gabriel A. Goenaga, who made it possible to come here, helped me adjust to my new surroundings, and has been an outstanding academic and personal mentor.

Dr. Alexander B. Papandrew, for the guidance, discussion, and essential feedback during the SAFC Modeling. His profound knowledge of the electrochemistry process has steered me towards becoming a more competent researcher.

Dr. Jamie A Lawton, for helping during the first simulation steps, for the discussion and collaboration during the macroscale process.

MSc. Nelly Cantillo, for the hard work obtaining the experimental data, for the discussion and feedback during the PGM-free modeling process, and for the support as a colleague and as a friend.

Dr. Shengqian Ma at USF, for providing the catalytic material for the PGM-free studies.

Dr. Steve Abel, for his help with the mathematical implementation and discussion for the 1D modeling.

Dr. Haixuan Xu, for his guidance with DFT calculations, discussion, and support during these processes.

Dr. David Keffer, for his help with the MD ideas and implementation for my PGM-free system.

My friend Michelle Aranha who has been an active participant in this modeling process, her feedback and encouragement every day, her useful advices and constant advice help me out during this process.

Dr. Marshall McDonell and Dr. Nick McNutt, for helping me in the learning process of managing HPC systems, DFT and MD implementations.

My colleagues in Zawodzinski's Group—David Wilson, Luke Severdio and Brian Fane—for the constant feedback and discussion about catalysis, chemistry, and electrochemical methods.

The NSF grant EPS-1004083–TN-SCORE—and COLCIENCIAS for funding.

The National Institute for Computational Sciences, NSF grant 1137097—Beacon Project—, the Newton HPC program at the University of Tennessee, and Extreme Science and Engineering Discovery Environment (XSEDE), NSF ACI-1548562 for the computational resources.

ABSTRACT

Fuel cells development required stable, active and more abundant catalytic materials. Oxygen reduction reaction (ORR) is the key process to enhance better activity and reduce the fabrication costs. Pt-based has proven to be the best catalyst for ORR and greater efforts has been made in terms of reducing the Pt content in the electrodes, reduce electrode thickness and enhance better catalytic activities. To overcome many of the challenges present, the catalyst layer studies are the great importance in the fuel cell community. Understanding catalyst layer with new catalytic materials, and configurations requires the development of methodological approach to relate structure, catalyst performance, and operational conditions.

Experimental approaches to describe catalyst layer are well defined. However, modeling methodologies for new catalyst layers are not clear. This work provides a multiscale modeling methodology to identify the main losses and parameters at the macroscale. Then, they will direct us toward the proper scale to describe the parameter/process with more detail.

Chapter 1 summarizes the main theoretical approaches to study ORR. Chapters 2 and 3 implement a macrohomogeneous model to identify the relevant parameters and to calculate the main losses for Solid Acid Fuel Cells SAFCs and Non-Precious Metal (NPM) or PGM-free systems. Chapter 4 is the extension of the results from chapter 3 towards understanding the active sites for NPM catalysts. Finally, chapter 5 illustrates the initial approach to simulate real active sites configuration.

The multiscale approach was applied to NPMCs due to larger overpotential compared with Pt-based catalyst. DFT calculations were used to evaluate activation energies. Direct four-electron pathway was used for Pt, Iron, Porphyrin and Iron Porphyrin systems. Porphyrin and Iron Porphyrin showed poor oxygen activation of compare with Pt and Iron. MD calculations of the Iron Porphyrin system illustrate some of the XRD characteristic peaks for carbon. However, we were not capable of identifying the Fe peaks. Further studies require

the search for ReaxFF potential to allow molecules reorganization and active sites identification.

TABLE OF CONTENTS

Introduction 1

1 Modeling Techinques for catalyst layers 3

Abstract 4

1.1 Introduction 4

1.2 Oxygen Reduction Reaction 8

1.3 ORR Kinetics 16

1.3.1 Tafel Slope 17

1.3.2 Exchange Current Density 18

1.4 Catalytic Materials for ORR 20

1.4.1 Pt-based Catalyst 22

1.4.2 ORR in Pt-based catalyst 23

1.4.3 Non-Precious Metal Catalyst (NPMCs) or Platinum Group Metal Free Catalyst (PGM-free) 28

1.4.4 NPMCs and active sites 32

1.5 Catalyst Layer Modeling 35

1.5.1 Macroscale modeling 37

1.5.2 Mesoscale modeling 38

1.5.3 Microscale modeling 39

1.6 Electrocatalysis Challenges 40

2 Macroscale Modeling of Solid Acid Fuel Cells 45

Abstract 46

2.1 Introduction 46

2.2 Model description 50

2.2.1 Model Equations 50

2.3 Model validation 52

2.4 Experimental 52

2.4.1 Cell Fabrication 52

2.4.2 Microstructural Analysis 54

2.4.3 Electrochemical Testing 56

2.5 Results and discussion 56
2.5.1 Experimental results analysis 56
2.5.2 Sensitivity analysis 61
2.5.3 Modeling Analysis 62
2.5.4 Overpotential analysis 76
2.6 Conclusions 81
3 Modeling Of Non-Precious Metal Catalyst Cathode Layer For PEMFCs 83
Abstract 84
3.1 Introduction 84
3.2 Model application 90
3.2.1 Model Assumptions 92
3.2.2 Other relations 92
3.2.3 Model Validation 93
3.3 Experimental 93
3.4 Results and discussion 98
3.4.1 Sensitivity analysis 103
3.4.2 Polarization curves fitting 106
3.4.3 Tafel Slopes 107
3.4.4 Roughness corrected factor 107
3.4.5 Concentration distribution 110
3.4.6 Permeability 113
3.4.7 Current distribution 113
3.4.8 Overpotentials 117
3.5 Conclusions 122
4 Microscale Modeling: Understanding PGM-Free Active Sites 124
Abstract 125
4.1 Introduction 125
4.2 First-principle modeling (ab-initio methods)[130] 130
4.2.1 Density functional theory 132
4.2.2 Exchange-correlation functionals 133
4.2.3 Pseudopotential (PP) approach 133
4.2.4 Nudged elastic band method (NEB) 133

4.3 Modeling of electrochemical systems....137
4.3.1 Assumptions....137
4.3.2 Gibbs energies treatment....138
4.3.3 Oxygen Reduction Reaction Modeling....140
4.3.4 Sabatier Principle and volcano plots....142
4.4 Results and discussion....144
4.4.1 Lattice Parameter....145
4.4.2 Relaxation steps....145
4.4.3 Activation Energies....149
4.4.4 Gibbs energy graphs....154
4.4.5 Volcano Plots....158
4.5 Conclusions....158
5 Mesoscale modeling: Steps Towards Understanding the active site....160
Abstract....161
5.1 Introduction....161
5.2 Experimental evidence....166
5.2.1 Perfusion Calorimetry....167
5.2.2 XRD....169
5.3 Mesoscale modeling....169
5.3.1 MD Potentials....170
5.3.2 Organic molecules potentials....173
5.3.3 Ensembles....177
5.3.4 General procedure for MD molecules modeling....182
5.3.5 Intramolecular potential parameters....184
5.4 Results....189
5.4.1 Calorimetry....189
5.4.2 XRD....190
5.4.3 MD Modeling results....190
5.5 Conclusions....199
General Conclusions....200
References....203
Appendix....219

Statistical test....220
Mann-Whitney U....220
Two-samples Kolmogorov-Smirnov....220
LAMMPS Fe Porphyrin Configuration File....221
LAMMPS INPUT FILE FOR Fe Porphyrin....227
Vita....230

LIST OF TABLES

Table 1.1 Fuel Cells Classification [8]..... 6
Table 1.2Electrode surfaces for ORR in aqueous solution[14]..... 12
Table 1.3 Intrinsic Exchange current values for different catalytic systems [29]. 21
Table 2.1 Statistical goodness of fit tests for SAFC system..... 53
Table 2.2 Experimental values..... 58
Table 2.3 Parameters values: base case..... 63
Table 2.4 Parameter values: optimized..... 68
Table 2.5 Activation, Ohmic and Concentration overpotentials a i≅0.2 A/cm^2 ... 77
Table 3.1 Statistical goodness of fit tests for NPMCs system. 94
Table 3.2 Experimental OCV and limiting current values. 102
Table 3.3 Fitted parameters: base case..... 105
Table 3.4 Parameter summary for 1mg catalyst loading. 108
Table 3.5 Parameter summary for 3mg catalyst loading..... 108
Table 3.6 Tafel variation parameter with respect to the mean 108
Table 3.7 Permeability variation parameter with respect to the mean..... 114
Table 3.8 Reversible electrode potential..... 118
Table 3.9 Activation, Ohmic and Concentration overpotentials at i≅0.2 A/cm^2 . 119
Table 4.1 Summary of the main DFT studies in PGM-free systems..... 131
Table 4.2 Simulation plan for Iron, Porphyrin and Iron Prophyrin 142
Table 4.3 Crystal Structure information for Pt and Fe..... 146
Table 4.4 Parameters for the Pt and Fe relaxation..... 147
Table 4.5 Simulation parameters for all systems 148
Table 4.6 Calculated reaction, adsorption, and free Gibbs energies. Metals (111) from CatApp. Porphyrin and Iron Porphyrin from this work. 153
Table 5.1 Experimental conditions..... 168
Table 5.2 Ensembles used in MD and MC simulations..... 179
Table 5.3 Iron Porphyrin molecule components..... 186
Table 5.4 OPLS-AA Non-Bonded Pairwise interactions 186
Table 5.5 Bond Stretching Parameters 187

Table 5.6 Angle Bending Parameters 187
Table 5.7 OPLS-AA Fourier Coefficients (kcal/mol) for Torsional Energy Functions 188
Table 5.8 MD System simulation data 194

LIST OF FIGURES

Figure 1.1 Multiscale methods to solve catalyst layer phenomena..... 7
Figure 1.2 Schematic representation of two and four electrons oxygen reduction reaction mechanism from Yeager and Adzic approaches. 10
Figure 1.3 Adsorption Models for O_2 and its reaction pathway in acid electrolytes[14]. 11
Figure 1.4 Tafel slope, as a function of OH coverage, for ORR assuming various rate-limiting steps on Pt(111) [31]. 19
Figure 1.5 Showing a) mass activity and b) specific activity at 0.9 V vs. RHE for a selection of nanoparticulate catalysts reported in literature[39]. 24
Figure 1.6 Surface model of active sites[54]. 27
Figure 1.7 FeN2+2/C: possible structure of most of the catalytic sites in Fe/N/C catalysts. FeN2/C: previously incomplete model of FeN2+2/C. FeN4/C: possible structure of the other catalytic sites in Fe/N/C catalysts[2]. 31
Figure 1.8 molecular orbitals of the five nitrogen coordinated Fe-centered sites providing the highest turnover frequency for this class of ammonia treated NPMCs[71]. 36
Figure 1.9 Fuel Cell losses representation. 42
Figure 1.10 Strategies to design catalyst to overcome the adsorbate-adsorbate relation that limits higher activities in Pt-based systems[96]. 44
Figure 2.1 CsH2PO4 phase diagram[102]. 48
Figure 2.2 SAFC cell components description. 55
Figure 2.3 SEM images of the SAFC showing the cathode thickness. a) 1.75 mg/cm^2 Pt b) 3.5 mg/cm^2 Pt c) 7 mg/cm^2 Pt. 57
Figure 2.4 Experimental Tafel slope for 3.5 mg/cm2 System in O_2..... 60
Figure 2.5 Permeability sensitivity values DC* = $1*10^{-11}$, $9*10^{-7}$, $2*10^{-6}$ - $7*10^{-6}$ [mol/cm-s-atm]. a) Loading: 1.75 mg/cm^2 Pt. b) Loading: 3.5 mg/cm^2 Pt. Tafel slope: 207 mv/dec b) Loading: 3.5 mg/cm^2 Pt. Tafel slope: 212 mv/dec. 64

Figure 2.6 Active area sensitivity in air. a) Loading: 1.75 mg/cm² Pt. Tafel slope: 200.5mv/dec b) Loading: 3.5 mg/cm² Pt. Tafel slope: 207 mv/dec b) Loading: 3.5 mg/cm² Pt. Tafel slope: 212 mv/dec. 64
Figure 2.7 Limiting current sensitivity in air. a) Loading: 1.75 mg/cm² Pt. Tafel slope: 200.5mv/dec b) Loading: 3.5 mg/cm² Pt. Tafel slope: 207 mv/dec b) Loading: 3.5 mg/cm² Pt. Tafel slope: 212 mv/dec. 65
Figure 2.8 Polarization curves fitting for air and oxygen at different loadings. a) 1.75 mg/cm² b) 3.5 mg/cm² c) 7mg/cm². 67
Figure 2.9 Calculated Tafel slopes for different loadings. 70
Figure 2.10 Calculated RCCD for different loadings. 71
Figure 2.11 Calculated roughness factor by using calculating i_0 values. 72
Figure 2.12 Calculated permeability values for different loadings..... 74
Figure 2.13 Current distribution across the catalyst layer a) 1.75 mg/cm² O_2 b) 1.75 mg/cm² Air c) 3.5 mg/cm² O_2 d) 3.5 mg/cm² Air e) 7 mg/cm² O_2 f) 7 mg/cm² Air. 75
Figure 2.14 Polarization curves with activation and ohmic overpotentials calculation from optimized Tafel parameters a) 1.75 mg/cm² O_2 b) 1.75 mg/cm² Air c) 3.5 mg/cm² O_2 d) 3.5 mg/cm² Air e) 7 mg/cm² O_2 f) 7 mg/cm² Air. 79
Figure 2.15 Overpotential activation, Ohmic and Mass transfer contribution at i≅0.2. Comparison with values for PEMFC at 80°C in Air at i≅0.1[110]. 80
Figure 3.1 Reaction environment schematic representation. 86
Figure 3.2 Possible active sites after pyrolysis..... 88
Figure 3.3 Fuel Cell scheme and electrodes reactions. 91
Figure 3.4 Schematic representation of the catalyst preparation. 96
Figure 3.5 Back-scattered and secondary electron images of the highly porous as-synthesized (A, B), 700°C pyrolyzed (C, D) showing the presence of iron nanoparticles, and acid treated (E, F) CHF-1 catalyst. The latter exhibits a lower density of metal particles and a higher porosity as a result of the acid leaching process [121]. 97

Figure 3.6 High-resolution (HR)TEM images of the 700°C pyrolyzed iron porphyrin catalyst (A) HRTEM image of the iron nanoparticle distribution on the catalyst structure. (B) HRTEM image showing an onion-like mesographitic nanoshell surrounding Fe particle. (C) HRTEM image showing the mesographitic structure of the carbon support. (D) HRTEM image of a typical NPMCs nanostructure involving carbon and metal aggregates [121]..... 97
Figure 3.7 RDE Polarization curves for our Iron Porphyrin material [121]..... 99
Figure 3.8 RDE Polarization curve Pt_3Ni[40]. 99
Figure 3.9 Experimental IR-free Polarization curves for different O2/Ar mass concentration feed. Operation temperature: 80°C. Anode: 0.3 mg Pt/cm² in 30% BASF. a) Cathode: 1mg/cm² Fe-PCPF/Nafion. Catalyst layer thickness: 14 μm. b) Cathode: 3mg/cm² Fe-PCPF/Nafion. Catalyst layer thickness: 72 μm..... 100
Figure 3.10 Experimental IR-free Polarization curves for different 20% O2/Ar and 100% O2 mass concentration feed. Operation temperature: 80°C. Anode: 0.3 mg Pt/cm² in 30% BASF. a) Cathode: 1mg/cm² Fe-PCPF/Nafion. Catalyst layer thickness: 14 μm. b) Cathode: 3mg/cm² Fe-PCPF/Nafion. Catalyst layer thickness: 72 μm. 100
Figure 3.11 Parameters Sensitivity for pure oxygen and 1mg/cm² loading Tafel slopes: 119 mv/dec and 68 mv/dec. a) Ari_o b) DC* c) I_{lim}..... 104
Figure 3.12 Polarization curves fitting for different O2/Ar mass concentration feed. Operation temperature: 80°C. Anode: 0.3 mg Pt/cm² in 30% BASF. a) Cathode: 1mg/cm² Fe-PCPF/Nafion. Catalyst layer thickness: 14 μm. b) Cathode: 3mg/cm² Fe-PCPF/Nafion. Catalyst layer thickness: 72 μm. 109
Figure 3.13 First and second Tafel slope behavior for oxygen concentration and catalyst loading variation. 111
Figure 3.14 RCCD parameter behavior for oxygen concentration and catalyst loading variation 111
Figure 3.15 Oxygen concentration and conversion across the catalyst layer. Weight/Weight percentage : a. 20%, b. 40%, c. 60%, d. 80% and, e. 100%.112

Figure 3.16 Permeability values a) Calculated from Darcy Law with modeled concentration profiles. b) Calculated from Springer Model, O_2 permeability in Nafion from Zhang, Lei et al., 2003 [123]. 115
Figure 3.17 Current Density distribution at different potentials. a) 20% O2, 1mg/cm² FePp. b) 20% O2, 3mg/cm². c) 100% O2, 1mg/cm² FePp. d) 100% O2, 3mg/cm² FePp. 116
Figure 3.18 Polarization curves with activation and ohmic overpotentials calculation from optimized Tafel parameters a) 20% O2 1mg/cm² FePp b) 100% O2 1mg/cm² FePp c) 20% O2 3mg/cm² FePp O2 d) 100% O2 3mg/cm² 120
Figure 3.19 Overpotentials contribution for pure oxygen and 20% case. Pt-based values from Arisetty et al. [110]. 121
Figure 4.1 Kramm and collaborators proposed structures from Mössbauer Spectroscopy [71]. 127
Figure 4.2 Heme Active sites representation[124] 127
Figure 4.3 Proposed ORR mechanistic pathways on Fe-N4/C and adjacent FeNPs/C in acidic and alkaline electrolyte[10]. 129
Figure 4.4FeN2+2/C type structure proposed by Szakacs and collaborators [126] 129
Figure 4.5 N-FeN2+2/C type structure proposed by Szakacs and collaborators [126] 129
Figure 4.6 Illustrative diagram of the nudged elastic band method [141]. 136
Figure 4.7 Schematic representation of Sabatier principle[145]. 143
Figure 4.8 Crystal Structures a)Pt (ccp) b)Fe(bcc) Relaxation steps 146
Figure 4.9 Kinetic Energy Cutoff. a) Pt b) Fe. 146
Figure 4.10 Monkhorst-Pack Mesh a) Pt b)Fe. 147
Figure 4.11 Potential Energy Curve to extract Lattice Parameters. a) Pt b) Fe.. 147
Figure 4.12 Kinetic Energy Cutoff for the simulation systems 148
Figure 4.13 Monkhorst-Pack Mesh for the simulation systems 148
Figure 4.14 Activation energy diagram for H_2O dissociation on Porphyrin. 151
Figure 4.15 Activation energy diagram for H_2 dissociation. 151
Figure 4.16 Activation Energy diagram for OH dissociation in Porphyrin. 151

Figure 4.17 Activation energy diagram for H2O dissociation. 152
Figure 4.18 Activation energy diagram for H_2 dissociation. 152
Figure 4.19 Activation energy diagram for OH dissociation. 152
Figure 4.20 Porphyrin corrected activation energies with CI-NEB. 153
Figure 4.21 Fe-Porphyrin corrected activation energies with CI-NEB. 153
Figure 4.22 Free energy diagrams for different (111) Metals [35]. a) Pt b) Ru c) Au d) Pd e) Rh f) Cu..... 156
Figure 4.23 Gibbs Energy for Our simulation system. a) Pt b) Fe c) Porphyrin d) Fe Porphyrin. 156
Figure 4.24 Gibbs energies for ORR model mechanism. Schematic representation of ORR on Pt-based catalyst [147]. 157
Figure 4.25 ORR Volcano Plot. 157
Figure 5.1 Synthesis scheme for Cu-TrPc/C complex covalently immobilized to BP2000 carbon support [148]. 163
Figure 5.2 XRD pattern of Cu-TrPc catalyst before and after pyrolysis from 600◦C to 950◦C. [148]. 163
Figure 5.3 Schematic representation of main structural changes occurring during HT of all Pc samples [149]. 164
Figure 5.4 Perfusion experiment set up. 168
Figure 5.5 Schematic representation of the perfusion calorimeter parts. 168
Figure 5.6 Calorimeter equilibration positions. 168
Figure 5.7 MD simulation scheme. 172
Figure 5.8 Thermostat comparison [159]. 181
Figure 5.9 Berendsen barostat and thermostat for different relaxation constants [159].....181
Figure 5.10 Fe Porphyrin bond types..... 186
Figure 5.11 Calorimetry results for copper triazole catalyst (Cu-TrPc).....191
Figure 5.12 Cu Kα x-ray diffraction patterns for the as-prepared catalyst (CHF-1), the catalyst after 700°C heat treatment (HT), and the catalyst after 700°C heat treatment followed by acid treatment and final 700°C heat treatment (HT+AT+HT)[121]. 191
Figure 5.13 Iron Porphyrin single molecule with wrong OPLS-aa parameters. . 192

Figure 5.14 Iron Porphyrin with the MM2 parameters from Marques work [165]. 192
Figure 5.15 Iron Porphyrin initial point..... 194
Figure 5.16 Iron Porphyrin final configuration 194
Figure 5.17 Total, Potential and Kinetic energy for the system..... 196
Figure 5.18. Typical radial distribution functions for Si in various forms: amorphous and liquid [167]. 196
Figure 5.19 Radial distribution of the final configuration..... 198

INTRODUCTION

The core of fuel cells is the catalytic material in charge of the reduction and oxidation reaction inside the electrodes. Pt-based catalysts are the catalyst of choice towards oxygen reduction reaction (ORR). Most catalyst employed are crystalline metallic systems, in particular, those corresponding to the platinum group such as Ru, Pd, Fe, Co, Ni, Cu, and Zn are used as ORR catalysts.

Catalyst layers build with these types of materials involve multiscale, multiphase and multicomponent phenomena. In addition to catalysis, the behavior of catalyst layers involves transport of reactants through porous media (gases or liquids), which occurs in the gas diffusion media (porous carbon structures), electronic transport trough porous carbons and protonic transport through electrolytes or ionomer.

To promote catalysis, the presence of an active site is required, which is a combination of three main components, which together form the triple phase boundary required for the reaction: electronic transport through porous or conductive materials, protonic transport across the ionomer, and catalyst particles to facilitate the reduction or oxidation reactions.

Recent efforts in catalysis have been focus on the replacement of Pt non-precious-metal-based (NPMCs) [1-3]. In order to reduce the Pt loading in cathodes without decreasing their performance there are three options, some of which can be used in combination: (1) enhancing Pt mass activity for ORR via alloying or core-shell nano structuring, (2) improving mass-transport properties of Pt-based cathodes, and (3) developing non-precious metal catalysts (NPMCs) with high performance for ORR [1, 4-6].

Either of the approaches mentioned above require the study and understanding of novel catalytic materials, ionomer and membrane-electrode assemblies. How to approach these newer catalysts or where to start was part of the process we developed in this study. First, we studied NPM catlyst and Solid Acid based catalyst layers with Pt. Initially, we applied standard experimental procedures to describe these system. However, in terms of modeling, most of these materials did not have any modeling approach at a time.

The work presented here illustrates the methodological modeling approach to understand novel materials and presented a couple between experimental design and modeling approach to describe non-conventional catalyst layer.

1 MODELING TECHINQUES FOR CATALYST LAYERS

Abstract

Modeling catalyst layers is a complicated task due to the complexity of its structure. These systems have different elements involving multiscale, multiphase and multicomponent problems. Fuel Cells catalyst layers have different components such as porous media support for electronic transport, ionomer for protonic transport and catalyst particles for electrochemical reactions

In order to design a catalytic system we need to take into account to understand the phenomena involve from the nanoscale up to the macroscale. This chapter gives us an insight into the main catalytic materials employ towards Oxygen Reduction Reaction (ORR), which is the key target towards fuel cells development; the phenomena involved in catalyst layers, and the modeling techniques apply to study these systems them.

1.1 Introduction

The need for clean and efficient use of energy rather than burning fuel in internal combustion engines instigated many companies to pursue fuel cell operated devices and vehicles available to the general public. A major challenge is to optimize the ORR, especially to make fuel cells operable in large-scale automotive applications. This challenge sparked a concentrated effort to improve fuel cell catalysts to meet the U.S. Department of Energy targets [7].

There are a wide variety of Fuel Cells, classified by temperature and mobile ions as Table 1 summarizes. The mobile ions can be transport either in liquid, polymeric or solid phase systems. Particularly, for Alkaline (AFCs), Polymer Electrolyte Membrane Fuel Cells (PEMFCs) and Solid Acid Fuel Cells (SAFCs) platinum group catalysts are the standard materials towards ORR. These Pt-based catalysts are crystalline metal systems combine with other metallic systems like Ru, Pd, Fe, Co, Ni, Cu, and Zn. They work either as nanoparticles to more complex catalyst structures like Pt_xM nanoframes.

Building catalyst layers involves multiscale, multiphase and multicomponent elements such as: 10 μm agglomerates of catalyst particles, support and ionomer, 20 to 50 μm clusters of agglomerates and 2 to 3nm catalyst particles, as Figure 1.1

illustrates. Relevant phenomena include transport of reactants through porous media (gases or liquids) in the gas diffusion media (porous carbon structures). Alternatively, the catalyst layer can be a separate entity between the membrane and gas diffusion layer. In the catalyst layer, the active site has three components, which together form the triple phase boundary required for the reaction: the carbon for electronic transport, the ionomer for protonic transport and the catalyst to facilitate the reduction or oxidation reactions.

In Fuel Cells, the cathode is the most studied electrode since it is the major source of losses and power density due to the five-orders-of-magnitude slower kinetics of the oxygen reduction reaction (ORR) on Pt. Moreover, the replacement of Pt and Pt alloys with non-precious-metal-based catalysts for the ORR is one important approach to achieving a sustainable and cost-effective power generation in Fuel Cells[1-3]. In order to reduce the Pt loading in cathodes without decreasing their performance there are three main options, some of which can be used in combination: (1) Pt mass activity increase by alloying or synthetizing core-shell nanostructures, (2) mass-transport improvement in Pt-based cathodes, and (3) the aforementioned non-precious metal catalysts (NPMCs) or Platinum Group Metal Free (PGM-free) development towards ORR [1, 4-6].

New catalytic materials and catalyst layer component studies raise questions when compared with Pt-based systems. For instance, what do the Pt- and PGM-free-based catalyst layers have in common? How can we identify and distinguish between performance-controlling factors in different catalyst layers? What makes one metal more suitable than another? What specific catalyst layer composition and structure are optimal? How do we or can we correlate energetics, structure and transport issues?

In order to probe these questions, it is important to set a baseline for comparison, which in this case will be Pt-based systems. Then the first step is to identify appropriate modeling methodologies for Pt-based systems for studies of performance, stability and catalyst layer phenomena.

Table 1.1 Fuel Cells Classification [8].

Fuel Cell Type	Mobile ion	Operating temperature	Application
Alkaline (AFC)	OH^-	50-200°C	Space vehicles
Proton Exchange Membrane (PEMFC)	H^+	30-100°C	Vehicles and mobile applications
Direct Methanol (DMFC)	H+	20-90°C	Suitable for portable electronic systems of low power
Phosphoric Acid (PAFC)	H+	~200°C	Series of 200-kW Combined Heat and Power (CHP) systems in use
Molten Carbonate (MCFC)	CO_3^{2-}	~650°C	Suitable for medium /large CHP systems, up to MW capacity
Solid Oxide (SOFC)	O^{2-}	500-1000°C	Suitable for all sizes of CHP systems, 2-kW to multi-MW

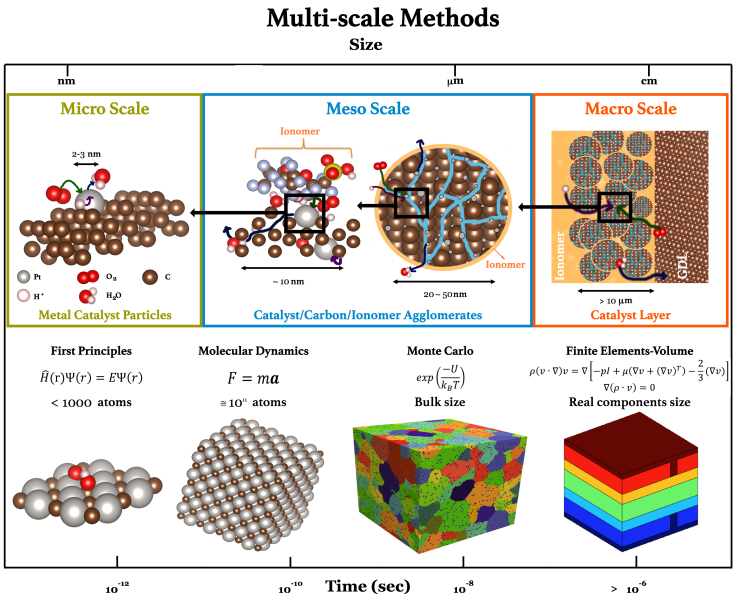


Figure 1.1 Multiscale methods to solve catalyst layer phenomena.

Pt-based catalyst layers contain microscopic, mesoscale and macrohomogeneous models. Microscopic models include local pore-level models as well as more detailed quantum mechanical models. The quantum mechanical models deal with detailed reaction mechanisms and elementary transfer reactions and transition states. Mesoscale models require microstructure detail description of the catalyst layer and study mainly, transport properties. Macrohomogeneous models are macroscopic in nature, use effective parameters to describe transport and kinetics and have every phase defined in each volume element and can be classified base on the length scale of the model [9].

As with Pt-based systems, the first step in modeling new catalyst layers is to identify and classify the main macroscopic parameters that affect the performance. Furthermore, we need to use robust and adequate experimental data sets, to be analyzed and to include as many independent and experimentally determined physical inputs as possible to reduce the degrees of freedom for fitting. Only then will a modeling study serve to reveal the physical basis of the important performance differences resulting from the use of given catalyst layer structures, on one hand, and different reaction pathways on the other [1, 4, 10]. The parameters we identify, as the key modeling parameters, will point out the modeling technique require for a deeper understanding of the catalyst layer phenomena

1.2 Oxygen Reduction Reaction

One of the major catalytic developments in the past decade is related to catalyst design to promote the oxygen reduction reaction with lower overpotential. To understand the challenges to overcome, we present a summary of this reaction, the main theory underlying its study and the major theory development to model this reaction.

The ORR is a multi-electron and multi-intermediate reaction path that includes a number of elementary reactions. Yeager was the first to propose two pathways for the ORR in acid solution in 1984[11]:

1. Direct 4-eletron pathway

$$\boldsymbol{O_2 + 4H^+ + 4e^- \rightleftharpoons 2H_2O} \qquad \textbf{Reaction 1.1}$$

With equilibrium potential $E^0 = 1.229V$ (vs. RHE)

2. Peroxide pathway

$$\boldsymbol{O_2 + 2H^+ + 2e^- \rightleftharpoons 2H_2O_2} \qquad \textbf{Reaction 1.2}$$

With equilibrium potential $E^0 = 0.67V$ (vs. RHE)

$$\boldsymbol{2H_2O_2 \rightleftharpoons 2H_2O + O_2} \qquad \textbf{Reaction 1.3}$$

With equilibrium potential $E^0 = 1.77$V (vs. RHE)

Both mechanism have been widely studied and are the common pathways accepted in the community. One of the modifications to this original idea was presented by Adzic et al. [12]. They proposed a parallel pathway, in which the direct and series mechanisms occur simultaneously, and the direct pathway is the dominant one. However, the detailed pathways are still under debate among different groups.

The representation made by Wroblowa et al[13] (Figure 1.2) is a good summary of both the Yeager and Adzic approaches. Figure 1.2 illustrates the general reaction mechanism. If the oxygen is adsorbed and goes through a direct pathway with rate constant k_1, the product is water. Otherwise, the oxygen adsorption can yield peroxide formation and thus a 2e- pathway. Even for the first electron transfer step, Yeager, Adzic and Damjakovic differ in their approaches [12, 14, 15].

The general approach involves multiple steps that involve the splitting of the O–O bond upon oxygen adsorption on the metal site. The adsorption can be done with three possible models. In the Griffith model, two oxygen atoms are adsorbed on top of one metal site. In the Pauling, one oxygen atom is adsorbed on the surface. In the bridge model, each oxygen is adsorbed in different sites as figure 1.3 illustrates [16]. Yeager derived three possible reaction paths based on these models, as figure 1.4 summarizes [14]. Moreover, he extended this study and classified numerous type of catalytic materials in aqueous solution based on these reaction mechanisms as table 1.2 summarizes and find the first electron reduction step as the liming step[14].

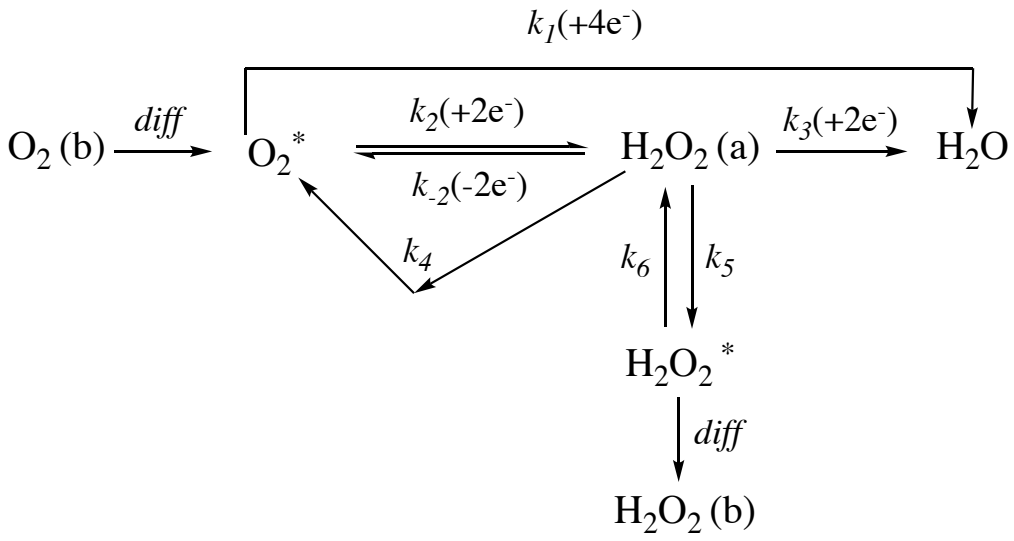


Figure 1.2 Schematic representation of two and four electrons oxygen reduction reaction mechanism from Yeager and Adzic approaches.

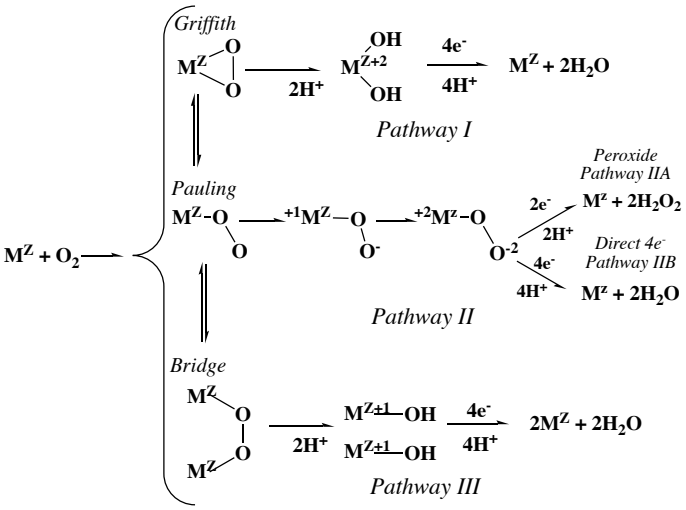


Figure 1.3 Adsorption Models for O_2 and its reaction pathway in acid electrolytes[14].

Table 1.2Electrode surfaces for ORR in aqueous solution[14]

Surface classification	Materials
Class I	*Reduction predominantly through HO_2^- formation*
	Graphite, most carbons
	Metals: Au, Hg, most oxide-covered metals
	Oxides: most transition metal oxides
	Transition metal macrocycles
Class II	*Reduction by both $4e^-$ and peroxide pathways*
	Pt, Pt alloys, platinum family metals
	Other metals: Ag, Pd
	Oxides: pyrochlores
	Some transition metal macrocycles (face-to-face porphyrins)
Class III	*Heterogeneous peroxide decomposition catalysts*
	Metals: Ag, Pt
	Oxides: spinels, perovskites, MnO_2
	Transition metal macrocycles

These early findings open the door to a theoretical approach towards ORR but limitations in theory and computational capacity to use quantum mechanics to calculate energies, structures, and reaction mechanisms for systems containing electrodes, adsorbates, and electrolytes delay its further development.

One of the main contributors to this area is the work of Anderson and collaborators who developed the reaction center model to include electrolyte effects and their relation to the overall reaction mechanism. They helped to develop a procedure to find adsorption energies for the intermediates on actual or potential electrocatalysts by including solvation energies for intermediates and finding the Gibbs energy relationship to the electrode potential and surface coverage [17-22].

Their main assumption, and the key to simplifying electron transfer processes, was to treat the adsorption energies as functions of the solution phase reversible potentials. This implies that the adsorption Gibbs energies for the intermediates formed during the electron transfer steps can be predicted as the reversible potential for each step and it should be equal to the reversible potential for the overall multielectron reduction[20].

If each electron and proton transfer step had 1.229 V reversible potential and low activation energy, the cathode electrocatalyst would deliver all the Gibbs energy of reaction as electrical work and would deliver it rapidly as[23]:

$$\Delta \boldsymbol{G = -nFU} \qquad \textbf{Equation 1.1}$$

Where ΔG is the Gibbs energy of the reaction, F is the Faraday constant and U is the electrode potential, which is calculated as the reversible potential on the surface [23]:

$$\boldsymbol{U_{surf}^{rev} = U^{0} + \frac{\Delta_{ads}E(Ox)}{F} + \frac{\Delta_{ads}E(R)}{F}} \qquad \textbf{Equation 1.2}$$

Where, $\Delta_{ads}E(Ox)$ and $\Delta_{ads}E(R)$ represent the adsorption energies of oxidation and reduction of each electron step and U^0 is defined as[23]:

$$U^0 = \frac{[E_{ox} - E_{red}]}{nF} + c \qquad \textbf{Equation 1.3}$$

Where E_{ox} and E_{red} represent the internal energies excluding zero-point vibrational effects. This has been proved to be in agreement with experimental values. The value of the constant depends on the H^+ treatment in the calculations.

Yeager's and Anderson's groups' approaches contributed to the development of theoretical applications for electrocatalysis. Another main contribution was made by Nørskov and collaborators who developed a methodology to calculate the overpotential in fuel cell cathodes including the effect of water by adding monolayers of water, neglecting effect of electric field due to its low contribution compared to overpotential and by relating the reaction energies to the electro-kinetics of the system[24].

This electro-kinetic model assumes that the activation barrier for the rate limiting proton-transfer step is equal to the larger of the free energy differences for the intermediates calculated as[24]:

$$\Delta G_1(U) = G_{HO* + \frac{1}{2}H_2}(U) - G_{O* + H_2}(U) = \Delta G_1(0) + eU = \Delta G_1(U_0) + e\eta \qquad \textbf{Equation 1.4}$$

$$\Delta G_2(U) = G_{H_2O}(U) - G_{HO* + \frac{1}{2}H_2}(U) = \Delta G_2(0) + eU = \Delta G_2(U_0) + e\eta \qquad \textbf{Equation 1.5}$$

These relations correspond to the stability of OH* and O* intermediates on the surface. Then, the rate constant can be calculated as:

$$k(U) = k_0 exp\left(\frac{-\Delta G(U)}{kT}\right) \qquad \textbf{Equation 1.6}$$

In terms of the current density, equation 1.6 can be expressed as:

$$i_k(U) = i_k^0 exp\left(\frac{e\eta}{kT}\right) \qquad \textbf{Equation 1.7}$$

$$i_k^0 = \tilde{\imath_k} exp\left(\frac{-\Delta G(U_0)}{kT}\right) \qquad \textbf{Equation 1.8}$$

Where i_k^0 is the exchange current and the $\tilde{\imath_k}$ is a constant calculated from experimental data. Equation 1.8 leads to a Butler-Volmer type relation as follow:

$$U = U_0 - blog\left(\frac{i_k}{i_k^0}\right)$$ **Equation 1.9**

Further development of this initial model, leads to the volcano trends in ORR activity as a function of the intermediate adsorption, which will be described in more detail in Chapter 5. Some important description of the thermodynamic theory for multi-electron transfer reaction was made by Koper [25], where three basic steps can be taken into account:

1. Formation of the surface-adsorbed superoxide intermediate

$$O_2 + H^+ + e^- \rightleftharpoons OOH_{ads}$$ **Reaction 1.4**

2. Simultaneous electron and proton transfer from OHH* as precursor for O-O bond breaking

$$OOH_{ads} + H^+ + e^- \rightleftharpoons 2OH_{ads}$$ **Reaction 1.5**

3. Reduction of the surface-bonded OH* to water

$$OH_{ads} + H^+ + e^- \rightleftharpoons H_2O$$ **Reaction 1.6**

In his approach he uses the value of the equilibrium potential to define the free energy of the oxygen molecule, taking the free energy of liquid water as the energy zero, $\Delta G(O_2) = 4.92eV$. The standard potentials for reactions 1.5 to 1.6 should satisfy:

$$\frac{E^0_{O_2/OOH} + E^0_{OOH/OH} + E^0_{OH/H_2O}}{4} = E^0_{O_2/H_2O} = 1.23V$$ **Equation 1.10**

In terms of the least favorable reactions, the zero thermodynamic overpotential, corresponding to the optimal catalyst, is achieved when:

$$\Delta G(OH_{ads}) = 1.23eV$$ **Equation 1.11**

$$\Delta G(OOH_{ads}) = 3 \times \Delta G(OH_{ads}) = 3.69eV$$ **Equation 1.12**

Equations 1.2 and 1.3 give us a theoretical value of the free energies of the intermediates. However, the strong correlation between them (OH, OOH and, O), generate relationships show in equation 1.4 and 1.5 found by Norskov et al. [26, 27] for (111) surfaces:

$$\Delta G(OH_{ads}) \approx 0.50 \times \Delta G(O_{ads}) + K_{OH}\ eV \qquad \textbf{Equation 1.13}$$

$$\Delta G(OOH_{ads}) \approx 0.53 \times \Delta G(O_{ads}) + K_{OOH}\ eV \qquad \textbf{Equation 1.14}$$

Where the 0.5 slopes in these equations reflect the double bond of OH and OOH. From equations 1.4-1.5 Koper concluded that the difference between the free energies is $3.29eV = K_{OOH} - K_{OH}$, while the theoretical diffference should be $2\times C_0$=2.46eV. The intermediate interaction is the reason for the non-zero overpotential for ORR for even the best catalyst.

Another important conclusion from Koper's study is that O-O bond breaking is not potential determining and allegedly never rate determining (Reaction 1.5). This agrees with earlier suggestions made by Yeager[11]. Finally, from the theoretical perspective, the minimum overpotential will be defined as

$$\eta_T = \frac{(K_{OOH} - K_{OH} - 2\times C_0)}{2} = 0.41V \qquad \textbf{Equation 1.15}$$

All these studies stimulated further analysis and catalyst improvement. One of the key aspects for understanding the ORR is to comprehend the oxygen and catalytic surface interaction. Moreover, it is crucial to know the nature and coverage of adsorbed reaction intermediates. However, to date there is no simple, adequate spectroscopic method for identifying adsorbed intermediates. To overcome the experimental limitations, computational studies can provide insights regarding intermediates, their geometries and energies and will help to select the catalytic materials that overcome the minimum overpotential to improve ORR in fuel cells.

1.3 ORR Kinetics

The analysis of the ORR reaction was presented from a thermodynamic perspective. When in fuel cells applications, it is desirable to have the ORR occurring at potentials close to the reversible electrode potential with a satisfactory reaction rate. The cathodic current can be calculated using the Butler-Volmer equation as[28]:

$$I_c = i^0_{O_2}\left(e^{\frac{n\alpha F\eta_c}{RT}} - e^{\frac{n(1-\alpha)F\eta_c}{RT}}\right) \qquad \textbf{Equation 1.16}$$

Where Ic is the oxygen reduction reaction current density, $i_{O_2}^0$ is the exchange current density, n is the number of electrons transferred in the rate determining step, α is the transfer coefficient, η_c is the overpotential for ORR, F is the Faraday constant, R is the gas constant, and T is the temperature in Kelvin. To obtain high current at low overpotential, the exchange current $i_{O_2}^0$, should be large, and/or $\frac{RT}{n\alpha F}$ should be small [29].

1.3.1 Tafel Slope

If the overpotential is large, the backward reaction is negligible and Equation 1.16 can be simplified as:

$$\boldsymbol{I_c = i_{O_2}^0 e^{\frac{n\alpha F\eta_c}{RT}}} \quad \textbf{Equation 1.17}$$

The plot of *log Ic* vs η_c gives a linear relationship, and the slope is $\frac{2.3RT}{n\alpha F}$. This slope is called the Tafel slope. The parameters determining the Tafel slope are $n\alpha$. The higher the Tafel slope, the faster the overpotential increases with the current density. Thus, for an electrochemical reaction to yield a high current at low overpotential, the reaction should exhibit a low Tafel slope or a large $n\alpha$. The electron transfer coefficient is a key factor determining the Tafel slope. For ORR, the transfer coefficient is dependent on temperature. On a Pt electrode, the transfer coefficient of ORR increases linearly with temperature in the range of 20–250°C [29]:

$$\boldsymbol{\alpha = \alpha_0 T} \quad \textbf{Equation 1.18}$$

α_0 is the electron transfer coefficient of ORR.

Tafel slope is an important kinetic parameter and its dependence on the electron transfer process makes it indirect descriptor of the structure role in the ORR process. For ORR, usually two Tafel slopes are obtained, 60 mV/dec and 120 mV/dec. These values can be deducted from reaction mechanism and assuming the potential steps.

The work of Adzic and collaborators [30] combines experimental data and a micro-kinetic model, with calculated activity and energy barriers for the ORR reaction. They found that the Tafel slope transition occurs at 0.77V and it is

related to the transition between adsorbed O and OH on Pt/C systems.

Holewinski and Linic expand this approach and study the Tafel slope behavior as a function of the OH coverage as figure 1.4 illustrates [31]. They proved that for electrode reactions, simultaneous changes in electrocatalytic turnover rate and the number of active sites could lead to nonlinear Tafel behavior and variable reaction orders. The reaction mechanism they studied was:

$$* + \boldsymbol{O_{2(g)}} + (\boldsymbol{H^+ + e^-}) \leftrightharpoons \boldsymbol{OOH^*} \qquad \textbf{Reaction 1.7}$$

$$\boldsymbol{OOH^*} + * \leftrightharpoons \boldsymbol{O^*} + \boldsymbol{OH^*} \qquad \textbf{Reaction 1.8}$$

$$\boldsymbol{O^*} + (\boldsymbol{H^+ + e^-}) \leftrightharpoons \boldsymbol{OH^*} \qquad \textbf{Reaction 1.9}$$

$$2\left(\boldsymbol{OH^*} + (\boldsymbol{H^+ + e^-}) \leftrightharpoons \boldsymbol{H_2O_{(g)}} + *\right) \qquad \textbf{Reaction 1.10}$$

Their kinetic model shows a double Tafel slope, shifting from −60 mV/dec to −120 mV/dec, as an indication of a mechanism that is limited by the initial reduction of O_2. They also show that intermediate species such as OH can block active sites and be present in high coverage, but can still be controlled by equilibrium. Co-adsorbed species such as water are not apparent from cyclic voltammetry but may still alter the kinetics through site blocking as well.

1.3.2 Exchange Current Density

The exchange current density is an important kinetic parameter representing the electrochemical reaction rate at equilibrium. For an electrochemical reaction, both forward and backward reactions can occur

$$\boldsymbol{O} + \boldsymbol{ne^-} \leftrightharpoons \qquad \textbf{Reaction 1.11}$$

At equilibrium, the net current density of the reaction is zero. The magnitude of the exchange current density determines how rapidly the electrochemical reaction can occur. The exchange current density of an electrochemical reaction depends on the reaction and on the electrode surface on which the electrochemical reaction occurs[29]. Therefore, electrode materials or catalysts have a strong effect on ORR kinetics. Different materials can give different exchange current densities.

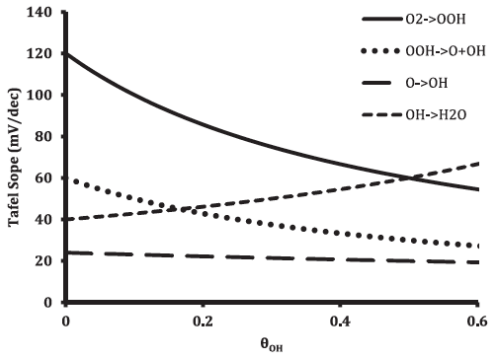


Figure 1.4 Tafel slope, as a function of OH coverage, for ORR assuming various rate-limiting steps on Pt(111) [31].

Table 1.3 lists the ORR exchange current densities on various electrode materials and its values are related to the true electrode area and to the reactant concentration (or partial pressure, for a gas). The use of the intrinsic exchange current density, obtained by correcting the exchange current density with the electrochemical surface area and can be calculated from equation 1.10[32]:

$$\boldsymbol{i_0^{app} = (ECSA)_c i_{O_2}^0 \left(\frac{P_{O_2}}{P_{O_2}^0}\right)^{\alpha}} \qquad \textbf{Equation 1.19}$$

Where i_0^{app} is the apparent exchange current density; (ECSA)c is the electrochemical surface area of the cathode catalyst; $i_{O_2}^0$ is the intrinsic exchange current density; $P_{O_2}^0$ is the standard O2 partial pressure; P_{O_2} is the actual O2 α is the transfer coefficient of ORR.

The relationship between exchange current density and temperature follows the Arrhenius equation as equation 1.11 illustrates.

$$\boldsymbol{i_{O_2}^0 = I_{O_2}^0 e^{-\left(\frac{E_a}{RT}\right)}} \quad \textbf{Equation 1.20}$$

Where $\boldsymbol{I_{O_2}^0}$ois the exchange current density at T = ∞, E_a is the activation energy. The temperature dependence of ORR on Pt electrodes have been investigated both in half-cells and in fuel cells. Equation 1.20 is equivalent to equation 1.7 and gives us a theoretical tool to study electrocatalyst behavior in newer catalytic materials.

1.4 Catalytic Materials for ORR

The oxygen reduction reaction is the major focus of efforts to improve fuel cells performance, as noted above. Pt and other group VIII metals are known to be very active as oxidation electrocatalysts. This is an illustration of the Sabatie Principle which suggests that the metals in middle of the periodic table demonstrate an optimal metal-adsorbate bond strength necessary to balance surface reaction steps and product desorption steps.

Table 1.3 Intrinsic Exchange current values for different catalytic systems [29]

Electrode material/ catalyst	ORR Exchange Current density A/cm²	Electron transfer coefficient	Electron transfer number in RDS	Measurement conditions
Pt	$2.8*10^{-7}$	0.48	-	At Pt/Nafion interface at 30°C
PtO/Pt	$1.7*10^{-10}$	0.46	-	At Pt/Nafion interface at 30°C
FePc	$1.3*10^{-7}$	-	-	In pH 1.3 solution
PtFe/C	$2.15*10^{-7}$	0.55	1	In 0.5M H_2SO_4 at 60°C
PtW2C/C	$4.7*10^{-7}$	0.45	2	In 0.5M H_2SO_4 at25°C
	$5.0*10^{-5}$	0.47	1	
Ru_xSe_y	$2.22*10^{-8}$	0.52	1	In 0.5M H_2SO_4 at25°C
$Ru_xFe_ySe_z$	$4.47*10^{-8}$	0.52	1	In 0.5M H_2SO_4 at25°C

Ccatalyst loss and deactivation tend to be quite severe in electrocatalysis due to the presence of solution, ions, and electric fields, which can lead not only to catalyst poisoning but also catalyst dissolution. This significantly limits the choice of catalytic materials to specific supported metals/alloys, metal oxides, and other stable inorganic materials such as chalcogenides or carbides [7, 33-36]. The catalysts used for ORR are typically carbon supported, leading to many issues such as contact resistance between metallic particles and the carbon matrix, particle dissolution and agglomeration and carbon support corrosion.

The most efficient catalyst found so far is platinum (or Pt alloys) due to its electronic properties, stability and resistance to the fuel cell environment. Platinum is partly to blame for the relatively high cost of PEM Fuel Cells due to the high loading necessary at the cathode (0.4 mg_{Pt}/cm^2)[37]. One strategy to reduce costs requires reducing the Pt loading, which requires better activity via alloying or core-shell nanostructuring[7, 33, 37-40] or developing Platinum Group Metal free (PGM-free) or Non-Precious Metals Catalyst (NPMCs) with high performance for ORR[1, 4, 41-47].

1.4.1 Pt-based Catalyst

The tareget for platinum reduction in fuel cells is roughly one order of magnitude to be similar to ladings in catalytic converters. This means that a catalyst with a stable activity of around 1.6 A/mg *mass activity* at 0.9 V measured in a fuel cell is required[37]. Pt-based catalyst development is a fast moving field and efforts have been focused on developing high-performance catalyst with low precious metal content [7, 37, 39, 40, 48].

To achieve this goal, two paths are pursued: (i) optimization of electrode structures so that the effect of reducing the cathode Pt-loading is limited to the purely kinetically predicted voltage loss over the entire current density range and (ii) implementation of more active Pt-alloy catalysts with reported mass activity gains in PEMFCs[37]. Through alloying Pt with non-noble metals and by generating different nanostructures the intrinsic activity of these materials can be increased. In this particular matter, the state of the art alloys are summarized in

figure 1.5[39].

The PtNi NSTF (nanostructure thin film) binary alloys are the most promising ones in terms of ORR activity, with mass activities exceeding those of carbon supported high surface area catalysts. The PtCo NSTF catalysts were significantly less active than their nickel-containing counterparts. With the exception of the PtNiFe NSTF, the ternary alloys do not approach the level of the PtNi. Finally, the content of Pt in the PtNi NSTF was further reduced in an effort to lower the total Pt loading, which did not lead to increased kinetic activities, and hence also did not yield increased mass activities.

When a Pt(111)-skin structure is prepared over a bulk single-crystal alloy of Pt_3Ni. the activity increases two orders of magnitude. Caged, hollow, or porous nanoparticles offer another promising approach for meeting these performance goals. The hollow interior diminishes the number of buried nonfunctional precious metal atoms, and their uncommon geometry provides a pathway for tailoring physical and chemical properties. $PtNi_3$ solid polyhedra are transformed into hollow Pt_3Ni nanoframes with surfaces that have three-dimensional (3D) molecular accessibility[40].

1.4.2 ORR in Pt-based catalyst

To understand the ORR on Pt-based catalyst, it is necessary to understand the chemisorption of oxygen molecule on the electrocatalyst surface. The adsorbate structure, bonding type, and energy are key element influencing adsorption effects on the reaction kinetics. Theoretical studies of chemisorption of oxygen molecule can provide information about the nature of bonding at the surface, bond strength, geometry, and site preferences of adsorbates.

Li and Balbuena performed DFT calculations to study the interactions of oxygen with platinum clusters. They found that for atomic oxygen, a bridge-site adsorption is the most stable structure. The adsorption energy for atomic oxygen shows a strong dependence on the metal cluster size and geometry. A bond-order conservation approximation analysis illustrates that the dissociation activation energies depend on the Pt cluster size [49].

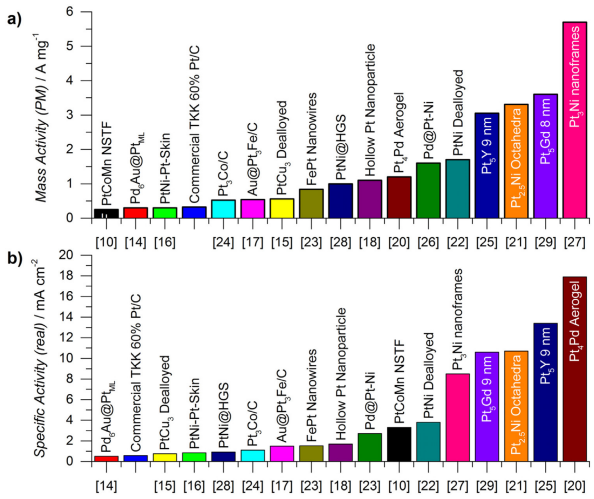


Figure 1.5 Showing a) mass activity and b) specific activity at 0.9 V vs. RHE for a selection of nanoparticulate catalysts reported in literature[39].

Others have shown that oxygen adsorption and reduction processes in nanosized electrocatalysts lead to considerably different catalytic activity from clusters versus extended surfaces[17, 21, 33]. These investigations suggest that effects observed upon particle size reduction go well beyond the increase in surface area and involve fundamental physical and chemical changes in the reaction steps. Han and his coworkers explicitly studied Pt nanoparticles with 1 and 2 nm sizes and compared their chemical adsorption properties to those of an extended flat Pt (111) surface. As atomic oxygen (O) and hydroxyl group (OH) are two intermediate species of importance in the ORR pathway, they focused on the effect of particle size and Pt coordination on the chemisorption energies of O and OH[50]. Based on their and Balbuena's calculations, the chemisorption energies of O and OH on the Pt(111) surface vary considerably from on that of 1 and 2 nm particles. Only sites near the center of the (111) facet on the 2 nm particle display similar adsorption energies to that on the Pt(111) bulk surface. While they find that on the bulk surface the fcc site is the most stable adsorption site, in agreement with previous work from Mavrikakis and collaborators[51], oxygen adsorption is strongest at bridge sites on the edges of the 2 and 1 nm particles.

For both particles, the maximum adsorption energy is larger than on the bulk surface. Depending on the location of sites, the adsorption energies at the fcc and hcp sites of the nanoparticles can be larger or small than that of the bulk surface value, with adsorption becoming stronger for site locations closer to the edge of the surface.

Further studies made by Norskov and collaborators [52, 53] allowed them to generate a model of the active site and describe when the reaction mechanism proceeds via a 4e- or a 2e- pathway. OOH and OH intermediates are significantly stabilized in a hydrogen-bonded network on a catalyst surface and they prefer to bind on sites which are in registry with the lattice of extended hydrogen bonded networks. However, when the O–O bond is broken in a chemical step, it dissociates to O and OH. Adsorbates formed on the interstitial sites, are less stable than intermediates within the hydrogen-bonding network due to weaker hydrogen bonding and repulsion from adsorbates within the hydrogen-bonding network.

They considered two different active surface sites [53]: lattice sites, ∗A, which have optimum hydrogen bond stabilization, and interstitial sites, ∗B, which have limited or no hydrogen bond stabilization (Figure 1.6). The interstitial sites provide free sites required for the dissociation of the O–O bond, which in a kinetic model would otherwise be strongly suppressed on the surface blocked with OH. They took the ∗A sites to be saturated at 1/3 ML coverage of OH, since this structure is found to be particularly stable. Each ∗A site in the structure is associated with an interstitial ∗B site, and one Pt site blocked by a solvating water molecule. Adsorption of O2 and formation of OOH on the interstitial sites in the hydrogen-bonded network is neglected on the interstitial sites (*B).

Mavrikakis et al. performed spin-polarized DFT calculations to study the ORR catalytic activity of platinum monolayers supported on close-packed transition metal surfaces [(Au(111), Pt(111), Pd(111), and Ir(111)]. They observed that OH removal is the rate-limiting step for ORR at the potential of 1.23 V. At a cell potential of 0.80 V, the proton/electron transfer steps become easier, and Pt*/Pd shows the highest activity among the surfaces examined, even higher than that of pure Pt(111). The activity of the other two surfaces, namely, Pt*/Au and Pt*/Ir, is lower due to the difficulty in OH removal and in O–O bond scission, respectively. Their findings provide additional insights into the ORR mechanism for these supported platinum monolayer surfaces.

From the studies above we have seem the catalytic activity dependence on oxygen adsorption energy, the dissociation energy of the O-O bond, and the binding energy of OH on the Pt surface. The electronic structure of the Pt catalyst (Pt d -band vacancy) and the Pt-Pt interatomic distance (geometric effect) can strongly affect these energies. Pt alloys have been studied as well and calculations have predicted that PtM (M=Fe, Co, Ni, etc.) alloys should have higher catalytic activity than pure Pt. This again has been proven by experiments by Norskov and collaborators [24].

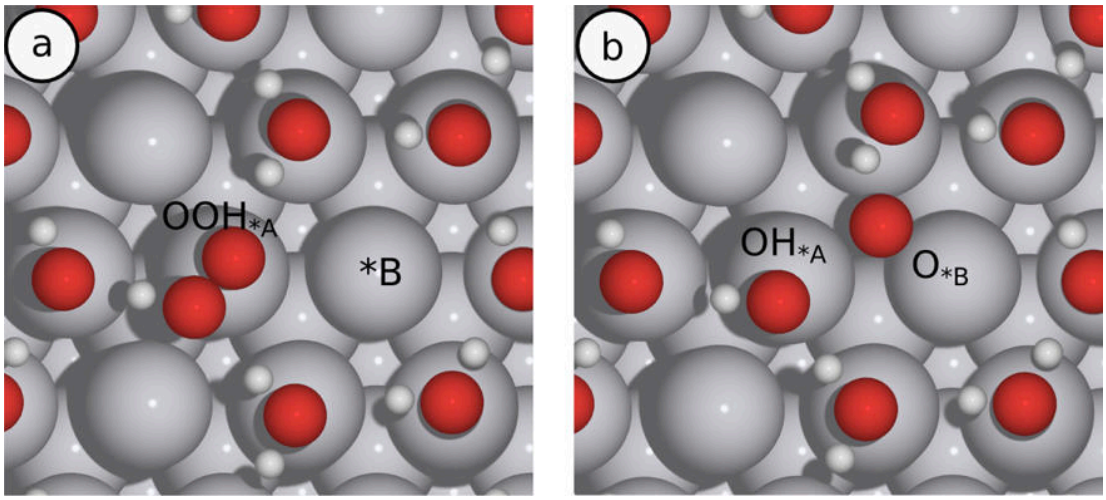


Figure 1.6 Surface model of active sites[54].

Stamenkovic et al. [55] found that on Pt_3Ni, the ORR is 90 times faster than on pure Pt. Unfortunately, dissolution of the transition metal alloyed in the PtM catalysts is a major drawback because these transition metals are electrochemically soluble at a potential range between 0.3 to 1 V vs. NHE in low pH media. More effort is needed to solve this problem.

To summarize for ORR in Pt systems, the evidence and confirmation of multiple Tafel slopes are related to the adsorption energies of O and OH and it is a function of OH coverage. To obtain the maximum catalytic activity, the adsorption energies of reactive intermediates and surface coverage should be balanced. If the catalyst binds oxygen too strongly, as in the case of Pt, the ORR activity is restricted by the rate of removing surface oxides and anions from surface. On the other hand, when the catalysts bind oxygen too weakly, the ORR activity is slowed down by the rate of transferring electron and proton to adsorbed oxygen.

1.4.3 Non-Precious Metal Catalyst (NPMCs) or Platinum Group Metal Free Catalyst (PGM-free)

Numerous groups have focused their attention on developing catalysts based on metals with higher natural abundance than Pt, such as Fe and Co. One of the first NPMCs studied was cobalt phthalocyanine as an ORR catalyst for fuel cells in 1964 by Jasinski [56]. Later, Ross and Wagner summarized the suitable ORR catalysts in four groups: metal oxides, chalcogenides (sulfides, selenides and tellurides), interstitial compounds (carbides, nitrides, silicides and borides) and organometallic compounds (aromatic macrocyclic porphyrins, phthalocyanines and related compounds) [57].

Catalysts derived from metal organic frameworks (MOFs) are a developing area due to the accessibility of metal cations within the MOF structure, the high volumetric density of metal-ion sites and high micropore surface to synthesize NPMC [43-46]. One important feature for NPMCs is the formation of a microporous structure for Me/N/C catalyst to enhance activities, as Jaouen et al. showed [58]. In this sense, the use of microporous organic polymer (MOP) networks as a nitrogen source is important in the development of more active

catalyst. Those formed from polypyrrole (PPy) and polyaniline (PANI) are the most common MOPs [5, 48, 59-63]. Among them, the organometallic compounds group has become the most studied. Particularly, iron- and cobalt- based macrocyclic compounds exhibit the highest catalytic activity for ORR [1, 4, 58, 62, 64, 65]. Recently, some papers reviewed the classification, mechanism, activity and performance of Pt-free catalysts [1, 37, 58, 63, 64]. Jaouen et al. reviewed the metal/nitrogen/carbon (Me/N/C) catalysts obtained through the pyrolysis of iron and/or cobalt precursors, nitrogen- and carbon- precursors for the ORR [1].

However, the stability and activity of NMPCs, especially in acidic electrolytes, is typically much lower than for Pt catalysts. Advancing this situation has been achieved mainly through brute force efforts, involving pyrolyzing many different carbon precursors and additives, due to the lack of understanding of its catalyst nature. Thus, it is imperative to elucidate fundamental aspects such as (a) the role of the transition metal in ORR activity or (b) the ORR active site nature (singular, bi-functional, multi-functional) and these are still unknown [1, 65].

Dodelet's research group at the INRS is one of the biggest groups working toward synthesis and active site identification. His group developed a unique strategy for NPMC synthesis by mixing a carbon support with iron-containing precursor and then subjecting the materials to a heat treatment in ammonia as the source of nitrogen [65-67]. These researchers determined that the ORR activity of this class of NPMC was influenced by the formation of micropores occurring during ammonia treatment, resulting from ammonia etching of the carbonaceous materials with a preference for the disordered carbon phase. They observed that, at a weight loss of approximately 35 %[66], ORR activity was optimized, owing to the maximum number of active sites formed, hosted in the micropores of the carbon support in a configuration similar to figure 1.7. Clearly, there is a marked benefit of having a higher number of micropores with uniform dispersion throughout the entirety of the NPMC catalyst particles in order to increase and maximize the active site density for this class of catalyst.

Advancing on these fundamentally significant findings, Dodelet's research team opted to use a pore filler method using highly microporous Black Pearls 2000 (BP) carbon support as the starting substrate for NPMC synthesis[47]. The

pores of the BP support were filled by ball milling with organic 1,10-phenanthroline and iron acetate as the source of nitrogen and iron, respectively.

This pore-filled composite was then subjected to pyrolysis in argon at 900 °C, inducing carbonization of the organic complexes to a disordered carbon phase, most likely accompanied by the formation of the proposed micropore-hosted active site structures entrapped within this phase. A second heat treatment in ammonia was then employed. This catalyst was found to possess high NPMC activity, approaching that of platinum catalyst at near open circuit potential and providing a volumetric activity of 99 A/cm^3 at an iR-corrected cell voltage of 0.8 V, approaching the DOE's 2010 target of 130 A/ cm^3.

Zelenay's group at the Los Alamos National Laboratory utilized a different approach to the development of highly active NPMCs [62]. An aniline precursor was used and polymerized in the presence of transition metal species (Fe and/or Co) and a high surface area graphitic Ketjen black support (alternatively they also used an ethylene diamine/Co impregnated carbon support). The authors claimed that the structural similarities between polyaniline (PANI) and the graphitic carbon support could enhance the interaction between the two species and effectively facilitate the formation of active site structures on the support surface during high temperature heat treatment (between 400 and 1,000 °C) in an inert environment.

Moreover, enhanced active site densities could be obtained due to the high nitrogen content of PANI, which is a prerequisite for ORR active site formation. The ordered structure of PANI further ensures the uniform distribution of nitrogen throughout the catalyst precursors and can allow for improved active site dispersion throughout the entire NPMC surface area. Following heat treatment, these catalysts were acid leached in 0.5 M H_2SO_4 at 80°C for 8 h, followed by another heat treatment under inert environment. This post treatment procedure is utilized in order to leach surface inactive species, such as metal and/or metal oxide nanoparticles that can block ORR active moieties.

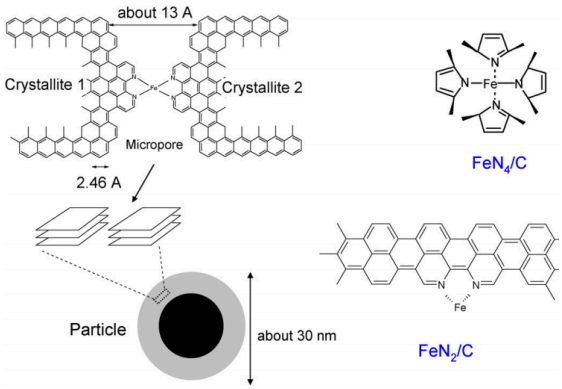


Figure 1.7 FeN2+2/C: possible structure of most of the catalytic sites in Fe/N/C catalysts. FeN2/C: previously incomplete model of FeN2+2/C. FeN4/C: possible structure of the other catalytic sites in Fe/N/C catalysts[2].

Similar post treatment acid leaching and pyrolysis techniques have been effective for improving the performance of NPMCs [46, 68], indicative of the importance of increasing active site exposure. By half-cell ORR kinetic investigations of the best reported PANI-based materials [62], a half-wave potential only ca. 59 mV below a commercial Pt/C catalyst-coated electrode with a Pt loading of 60 μg/cm^2 was achieved in acid media. Moreover, in MEA testing a maximum MEA power density of 0.55 W/cm^2 was obtained, coupled with promising operational stability demonstrated through half-cell and MEA degradation protocols. In this study, appropriate selection of precursor materials and careful control and optimization of the fabrication techniques resulted in a high density of active site formation.

1.4.4 NPMCs and active sites

Although there is significant debate in the scientific community on the exact nature of the active site structures associated with NPMCs[1, 69], progress made in recent years toward understanding the overall impact of catalyst properties and fabrication techniques in order to deliberately modulate the turnover frequencies will be discussed in this section. Primarily, the uncertainty with heat-treated NPMCs lies in elucidation of the exact identity of the sites responsible for ORR activity. Several authors claim that transition metal centers are not the locale for ORR activity and that performance is governed by catalytically active nitrogen–carbon species[10, 46, 70]. Graphitic nitrogen, pyridinic nitrogen, or edge plane exposure sites arising due to nitrogen incorporation have been claimed to provide the most activity out of available species.

Other authors claim that metal-centered structures comprise the locale for catalytic activity [71-74], such as in the case of non-pyrolyzed transition metal macrocycles. For these cases, the impact of the metal type, redox behavior, electronic properties, and ligand effects will be influential toward the inherent ORR activity or turnover frequency of each active site structure. During high-temperature heat treatments, it is extremely difficult to predict, control, and

probe the atomic reconfigurations occurring, so several researchers have turned to studies on non-pyrolyzed macrocycle NPMCs for fundamental insight into the factors governing catalytic activity.

The nature of the environment surrounding the active site metal center will also have a direct impact on catalytic turnover frequencies, elucidated by the difference in activity observed between various macrocycle structures (i.e., phthalocyanine of porphyrin). Furthermore, substituent groups are capable of tailoring the physicochemical properties of the metal-centered active site structures. For example, Baker et al.[75] investigated several substituted iron phthalocyanine structures and suggested that the presence of substituent groups could influence the electron density of the active metal centers. While studies of this nature (non-pyrolyzed) provide a good foundation for the design and development of future generation NPMC, reliable techniques of transferring over the concepts to pyrolyzed NPMC are necessary.

Recently, investigations have shifted to focus on how the physicochemical properties and surrounding environments of the metal-centered active site structures in NPMCs can positively impact ORR turnover frequencies. Using carbon black-supported Fe macrocycles as a starting point, Kramm et al. [72] used X-ray photoelectron spectroscopy coupled with Mossbauer spectroscopy to probe the electronic properties of coordinated Fe-nitrogen active site structures remaining after high-temperature pyrolysis. The authors observed that increasing pyrolysis temperatures would lead to an increase in the electron density of the metal ion center, ultimately leading to improved ORR kinetics observed for these samples. These results can be linked to the fundamental investigations on non-pyrolyzed NPMCs, whereby heat treatment at different temperatures will enhance interactions between the macrocycle complex and the carbon support, modifying the active site surrounding environment and tuning the ligand–metal center interactions. This can potentially exert electron-donating behavior to the Fe ion centers and improve the overall turnover frequency of each individual active site structure. This investigation provides fundamental significance because it demonstrated the possibility of modulating the turnover frequencies of

metal-centered active sites in pyrolyzed NPMCs by tuning the specific electronic and structural properties of the surrounding environments.

Zagal et al.[76] provided a similar report on a series of non-pyrolyzed and pyrolyzed NPMCs that associated differences in the catalytic activity to variations in the redox potential of the metal centers. Using different precursor materials, synthesis techniques, and pyrolysis temperatures can lead to these variations, and developing effective strategies to deliberately control the electrochemical properties of the metal centers should be a focus of future investigations.

Fundamental active site investigations using Mossbauer spectroscopy was recently applied to the class of NPMCs prepared by impregnation of a carbon support with iron acetate, followed by heat treatment in ammonia[71]. Five different Fe species were observed in the developed catalysts, three of which consist of the $Fe–N_4$ moieties believed by these researchers to be the locale of ORR activity. The structure the authors concluded as most active for the ORR is illustrated in figure 1.8. They further proposed a mechanism for the formation of various Fe species in this class of ammonia-treated catalyst that can aid further investigations toward the development of NPMC, where deliberate control strategies can be applied in order to preferentially form active site structures with optimal surrounding environments and improved turnover frequencies. While it is undoubtedly difficult to predict and control the structural, electronic, and compositional changes occurring during high-temperature treatment of NPMC, emerging strategies can offer the potential to modulate active site turnover frequencies in NPMC based on deliberate control of the synthesis techniques and catalyst precursors.

A summary of the NPMCs materials is as follow:

- The ORR catalytic activity and stability of heat-treated NPMCs require a carbon support, a source of metal and N, and thermal treatment at appropriate temperatures.
- The metal content in these catalysts plays an important role in catalyst activity and stability improvement. A saturated metal content has been identified as a major limiting factor for further improvement of the

catalyst activity. Some innovative approaches to push the metal saturation point higher are necessary.

- The N content and the presence of a disordered or heterogeneous phase on the carbon-support surface seem to be the main requirements for an effective catalyst. Exploring and developing new support materials with optimized N content and surface morphology are required to enhance activities.
- The enhancement mechanisms of activity and stability after heat treatment are not fully understood yet. It is necessary to answer the question of whether the metal is part of the active catalytic site, as well as to identify the nature of the catalytic site.
- In general, the catalytic activity and stability of NPMCs are still below those of a Pt-based catalyst.

1.5 Catalyst Layer Modeling

Oxygen reduction in a fuel cell electrodes is a complicated process that involves contributions from the catalyst structure. When modeling catalyst layers, we are increasing the complexity level by adding ionomer, carbon support and reactants transport into the mixture as Figure 1.1 illustrates. Catalyst layers have different components: agglomerates of catalyst particles surrounded by ionomer thin films with size around 10 μm, group of agglomerates between 20 to 50 μm, catalyst particles between 2 to 3nm, as well as, reactants, and products. In order to design our catalytic system we need to take into account phenomena from the nanoscale up to the macroscale.

The phenomena involved within the catalyst layers include thermodynamics. which accounts for the minimum energy required to catalyze electrochemical reactions, the kinetics of the oxidation and reduction reactions expressed in terms of the potential and current density, ohmic losses related to the resistance to electronic and ionic transport through the porous media and the mass transfer limitations directly related to the reactant and product delivery to and from the electrocatalytic site [9].

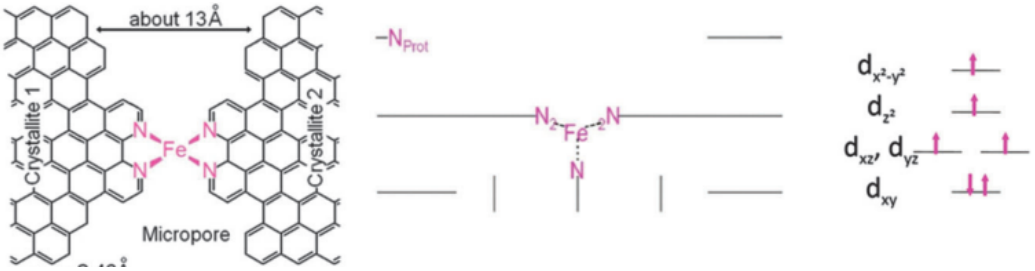


Figure 1.8 molecular orbitals of the five nitrogen coordinated Fe-centered sites providing the highest turnover frequency for this class of ammonia treated NPMCs[71].

Figure 1.1 represents the range of scales and the methods used to solve phenomena in different scales. Typically, fine-scale methods are physics-based. Particularly, for catalyst layers we have phenomena in the different time and distance scales: (i) heterogeneous electrochemical reactions in the nanoscale; (ii) proton, electron and gases transport in the mesoscale; and (iii) gases and water transport through membranes and porous media in the macroscale.

1.5.1 Macroscale modeling

On this scale we can identify the global parameters related with the fuel cell operation. This scale requires the usage of Navier-Stokes, Energy Transport, Stefan-Maxwell and Buttler-Volmer equations together with Ohm's law. These types of models are designed to relate Fuel Cell macroscopic behavior (polarization curves, OCV, Tafel Slopes, Power Density Curves) with effective medium models. Most of these macroscopic studies offer detailed information on fluid flows, heat transfer, chemical reactions, water management, bipolar plates design and many design-oriented phenomena[9, 77, 78].

1.5.1.1 Macrohomogeneous models

Weber [9] reviewed the different models used to describe Pt-based systems. These first models were '0D' and '1D' models described by Springer et al. [79], Bernardi and Verbrugge [80] and multiphase, muldimensional models by Fuller and Newman[81] and, Nguyen and White[82].

In the Springer model, they worked with a well-humidified fuel cell and considered losses at the Pt/ionomer interface and gas-transport and ionic conductivity limitations in the catalyst layer; Bernardi and Verbrugge kept the membrane hydration constant and focused on porous electrodes and Stefan-Maxwell equations in the catalyst layers. Fuller and Newman as well as Nguyen and White focused on multiphase phenomena, mainly working on water management within the catalyst layers in the context of a CFD (Computational Fluid Dynamics) approach. These three groups of models were called "Affiliate Models" by Weber [9] and represent the main group of macroscopic models present in literature.

Macroscale models are lumped parameter or effective medium models. An example is the 0-D-type models or interface models, where a single equation is used without regard to the detailed structure of the catalyst layers. 1-D-type models, account for changes across the layer or, in more localized versions, account for local effects in the agglomerate which is represent as a geometric arrangement of spherical particles of radius R_{agg}, with the same shape and size. In the model, the reactant or product diffuses through the electrolyte film surrounding the particle and into the agglomerate, where it diffuses and reacts. Typically, those models that account for changes across the layer are called porous-electrode, macrohomogeneous, or thin-film models, and those that account for changes in the agglomerate are called agglomerate models. 2-D-type models include effects on both length scales (porous and agglomerate) and are known as embedded macro homogeneous models [9].

1.5.2 Mesoscale modeling

In this scale we account for transport phenomena occurring at the surface and grain boundaries. We can calculate bulk transport properties, rheology of fluids, configurationally properties and macromolecular dynamics. The simulation times go from 100ps to 100ns and size between nanometers up to micrometers. Some applications of these models include GDL microstructure and pressure effects studies [83, 84], transport in proton conductors[85, 86], structural analysis of metallic alloys [87, 88] and reaction pathways [89]. The most common methods are Dynamic Monte Carlo (DMC) and Molecular Dynamics (MD).

These methods allow one to obtain information on the energetics of single atoms or molecules, or a small ensemble of molecules, interacting with a surface. However, a simulation of the overall dynamic behavior of an extended catalyst with many adsorbates interacting and reacting with each other is currently beyond the scope of any quantum chemical or molecular dynamics calculation [90].

Classical MD simulations rely on model potentials describing the interactions between the particles in the system, rather than a first-principles calculation of the system energy at each time step. These interactions make the outcome

potential selection dependent. The potentials are normally either fit to experimental results, or based on first-principles calculation. DMC simulations are similar to Metropolis-type Monte Carlo simulations, with the main difference that it involves an exact introduction of time into the Monte Carlo method by providing a numerical solution to the so-called dynamic Master Equation. The standard approach to kinetic modeling of surface-catalyzed reactions is to express all reaction rates in terms of average coverages. Basically, it amounts to assuming a perfect mixing of all reaction partners and hence neglects effects of ordering, island formation, or inhomogeneous surface properties[90].

Recently, ab initio or the first-principle molecular dynamics (AIMD), which is based on Car and Parrinello's technique, has become a valuable method for study condensed matter structure and dynamics, in particular liquids, surfaces, and clusters. The basic idea underlying AIMD method is to compute the forces acting on the nuclei from electronic structure that are calculated "on the fly" as the molecular dynamics trajectory is generated. In this way, the electronic variables are not integrated out beforehand, but are considered as active degrees of freedom. Thus, the Car-Parrinello (CP) algorithm overcomes limitations of standard empirical-potential approaches employed in classical molecular dynamics and provides direct information about the electronic structure [16].

1.5.3 Microscale modeling

In this scale we can describe crystal structure, molecular structure, electronic structure, chemical bond and electrocatalysis. The time scale of the phenomena is between femtoseconds to nanoseconds and the sizes go from angstroms to 10nm approximately. Due to the nature of the interactions occurring at this scale the maximum simulation size is approximately hundreds of atoms. In electrocatalysis, the nature of aqueous/solid interface makes electrocatalytic systems more complex compared with simple heterogeneous gas phase systems. The metal or metal oxide/support interfaces create sites with unique structural and electronic characteristics, novel multifunctional sites, and/or sites that promote proton and electron transfer[91]. Moreover, these sites include the presence of solution, ions, charged interfaces, complex surface potentials, and

electric fields that change the surface chemistry and catalysis that occurs in these environments.

Early electrocatalytic studies were limited to measurements of macroscopic kinetics with little understanding of the elementary molecular transformations, the active sites or the influence the atomic and the electronic structure [34]. Nørskov and colleagues developed a simple method that relates gas phase surface reaction energies to reaction energies at different applied potentials [24, 33, 36, 52-54], Anderson developed the reaction center model [18-22], Rossmeisl et al. used explicit protons at the water/metal interface to establish the double-layer interface [92], Wieckowski et al., Neurock and collaborators have modeled electrochemical systems by carrying out gas phase calculations on well-defined model clusters and surfaces and including local water molecules as well as the influence of potential [91, 93, 94]. These approximations allow us to use first principle methods to study complex electrochemical reaction and its description is as follows.

1.6 Electrocatalysis Challenges

From the macroscopic perspective, we can study and fit polarization curves behavior with simple models with some parameters. For instance, 3D models require the parameters to describe each domain and experimental data such as membrane conductivity in the MEA as well as in the catalyst layer, carbon conductivity, binary diffusion coefficients of the reactants, stoichiometric composition ratios, Tafel slope values, exchange currents, reactants viscosity, and more depending on how many components we incorporate in our model. To reduce the degree of freedom in these types of models, it is useful to obtain quality experimental data and obtain more physical parameters from measurements. However, macrohomogeneous descriptions typically lack treatment of more complex phenomena.

We can use macrohomogeneous models as a starting point to identify the major contribution to fuel cell losses and to facilitate selection of the proper modeling technique to understand the source of losses and how to overcome them to enhance performance. Figure 1.9 illustrates the main fuel cell losses.

Often, the treatment of experimental data with 1-D or 2-D dimensional models fails to represent the activation losses region when fitting these types of curves.

For 3-D models the challenge is to find reliable physical parameters for input into the model, such as diffusion coefficients and conductivity values for catalyst layer components. Even if the catalyst is simply described as a source term much of the time, these types of models are great tools to design for better reactant distribution, operation conditions, heat transfer and fuel cell stacks configurations.

The study of proton conduction and the structural configuration of metallic systems is the focus of mesoscale models but the interaction between catalyst, ionomer and support still remains a challenge for a better understanding of the environment around active sites in Pt and PGM-free systems.

Microscopic models can capture the essence of electrocatalysis of transition-metal surface catalysts. A central concept is that of energy scaling relations which, together with activity maps and the d-band model. have made it possible to develop a quantitative understanding of trends in transition-metal catalysis and enabled prediction of new catalysts [95]. These models have elucidated the intrinsic activity and selectivity, the effects of particle sizes and additives as well as, coverage effects and adsorbates-adsorbates interactions [95].

There are still challenges to overcome for a thorough description of the adsorbate-adsorbate interactions and the ionomer and support effects on electrocatalysis. Methodology was developed for metallic systems with well-defined structures but it has not been implemented for amorphous systems due to the difficulty to identify active sites. Figure 1.10 illustrates the role of multiple sites, confinement effects and further strategies to improve electrocatalysis design. It might be necessary to find ways to stabilize one adsorbed state or transition state without stabilizing others by designing specific and multi-site surfaces. Most of the discussion about the ORR reaction mechanism in Pt-based system points to the strong interaction between O and OH on these surfaces. Figure 1.10 envisions the creation of multi-dimensional active sites to break the scaling relation between O and OH adsorbates.

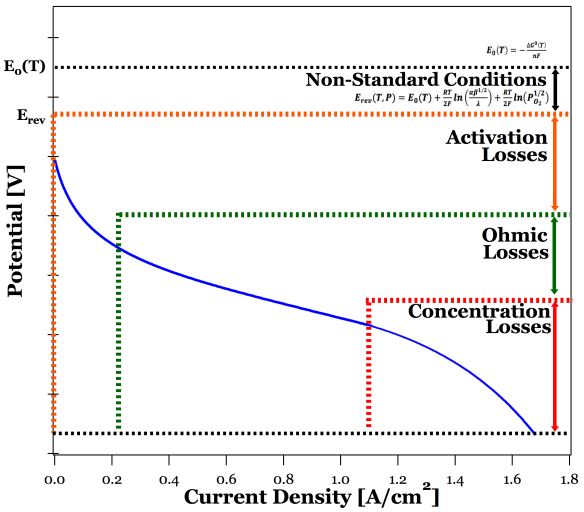


Figure 1.9 Fuel Cell losses representation.

NPMCs appear as an interesting solution from these strategies due to the possible multi-site and multi-dimensional character of these catalysts. The challenge here is to find a way to correlate the Pt-based systems and active sites for NPMCs to apply the methodology that has been successful in the ORR understanding. My approach to this problem includes the analysis of macroscopic results from MEAs with NPMCs and SAFCs, for the latter of which macroscopic models are rarely found in literature to date. These models provide insight into the performance description from the overpotential analysis. Moreover, we can clearly observe the mass transport influence on the ORR performance for these newer materials.

This approach allows me to corroborate the activation overpotential as the main loss in NPMCs and mass transport losses for SAFCS. The NPMCs system was taking to further expand our analysis and I used DFT calculations to decompose the catalytic material into its elemental components and correlate the activity of the Porphyrin with and without the metal center in comparison with metallic systems.

Finally, an introductory approach towards structural changes in the catalyst layers with pyrolysis from MD calculations was presented. The purpose of this methodology was to understand the evolution of the active center as pyrolysis occurred. However, lack of modeling studies in this area, with few potentials available to describe the inter and intra molecular interactions for iron Porphyrin, proved to be beyond the scope of this work but it gave a starting point towards understanding active sites formation.

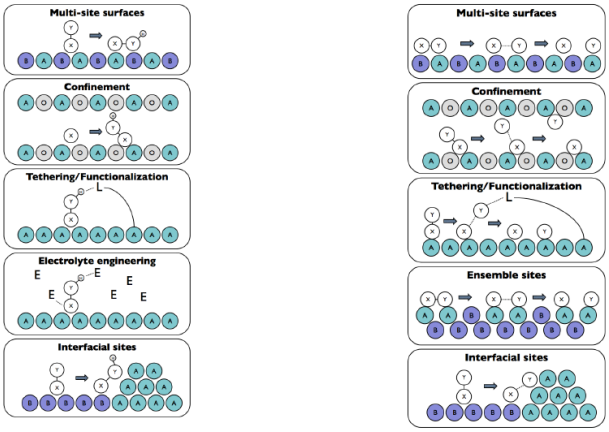


Figure 1.10 Strategies to design catalyst to overcome the adsorbate-adsorbate relation that limits higher activities in Pt-based systems[96].

2 MACROSCALE MODELING OF SOLID ACID FUEL CELLS

A version of this chapter was submitted to the Journal of Power Sources: *A Parametric Study of the Solid Acid Fuel Cell Cathode* by Diana Orozco-Gallo, Ondrej Dyck, Alexander B. Papandrew, and Thomas A. Zawodzinski.

Abstract

A one dimensional macrohomogeneous model of a Solid Acid Fuel Cell (SAFC) is developed to identify the dominant parameters affecting cell performance. The model parameters were estimated through a computational sensitivity analysis in which one model parameter was varied to assess the range of values of that parameter yielding convergence and qualitatively reasonable fits. Using this analysis to provide initial values, the model was used to simultaneous fit a set of polarization curves with physical input data (derived from measurements) and model parameters. The Tafel slopes obtained in the model agree with those calculated assuming a single-electron transfer rate-limiting step and a transfer coefficient of 0.5 at 250°C. The Open Circuit Voltage (OCV) drop agrees closely with the theoretical value at 250°C. Based on the sensitivity analysis, permeability and roughness factor are key parameters for higher performance. Calculated current density distribution and a breakdown of contributing overpotentials are calculated using the model parameters and presented. The results show the importance of limitations in available surface area and mass transport to the catalytic surface as the limiting processes in SAFC performance. This points to, decreasing catalyst layer thickness and improved microstructural configuration as targets for SAFCs performance improvement.

2.1 Introduction

Solid Acid Fuel Cells (SAFCs) employ proton conductors that become highly conductive above a certain temperature, referred to as the 'superprotonic' transition[97]. The most practical and developed of these is the CsH_2PO_4 (CDP) electrolyte, which undergoes this transition at 228°C. Figure 2.1 illustrates the CDPP phase diagram where solid CsH2PO4 exists at the low-temperature, high-humidity region of the phase diagram, solid CsPO3 at the high-temperature, low-humidity region, and liquid CsH2(1-x)PO4-x exists in a narrow range of conditions at high temperature and high humidity.

CDP-based SAFCs typically operate at 250°C where the cubic and conductive phase is predominant. Operation at this temperature imparts tolerance to fuel stream impurities such as CO[98-100], which could enable SAFC systems to operate on minimally processed fuels such as natural gas or methanol. The solid nature of the electrolyte additionally renders the membrane particularly resistant to reactant crossover.

The unique characteristics of the CDP electrolyte pose several challenges to SAFC optimization, particularly in the area of cathode microstructure. The lack of oxygen solubility in CDP demands that an active site be located at the intersection of the electrolyte, catalyst, and pore. To address this requirement, an approach in which electrolyte particles are coated evenly in catalyst material to maximize available electrochemical surface area was developed. In this catalyst layer construct, high Pt loading in needed since the Pt catalyst also acts as the electronic conductor and and thus must form a contiguous path throughout the electrode. Though this configuration is an improvement over earlier approaches, the mass-normalized activity of Pt in SAFC cathodes remains unsatisfactory and high Pt loadings are needed

In this contribution, we describe a model of the performance of an SAFC cathode. In SAFCs, several features of the electrode lend themselves to relatively simple modeling approaches. Most important among the simplifying features is the absence of liquid water, which significantly complicates the modeling of PEM fuel cells. A successful model must consider the thermodynamics and kinetics of the electrode reactions, ohmic losses related to the resistance of the electronic and ionic species traveling through the catalyst layer and mass transfer limitations directly related to the reactant access to the electrocatalytic site [9, 33, 37]. Many modeling approaches are possible but given its relative simplicity and direct connection to physically meaningful parameters, that of Springer et al. [101] is used here as a framework. That model is isothermal and considers polarization and electrode effects only through a simple 0-D polarization equation in a 1-D model. Within the cathode, they examined utilization of the catalyst and the effects of performance on various parameters such as the diffusion-medium porosity and the inlet-gas composition.

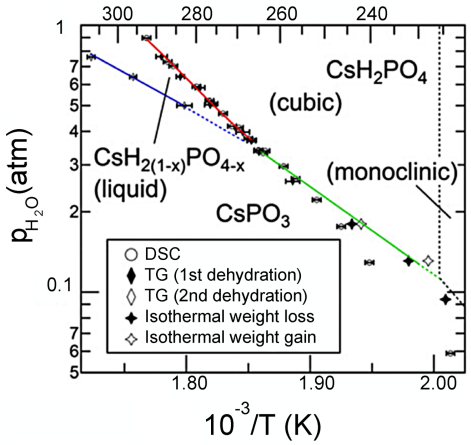


Figure 2.1 CsH2PO4 phase diagram[102].

The cathode is treated as a uniformly distributed layer, and the model does not treat flooding [9, 79, 101]. These features are adequate representations of the SAFC case, in which liquid water is absent.One feature of our study that is infrequently found in the modeling body of work is its close coupling to physical parameters, especially derived from measurements, available as input. Also, our emphasis is on the simultaneous description of multiple data sets tailored to provide maximum information. If we are to use models as a path to understand, it is important to reduce the number of variables used in the model fitting and to use data sets that are sufficiently detailed to allow meaningful probes of the fit.

An example of this is our treatment of the 'kinetic' region of the polarization curves. Typical polarization curves collect data points with spacing of ~20 to 50 mV. This provides only a few points in the kinetic region with the result that this aspect is rarely fit satisfactorily. Here we intentionally create data sets with many more points taken in that region, putting more emphasis on achieving a fit to the observed kinetics and thereby giving a higher level of confidence in the result.

Our goal in modeling SAFC catalyst layers is to identify the main macroscopic parameters that affect the performance. By implementing extensive sensitivity tests of model parameters and selecting appropriate experimental data sets, a macroscopic modeling study can serve to reveal the physical basis of the important performance differences resulting from the use of given catalyst layer structures, on one hand, and different kinetics on the other.

Finally, we provide a few comments on the expectations regarding physical properties of the catalyst layer that shape our analysis and that are rather different from those encountered in analogous PEM fuel cells. First, the cell operates at high temperature, suggesting differences in kinetic and thermodynamic parameters but also in mass transport parameters. However, the catalyst layers used are quite thick. The CDP electrolyte is essentially impermeable to gases. Based on the latter two features, offset by higher intrinsic mass transport rates in the gas phase from the higher temperature, we are uncertain of the overall resulting effective transport rates but can reasonably expect them to be somewhat slow.

2.2 Model description

2.2.1 Model Equations

The cathode catalyst layer model highlights the effects of limited fluxes of oxygen in this layer coupled to the electrochemical reaction. Equations 2.1 through 2.4 are the basic equations given by Springer et al, which take into account variations of parameters along the x coordinate of the catalyst layer, the direction normal to the planes of the flow channel and membrane. In the x-coordinate, x = x_2 specifies the catalyst layer/flow channel interface, and x = $x_{\delta CL}$ specifies the catalyst layer/membrane interface.

$$\frac{\partial \eta}{\partial x} = \frac{I\delta_{CL}}{\sigma} = IR_{CL} \qquad \textbf{Equation 2.1}$$

$$\frac{\partial I}{\partial x} = p_{O_2}\frac{C}{C^*}A_r i_0 exp\left[\left(\frac{\eta}{b}\right)\right] \qquad \textbf{Equation 2.2}$$

$$\frac{\partial \frac{C}{C^*}}{\partial x} = \frac{I - I_l}{p_{O_2} I_D} \qquad \textbf{Equation 2.3}$$

$$I_D = \frac{nFDC^*}{\delta_{CL}} \qquad \textbf{Equation 2.4}$$

Boundary conditions:

$$x = x_2 \qquad \frac{C}{C^*} = 1, \eta = E_{eq} - OCV \qquad \textbf{Equation 2.5}$$

$$x = x_3 = x_{\delta_{CL}} \qquad \frac{\partial \frac{C}{C^*}}{\partial x} = 0, \frac{\partial I}{\partial x} = 0 \qquad \textbf{Equation 2.6}$$

In these equations, R_{CL} represents the resistance through the cross-sectional area of the catalyst layer; I_D is a characteristic limiting diffusion current density. The experimentally controlled variables considered are the overpotential (η), the current density (I) and the oxygen partial pressure (p_{O_2}). Equation 2.1 is an ohmic relationship between local current density and the local variation of η, determined by the protonic resistivity of the catalyst layer. Equation 2.2 describes the local rate of current generation within the catalyst layer in terms of the oxygen partial pressure at the catalyst layer/flow channel interface, the local concentration of oxygen relative to its concentration at the catalyst layer/gas

interface, and the local overpotential. In this equation b represents the Tafel slope. Equation 2.3 describes the gradual transformation of the oxygen flux to a protonic current along x, such that the sum of the two fluxes is kept constant and equal to the oxygen flux at the catalyst layer/flow channel interface.

The remaining parameters, which define the behavior of the cell for each set of operating conditions, include the cathode inlet gas. The key parameters for this system are described below:

- **i_0:** exchange current calculated from the Tafel slope parameter and as interpolation of the tafel region. As follow:

  Tafel region equation,

  $$i = i_0 e^{-\alpha f \eta} \qquad \textbf{Equation 2.7}$$

  From here:

$$\eta = \frac{2.3RT}{\alpha F} log i_0 - \frac{2.3RT}{\alpha F} log i \qquad \textbf{Equation 2.8}$$

  Where the Tafel slope is defined as:

$$b = -\frac{2.3RT}{\alpha F} \qquad \textbf{Equation 2.9}$$

- **A_r**, the ratio of actual catalyst surface area per unit geometric surface area, essentially a 'roughness factor.' (We note that these first two terms are not introduced as separated paramters in the fits to follow.)
- **DC***, the product of the effective diffusion coefficient of oxygen (cm^2/s) treated as the permeability of oxygen within the CDP-based catalyst layer. It comes from finding the right diffusion coefficient effective value. For solids in porous media the equation for gas phase system follow an Arrhenius type formula (well known and widely used in literature)[103]:

$$D_i = D_0 * \exp(-E/RT) \qquad \textbf{Equation 2.10}$$

  As these values are not tabulated for CDP, our approach is to find the initial value for O2, and air, then use the Bruggeman relation to calculate the effective diffusion coefficient[104]:

$$D_i^{eff} = \varepsilon^{1.5} D_i$$ **Equation 2.11**

- Ari_o: Roughness-corrected current density (RCCD)

2.3 Model validation

For each set of experimental and fitted data, we performed two nonparametric statistical tests: Mann-Whitney U[105] and Kolmogorov-Smirnov[106]. For Mann-Whitney U test the null hypothesis is that two populations are the same for all data points. For a Two-sample Kolmogorov-Smirnov test the null hypothesis that the one-dimensional probability distributions of the data points do not differ one from the other.

In both cases, the observations must be independent and the data nominal or ordinal. The null hypothesis is rejected if the p-value is smaller than the significance (See appendix – Statistical tests). Table 2.1 condenses the statistical test results for both fuel cell models showing that the modeled data represents the experimental with a 97% of confidence.

2.4 Experimental

Dr. Alexander Papandrew fabricated the MEAs and recorded the electrochemical testing. Dr. Ondrej Dyck realized the structural analysis presented described in this section.

2.4.1 Cell Fabrication

Solid acid fuel cells were fabricated using an anode-supported configuration similar to those described previously[107-109]. Using a bilayer sintered stainless steel (grade 304) mesh disc (2.85 cm^2) as an anode current collector and structural support, anode, membrane, and cathode layers were sequentially formed by uniaxial compression of powdered composites in a stainless steel as ne 2.2 illustrates. Anodes were formed at 90 MPa from a mechanical mixture of CDP, 60wt%Pt supported on carbon black (Vulcan XC-72R, Cabot Corp.) and naphthalene (a fugitive binder) in a 3:1:1 ratio, respectively, by weight. The CDP membrane was applied to the anode at 125 MPa and was approximately 50 μm in thickness.

Table 2.1 Statistical goodness of fit tests for SAFC system

% O2	Test	p-value	Statistic	Decision
O2_7mg	Mann-Whitney	0.957	-0.054	Retain H_o
	KS	1.000	0.031	Retain H_o
Air_7mg	Mann-Whitney	1.000	0.000	Retain H_o
	KS	1.000	0.032	Retain H_o
O2_3.5mg	Mann-Whitney	0.999	-0.001	Retain H_o
	KS	1.000	0.062	Retain H_o
Air_3.5mg	Mann-Whitney	1.000	0.000	Retain H_o
	KS	1.000	0.032	Retain H_o
O2_1.75mg	Mann-Whitney	1.000	0.000	Retain H_o
	KS	1.000	0.064	Retain H_o
Air_1.75mg	Mann-Whitney	1.000	0.000	Retain H_o
	KS	1.000	0.031	Retain H_o

Cathode electrocatalyst powders were synthesized via a method described previously in the literature[107, 108]. CDP particles with a specific surface area of approximately 2 m^2/g were mechanically combined in a glass vial with an appropriate quantity of Pt(II) pentanedionate(Acros Organics). The coarse mixture was heat-treated at 210°C in a deoxygenated N_2-water vapor atmosphere, resulting in the vapor deposition of a conformal layer of Pt nanoparticles decorating all exposed surfaces of the CDP particles. The Pt precursor content was adjusted to arrive at 20wt% Pt^0 on CDP, which was validated gravimetrically.

From this common feedstock of cathode electrocatalyst powder, SAFCs of various cathode thickness(and thus Pt loading) were fabricated by laminating the powders to directly to the CDP membrane via uniaxial compression at 23 MPa. SAFCs were formed using 25 mg, 50 mg, and 100 mg of the 20wt% Pt@CDP catalyst powder, respectively yielding cathode Pt loadings of 1.75 mg_{Pt}/cm^2, 3.5 mg_{Pt}/cm^2, and 7.0 mg_{Pt}/cm^2. Cathode current collectors were comprised of a coarse single-layer stainless steel (grade 316) mesh and a carbon paper interlayer (SGL 34AA).

2.4.2 Microstructural Analysis

Freestanding SAFC cathodes were fabricated in a manner similar to the route detailed above, but densification of the dry cathode powders proceeded between two Kapton discs rather than atop the CDP membrane. The cathodes were easily separated from the Kapton for SEM and FIB-SEM analysis. The freestanding cathode samples were embedded in epoxy for FIB-SEM analysis in a Zeiss Auriga Dual Beam FIB/SEM. Image stacks were segmented using the Trainable Weka Segmentation plugin for Fiji/ImageJ and further analyzed using Fiji to derive electrode physical parameters.

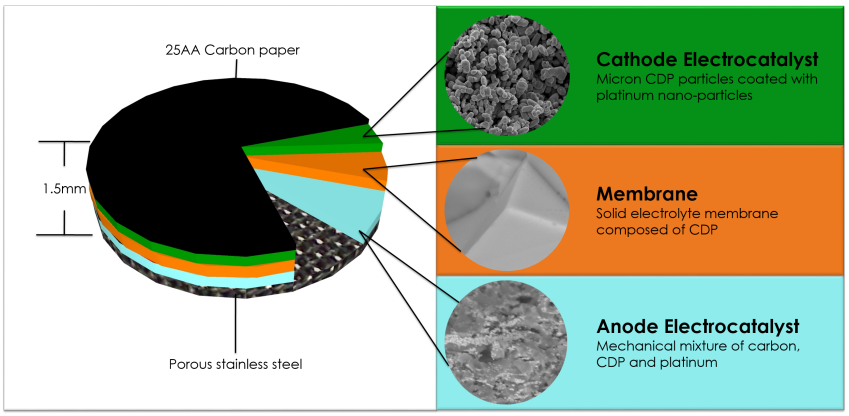


Figure 2.2 SAFC cell components description.

2.4.3 Electrochemical Testing

Fuel cell testing was conducted using stainless steel test rigs at a temperature of 250 °C with gases hydrated to a dew point of 75 °C (approximately 0.35 bar water partial pressure). Anodes were supplied ultrahigh-purity H_2 and cathodes were supplied either compressed air from a centralized compressor, or ultrahigh-purity O_2. Polarization curves were recorded with a Bio-Logic VSP potentiostat by scanning the working electrode potential at 10 mV s−1 from the open circuit potential to a cell potential of 0 V. Before and after the recording of the polarization curves, potentiostatic electrochemical impedance spectroscopy (EIS) was performed in a frequency range from 200 kHz to 200 mHz at 0.8 V cell voltage with a single sine perturbation amplitude of 10 mV. The high-frequency intercept of the EIS spectrum was used to eliminate the ohmic resistance of the cell from the polarization curves, yielding what we refer to as iR-free polarization curves. This protocol was repeated cyclically on an hourly basis, during which the cell was held at 0.6 V. Each cell was operated in an air atmosphere for several hours, and subsequently held at 0.6 V while 100% O2 was introduced to the cathode.

The cyclic protocol was resumed after the current density in the new cathode atmosphere reached steady state. After completion of testing, the cells were sectioned via fracture and samples were mounted for cross-sectional examination in a Hitachi TM-3000 SEM operating at 15 kV for determination of electrode thickness. Figure 2.3 shows the SEM images used to calculate the cathode thicknesses. The experimental values obtained are summarized in table 2.2.

2.5 Results and discussion

2.5.1 Experimental results analysis

The experimental data to be fit consists of several polarization curves obtained for SAFCs. When compared to typical PEM cells modeled by Springer, the catalyst loading is quite high and catalyst layers are relatively thick.

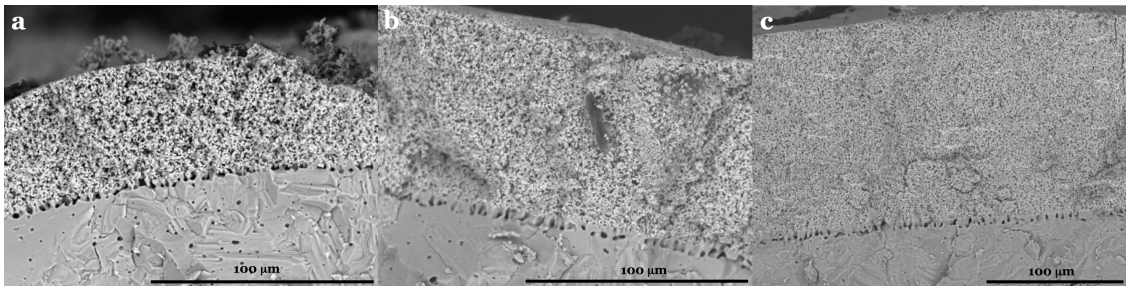


Figure 2.3 SEM images of the SAFC showing the cathode thickness. a) 1.75 mg/cm² Pt b) 3.5 mg/cm² Pt c) 7 mg/cm² Pt.

Table 2.2 Experimental values

Experimental Values	S1		S2		S3	
Temperature of operation [°C]	250		250		250	
Dew Point [°C]	75		75		75	
Mean porosity	50%		50%		50%	
Catalyst layer thickness [µm]	44+/-9		84+/-5		148+/-4	
Metal loading [mg/cm²]	1.75		3.5		7	
	Air	O2	Air	O2	Air	O2
Catalyst Layer Resistance [Ωcm²]	0.232	0.231	0.225	0.227	0.200	0.199
OCV	0.980	1.011	0.988	1.015	0.990	1.021
Limiting current [A/cm²]	1.19	1.62	1.36	1.92	1.41	2.15
Tafel Slope [mV/dec]	209.5	206.5	211.7	203.3	200.5	221

The model requires multiple inputs. Table 2.2 presents the physical property values for the different MEAs and tests along with some determined with independent experiments. The mean porosity was determined to be 50% by analysis of FIB-SEM slices of a representative cathode sample. As expected, catalyst layer thickness (determined by SEM) increases roughly proportionally with Pt loading.

The deviation from linearity may be attributed to the catalyst distribution on the carbon support along with slight differences in compression from the pressure applied during the electrode assembly. The Tafel slope shown in table 2.2 are those derived from a fit of the Tafel equation to the polarization data for each case of air or oxygen at the various loadings as figure 2.4 represents.

The OCV is a function of the temperature and pressure variation. For our system at 250°C the OCV is equal to 1.12V which is equivalent to the reversible potential for the oxygen reduction reaction calculated as:

$$E_{rev}(T,P) = E_0(T) + \frac{RT}{2F} ln\left(\frac{\alpha\beta^{1/2}}{\lambda}\right) + \frac{RT}{2F} ln\left(P_{O_2}^{1/2}\right) \qquad \textbf{Equation 2.12}$$

$$E_0(T) = -\frac{\Delta G^0(T)}{nF} = -\frac{\sum_i \nu_i\left(\overline{g}_{f,i}^0 - \Delta H(T) - T\Delta S(T)\right)_i}{nF} \qquad \textbf{Equation 2.13}$$

$$E_0(T) = -\frac{\Delta G^0(T)}{nF} = -\frac{-217934.68}{2\times 96485} = 1.13V \qquad \textbf{Equation 2.14}$$

Where E_o represents the standard voltage for oxygen. $\overline{g}_{f,i}^0$, is the Gibbs formation energy of the i compound, ν_i the stoichiometry coefficients. α, β, λ represent the molar fraction of hydrogen, oxygen and water respectively. The molar fraction of the reactants is close to one, based on the high stoichiometry imposed by the fixed reactant flow rates of 40 sccm and 75 sccm for hydrogen and air/oxygen, respectively.

The second term in equation 2.12 vanishes so we find the OCV from equation 2.12[28]:

$$OCV_{O_2} = E_0(T) + \frac{RT}{zF} ln\left(\frac{P_{H_2} P_{O_2}^{\frac{1}{2}}}{P_{H_2O}}\right) = 1.12V \qquad \textbf{Equation 2.15}$$

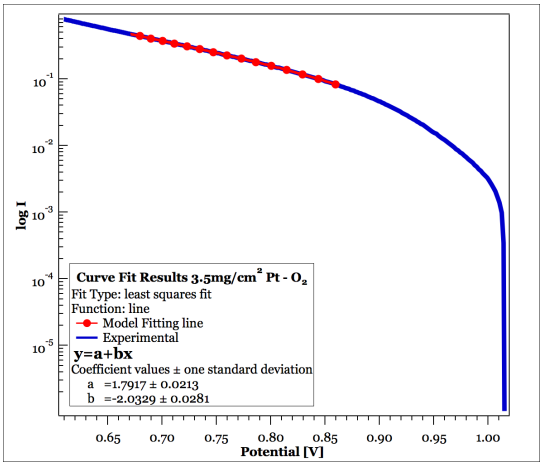


Figure 2.4 Experimental Tafel slope for 3.5 mg/cm2 System in O_2.

To calculate the expected variation in OCV when we switch from oxygen to air, for the same hydrogen and relative humidity, equation 2.15 is reorganized to express the OCV as:

$$\Delta OCV = \frac{RT}{4F} ln\left(\frac{p_{O_2}}{p_{O_{2,air}}}\right) \approx 0.018V \qquad \textbf{Equation 2.16}$$

$$OCV_{Air} = OCV_{O_2} - \Delta OCV = 1.11V \qquad \textbf{Equation 2.17}$$

The observed OCV values obtain for air are within approximately 1% of those calculated.

SAFC polarization curves do not exhibit a sharp limiting current, indicating that the slow mass transport in this system does not lead to reactant 'starvation' under the test conditions. The observed maximum current values decrease as a combination of oxygen concentration depletion and catalyst thickness increase.

2.5.2 Sensitivity analysis

Understanding the parameter sensitivity of our model is a key step in developing a base case for fitting to our experimental data, First we calculated and selected the experimental Tafel slopes from log I vs. potential plot (table 2.2). Then, using this value, we modified one parameter at a time per simulation to find the base case values as table 2.3 summarizes. Finally, the effects of varying each parameter individually are illustrated in figures figures 2.5, 2.6 and 2.7. In this preliminary step, we are seeking to define a range of each parameter value in which the model will converge and yield qualitatively reasonable behavior.

Figure 2.5 illustrates the sensitivity to the permeability parameter (DC*) in air for each loading. The values yield satisfactory results over a specific range. For small values of DC*, the simulations do not converge or the maximum current obtained is unrealistic. Permeability values (DC*) modified the diffusion current obtained as equation 2.4 states. If the diffusion current is small (red lines in figures 2.5a, 2.5b and 2.5c), equation 2.3 is multiplied by a high order of magnitude constant, causing convergence under unrealistic conditions. When the diffusion current is higher than the maximum current, the calculation does not converge due to negative concentration values in equation 2.3. Summarizing, the permeability values modify the diffusion current behavior, making the model

convergence sensitive to the selection of this parameter.

Figure 2.6 represents the model sensitivity to the RCCD term, $A_r i_o$, for each loading. The model will converge for any value of $A_r i_o$ lower than 1. This parameter is represented in equation 2.2 as the prefactor of the exponential kinetic behavior. It does not affect convergence unless the value reaches a point where the boundary conditions are not satisfied (equations 2.5 and 2.6). In this case, the end of the dashed lane in figures 2.6a, 2.6b and 2.6c represent the boundary condition satisfaction. The active area is not a sensitive parameter for model convergence but is critical to understanding the catalyst utilization within the layer and therefore, it must be chosen within a rational range.

Figure 2.7 shows the effect of varying limiting current (I_{lim}). As discussed above, SAFCs do not show the sharp decay typically found in mass transport limited systems. In our case, limiting current values are used to calculated the diffusion current and thus influence the concentration distribution within the catalyst layer. To obtain convergence, the value must be close to the maximum current. Otherwise the calculation does not converge. This parameter is remarkably sensitive because the range of variation has to be less than 2% to be within the convergence range. However, this is not a fitting parameter but rather provides a method to estimate the limiting current, which cannot be directly extracted from the polarization curve. Once the value is set, no further optimization is required.

2.5.3 Modeling Analysis

The sensitivity analysis provides a set of base case parameters to initialize the simulation, as shown in table 2.3. Then, we performed a fit of the polarization curves by using backward Euler method with a step of $1/\delta_{CL}$. The Newton-Rapshon's method was applied for numerically solving the equations in Matlab. The optimization was carrying out by finding the local minimum of each parameter with the simplex method. Finally, the global minimum was obtained with these values as initial point. Once the values are defined, the model determines the RMS fit to calculate Tafel slopes, cathodic overpotential and polarization curve values.

Table 2.3 Parameters values: base case

Parameter	Air	O_2
Active area - $A_r i$* (A/cm²)	25mg: $0.42*10^{-4}$ 50mg: $0.42*10^{-4}$ 100mg: $0.42*10^{-4}$	25mg: $0.42*10^{-4}$ 50mg: $0.42*10^{-4}$ 100mg: $0.42*10^{-4}$
Permeability – DC* (mol/cm-s-atm)	25mg: $2.9*10^{-6}$ 50mg: $2.9*10^{-6}$ 100mg: $2.9*10^{-6}$	25mg: $2.9*10^{-6}$ 50mg: $2.9*10^{-6}$ 100mg: $2.9*10^{-6}$
Tafel slope (mv/dec)	25mg: 209.5 50mg: 211.7 100mg: 200.5	25mg: 206.5 50mg: 202.6 100mg: 220.1
Limiting Current (A/cm²)	25mg: 1.2 50mg: 1.2 100mg: 1.2	25mg: 1.2 50mg: 1.2 100mg: 1.2

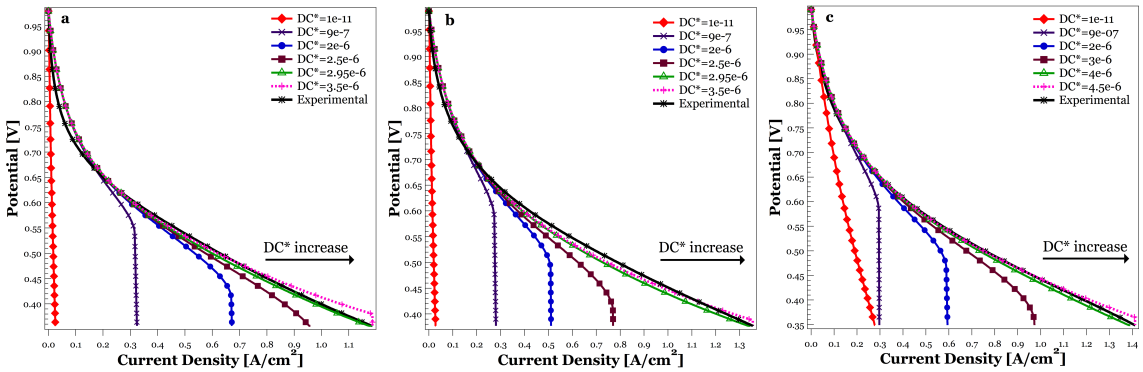


Figure 2.5 Permeability sensitivity values DC* = $1*10^{-11}$, $9*10^{-7}$, $2*10^{-6}$ - $7*10^{-6}$ [mol/cm-s-atm]. a) Loading: 1.75 mg/cm² Pt. b) Loading: 3.5 mg/cm² Pt. Tafel slope: 207 mv/dec b) Loading: 3.5 mg/cm² Pt. Tafel slope: 212 mv/dec.

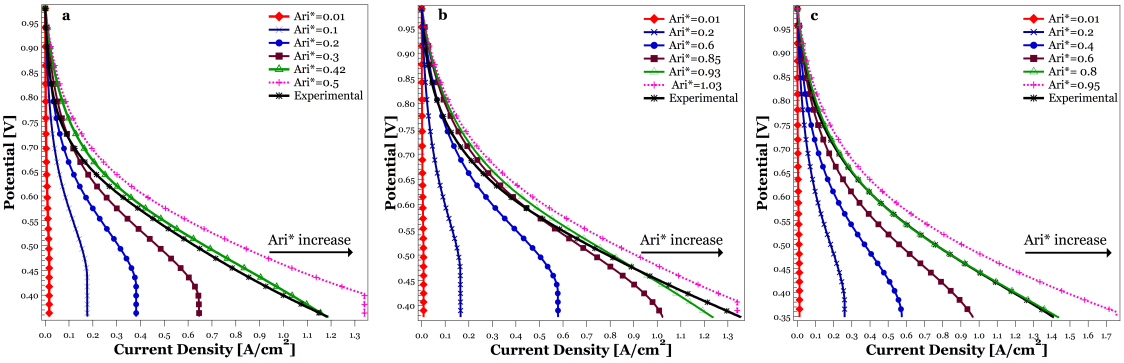


Figure 2.6 Active area sensitivity in air. a) Loading: 1.75 mg/cm² Pt. Tafel slope: 200.5mv/dec b) Loading: 3.5 mg/cm² Pt. Tafel slope: 207 mv/dec b) Loading: 3.5 mg/cm² Pt. Tafel slope: 212 mv/dec.

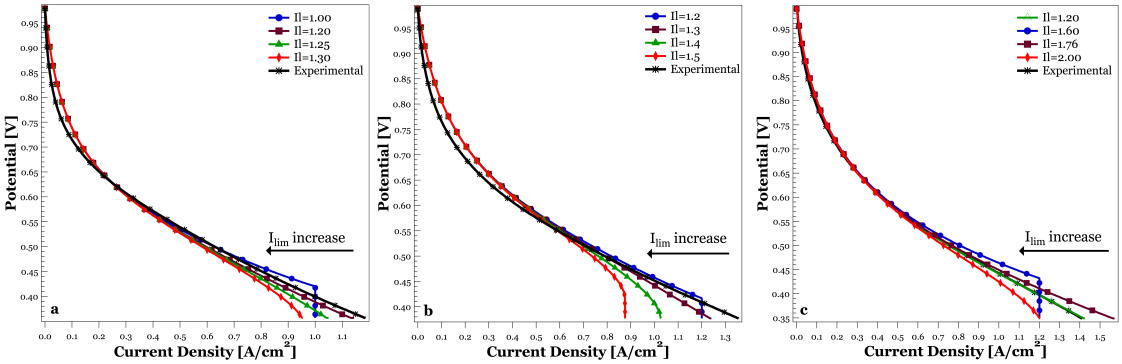


Figure 2.7 Limiting current sensitivity in air. a) Loading: 1.75 mg/cm² Pt. Tafel slope: 200.5mv/dec b) Loading: 3.5 mg/cm² Pt. Tafel slope: 207 mv/dec b) Loading: 3.5 mg/cm² Pt. Tafel slope: 212 mv/dec.

Figure 2.8 shows the fitted polarization curves. In general, the fits are excellent. Comparing air vs. oxygen curves, the performance decreases around 30% with oxygen dilution. The OCV is higher with pure oxygen as a result of the OCV dependence on oxygen partial pressure and it is also higher with higher loading. Moreover, the current decrease between air and oxygen is more severe at higher loadings. These phenomena are consequences of the significant additional mass transport limitations in the air case, especially through a thick catalyst layer with modest porosity.

The Tafel slopes obtained are summarized in table 2.4 and illustrated in figure 2.9. In both cases, the standard deviation is lower than 3mv/dec, so we can conclude that the kinetic parameters can be considered constant. These Tafel results are in agreement with those calculated at this temperature assuming a rate-limiting step with 1 e- and a of 0.5. The limited variation of the Tafel slope values from the base parameters suggests that the Tafel slope values determined initially would suffice to capture the catalysis behavior.

Figure 2.9 illustrates the results for the Tafel slope. The standard deviation is not more than 3mv/dec, so we can conclude that the kinetic parameters are approximately constant. These Tafel results corroborate expected behavior. They should not be concentration-dependent because the losses are associated with the catalyst behavior rather than the mass transfer; thus, the values are expected to be close to each other, independent of the loading and oxygen concentration. Moreover, the calculated values oscillated around the theoretical value of 207 mv/dec, calculated from equation 2.9. The remarkable close approximation of the Tafel slope in comparison with the experimental values, is a mixture of using the experimental Tafel values as starting point and the right Tafel region (Potential>0.77V as suggested by Springer and collaborators[30]).

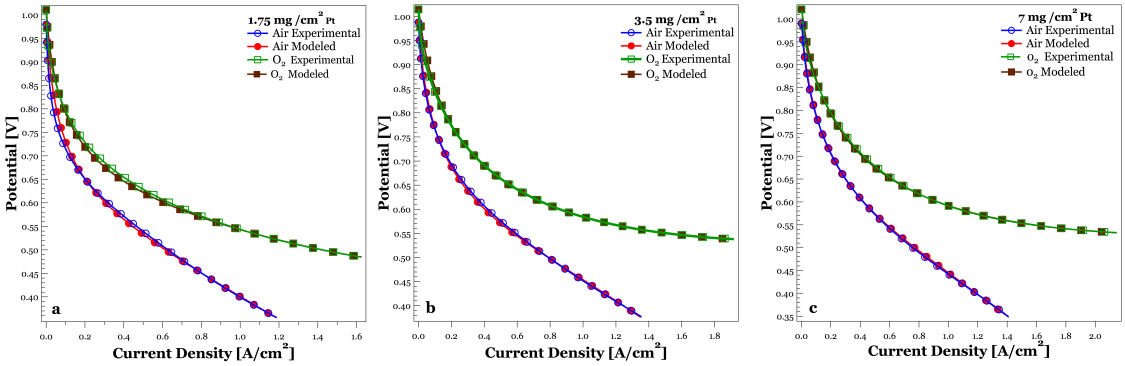


Figure 2.8 Polarization curves fitting for air and oxygen at different loadings. a) 1.75 mg/cm² b) 3.5 mg/cm² c) 7mg/cm².

Table 2.4 Parameter values: optimized

Parameter	Air	O_2
Active area - $A_r i^*$ (A/cm^2)	25mg: $7.2*10^{-6}$ 50mg: $7.4*10^{-6}$ 100mg: $7.5*10^{-6}$	25mg: $1.60*10^{-6}$ 50mg: $1.79*10^{-6}$ 100mg: $2.18*10^{-6}$
Roughness factor - A_r	25mg: 3.00 50mg: 3.22 100mg: 3.42	25mg: 0.68 50mg: 0.74 100mg: 0.87
Exchange current - i_o (A/cm^2)	25mg: $2.40*10^{-6}$ 50mg: $2.30*10^{-6}$ 100mg: $2.19*10^{-6}$	25mg: $2.35*10^{-6}$ 50mg: $2.42*10^{-6}$ 100mg: $2.52*10^{-6}$
Permeability – DC* (mol/cm-s-atm)	25mg: $5.53*10^{-7}$ 50mg: $3.01*10^{-7}$ 100mg: $7.58*10^{-7}$	25mg: $2.1*10^{-6}$ 50mg: $1.97*10^{-6}$ 100mg: $2.36*10^{-6}$
Tafel slope (mv/dec)	25mg: 200.5 50mg: 207 100mg: 212	25mg: 201.0 50mg: 202.6 100mg: 210.9

Figure 2.10 illustrates the RCCD behavior compared to that calculated by Springer et. al for Pt at 80°C. The RCCD factor is the product of a term that corrects the geometric area to yield the real active area (Ar) and a current density term. RCCD plays the role of the io in a Butler-Volmer analysis. As has been discussed, the determination of a true value of io for the ORR is difficult because the state of the Pt surface changes (between a bare and oxidized surface) as one extrapolates toward zero overpotential, the conventional way to determine i_o. Gottesfeld and Springer have suggested using i=0.9V as a proxy for i_o. In our case, much less can be inferred regarding the ORR nor can we truly estimate the true surface area (e.g. from a hydrogen adsorption peak) as figure 2.11 illustrates.

For each condition (O2 vs, air) the values are approximately constant and the ratio of the values obtained from the fits of curves from cells operating on air and oxygen differs by a factor of roughly 2.5. This term is in essence a reflection of the kinetics of the ORR. Inspection of the sensitivity analysis for this parameter (figure 2.6) shows that the RCCD term has a strong influence.

The fits shown are quite sensitive to the parameter, with implications throughout the curve. From this we conclude that this is a critical parameter for cell operation. Also, we should note that the observed parameters are substantially lower in value than the corresponding term in the Springer model, which was based on data acquired at 80 °C. The second one is associated with a decrease in the electrochemical active area.

By having oxygen excess, all the available reaction sites are producing vapor phase water that can be absorbed on these sites. If the adsorption of water is strong, every reaction site can become unavailable for the excess oxygen. As consequence, the apparent electrochemical active area decreases and the final value of these parameters for oxygen are smaller than for air. Indeed, once the roughness factor is separated from the parameter, the difference between oxygen and air roughness factor is evident as figure 2.11 represents.

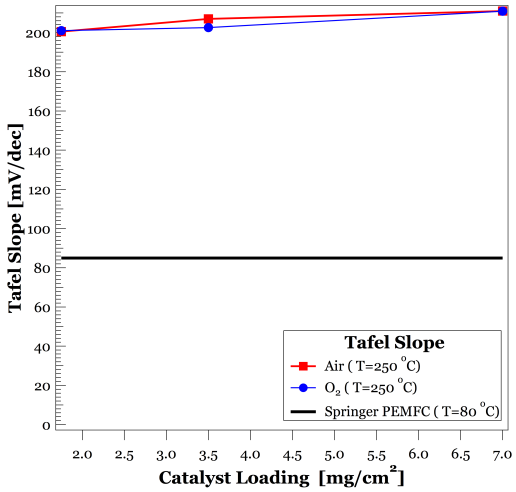


Figure 2.9 Calculated Tafel slopes for different loadings.

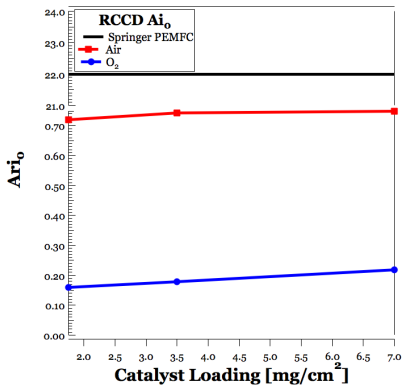


Figure 2.10 Calculated RCCD for different loadings.

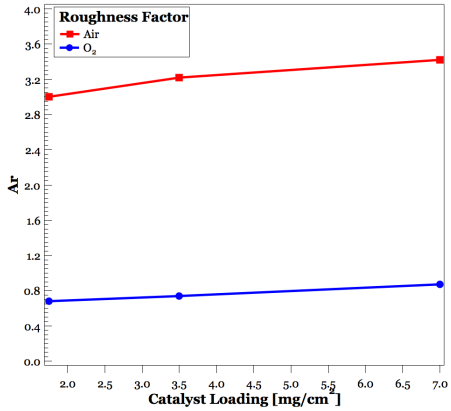


Figure 2.11 Calculated roughness factor by using calculating i_o values.

Figure 2.12 shows the permeability (DC) values, which are fairly similar for a given gas. The difference in values between air and oxygen for the SAFC fits is roughly a factor of 4 on average and is therefore likely to be a direct consequence of the difference in concentration of the gas being transported (O2 vs. air) across the catalyst layer.

Note that the difference is slightly less than the theoretical factor of 5, perhaps reflecting effects of porosity on mass transport. Compared with PEM Fuel Cells, the permeability values are significantly higher due to the high diffusion rates at high temperature.

Figure 2.13 shows the calculated distribution of local current density across the catalyst layer at different voltages (0.6V, 07V, 0.8V) for oxygen (figure 2.13a, 2.13c and 2.13e) and air (figure 2.13b, 2.13d and 2.13f). The reaction rates for oxygen are roughly two times higher than those for air at every potential due to higher reactant concentration. Moreover, the air case shows a limiting situation with respect to gas transport, indicated by the inflections in the curves, as the local current density drops close to the CL/membrane interface (x=1).

The modeling results show decay in current density near this boundary as consequence of the interplay between charge and reactant transport through the catalyst layer. The non-uniformity of the current density profile throughout the catalyst layer suggests that the transport is an important factor at all voltages probed. This is even the case for oxygen-fed cathodes.

As we increase the loadings, the conversion at higher overpotential seems to become less homogenous across the layer. This is consistent with strong mass transport control, increasing with thicker layers.

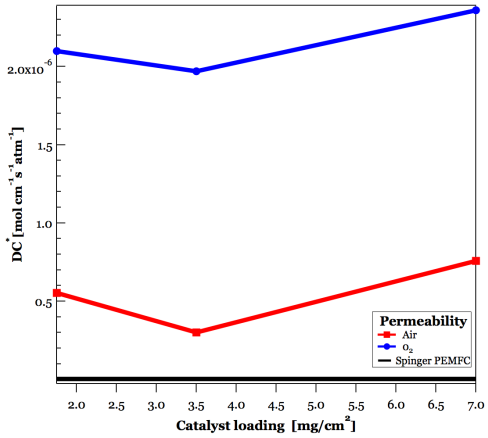


Figure 2.12 Calculated permeability values for different loadings.

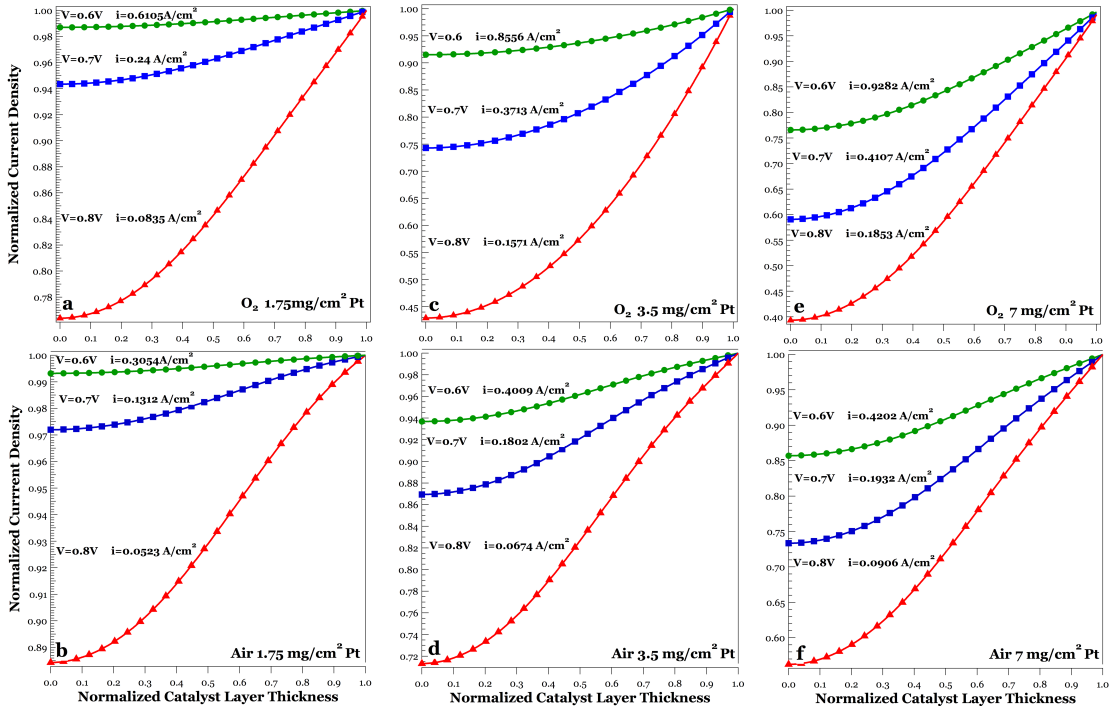


Figure 2.13 Current distribution across the catalyst layer a) 1.75 mg/cm² O_2 b) 1.75 mg/cm² Air c) 3.5 mg/cm² O_2 d) 3.5 mg/cm² Air e) 7 mg/cm² O_2 f) 7 mg/cm² Air.

2.5.4 Overpotential analysis

Based on our analysis of the fitted parameters and the current distribution we calculated the losses to verify the validity of our arguments in terms of transport and charge transfer within the catalyst layer, as well as, kinetic behavior. The cell potential is calculated as[28]:

$$E_{cell} = E_{rev}(p_{H_2}, p_{O_2}, T) - \eta_{act} - \eta_{ohm} - \eta_{con} \qquad \textbf{Equation 2.18}$$

Where $E_{rev}(p_{H_2}, p_{O_2}, T)$, represents the reversible electrode potential at the temperature and operation pressure and is calculated with equation 2.12. η_{act}, represents the activation overpotential and can be calculated with equation 2.8 for ORR due to its sluggish kinetics compare with hydrogen. η_{ohm}, is the ohmic overpotential associated with the catalyst layer resistance and can be calculated as:

$$\eta_{ohm,i} = iR_i \qquad \textbf{Equation 2.19}$$

R_i, represents the MEA resistance obtained from the in-situ measurements for the different catalyst thicknesses. These values are tabulated in table 2.2. η_{con}, represent the mass transfer overpotentials and it can be calculated from equation 2.12.

Figure 2.14 graphically shows the contribution of the various overpotential loss terms to the polarization curves. Blue, green and grey areas represent the concentration, ohmic and activation polarization respectively. For convenience, we also extract values of the overpotentials at several current density values for the various cases, tabulated in table 2.5.

Based on figures 2.14, 2.15 and, table 2.5, we can draw a few basic conclusions. For all cases, there is substantial mass transfer loss even at modest current density. Remarkably, even at 200 mA/cm2, mass transport losses are the major polarization source for air systems with values higher than 40% as table 2.5 illustrates. For oxygen systems, the main source is the activation losses with values higher than 50% and the mass transport losses represent the second larger losses with a contribution higher than 23%.

Table 2.5 Activation, Ohmic and Concentration overpotentials a i≅0.2 A/cm²

Loading [mg/cm²]	Thickness [µm]	η_{act} [mV]		η_{ohm} [mV]		η_{mt} [mV]	
		Air	O2	Air	O2	Air	O2
1.75	44	227.18	228.14	60.31	59.99	782.26	721.87
		21.2%	22.6%	5.6%	5.9%	73.1%	71.5%
3.5	84	235.52	229.35	56.06	56.19	749.03	678.26
		22.6%	23.8%	5.4%	5.8%	72.0%	70.4%
7	148	242.11	237.84	49.51	49.53	741.44	665.11
		23.4%	25.0%	4.8%	5.2%	71.8%	69.8%

The large contribution from mass transport losses is somewhat expected due to the large catalyst layer thickness relative to its low temperature counterparts. Moreover, it is higher as a proportion of limiting current for air as a consequence of the mass transport effects discussed above.

The catalyst layer thickness and limited accessible area negates the benefits of larger diffusion coefficients at higher temperatures. Ohmic losses and activation are bigger in the oxygen case but this is a consequence of the higher current densities obtained compared to the air systems.

SAFC activation losses decrease with higher temperatures, in contrast with the PEM counterparts based on the work from Arisetty and collaborators [110]. For our system, the activation overpotential is reduced 35% as a direct consequence of faster kinetics enhanced with temperature.

Ohmic losses are six times and mass transfer losses are two hundred times bigger than for PEM in air at 80°C. Therefore, the presence of large ohmic and mass transfer losses at lower current densities points toward. Decreasing catalyst layer thickness and improved microstructural configuration as targets for SAFCs performance improvement.

It is instructive to compare the physical parameters emerging from the model of the SAFC system to corresponding results in PEMFC systems. The difference in Tafel slope values, as noted above, reflects the temperature change between the two technologies. One striking difference is the much lower value of the $A_r i_o$ in the SAFC relative to that calculated by Springer et al. In our judgment, both area and current density terms contribute to this difference.

In an SAFC, the available active catalyst surface is the perimeter circumscribed by the Pt contact at an air-CDP interface. This is a key limitation of the catalyst layer design used in this work. It is reasonable to assume that the available surface area is a small fraction of that expected based on fully divided nanoparticles of Pt.

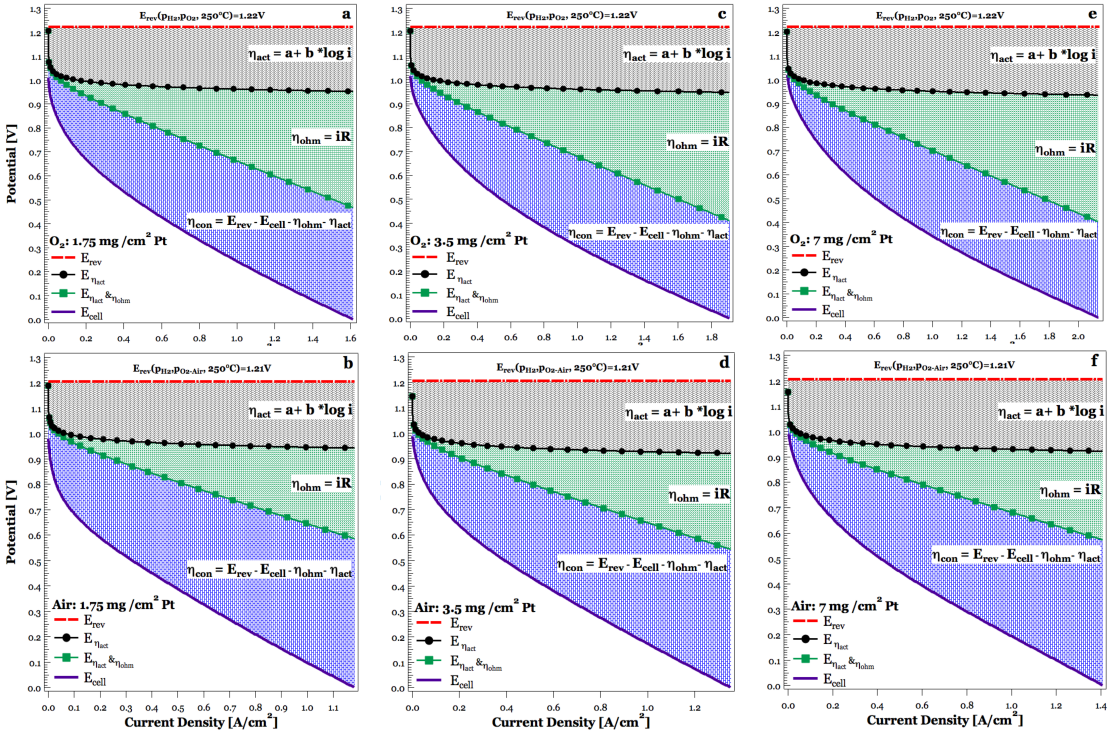


Figure 2.14 Polarization curves with activation and ohmic overpotentials calculation from optimized Tafel parameters a) 1.75 mg/cm² O_2 b) 1.75 mg/cm² Air c) 3.5 mg/cm² O_2 d) 3.5 mg/cm² Air e) 7 mg/cm² O_2 f) 7 mg/cm² Air.

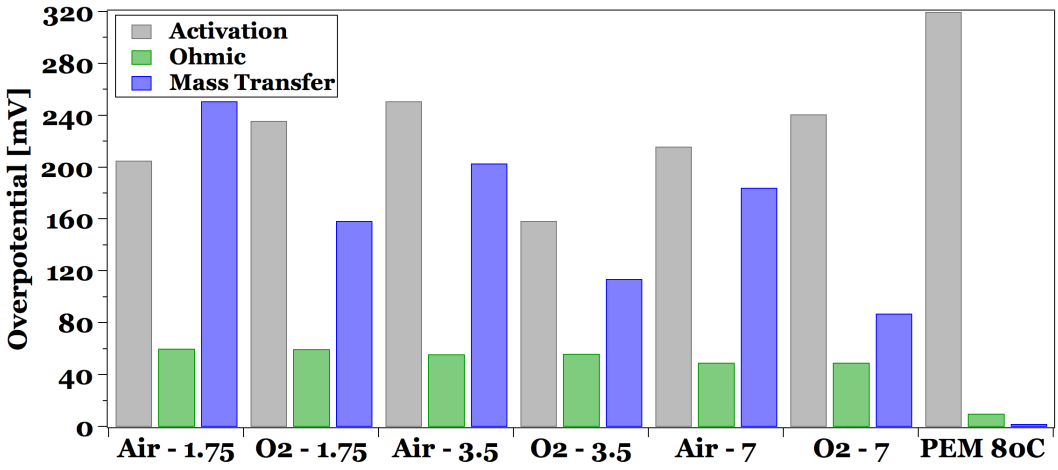


Figure 2.15 Overpotential activation, Ohmic and Mass transfer contribution at i≅0.2. Comparison with values for PEMFC at 80°C in Air at i≅0.1[110].

In spite of the high loading of Pt, the occlusion of the surface by CDP leads to much lower effective surface area contributing to the 'roughness' term, i.e. the ratio of real to geometric area. It is perhaps surprising to think that i_o, the exchange current density 'proxy,' could be lower at the substantially higher temperature. However, it should be kept in mind that the rate-limiting step for the ORR likely includes the initial chemisorption of oxygen. This is a rather weak process and is therefore significantly less favorable at the elevated temperature of the SAFC. Indeed, even hydrogen chemisorption can be difficult to observe under SAFC conditions.

2.6 Conclusions

In this study we developed and evaluated a macrohomogeneous model of SAFCs, through several steps, we obtained excellent fits with errors less than 3%. This demonstrates that our methodology of linking quality experimental data and simultaneous fitting can lead to useful information about the physical parameters of the system and allow us to use model predictions to better understand polarization phenomena. We calculated the polarization phenomena in solid acid fuel cells in successive steps. This modeling study provides us with a basis for considering cells employing Pt coated CDP particles in the catalyst layers. Sensitivity Analysis provided us with a suitable set of initial parameters to enhance agreement between experimental and modeled data. Moreover, it shows us that permeability and limiting current selection are crucial to describe our system. Active area is not as sensitive but its values must be selected properly to be able to describe the phenomena inside the cathode. OCV and Tafel results are in agreement with the theoretical values, which validates our kinetics argument to describe the model and the necessity of robust experimental design to feed the model. The limiting processes in SAFC performance arise from limitations in available surface area and the difficulty of mass transport to this surface.

Permeability values shown here are higher than for a low temperature counterpart as a result of higher diffusion coefficients as a consequence of temperature increased. The difference between air and oxygen is directly related

to the concentration depletion and mass transport effects. We introduced the RCCD factor as a key operation parameter that corrects the geometric area to yield the real active area (Ar) and with a current density term. We did not attempt to separate Ari* mainly because of the unknown Pt surface structural changes (between a bare and oxidized surface) when extrapolating Tafel plots toward zero overpotential. Low values of this parameter reflect a decrease in the accessible electrochemically active area most likely due to the constraints of the SAFC electrode architecture employed, in which the impermeable CDP coats much of the catalyst.

Concentration polarization losses in SAFCs represent the major polarization source when operating on air across the entire current density range. Activation losses represent a major source of loss in oxygen but mass transfer is also important. Thus, we conclude that in order to improve performance and be competitive against its low temperature counterparts, we need to decrease the thickness and improve the microstructural configuration of the catalyst layer.

3 MODELING OF NON-PRECIOUS METAL CATALYST CATHODE LAYER FOR PEMFCS

A version of this chapter was submitted to the Electrochimica Acta Journal: *Modeling Of Non-Precious Metal Catalyst Cathode Layer For PEMFCs* by D. C. Orozco, J. S. Lawton, N. M. Cantillo, G. A. Goenaga, and T. A. Zawodzinski.

Abstract

Proton exchange membrane fuel cell (PEMFC) performance is affected by parameters such as oxygen concentration, catalyst loading, electrode layer thickness, permeability and active area. These parameters are of particular interest for the cathode oxygen reduction reaction (ORR), due to its slower kinetics compared with the anode hydrogen oxidation reaction (HOR). Furthermore, when Pt is replaced with non-precious metal catalyst (NPMC) for the ORR, higher 'catalyst' loadings are needed to compensate for lower catalytic activities. In order to achieve an understanding of the relative importance of the various effects, a Springer-type model is applied. Results illustrate the substantial effect of the variation of oxygen concentration across the catalyst layer and the effect of the catalyst layer over the parameters studied. The model gives us information about ORR kinetics, the most sensitive parameters for describing the catalyst layer for the cathode as well as the interplay between thickness, loading and transport effects. Furthermore, the overpotential analysis verifies the deprived kinetics of NPMCs systems and leads us towards study of the catalytic sites nature as the target to improve performance.

3.1 Introduction

The most common configuration of catalyst layers with Pt-based catalysts in PEM cells included catalyst particles on an amorphous or partly graphitized carbon support in a composite and an ionomer to provide the reaction environment, as figure 3.1 illustrates. Characterization techniques are suitable to elucidate active sites in Pt-based catalyst due to its electronic characteristics and size. For instance, SEM to measure catalyst layer thickness, TEM to detect the catalyst dispersion and size, and XRD to identify the metallic structure of the catalyst. Even then, there are still significant outstanding issues that arise for low Pt loadings. While Figure 3.1 indicates the general aspects of the catalyst environment, detailed knowledge concerning the interactions of ionomer with

solid components is missing. For NPMCs, this situation is compounded by the inability to obtained unambiguous clarifying information from most characterization techniques. Moreover, understanding the mechanistic aspects of NPMCs performance in fuel cell is still tied to the active site chemical and physical structure and there is little or no direct evidence to reveal this. Finally, multiple methods and 'recipes' are used to prepare different NPMCs. These inevitably lead to different final structures.

Consideration of the active site in NPMCs raises many questions about function of this site. For example: What is the role of the metal center? Is it an integral and electrochemically active part of the catalytic site or is the metal just a chemical catalyst for the formation of special oxygen reducing N-doped carbon structures. Three main active sites structures were proposed by Veen [111], Yeager[11], and Wiesener [112] in the 1980s. Seemingly, the three of them are simultaneously present in Fe (or Co)-based catalysts for ORR in acidic media. Their activity and relative population are different, depending on the choice of the metal precursor, nitrogen precursor, structural properties of the carbon support, and the synthesis procedure [113].

The model of active site proposed by van Veen, implies that the thermal treatment (500-600°C) does not lead to the complete destruction of the macrocycles, but rather to a ligand modification, which keeps the Me–N4 moiety intact (pyridinic in further literature). They studied the propose structure by using Extended X-Ray Absorption Fine Structure (EXAFS), in this technique the peaks obtained must be fitted to a set of structure by using Fourier transform. Venn and collaborators performed single-shell fits on the separate peaks for the first three nearest-neighbor atom shells in order to minimize any mutual interference effects on the data analysis.

By choosing the proper reference compounds and results the distances to the first-neighbor atom shell can be determined with an accuracy of 0.002 nm. In contrast, the coordination number for the first and second shells the oscillation is around 20% [114].

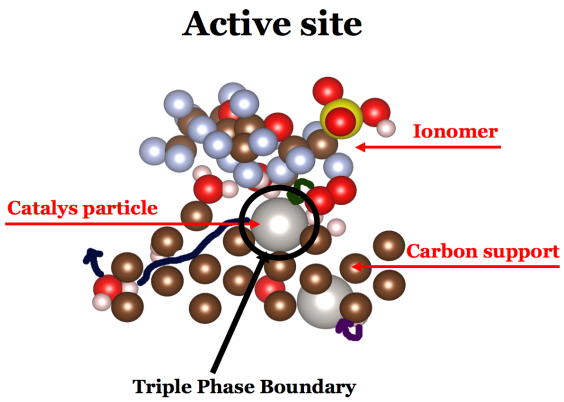


Figure 3.1 Reaction environment schematic representation.

Yeager and coworkers, who were working at higher pyrolysis temperatures (800–850°C), proposed macrocycle decomposition. At 800 °C, most of the metal becomes a mixture of oxides and metal. Upon contact with an electrolyte solution, oxide species undergo dissolution. Metallic ions subsequently adsorb or coordinate to thermally formed sites on the carbon surface, most likely involving one or more nitrogen atoms (FeN_{2+2} in further literature) bound to the carbon surface, but of a type different from the macrocycle-derived Me–N4 centers proposed by van Veen and coworkers[11, 115, 116].

Yeager and collaborators found the structure description by employing visible reflectance spectroscopy of macrocycles on graphite, Pt and Au substrates. This technique in particular is sensitive to electronic and vibrational process and its great for clay mineralogy, OH-bearing minerals, olivines and pyroxenes. They also employed Raman spectroscopy to sense vibrational effects on the sample in and out of the macrocycle plane[117].

In Wiesener approach, the Co or Fe ions of the adsorbed N4-chelates promoted the decomposition of the chelate upon thermal heat treatment followed by the formation, at high temperature, of CNx (pyrrolic in further literature), a special form of carbon bearing nitrogen atoms that would be the true catalyst. In this scenario, the metal is believed to be only an intermediate and has no role in the electroreduction of oxygen [112]. Their X-ray diffraction (XRD) showed that there is a decisive change of the metal chelate between 370 and 510°C. The strongly structured spectrum of the organic compound turns into a spectrum typical of carbon, whereas the typical graphite lines at 25.9° and 15.5° begin to develop from 500°C and from 89O°C[112, 118]. XRD has become one of the most useful techniques to track the structural changes. However, the information for unknown coordination leads to speculation unless used together with local chemistry characterization techniques such as EXAFS or XPS. Figure 3 summarizes the proposed active sites found for current research groups but that are based in the Yeager's, Veen and Wiesener contributions.

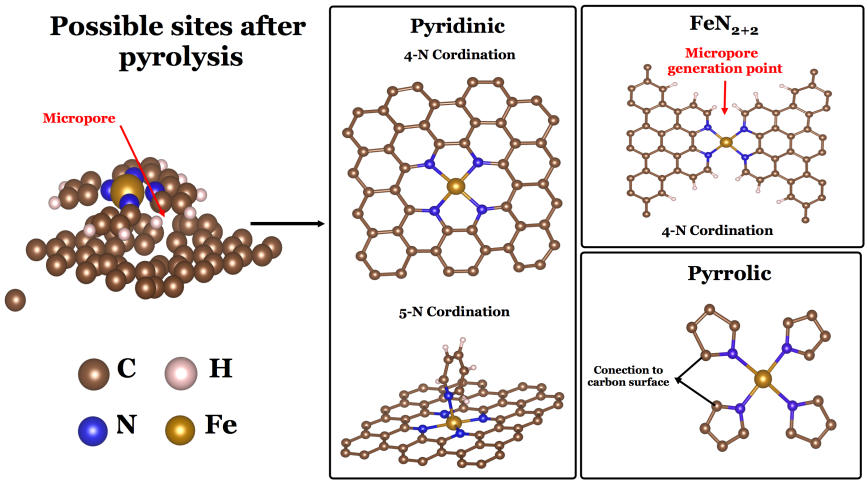


Figure 3.2 Possible active sites after pyrolysis.

One important benchmark used when evaluating NPMCs is the DOE activity target which differs from Pt-based catalysts because the nature of their catalytic sites. Pt-based electrocatalysts are evaluated for their mass and specific activities at 900 mV iR-free in PEM fuel cells under operating conditions. The 2017 target for NPMCs-based electrocatalysts for the cathode of H2 /O2 (Air) PEM fuel cells was first set at a volumetric activity of 300 A/cm^3 measured at 800 mV, iR-free. The fuel cell operating conditions are the same as for Pt-based electrocatalysts.
The catalytic activity for NPMCs is expressed in terms of the volume of the electrode (A/cm^3) in contrast to Pt-based catalysts (A/cm^2), which have a much higher raw material cost and are generally used with high weight percent of Pt on a conductive support, leading to electrodes lower than 10 μm of thickness. Furthermore, when Pt is replaced with NPMCs, the actual catalytic site density in a given formulation is usually unknown thus, higher catalyst loadings are needed to compensate for lower catalytic activities resulting in much thicker cathodes (up to 100 μm thick), which include the carbon support[113].

From these initial remarks, we realize the complexity of NPMCS catalyst layers. Active site identification, performance evaluation and possible mass transfer limitations in the thicker catalyst layers led us to develop a strategic methodology to estimate the main parameters in these materials such as catalyst loading and thickness, diffusion coefficients and active catalyst surface area using modeling techniques.

Polarization curves measured under a single experimental condition are woefully inadequate as sufficient data sets for most models. Though such curves can be fit (quite easily), the values of physical parameters derived from the fit are not reliable. If we are to use modeling to deduce key limiting factors in NPMCs performance, it is critical to use adequately complex experimental data sets for analysis and to include as many independently and experimentally determined parameters as are available to reduce the degrees of freedom. Only then, a modeling study will serve to reveal the physical basis of catalyst layer structures and non-precious reaction pathways effects on performance.

In this study, we examined NPM-based catalyst layer performance to include the rather significant mass transfer effects that arise from the need to use thicker layers. To analyze these effects, a Springer-type model was applied as described in section 2.2. First, we experimentally measure a family of curves for different oxygen partial pressures using catalyst layers of different thicknesses. Then, we use simultaneous fits of all of the curves with only a single model variable, pO_2, and directly derived properties from SEM, BET and TEM. The model reveals significant effects from oxygen variation, the effect of the catalyst layer thickness on the parameters studied and the overpotential contribution to the overall losses.

3.2 Model application

A typical PEMFC, schematically shown in figure 3.3, is a layered architecture and consists of the anode and cathode electrodes compartments, separated by a proton conducting polymer membrane. Both sides include gas flow channels, gas diffusion layers (GDL) and catalyst layer (CL). Usually, two thin catalyst layers are coated on both sides of the membrane, forming a membrane-electrode assembly (MEA).

Hydrogen and oxygen combine electrochemically within the active catalyst layers to produce electricity, water and heat. The gas diffusion layer allows the transport of reactants to and products out off the reaction sites while conducting electrons and heat. The hydrogen oxidation reaction (HOR) occurs at the anode catalyst layer and oxygen reduction reaction (ORR) in the cathode catalyst layer. As mentioned before, due to slower kinetics the ORR is a source of large voltage losses in the PEMFC, making the cathode the electrode of primary importance for overall PEMFC performance improvement.

The catalyst layer and gas diffusion layer play a crucial role in the PEMFC water management aimed at maintaining a delicate balance between reactant transport from the gas channels and water removal from the electrochemically active sites [119].

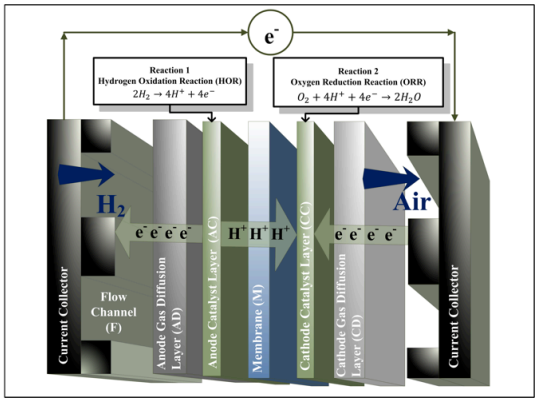


Figure 3.3 Fuel Cell scheme and electrodes reactions.

3.2.1 Model Assumptions

To develop the model, it was necessary to assess what effects needed to be taken into account. The effects of the internal generation of liquid water, ionic conductivity variations within the catalyst layer, or variations of the rate of the interfacial ORR process are not considered in light of the known major effect of NPMC kinetics. Also, the electronic conductivity loss within the CL is considered negligible. In addition, the gas mixture was considered ideal, single-phase flow with steady state and isothermal operation at T=353K. Finally, the depletion of oxygen within the gas flow channel (figure 3.1) is described by defining an effective uniform concentration of oxygen in the flow channel equal to the average of cathode inlet and cathode outlet gas stream concentrations.

Model equations and key parameters are the same as describe in section 2.2. Some modifications made for NPMCs is about the treatment of the Tafel regions where we found the presence of two Tafel slopes. Then, to calculate the overpotential point where the Tafel slope switch, we calculate the slope change from the plot η vs log I as:

$$\eta_{ts} \rightarrow \left(\frac{\partial \eta}{\partial(\log I)}\right)_{i} \neq \left(\frac{\partial \eta}{\partial(\log I)}\right)_{i+1} \qquad \textbf{Equation 3.1}$$

For $\eta \leq \eta_{ts}$ (lower overpotentials)

$$\frac{\partial I}{\partial x} = p_{O_2} \frac{C}{C^*} A_r i_0 exp\left[\left(\frac{\eta}{b_1}\right)\right] \qquad \textbf{Equation 3.2}$$

For $\eta > \eta_{ts}$ (higher overpotentials)

$$\frac{\partial I}{\partial x} = p_{O_2} \frac{C}{C^*} A_r i_0 exp\left[\left(\frac{\eta}{b_2}\right)\right] \qquad \textbf{Equation 3.3}$$

3.2.2 Other relations

Permeability calculated with Darcy Law.

$$K = \frac{\mu v_m \delta_{CL}}{\Delta P} \qquad \textbf{Equation 3.4}$$

v_m: Calculate as Q/A (Q: flow rare, A: cross-sectional area)

ΔP: (Calculated from the concentration distribution)

3.2.3 Model Validation

Similarly than for SAFCs case, for each set of experimental and fitted data, we performed two nonparametric statistical tests: Mann-Whitney U[105] and Kolmogorov-Smirnov[106]. Table 3.1 summarizes the statistical test results for both fuel cell models showing that the modeled data represents the experimental with a 95% level of confidence.

3.3 Experimental

MSc. Nelly Cantillo and Dr. Gabriel Goenaga performed the experimental results showed in this chapter as part of our NPMCs research initiative. The catalyst evaluated here was synthetized by Ma et al. [120], a porphyrin-based conjugated porous organic polymer, named CHF-1 (CHF denotes covalent heme framework), from a custom-designed porphyrin complex, iron (III) meso-5,10,15,20-tetrakis (4-bromophenyl) porphyrin chloride (Fe(tbpp)Cl), as a building block. This mixture was stirred at room temperature under argon atmosphere overnight, and subsequently cooled in an ice bath. Finally, a 50% acetic acid solution was added and the resulting mixture was stirred for another night and then washed and dried in vacuum to give CHF-1 in 78% yield [121].

The as-prepared catalyst was thermally activated under inert atmosphere (N2 gas) at 700°C for 1 hour. This was followed by acid treatment in 0.5M H_2SO_4 at 80°C for 8 hours, to remove excess metal generated during pyrolysis. Then, the sample is subjected to a second heat treatment at 700°C for 1 hour in an inert atmosphere to promote the formation of additional catalytic centers. Figure 3.4 illustrates the catalyst synthesis process schematics in which we create a catalytic powder with a given active site densities (prepared catalyst). Subsequently, we activate the catalytic powder material to create a pyrolyzed catalyst with micropores formation arising from the structure reorganization under acid treatment and temperature activation.

Table 3.1 Statistical goodness of fit tests for NPMCs system.

% O2	Test	p-value	Statistic	Decision
100_1mg	Mann-Whitney	0.800	-0.253	Retain H_o
	KS	1.000	0.296	Retain H_o
100_3mg	Mann-Whitney	0.436	-0.778	Retain H_o
	KS	0.865	0.600	Retain H_o
80_1mg	Mann-Whitney	0.680	-0.413	Retain H_o
	KS	0.998	0.389	Retain H_o
80_3mg	Mann-Whitney	0.893	-0.135	Retain H_o
	KS	1.000	0.306	Retain H_o
60_1mg	Mann-Whitney	0.724	-0.354	Retain H_o
	KS	1.000	0.724	Retain H_o
60_3mg	Mann-Whitney	0.382	-0.875	Retain H_o
	KS	0.824	0.629	Retain H_o
40_1mg	Mann-Whitney	0.685	-0.405	Retain H_o
	KS	1.000	0.267	Retain H_o
40_3mg	Mann-Whitney	0.436	-0.779	Retain H_o
	KS	0.987	0.450	Retain H_o
20_1mg	Mann-Whitney	0.468	-0.726	Retain H_o
	KS	0.991	0.468	Retain H_o
20_3mg	Mann-Whitney	0.264	-1.117	Retain H_o
	KS	0.832	0.624	Retain H_o

The MEAs were prepared by spray-painting the catalyst inks over a 5-cm^2-gas diffusion layer made from carbon paper with a carbon coating (SIGRACET® Gas Diffusion Media, Type GDL 25 BC). The Nafion® content in the dry cathode was 30 wt. %. The anode electrodes were prepared in house, hand painting on the GLDs catalysts inks prepared with 30% platinum on Vulcan XC-72 (BASF) in a 1:2 ratio Pt to Nafion ionomer. Anode loadings were 0.3 mg/cm^2. The cathode and anode electrodes were hot-pressed on either side of a 212 Nafion® membrane at 140°C for 10 minutes using a load of 1000 Kg.

The fuel cell tests were performed on a single-cell Test station from Fuel Cell Technologies with a BioLogic VSP3 multichannel potentiostat connected to a 10A booster. The temperature for all experiments was held at 80 °C; the back pressure was set to 2 bar for both, anode and cathode sides, and all gases were fed at 100% RH. The flow rates were 100 ml/min for H2 at the anode side and 200 ml/min for O2 and O2/Ar mixtures at the cathode side.First, the open circuit voltage (OCV) was held for 10 minutes then the voltage was held at 0.6 V for 15 minutes, followed by 0.4 V for 10 minutes for conditioning. A polarization curve was then recorded by scanning the cell voltage from open circuit potential down to 0.5 V at 0.005V/s scan rate and from 0.5 V to 0.2 V at 0.025V/s scan rate. Measurements were performed with different oxygen concentrations in the cathode feeding, ranging from 20 to 100% in 20% increments. The surface area and the pore size and volume of the catalysts were measured with a Quantachrome Instruments Autosorb iQ with nitrogen as the adsorbate. Brunauer-Emmett-Teller (BET) and Barrett-Joyner-Halenda (BJH) Pore Size ND Volume Analysis was employed for to analyze this data. The quantification of the metal was performed using Inductively Coupled Plasma/Optical Emission Spectrometry (ICP-OES). XRD, SEM (Figure 3.5) and TEM (Figure 3.6) were used to characterize the materials. XRD patterns were measured with a Bruker D2 Phaser diffractometer with Cu Kα radiation. For SEM imaging, a Hitachi S-4800 field emission scanning electron microscope was employed; this equipment features a resolution of 1.0 nm and a variable acceleration voltage of 0.5-30 kV. A 300 kV HF-3300 TEM/STEM, with a cold-field emission gun and 0.13 nm resolution was used to analyze the microstructure of the materials.

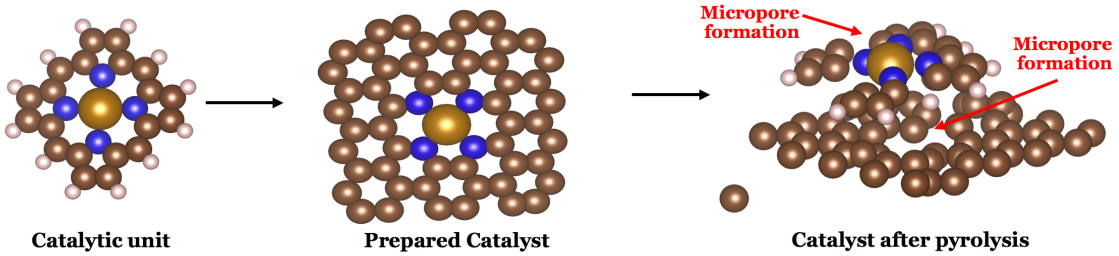


Figure 3.4 Schematic representation of the catalyst preparation.

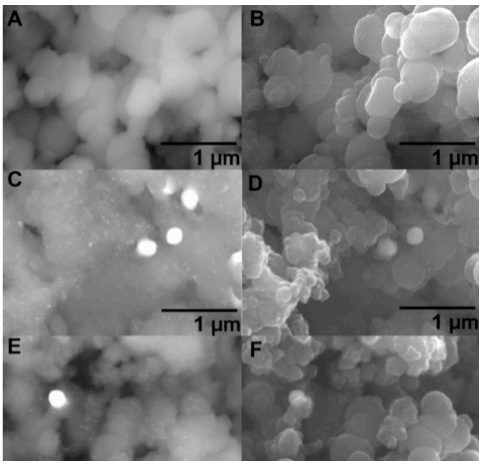


Figure 3.5 Back-scattered and secondary electron images of the highly porous as-synthesized (A, B), 700°C pyrolyzed (C, D) showing the presence of iron nanoparticles, and acid treated (E, F) CHF-1 catalyst. The latter exhibits a lower density of metal particles and a higher porosity as a result of the acid leaching process [121].

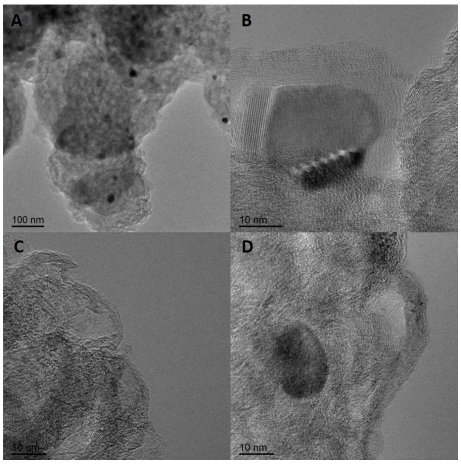


Figure 3.6 High-resolution (HR)TEM images of the 700°C pyrolyzed iron porphyrin catalyst (A) HRTEM image of the iron nanoparticle distribution on the catalyst structure. (B) HRTEM image showing an onion-like mesographitic nanoshell surrounding Fe particle. (C) HRTEM image showing the mesographitic structure of the carbon support. (D) HRTEM image of a typical NPMCs nanostructure involving carbon and metal aggregates [121].

3.4 Results and discussion

The experimental data to be fit consists of several polarization curves obtained for NPMCs as figure 3.7 illustrates. When compared to typical Pt-based PEM cells (δ_{CL}<10 μm), the catalyst loading is quite high and catalyst layers are relatively thick (δ_{CL}: 14 μm and 72 μm). The best Pt catalyst to date is Pt3Ni nanoframes, synthetized by Stamenkovic and collaborators at Argonne National Lab, with activity of 5.7 A/mg-Pt. Figure 3.7 illustrates the RDE results for this material, showing great activity improvement with respect to Pt/C and PtNi/C alloys.

The onset potential for this catalyst is higher compare to other Pt materials and the authors calculated an improvement higher than 16 compare to Pt/C [40]. In contrast, our catalytic material, showed in figure 3.8, exhibits lower onset potential with respect to Pt, Pt/C and Pt_3Ni as a reflection of poor catalytic activity.

Figure 3.10 illustrates the experimental case for pure oxygen and 20% O2/Ar that is the closest case to air operation. The current density for the 20% mixture is similar in both cases. However, for pure oxygen the limiting current reduces in the thicker case as an indication of transport limitation generated by active sites density and catalyst layer configuration.

Table 3.2 summarizes OCV and current limiting values for our evaluated systems. The OCV is a function of the temperature and pressure variation; at 80°C the OCV is equal to 1.177V which is equivalent to the reversible potential for the oxygen reduction reaction calculated as:

$$\boldsymbol{E_{c,rev}(T,P) = E_{0,c}(T) + \frac{RT}{2F} ln\left(\frac{\alpha\beta^{1/2}}{\lambda}\right) + \frac{RT}{2F} ln\left(P_{O_2}^{1/2}\right)} \qquad \textbf{Equation 3.5}$$

$$\boldsymbol{E_{0,c}(T) = -\frac{\Delta G^0(T)}{nF} = -\frac{\sum_i \nu_i\left(\overline{g}_{f,i}^0 - \Delta H(T) - T\Delta S(T)\right)_i}{nF}} \qquad \textbf{Equation 3.6}$$

$$\boldsymbol{E_{0,c}(T) = -\frac{\Delta G^0(T)}{nF} = -\frac{-226116.8}{2\times 96485} = 1.172V} \qquad \textbf{Equation 3.7}$$

Where E_o represents the standard voltage for oxygen. $\boldsymbol{\overline{g}_{f,i}^0}$, the Gibbs formation energy of the i compound, ν_i the stoichiometry coefficients. α, β, λ represent the mole fraction of hydrogen, oxygen and water respectively.

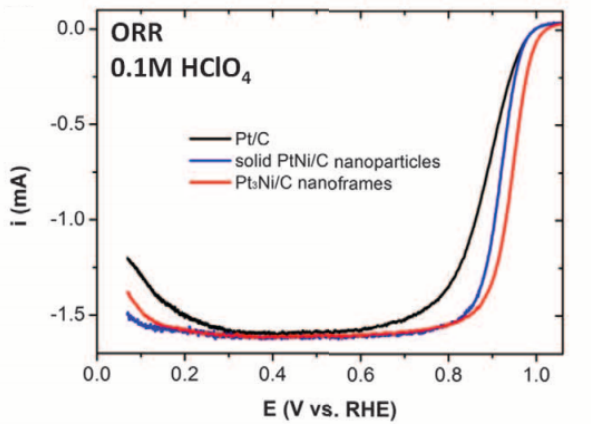


Figure 3.7 RDE Polarization curves for our Iron Porphyrin material [121].

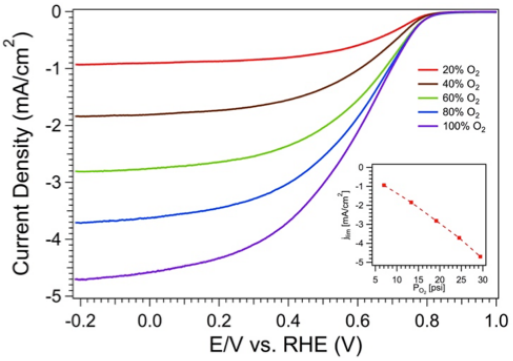


Figure 3.8 RDE Polarization curve Pt_3Ni[40].

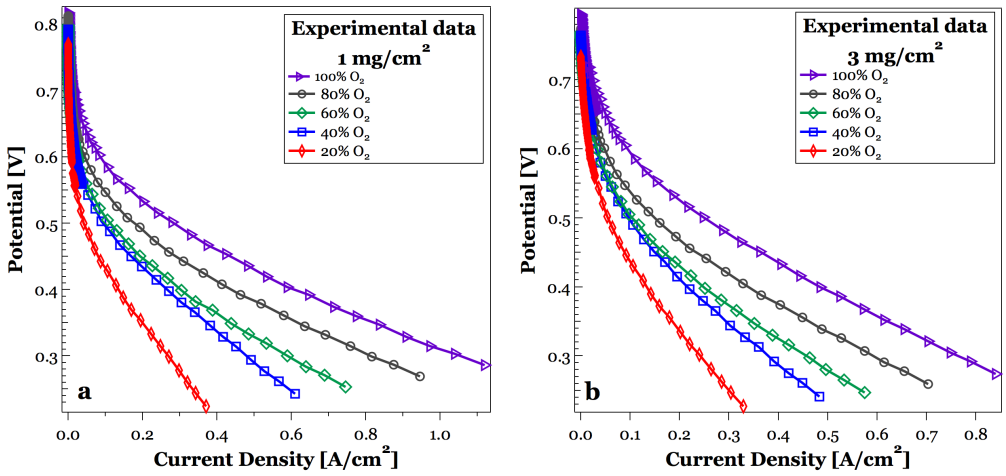


Figure 3.9 Experimental IR-free Polarization curves for different O2/Ar mass concentration feed. Operation temperature: 80°C. Anode: 0.3 mg Pt/cm² in 30% BASF. a) Cathode: 1mg/cm² Fe-PCPF/Nafion. Catalyst layer thickness: 14 µm. b) Cathode: 3mg/cm² Fe-PCPF/Nafion. Catalyst layer thickness: 72 µm.

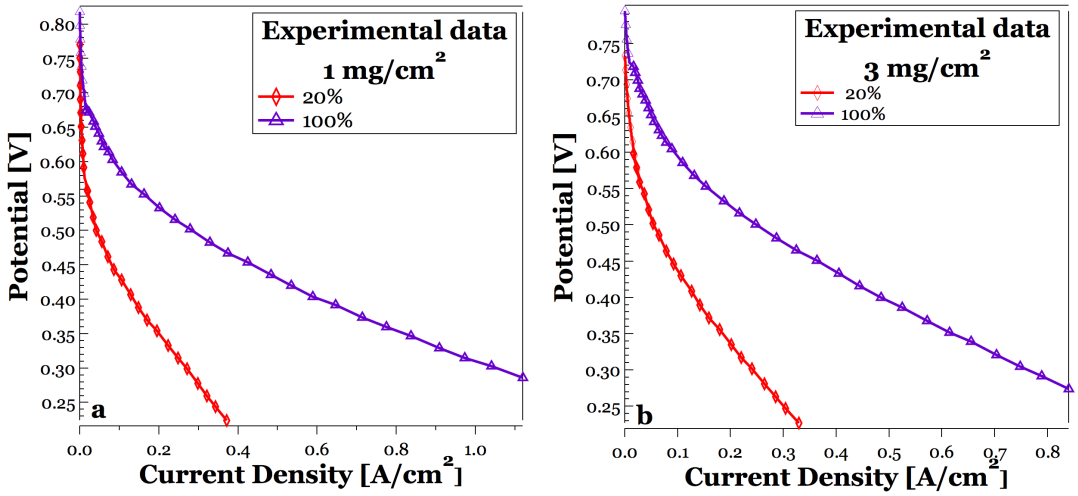


Figure 3.10 Experimental IR-free Polarization curves for different 20% O2/Ar and 100% O2 mass concentration feed. Operation temperature: 80°C. Anode: 0.3 mg Pt/cm² in 30% BASF. a) Cathode: 1mg/cm² Fe-PCPF/Nafion. Catalyst layer thickness: 14 µm. b) Cathode: 3mg/cm² Fe-PCPF/Nafion. Catalyst layer thickness: 72 µm.

The mole fraction of the reactants is close to one, based on the stoich 2:1 oxygen to hydrogen**.** Second term in equation 3.2 vanished then, OCV is calculated from equation 12[28]:

$$\boldsymbol{OCV_{O_2} = E_0(T) + \frac{RT}{zF} ln\left(\frac{P_{H_2} P_{O_2}^{\frac{1}{2}}}{P_{H_2O}}\right) = 1.177V} \qquad \textbf{Equation 3.8}$$

To calculate the expected variation in OCV when we switch from oxygen to air, for the same hydrogen and relative humidity, equation 3.2 is reorganized to express the OCV as:

$$\boldsymbol{\Delta OCV = \frac{RT}{4F} ln\left(\frac{p_{O_2}}{p_{O_{2,mix}}}\right)} \qquad \textbf{Equation 3.9}$$

Equation 3.5 is valid if we assume the main contribution is given by oxygen. For PEM Fuel Cells, the OCV can be calculated as[122]:

$$\boldsymbol{E^{OCV} = E_{c,rev}^{nerst}(T,P) - E_{a,rev}^{nerst}(T,P)} \qquad \textbf{Equation 3.10}$$

Where, $E_{c,rev}^{nerst}(T,P)$ and $E_{a,rev}^{nerst}(T,P)$ are the reversible potentials cathodic and anodic. Similarly than for oxygen, the anodic potential can be expressed as[122]:

$$\boldsymbol{E_{a,rev}^{nerst}(T,P) = E_{0,a}(T) + \frac{RT}{2F} ln\left(\frac{[H^+]^2}{P_{H_2}}\right)} \qquad \textbf{Equation 3.11}$$

Finally, the theoretical fuel cell OCV is expressed as[122]:

$$\boldsymbol{E_{theor}^{OCV} = E_{0,c}(T) - 0.000846(T - 298.15) + \frac{RT}{4F} ln\left[P_{O_2}\left(P_{H_2}\right)^2\right]} \qquad \textbf{Equation 3.12}$$

It is evident from figure 3.7 and the OCV values summarized in table 3.2 that the oxygen partial pressure and catalyst layer configuration play an important role in the catalyst activity. As stated in equation 3.9, the OCV is a function of the oxygen and hydrogen concentration but other factors influencing its behavior are hydrogen crossover and the mixed potential generated by parallel reactions. However, due to the unknown nature of the active site is difficult to make a hypothesis at this stage. For instance, in Pt systems this mixed potential is often related with the parallel reaction of Pt to produce platinum oxides.

Table 3.2 Experimental OCV and limiting current values.

% O_2	1mg/cm² Fe-PCPF/Nafion			3mg/cm² Fe-PCPF/Nafion		
	OCV [V]	OCV_t [V]	I_{lim} [A/cm²]	OCV [V]	OCV_t [V]	I_{lim} [A/cm²]
20	0.7705	1.119	0.394	0.7334	1.119	0.324
40	0.7932	1.126	0.628	0.7644	1.126	0.416
60	0.7987	1.128	0.809	0.769	1.128	0.513
80	0.8128	1.129	0.997	0.7737	1.129	0.569
100	0.8179	1.131	1.17	0.7949	1.131	0.655

3.4.1 Sensitivity analysis

We analyzed the parameters sensitivity with the same procedure than for SAFCs. However, in the NPMCs case, the strong relation among parameters made difficult the usage of the experimental Tafel slopes as initial point. Even so, those values (not presented here) were used to analyze the main parameters behavior. Figure 3.11 shows the sensitivity analysis for the pure oxygen case and 1mg/cm^2 loading. This figure reveals that one parameter is not enough to fit the polarization curve. However, the procedure allows us to narrow the base case parameters summarized in table 3.3.

Figure 3.11a represents the model sensitivity to the RCCD term, $A_r i_o$. The model will converge for any value of $A_r i_o$ lower than $3*10^{-3}$. Moreover, its strong relation with the Tafel slope selection makes this value an upper limit, rather than a real parameter value. Figure 3.11b shows the sensitivity to permeability (DC*). The values yield satisfactory results over a specific range, giving us an upper limit value of the parameter. For values smaller than $1*10^{-11}$, the simulations do not converge or the maximum current obtained is unrealistic. Permeability values (DC*) modified the diffusion current and the shape at higher current densities is its reflection as figure 3.11b illustrates. In summary, the permeability values modify the diffusion current behavior, making the model convergence sensitive to the selection of this parameter.

Figure 3.11c shows the effect of varying limiting current (I_{lim}). The interesting part about it is the shape modification at lower potentials. If the limiting current surpasses the maximum current, the convergence is not achieved. However, this is not a fitting parameter but rather provides a method to estimate the limiting current, which cannot be directly extracted from the polarization curve. Once the value is set, no further optimization is required.

The Tafel slopes values were not possible to get with the same procedure as for SAFCs. The approach was to assume one single slope value and then, let the simulation run to optimize the base case parameters as summarized in table 3.3.

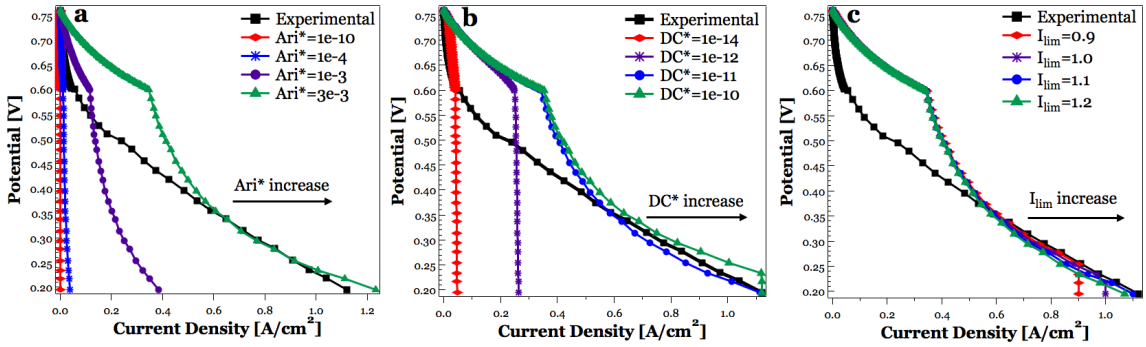


Figure 3.11 Parameters Sensitivity for pure oxygen and 1mg/cm² loading Tafel slopes: 119 mv/dec and 68 mv/dec. a) Ari_o b) DC* c) I_{lim}.

Table 3.3 Fitted parameters: base case

Parameter	P_{O2}	1 mg		3 mg	
Active area - $A_r i^*$ (A/cm²)	20%	$2.5*10^{-4}$		$2.5*10^{-4}$	
	40%	$2.5*10^{-4}$		$2.5*10^{-4}$	
	60%	$2.5*10^{-4}$		$2.5*10^{-4}$	
	80%	$2.5*10^{-4}$		$2.5*10^{-4}$	
	100%	$2.5*10^{-4}$		$2.5*10^{-4}$	
Permeability – DC* (mol/cm-s-atm)	20%	$3.8*10^{-11}$		$3.8*10^{-11}$	
	40%	$3.8*10^{-11}$		$3.8*10^{-11}$	
	60%	$3.8*10^{-11}$		$3.8*10^{-11}$	
	80%	$3.8*10^{-11}$		$3.8*10^{-11}$	
	100%	$3.8*10^{-11}$		$3.8*10^{-11}$	
		Tafel 1	Tafel 2	Tafel 1	Tafel 2
Tafel slope (mv/dec)	20%	120	109	109	80
	40%	110	109	110	109
	60%	110	109	110	109
	80%	110	109	110	109
	100%	110	109	110	109
Limiting Current (A/cm²)	20%	0.4		0.3	
	40%	0.6		0.4	
	60%	0.8		0.5	
	80%	1.0		0.6	
	100%	1.2		0.7	

3.4.2 Polarization curves fitting

The base case parameters initialize the simulation, as shown in table 2.3. Then, we performed a fit of the polarization curves by using backward Euler method with a step of 1/δCL. The Newton-Rapshon's method was applied for numerically solving the equations in Matlab.

The optimization was carrying out by finding the local minimum of each parameter with the simplex method. Finally, the global minimum was obtained with these values as initial point.

Figure 3.12 illustrates the polarization curves fitting for the different loadings with a 95% of confidence for both sets. Tables 3.4 and 3.5 illustrate the parameters resulting from the optimization process. A comparison between the base and optimized parameters (tables 3.4 and 3.5) denote Tafel slopes and DC* values as a correct estimate.

For the 1mg case, permeability values are in the same order of magnitude than the base ones. However, for the 3mg case they differ by one order of magnitude. The first Tafel values are closer to the base case and the second Tafel values are lower than the based ones. These results indicate the presence of two Tafel regions, which will be further discussed. The main adjustment is for RCCD, which did not follow the initial sensitivity analysis, thus, indicating its strong relation to the Tafel values selection.

Figure 3.12 illustrate the polarization curves fitting, highlighting the oxygen partial pressure depletion effect on current density. The OCV values decreased proportional to oxygen as expected from equation 3.6. The difference between OCV_{theor} and the OCV measure is up to 0.4V. This implies that without operation, the activation overpotential is at least 400mV.

When comparing oxygen vs. the 20% fits, for 1mg and 3mg, the performance decreases around 66% and 50% respectively. These observations are consequences of the poor catalytic activity on one hand, and additional mass transport limitations for the mixtures mostly, in thicker catalyst layers.

3.4.3 Tafel Slopes

Figure 3.13 illustrates the results for Tafel regions. The Tafel values variation is less than 3% in comparison with the mean value, as expressed by the variation coefficient in table 3.6. In both cases, the standard deviation is lower than 3mv/dec. As conclusion, the kinetic parameters can be considered constant.

Assuming the reaction mechanism proposed by Holewinski and Linic (figure 1.4) [31], for the oxygen adsorption as limiting step and coverage equal to zero, the Tafel slope is 120mv/dec. As coverage increases, the Tafel slope value decreases until 60 mv/dev. Thus, Tafel 1 corresponds to oxygen adsorption limiting step and coverage around 0.05. In other words, the Tafel 1 represents the oxygen interaction with the Fe Porphyrin active site.

Tafel slopes of 60 mv/dec represents simultaneous O – O bond breaking and adsorption on the active site. Moreover, the O-O bond breaking is not a potential determining step and the Tafel values represent the OH* and O* interaction with the surface. The double Tafel slope for Pt system indicates surface cleaning from platinum oxides, which are present at higher potentials (>0.9V).

However, for NPMCs, oxides presence is a very unlikely scenario based on the low OCV values we found. The only possible explanation for the double Tafel slope then, is the presence of a second active site. Therefore, we conclude that both sites have O adsorption as limiting steps and the coverage modify the reaction environment.

3.4.4 Roughness corrected factor

Figure 3.14 illustrates RCCD behavior as function of the loading and the oxygen concentration. RCCD as discussed in the SAFC case, is difficult to separate this term into its components due to the difficulty to calculate the exchange current. If our Tafel slopes analysis is true, we might have the presence of multiple active sites with their own exchange current value. Moreover, our analysis also suggests that the extrapolation towards zero overpotential as coverage is not zero, is not a good estimate.

Table 3.4 Parameter summary for 1mg catalyst loading.

% O2	Tafel 1 [mV/dec]	Tafel 2 [mV/dec]	K[m²]	DC* [mol cm⁻¹ s⁻¹ atm⁻¹]	$A_r i_o$ - RCCD [mA/cm²]
20	106	81	2.6 x10⁻¹⁴	1.18e-13	0.064
40	104	76	3.1 x10⁻¹⁴	8.43e-14	0.068
60	100	74	8.0 x10⁻¹⁴	9.27e-14	0.129
80	114	78	2.8 x10⁻¹⁴	6.13e-14	0.154
100	102	72	8.9 x10⁻¹⁴	8.97e-14	0.265

Table 3.5 Parameter summary for 3mg catalyst loading.

% O2	Tafel 1 [mV/dec]	Tafel 2 [mV/dec]	K [m²]	DC* [mol cm⁻¹ s⁻¹ atm⁻¹]	$A_r i_o$ - RCCD [mA/cm²]
20	107	82	1.2 x10⁻¹³	1.18E-13	0.076
40	104	81	8.4 x10⁻¹⁴	8.43E-14	0.079
60	104	82	9.3 x10⁻¹⁴	9.27E-14	0.134
80	108	80	6.1 x10⁻¹⁴	6.13E-14	0.162
100	114	80	9.0 x10⁻¹⁴	8.97E-14	0.252

Table 3.6 Tafel variation parameter with respect to the mean

	1mg		3mg	
% O2	Tafel high η	Tafel low η	Tafel high η	Tafel low η
$\bar{x}$	106.7 mV/dec	74.8 mV/dec	101.2 mV/dec	70.5 mV/dec
σ	2.9	1.1	1.7	3.4
σ^2	1.7	1.1	1.3	1.9
VC(%)	1.6	1.4	1.3	2.6

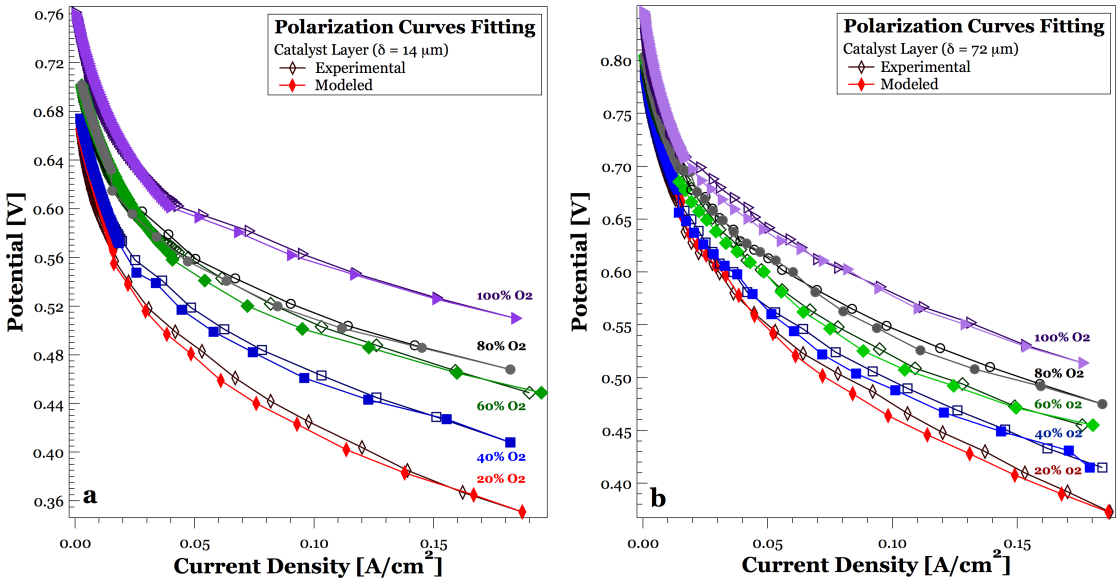


Figure 3.12 Polarization curves fitting for different O2/Ar mass concentration feed. Operation temperature: 80°C. Anode: 0.3 mg Pt/cm² in 30% BASF. a) Cathode: 1mg/cm² Fe-PCPF/Nafion. Catalyst layer thickness: 14 μm. b) Cathode: 3mg/cm² Fe-PCPF/Nafion. Catalyst layer thickness: 72 μm.

From figure 3.14 is possible to infer that the RCCD values are reflection of the exchange current behavior which is express as[28]:

$$i_0 = FAk^0 C_O^{(1-\alpha)} C_R^{\alpha} \qquad \textbf{Equation 3.13}$$

Equation 3.10 represents the exchange current functionality on oxygen concentration; RCCD decay from oxygen to 20% mixture is a direct consequence of this relation. The optimized value decrease, from its original approximation, indicates not only the importance of this parameter for modeling but also represents the intrinsic kinetics of our catalytic system. Moreover, our values are two orders of magnitude lesser than the values reported by Springer, which imply lower electrochemical active area for our material.

3.4.5 Concentration distribution

Figure 3.15 illustrates the concentration variation across the catalyst layer. The oxygen concentration conversion is higher for the 3mg/cm2 loading than with the 1mg/cm2 as a direct consequence of increasing the amount of active sites. In general for both systems, there is a low conversion area closer to the GDL/CL interface that might be related with oxygen transport to the active sites. The conversion becomes more effective closer to the catalyst/membrane interface driven mainly by the protons availability for the reaction.

The oxygen conversion for the 20% case (Figure 3.15a) is the highest, which means all the oxygen entering to the catalyst layer is reacting. In contrast, the 100% case (Figure 3.15d) has the lower conversion, which means a small portion of the oxygen entering the catalyst layer is reacting. The conversion decrease for the lowest loading represents the small density of active sites. For higher loadings, the decrease is not as severe but it is significant. In both cases, MEA's degradation contributes to conversion decrease as a result of longer operation hours and catalyst deactivation during continuous operation, which was the case for this MEA's. The constant input flow rate might generate severe transport effects and increase the catalyst degradation in both MEAs. For instance, with the lower thickness, the flow rate can be faster enough than the residence time of oxygen inside the catalyst layer is not adequate for the reaction to occur and thus, the conversion is lower.

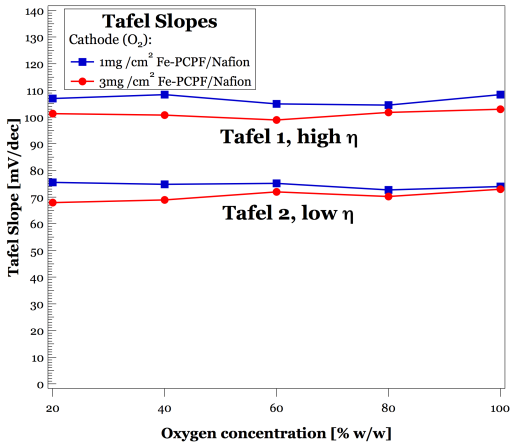


Figure 3.13 First and second Tafel slope behavior for oxygen concentration and catalyst loading variation.

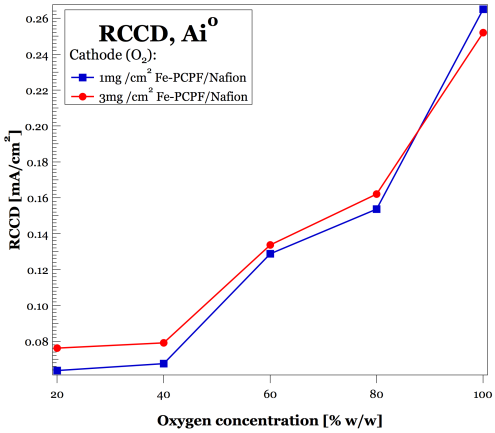


Figure 3.14 RCCD parameter behavior for oxygen concentration and catalyst loading variation

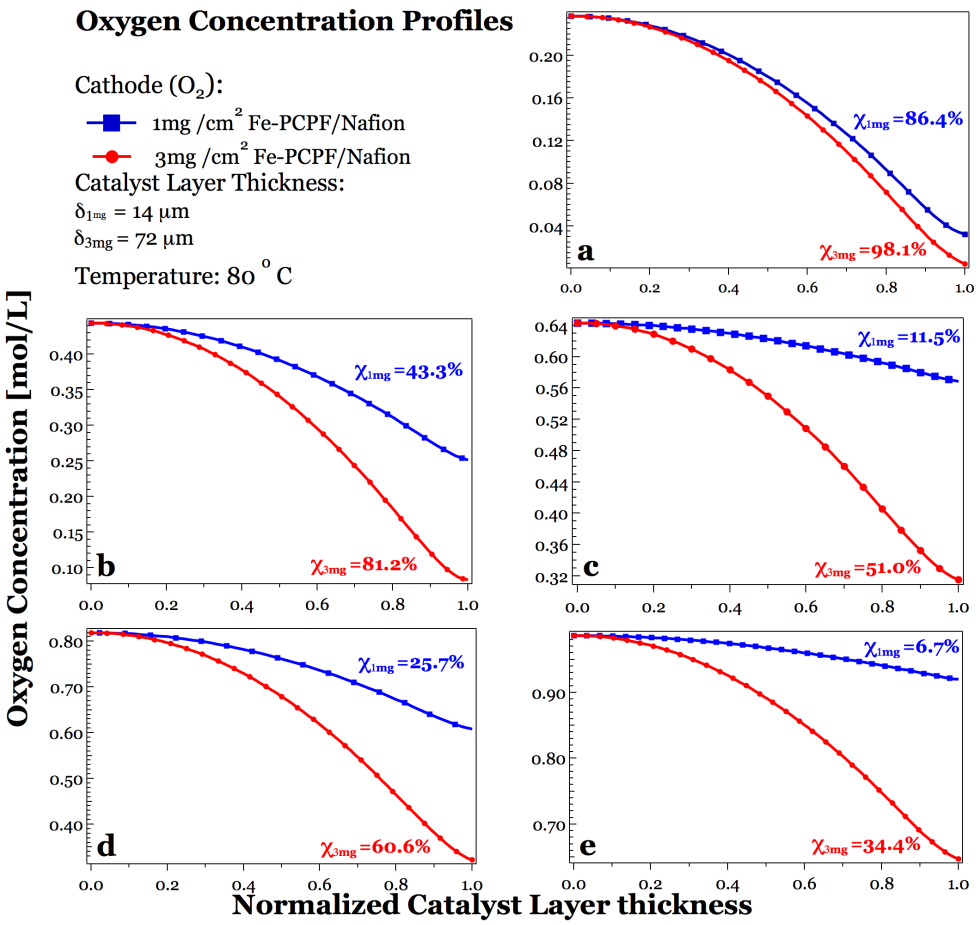


Figure 3.15 Oxygen concentration and conversion across the catalyst layer. Weight/Weight percentage : a. 20%, b. 40%, c. 60%, d. 80% and, e. 100%.

3.4.6 Permeability

Figure 3.16 illustrates the permeability behavior and table 3.7 summarized these values. The variation of these parameters represent by the error bars does not allow us to treat the parameter as constant. We used equation 3.1 to calculate permeability and compared it with our model as figure 3.16a illustrates. Darcy's law gives as an insight of the reactants penetration rate to the catalyst layer. In general, gas transport across the catalyst layer is slow and it is reflected in the low permeability values.

Figure 3.16a represents the penetration rate, which is faster for lower loadings. The baseline in figure 3.16b represents oxygen permeability in Nafion® [123], which are closer to the thinner catalyst layer values. One possible explanation is the higher ionomer content at lower loading. However, pure oxygen permeability is the same for both catalyst layers, which implies that the variability has to do with the mixture properties and its transport inside the catalyst layer.

3.4.7 Current distribution

Figure 3.17 shows the calculated distribution of local current density across the catalyst layer at different voltages (0.5V, 0.6V, 0.64V) for oxygen and 20% mixture. The behavior is presented for low loading (Figure 3.17a and 3.17c) and high loading (Figure 3.17b and 3.17d). The difference in these graphs is minimum, if we take into account the small changes in current density. The 20% case (Figure 3.17a and 3.17b) shows a limiting situation with respect to gas transport, indicated by the inflections in the curves, as the local current density drops close to the CL/membrane interface (x=1).

The modeling results show decay in current density near this boundary as consequence of the interplay between charge and reactant transport through the catalyst layer. The low conversion for all voltages throughout the catalyst layer implies poor catalytic performance. This is even the case for oxygen-fed cathodes and higher loadings. This is consistent with the OCV decrease and poor performance shown in the polarization curves.

Table 3.7 Permeability variation parameter with respect to the mean

	1mg		3mg	
Statistics	**K**	**DC**	**K**	**DC**
$\bar{x}$	5.1E-14	8.9E-14	8.9E-14	1.2E-10
σ^2	9.6E-28	4.1E-28	4.1E-28	5.3E-21
σ	3.1E-14	2.3E-14	2.0 E-14	7.3E-11

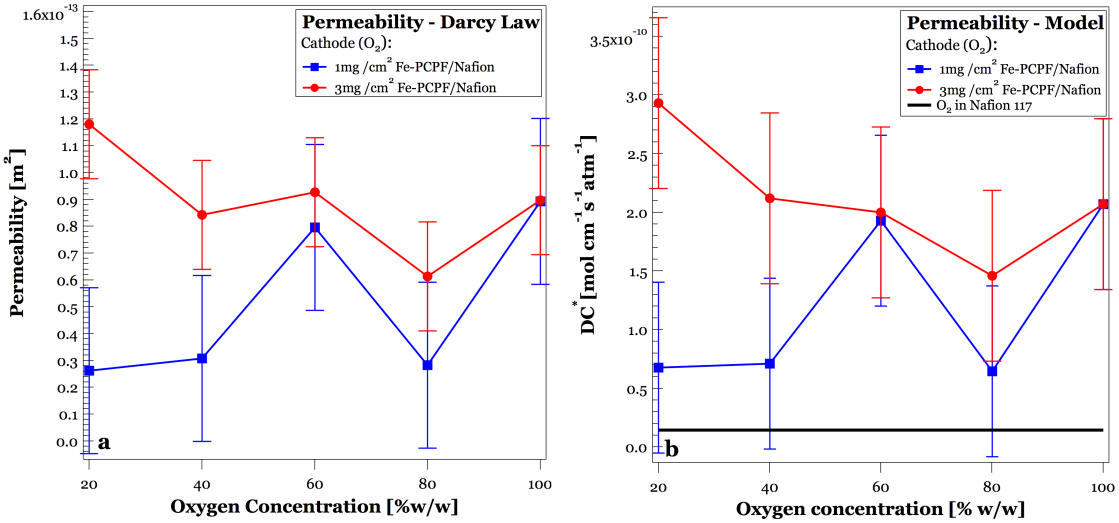


Figure 3.16 Permeability values a) Calculated from Darcy Law with modeled concentration profiles. b) Calculated from Springer Model, O_2 permeability in Nafion from Zhang, Lei et al., 2003 [123].

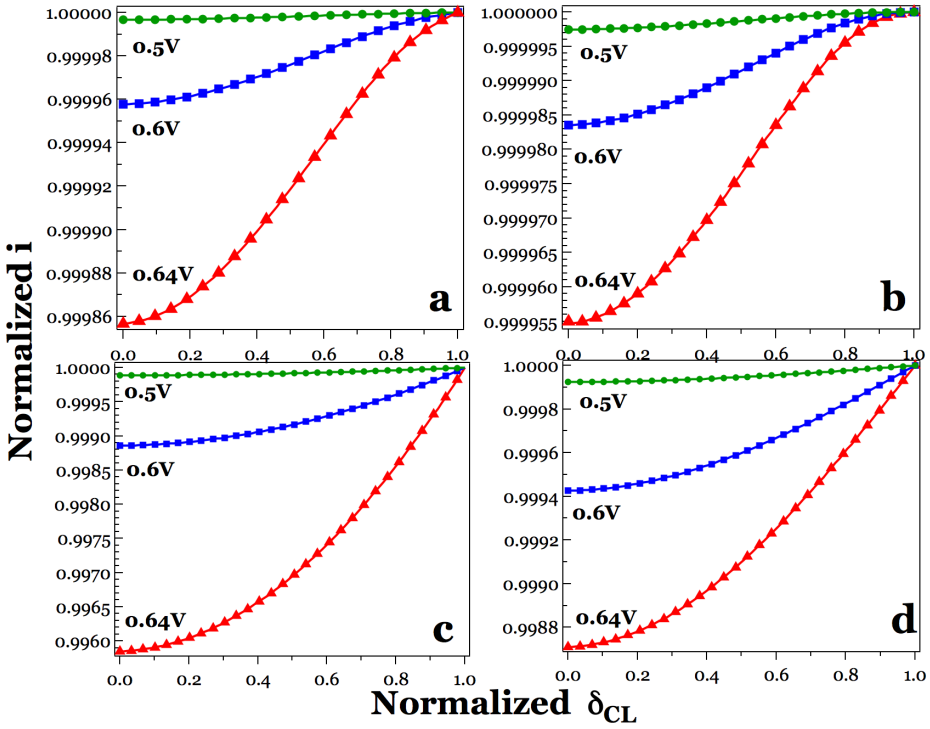


Figure 3.17 Current Density distribution at different potentials. a) 20% O2, 1mg/cm² FePp. b) 20% O2, 3mg/cm². c) 100% O2, 1mg/cm² FePp. d) 100% O2, 3mg/cm² FePp.

3.4.8 Overpotentials

Based on our analysis of the fitted parameters, concentration distribution, permeability and the current distribution we calculated the losses to verify the validity of our arguments in terms of transport and charge transfer within the catalyst layer, as well as, kinetic behavior. The cell potential is calculated as[28]:

$$E_{cell} = E_{rev}(p_{H_2,} p_{O_2,} T) - \eta_{act} - \eta_{ohm} - \eta_{con} \qquad \textbf{Equation 3.14}$$

Where $E_{rev}(p_{H_2,} p_{O_2,} T)$, represents the reversible electrode potential at the temperature and operation pressure and is calculated with equation 3.5. η_{act}, represents the activation overpotential (calculated for both higher and lower overpotentials) and can be calculated for ORR due to its sluggish kinetics compare with hydrogen as:

$$\eta_i = \frac{2.3RT}{\alpha F} log i_{0,i} - \frac{2.3RT}{\alpha F} log i \qquad \textbf{Equation 3.15}$$

η_{ohm}, is the ohmic overpotential associated with the catalyst layer resistance and can be calculated as:

$$\eta_{ohm,i} = iR_i \qquad \textbf{Equation 3.16}$$

R_i, represents the MEA resistance obtained from the in situ measurements. These values are tabulated in Table 3.. η_{con} represents the mass transfer overpotential, which can be calculated from equation 3.10.

For our system, the reversible electrode potential was calculated from equation 3.2 and summarized in table 3.8. The losses are summarized in table 3.9 and were calculated for a fixed current density of 0.1 A/cm^2. Figure 3.18 represents the losses contribution for pure oxygen and 20% oxygen (closer to oxygen in air composition).

Certainly, activation losses are the major polarization source for NPMCS with values higher than 90% as table 3.9 illustrates. This result was expected due to the lower OCV values for each system, which highlights the sluggish ORR kinetics. Moreover, the percentage is higher for the 1mg/cm^2 MEA as consequence of the low density of active sites. On the other hand, the proportion of the loss associated with kinetic limitations decreases with oxygen concentration.

Table 3.8 Reversible electrode potential

Oxygen Concentration	20	40	60	80	100
E_{rev} [V]	1.167	1.171	1.174	1.176	1.177

Ohmic losses represent around 4% of the losses. For pure oxygen systems, these percentages are higher as a consequence of higher reaction rates and active sites saturation. In general, for both systems, the ohmic potential values are approximately constant and in agreement from the experimental resistance values.

Concentration polarization (i.e mass transport) losses for the 1mg/cm^2 MEA increase with the oxygen dilution. For lower concentration, these sites would not achieve saturation thus; the concentration effects are not present. As we increased oxygen concentration the saturation is reached, thus the transport become more important. It is important to indicate current density might be not the right parameter to choose for overpotential calculation due to low performance shown in the systems.

Concentration polarization losses for the 3mg/cm^2 MEA do not follow any tendency. However, the highest (i.e. worst) value is obtained for 20% case, which illustrates the expected transport effect relative to pure oxygen. The transport effect is higher than for the 1mg/cm^2 case, which reflects the catalyst layer thickness increase.

Based on Figure 3.18, 3.19 and table 3.9, we can draw a few basic conclusions. For all cases, activation losses represent the overwhelming majority of the losses. Ohmic and concentration losses are modest and not strongly representative due to the predominant kinetic driven system. Concentration polarization losses are higher for thicker catalyst layers with a contribution as large as 8.3%. Ohmic losses are approximately constant for both systems with contributions up to 3.6%.

Table 3.9 Activation, Ohmic and Concentration overpotentials at i≅0.2 A/cm²

% O2		1 mg/cm² FeP Losses [mV]	% Loss		3 mg/cm² FeP Losses [mV]	% Loss
20	η_{act}	730.5	95.7	η_{act}	621.6	88.8
	η_{ohm}	21.3	2.7	η_{ohm}	20.1	2.9
	η_{con}	11.5	1.6	η_{con}	58.4	8.3
40	η_{act}	668.0	94.7	η_{act}	638.6	92.8
	η_{ohm}	19.0	2.7	η_{ohm}	23.0	3.3
	η_{con}	18.5	2.6	η_{con}	26.4	3.9
60	η_{act}	631.4	93.9	η_{act}	603.0	89.8
	η_{ohm}	20.4	3.0	η_{ohm}	23.7	3.5
	η_{con}	20.6	3.1	η_{con}	45	6.7
80	η_{act}	631.4	93.3	η_{act}	610.5	90.2
	η_{ohm}	22.5	3.35	η_{ohm}	24.4	3.6
	η_{con}	22.5	3.35	η_{con}	16.4	2.4
100	η_{act}	578.3	90.7	η_{act}	581.9	91.7
	η_{ohm}	20.7	3.2	η_{ohm}	24.4	3.8
	η_{con}	38.7	6.1	η_{con}	28.1	4.4

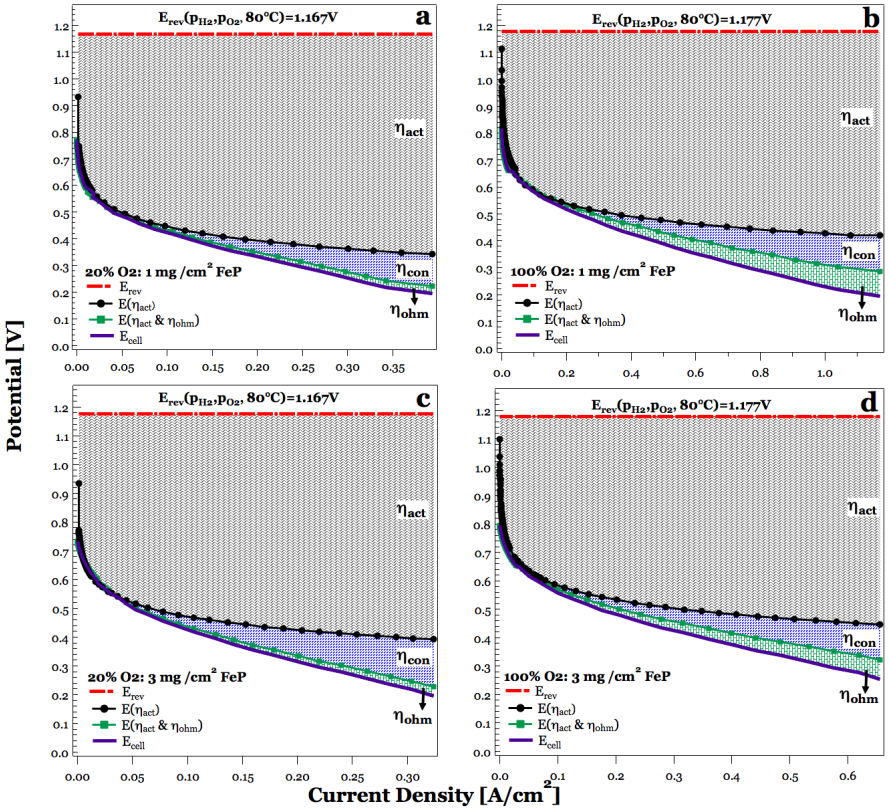


Figure 3.18 Polarization curves with activation and ohmic overpotentials calculation from optimized Tafel parameters a) 20% O2 1mg/cm² FePp b) 100% O2 1mg/cm² FePp c) 20% O2 3mg/cm² FePp O2 d) 100% O2 3mg/cm²

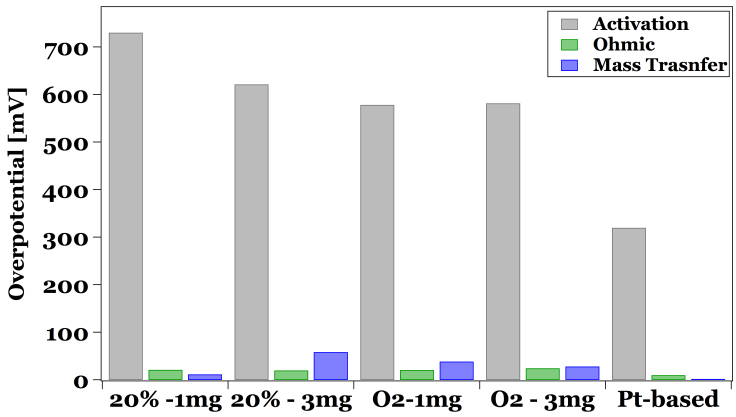


Figure 3.19 Overpotentials contribution for pure oxygen and 20% case. Pt-based values from Arisetty et al. [110].

The activation overpotential increases when the oxygen partial pressure decreases as direct consequence of the change in partial pressure (lower current densities, *log i,* behavior). The ohmic and concentration overpotential is higher in the lower loading case and might be associated with higher degradation rates combined with the oxygen transport and less active site per area within the catalyst layer.

Figure 3.19 shows the overpotential calculation in joint work between Argonne and Los Alamos Lab [110]. They evaluated the effect of loading decreasing in the polarization values and life cycling. The higher loading catalyst at 0.1 A/cm^2 presented overpotential values of 300mV before 10000 cycling. If we compared this result with our catalyst, our overpotential values are twice as bigger as their catalyst. This suggests us that this type of material is not very active towards ORR compare to Pt. Moreover, mass transfer losses and ohmic losses presence in our systems indicates the catalyst layer thickness effect on performance.

3.5 Conclusions

The Springer-type model gives us important insight in the catalyst behavior under different operational conditions and it represents different aspects related with the physics of the system. The polarization phenomena were modeled in successive steps. We identified activation losses as the major polarization source. Ohmic losses are approximately constant and validate the methodology employed to build the MEAs. Concentration losses are the second larger source of losses. The limiting process in NPMCs arises from limitations in active site density, low catalyst performance and the mass transport issues to this catalytic surface.

Furthermore, the quality of the experimental data is important for parameter optimization and fitting adjustment. The oxygen partial pressure dramatically influences fuel cell performance, affecting directly the OCV and limiting current values. Moreover, the thickness of the catalyst layer greatly affects performance due to mass transport losses increase, which is reflected in the permeability variability and the low conversion.

Another important conclusion is the strong correlation between the catalyst thickness, loading and transport behavior through the catalyst layer. Active area, concentration and permeability behavior show some evidence of the influence of the fluid nature, directly related with the effective usage of the active sites, the porous structure and gas composition. Further studies will require more catalyst layer thickness experiments to elucidate the parameters behavior as a function of the catalyst thickness, porosity distribution, and geometrical active area as an insight into the oxygen utilization and catalyst layer composition.

Two Tafel slopes were found during this modeling work and they suggest the existence of two different active sites within the catalyst layer configuration. Moreover, both of these sites have oxygen adsorption limiting steps but it main difference is the surface coverage. Further microscopic modeling studies of the possible sites will give us an insight into the reaction mechanism and validate our Tafel slopes hypothesis. Our overpotential analysis also show lowly catalytic activity of the Fe Porphyrin under study, with activation over potentials twice as bigger as O.4A/cm compared with Pt catalyst at the same current density. Moreover, mass transfer losses presence points towards thickness reduction as part of the performance improvement.

4 MICROSCALE MODELING: UNDERSTANDING PGM-FREE ACTIVE SITES

Abstract

PGM-Free catalyst active site identification is one of the most discussed topics in the field. Based on our simulation results from the macroscopic model, we identified the intrinsic rate and accessible surface (the roughness corrected exchange current density) as key factors in understanding catalyst layers based on PGM-free materials. The morphology of these materials is not well understood due to the pyrolysis required to achieve catalytic behavior towards ORR. My approach is to understand the elements involved in the reaction process and to 'decompose' the catalytic material into its elemental components to understand the role of the metallic center and the Iron Porphyrin in the ORR process. First-principle calculations were used to obtain the relaxed structures and to calculate the activation energies involved in the four-electron oxygen reduction mechanism. All DFT simulations were carried out using Quantum Espresso. The coordinates of the metal atoms, porphyrin and iron porphyrin along with all of the atoms in the adsorbates were fully optimized. Transition states were isolated using the climbing nudged elastic band method (CI-NEB). Gibbs energy diagrams for ORR and volcano plots were obtained to classify the catalytic behavior of Fe, Porphyrin and Iron Porphyrin compared with Pt-based and metallic systems.

4.1 Introduction

In electrocatalysis, the nature of the aqueous/solid interface makes electrocatalytic systems more complex compared with simple heterogeneous gas phase systems [91]. Electrocatalytic systems have solution, ions, charged interfaces, complex surface potentials, and electric fields that change the surface chemistry and thus catalytic behavior. These interfaces tend to significantly promote polar reactions and direct heterolytic bond activation steps. One of the main challenges in electrocatalysis is the ability to spectroscopically resolve molecular intermediates due to the complexity of the aqueous/metal interface. Moreover, early electrocatalytic studies were limited to measurements of macroscopic kinetics with little understanding of the elementary molecular transformations, the active sites or the influence the atomic and the electronic structure [34]. Nørskov and colleagues developed a simple method that relates

gas phase surface reaction energies to reaction energies at different applied potentials [24, 33, 36, 52-54], Anderson developed the reaction center model, simulating the reversible potentials and activation energies for non-catalyzed oxygen reduction to water and the reverse oxidation reaction to introduce the electron-donor molecule interaction with a chosen ionization potential [17-22], Rossmeisl et al. used explicit protons at the water/metal interface to establish the double-layer interface [92], Wieckowski et al., Neurock and collaborators have modeled electrochemical systems by carrying out gas phase calculations on well-defined model clusters and surfaces and including local water molecules as well as the influence of potential [91, 93, 94].

These contributions drove the modeling of Pt-based systems growth in the past decade. However, the difficulty in understanding the PGM-free active sites has stimulated the development of computational model systems in conjunction with experimental results from characterization techniques such as X-ray adsorption near-edge spectral (XANES), extended XAS fine structure (EXAFS), X-ray photoelectron spectroscopy (XPS), Mössbauer spectroscopy[58, 63, 71]. Initially, Jaouen and collaborators [58] found the presence of two main active sites. The first sites is a pyridinic nitrogen with $3e^-$ in sp^2 orbitals and 1 electron in a p orbital and the second one is a pyrrolic or graphitic-N_1-position with $3e^-$ in sp^2 orbitals and $2e^-$ in p orbitals. Further studies with Mossbauer spectroscopy showed three doublets assigned to a FeN_4-like site as figure 4.1 illustrates[58, 71].

The debate about the active site still prevails and some computational efforts have been devoted to understanding the active site nature. One of the first simulation efforts came from modeling heme proteins, which are a family of iron-porphyrin complex and are well known for their electron transport capability. Bikiel and collaborators [124] studied the distal and proximal effects of the heme-O2 complex to understand the O2 affinity of a heme protein (Fe-O interaction) by using DFT implementations in SIESTA using PBE functional and the Car-Parinello scheme.

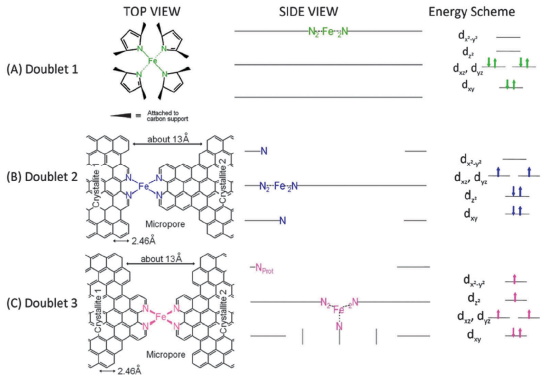


Figure 4.1 Kramm and collaborators proposed structures from Mössbauer Spectroscopy [71].

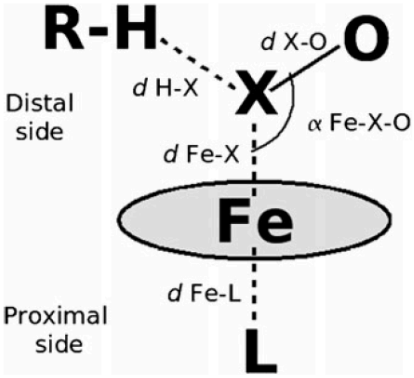


Figure 4.2 Heme Active sites representation[124]

PBE functional results were in agreement with experimental values of bond and geometrical parameters. This work concludes that the oxygen affinity is most likely for the distal site since the ligands tend to bind strongly on the proximal side, increasing oxygen affinity in the distal site [124]. Kiefer and collaborators simulated Fe-N_x/C motifs in graphene to identify the defects and binding energies of different adsorbates present in Fe-N_x/C ORR electrocatalyst. They identify the Fe-N_3/C as one of the defects present in these catalysts [125] and also calculated the reaction pathways for 2e- and 4e- at zero potential. They showed that the formation of graphitic in-plane Fe–N_4 sites is energetically favorable relative to the formation of Fe–N_2 sites. Therefore graphitic Fe–N_4 sites are expected to be the catalytic sites for ORR in Fe–N_x–C (x=2,4) electrocatalysts with the activity being attributed to the Fe electronic structure [70].

Tylus and collaborators studied the role of these active centers on the mechanistic pathways. In their study they found that ORR active metal centers on carbonaceous surfaces include Fe cations coordinated by pyridinic nitrogen atoms and very durable forms of metal nanoparticles (FeNPs/C). They proposed the reaction mechanism based on their computational and experimental studies as shown in Figure 4.3 [10].

Szakacs and collaborators studied two basic FeN_{2+2}/C-type catalytic structures as well as a structure including the FeN_4 moiety in an extended graphene sheet. According to the calculations, all the model structures possess catalytic activity, with the exception of FeN_{2+2}/C(B)(Figure 4.4) and N–FeN_{2+2}/C(B)(Figure 4.5). Their calculations also predict stronger binding in the case of side-on O2 than for end-on O2 in the three pyridine-free structures. This conclusion is further strengthened by the fact that FeN_{2+2}/C(A) and N–FeN_{2+2}/C(A) are predicted to have the lowest formation energy of all the structures considered here. FeN_{2+2}/C(A) and N–FeN_{2+2}/C(A) bind O2 side-on and end-on, respectively.

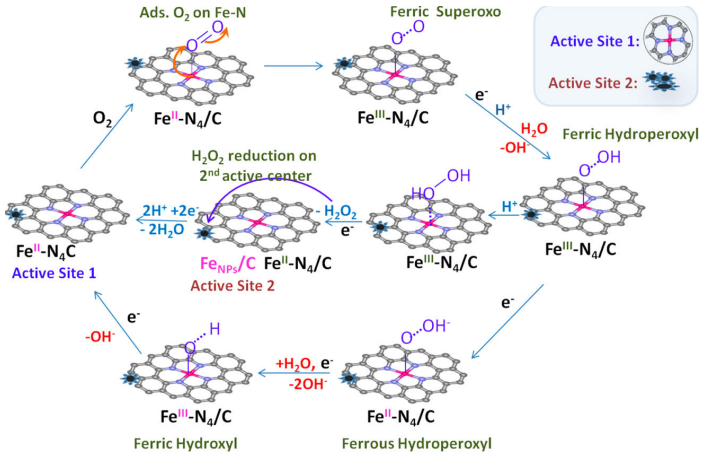


Figure 4.3 Proposed ORR mechanistic pathways on Fe-N4/C and adjacent FeNPs/C in acidic and alkaline electrolyte[10].

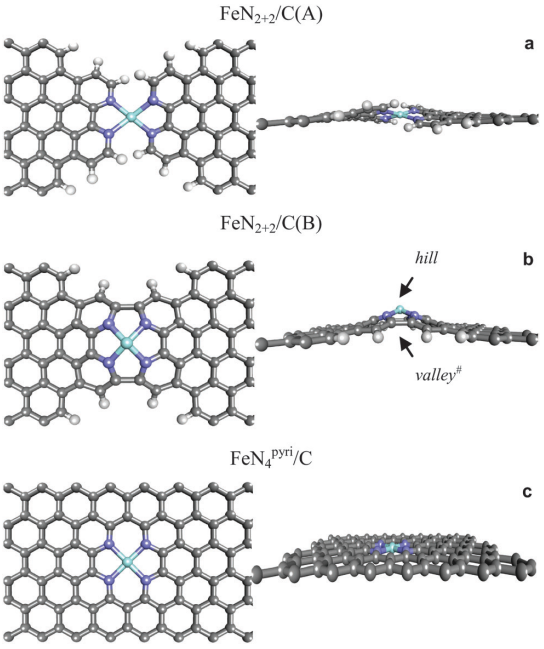


Figure 4.4FeN2+2/C type structure proposed by Szakacs and collaborators [126]

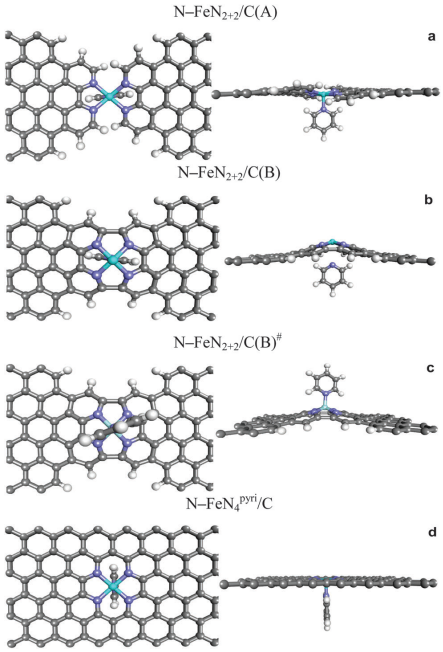


Figure 4.5 N-FeN2+2/C type structure proposed by Szakacs and collaborators [126]

Table 4.1 summarizes most of the studies for PGM-free catalyst including material type, the exchange-correlation functional for the DFT calculations, and main conclusions from each study. From these studies, the presence of multiple active sites seems to be the tendency. The four-electron reaction is the preferred pathway for iron Porphyrins. The GGA-PBE exchange functional cover the majority of simulation cases followed by B3LYP. ORR is catalyzed on edge sites for N-doped systems while for Fe Porphyrins sites imbedded inside the catalytic structure seems to be the most active site. However, there is not consensus about the active sites, FeN_x coordination, and the role of the Fe NPs on active sites formation. We also need to classify, based on activity, the most probable structures and how the structure behaves based on the metal center. Just one study described the use of a volcano plot as mean to classify active materials.

This chapter focuses on applying Pt-based system concepts to PGM-free catalyst. I concentrated on iron porphyrin molecules to understand their catalytic features before considering them as an active component of the catalyst layer. All DFT simulations were carried out using the Quantum Espresso open source code[127]. The coordinates of the metal atoms, porphyrin and iron porphyrin along with all of the atoms in the adsorbates were fully optimized. Transition states were isolated using the climbing nudged elastic band method (NEB)[128, 129].

4.2 First-principle modeling (ab-initio methods)[130]

Reaction energy calculations require the use of atomistic modeling methods that includes electronic interactions. Ab-initio methods consider nuclei and electrons as the basic particles and their interactions are described by quantum mechanics as a function of the atomic numbers of the constituent atoms. The idea of first principle methods is to study the interactions of positive nuclei and negative electron interactions. First principle methods are based on the Schrödinger wave equation proposed in 1926 and are described as follow:

$$\widehat{H}\Psi(r_i, r_I, t) = E\Psi(r_i, r_I, t) \qquad \textbf{Equation 4.1}$$

Table 4.1 Summary of the main DFT studies in PGM-free systems

Material	XC Functional	Main Conclusion	Reference
Fe and Co Phthalocyanines and Porphyrins	GGA – PW91	Reaction in solution and alkaline media. Two Tafel slopes 42 and 120mv/dec.	[131]
N doping graphene	GGA - PBE	Pyridinic N is the most stable configuration For doped N in a graphene cluster and more active towards ORR	[132]
Fe(Co)-N_x/C	BLYP	Fe on edges is not active towards ORR. Fe imbed in graphene-types structures more active. $4e^-$ reaction pathway	[133]
N-Doped Graphene	B3LYP	Pyridinic and pyrrole structures both active and with $4e^-$ reaction pathway	[134]
Quaternary N doping graphene edges.	B3LYP	ORR more favorable on N-edge. $4e^-$ reaction pathway	[135]
Co-N_x/C	GGA - PBE	Co–N_4 defect motifs are energetically favorable. $2x2e^-$ reaction pathway	[136]
N-Doped Graphene with transition metals, M	GGA – PBE	CI-NEB usage for adsorption energies calcualtions. The most active towards ORR are the N-graphene with Fe, Co, Ni and Cu	[137]
Fe-N_4/Fe-N_2	GGA – PBE	Fe-N_4 more active and possible site after pyrolysis. $4e^-$ reaction pathway	[70]
Fe-Phthalocyanine	GGA – PW91	Hydrazine catalysis. Volcano trends for different Fe magnetic state	[138]
Fe and Co Phthalocyanines and Porphyrins	GGA – PBE	Structure stabilization in acidic media. Metal ions exchange with protons is not the responsible for degradation	[139]
FeN2+2/C, N-FeN2+2/C	GGA – PBE	Their calculations also predict a stronger binding in the case of side-on O2 than for end-on O2 in the three pyridine-free structures.	[126]

Where, $\hat{H}$: Hamiltonian operator, Ψ: Wave function, E: System energy, r_i: electron coordinates and r_I: nucleus coordinates. However, solving this equation analytically is only possible for hydrogen due to the strong interaction between electron density and the neighbor particles. Simplifications have been made in order to deal with these of interactions. Density Functional Theory is the preferred method used in literature.

4.2.1 Density functional theory

In this theory, the Kohn-Sham equations (equation 4.2) are equivalent to the Schrödinger equation 4.1, with the mathematical difference that all unknown quantum effects are involved only in the exchange-correlation term (E_{xc}). The Kohn-Sham approach used the electron density as the main variable to solve the n-electron problem. It reduces the problem from 3n-dimensional to n-separate 3-dimensional density electrons, ρ(x,y,z), and it is an observable quantity (does not depend on the number of electrons after it is constructed in a system).

$$\left[-\frac{1}{2}\boldsymbol{\nabla^2} + \boldsymbol{U_{eff}(r)}\right]\boldsymbol{\phi_i(r)} = \boldsymbol{\varepsilon_i\phi_i} \rightarrow \boldsymbol{\hat{H}_{KS}\phi_i(r)} = \boldsymbol{\varepsilon_i\phi_i} \qquad \textbf{Equation 4.2}$$

The final result is a map of the n-electron system (interacting) on the one-electron system (non-interacting) under the given external energy. All the interacting effects are identified as:

$$\boldsymbol{E_{kin} = E_{kin}^{non} + E_{kin}^{int}} \qquad \textbf{Equation 4.3}$$

$$\boldsymbol{E_H + E_x \rightarrow E_H + E_x + E_c^{int}} \qquad \textbf{Equation 4.4}$$

$E_{kin}^{non,int}$ Represent the noninteracting and interacting kinetic energies (correlated). Regrouping all the interacting terms together we have the exchange-correlation energy, E_{xc}:

$$\boldsymbol{E_{xc} = E_x + E_c^{int} + E_{kin}^{int} = E_x + E_c} \qquad \textbf{Equation 4.5}$$

E_x represents the HF exchange energy while E_c the correlating part of the kinetic and electron-electron interacting terms. It is possible to say that DFT depends on two main factors: i) the Exc approximations and ii) the size of the system, which should be on the order of hundreds of atoms. The calculation of

the Exc is an important challenge in the calculation of the total energy for a specific system in quantum mechanics.

4.2.2 Exchange-correlation functionals

The value of the exchange-correlation functional determines how much error will be involved in a DFT calculation. Normally, this energy value is less than approximately 10% of the total energy, but it is crucial in determining material properties, such as bonding, spin-polarization, and band gap formation. The most common functionals are LDA (local density approximation), GGA (Generalized Gradient Approximation) and hybrid functionals. The most common GGA functionals are PW91 (Perdew et al., 1992, Perdew and Wang, 1992) and PBE (Predew, Burke, and Ernzerhof, 1996). The hybrid functionals are GGA-type with some (around 25%) of the accurate exchange energy from the Hartree-Fock method. The B3LYP is a three-parameter functional fitted to atomization energies, ionization potentials, etc. It can describe systems with faster variations in electron density or with long-range interaction such as the van der Waals type. It is generally best suited for calculations of bond energies, chemical transition-state barriers, band gap, etc.

4.2.3 Pseudopotential (PP) approach

The pseudopotential approach (Heine 1970) approximates the characteristics of the true potential by dividing electrons into two groups in terms of their contributing significances, effectively freezing the nucleus and the core electrons together, and 'pseudizing' the remaining valence wave functions. From the computational point of view, the core electrons are removed and thus the calculations deal only with the active valence electrons. The nuclear charge is screened by the core electrons and has much less effect (weaker and smoother attractive force) on the valence electrons.

4.2.4 Nudged elastic band method (NEB)

To identify the reaction paths and specifically the minimum energy path (MEP), it is necessary to use a DFT simulation to calculate the forces and extract them. Many different methods could be useful to find the reaction paths (MEP)

and the saddle points: i) conventional approach, ii) drag method or adiabatic mapping and iii) dynamic-reaction-coordinate methods. The first and second methods are computationally demanding and they need a suitable reaction coordinate beforehand to obtain an adequate guess of the MEP. The dynamic-reaction-coordinate methods are divided in two types: i) methods of iterative refinement of the transition state from an initial guess using a local reaction coordinate, and ii) methods of a chain of intermediate states to approximate the whole MEP [89, 128, 140].

The chain-of-states methods are widely used because they do not yield the transition state itself, only intermediate states close to the transition state, their convergence and description of more complicated reactions with several saddle points along the MEP [89, 128, 140]. The nudged elastic band method (NEB) lands in this category and it is used to scan the potential energy surface (PES) searching for the transition state due to its easy and fast convergence. The method requires evaluation of the interaction energy and the first derivative of the energy with respect to reaction coordinates. Decoupled path representation (flexible path) guarantees a continuous path even when multiple MEPs exist [89, 128, 140, 141].

This method scans the PES searching for the transition state and the values of the energy barriers by constructing a chain of images R_i (possible states) along a specific reaction pathway with an initial image (initial reactant state) and a final image (final products state) [89, 128, 140, 141]. These images (intermediate states) describe a minimum energy path for a specific reaction. In this method, the initial configuration of the reaction path is generated from a linear interpolation between the initial and the final state. This method adds an interaction between the adjacent images R_i, the net spring forces $F_i^{S\parallel}$, to ensure the continuity in the reaction path (elastic band).

On the path only the tangential component of the spring forces (Equation 1.45) is considered. In this term, all images are well distributed along this minimum energy path (MEP) because of the spring force constants k (Equation 1.46) [89, 128, 140, 141]. Moreover, NEB also takes into account the forces due to the real

potential gradient acting on the path $F_i^{\perp}$ (Figure 4.6 - Equation 4.7). The perpendicular component of this force leads the images toward the MEP, whereas the tangential component of this gradient force leads the images toward the reactant or product state, so this parallel component of the gradient force is neglected. This description is depicted by the equations [141]:

$$\boldsymbol{F_i^{NEB} = F_i^{S\parallel} + F_i^{g\perp}} \qquad \textbf{Equation 4.6}$$

$$\boldsymbol{F_i^{S\parallel} = k(|R_{i+1} - R_i| - |R_i - R_{i-1}|)\hat{\tau}_i} \qquad \textbf{Equation 4.7}$$

$$\boldsymbol{F_i^{g\perp} = -\nabla V(R_i) - (-\nabla V(R_i) \cdot \hat{\tau}_i)\hat{\tau}_i} \qquad \textbf{Equation 4.8}$$

Where V is the potential acting on the path. Equation 4.6 can be interpreted as the sum of potentials of the different images in the calculation of the MEP and the equation 4.6, as the energy to keep adjacent the images of the MEP. The equations 4.6-4.8 are solved variationally [141], allowing the calculation of the saddle points and the minimum energy path once the convergence in the forces is reached. Finally, the highest point (saddle point) along the MEP is considered as the transition state in the reaction path and the free energy barrier is determined [89, 128, 140, 141].

4.2.4.1 Climbing Image NEB

The climbing image NEB (CI-NEB) method constitutes a small modification to the NEB method [128]. Information about the shape of the MEP is retained, but a rigorous convergence to a saddle point is also obtained. This additional feature does not add any significant computational effort. After a few iterations with the regular NEB, the image with the highest energy i_{max} is identified. Equation 4.7 is replaced by:

$$\boldsymbol{F_{i_{max}}^{\parallel} = -\nabla V(R_{i_{max}}) + 2\nabla V(R_{i_{max}})|_{\parallel}} \\ \boldsymbol{= -\nabla V(R_{i_{max}}) + 2\nabla V(R_{i_{max}}) \cdot \hat{\tau}_{i_{max}} \cdot \hat{\tau}_{i_{max}}} \qquad \textbf{Equation 4.9}$$

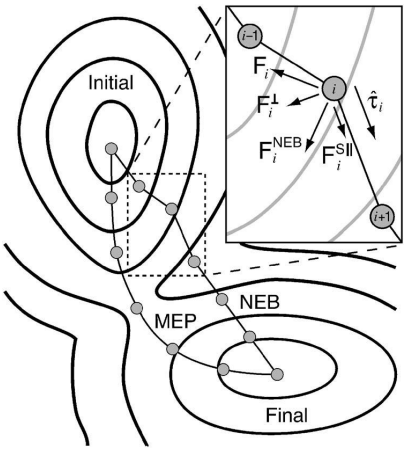


Figure 4.6 Illustrative diagram of the nudged elastic band method [141].

This is the full force due to the potential with the component along the elastic band inverted. The spring forces do not affect the maximum energy image at all. Qualitatively, the climbing image moves up the potential energy surface along the elastic band and down the potential surface perpendicular to the band. The other images in the band serve the purpose of defining the one degree of freedom for which a maximization of the energy is carried out. Since the images in the band eventually converge to the MEP, they give a good approximation to the reaction coordinate around the saddle point. As long as the CI-NEB method converges, the climbing image will converge to the saddle point. Since all the images are being relaxed simultaneously, there is no additional cost of turning one of the images into a climbing image.

The spring forces do not affect the climbing image. Therefore, the spacing of the images will be different on each side of the climbing image. As it moves up to the saddle point, images on one side will get compressed, and on the other side spread out. Two or more climbing images can be specified if the MEP appears to have two or more high maxima that are close in energy. The only issue is to have enough images close to the climbing images to get a good estimate of the reaction coordinate, since this determines the climbing direction.

4.3 Modeling of electrochemical systems

ORR catalysis complexity on Pt-based systems was illustrated in Chapter one. New catalytic material studies require the selection of the adequate model system as well as the assumptions involve.

4.3.1 Assumptions

Electrochemical reactions are surface reactions at an electrode and they involve electron transfer processes. This kind of reaction differs from gas-surface reactions in many aspects[95]:

1. The chemical potential of the electrons entering the reaction is controlled by the potential of the electrode.
2. The surface species, as well as the reactants and products, will be solvated by the electrolyte. Reactant and product solvation in the bulk electrolyte are the same as in liquid-phase chemistry.

3. Solvation events can contribute to activation free energies during transfer of molecules or ions to or from the surface. Since the solvent molecules at the surface are constrained by the presence of the surface, they respond slowly to perturbations, and the processes need not be adiabatic (constant temperature assumption, heat interchange with the surroundings) with respect to the solvent degrees of freedom. This could result in "apparent" activation free energies that are larger than the ones you would get if the solvent could relax completely during the process.
4. The electric field at the solid–electrolyte interface will change the adsorption energy.
5. The electron transfer itself can be rate limiting.

4.3.2 Gibbs energies treatment

The adsorption energies are functions of the solution phase reversible potentials. Then, the adsorption Gibbs energies for the intermediates can be predicted as the reversible potential for each step and it should be equal to the reversible potential for the overall multielectron reduction [20]. We calculated the Gibbs free energies from DFT adsorption energies making the following assumptions:

1. Molecular water and hydrogen are chosen as references

$$G_{H_2O_{(g)}} = G_{H_{2(g)}} = 0 \qquad \textbf{Equation 4.10}$$

2. For electrode potential, U=0 vs the standard hydrogen electrode (SHE), the hydrogen evolution and oxidation reactions are at equilibrium. Therefore, at U = 0 V (RHE), the free energies of the solvated protons and the electrons in the solid are equal to the free energy of gas phase hydrogen at atmospheric pressure. This assumption is known as the computational hydrogen electrode (CHE).

$$2(H^+ + e^-) \leftrightharpoons H_{2(g)} \qquad \textbf{Reaction 4.1}$$

$$\Delta G_{rxn,4.1}(U = 0) = G_{H_{2(g)}} - 2G_{(H^+ - e^-)} = 0 \qquad \textbf{Equation 4.11}$$

$$G_{H_{2(g)}} = 2G_{(H^+ - e^-)} = 0 \qquad \textbf{Equation 4.12}$$

3. To express the Gibbs free energy as a function of the adsorption energies obtained from DFT calculation a correction in terms of the zero-point vibrations (ZPE) is necessary, as equation 4.13 illustrates. I used the data from Nørskov's[24] and Rossmeisl's [142]work. Equation 4.15 and 4.16 represented the correction required to calculate the reaction Gibbs energies at T=300K.

$$\Delta G_i = \Delta E_i + ZPE - T\Delta S \qquad \textbf{Equation 4.13}$$

$$\mathbf{ZPE} = \sum_{\mathbf{i}} \frac{\mathbf{1}}{\mathbf{2}} \hbar \boldsymbol{\nu}_{\mathbf{i}} \qquad \textbf{Equation 4.14}$$

$$\Delta G_O = \Delta E_O + 0.05eV \qquad \textbf{Equation 4.15}$$

$$\Delta G_{OH} = \Delta E_{OH} + 0.35eV \qquad \textbf{Equation 4.16}$$

4. The Gibbs free energy for reaction 4.2 at zero potential is 3.20 eV, independent of the surface [36]:

$$OOH^* + 2(H^+ + e^-) \leftrightharpoons OH^* + H_2O_{(g)} \qquad \textbf{Reaction 4.2}$$

$$\Delta G_{rxn,4.2} = G_{OH^*} + G_{H_2O_{(g)}} - G_{OOH^*} - 2G_{(H^+ - e^-)} = -3.20eV \qquad \textbf{Equation 4.17}$$

Then,

$$G_{OOH^*} = G_{OH^*} + 3.20eV \qquad \textbf{Equation 4.18}$$

5. The overall Gibbs reaction free energy for the ORR reflects the ideal 1e- step potential, where each step will be the reversible oxygen potential at standard conditions:

$$O_{2(g)} + 4(H^+ + e^-) \leftrightharpoons 2H_2O_{(g)} \qquad \textbf{Reaction 4.3}$$

$$\Delta G_{rxn,4.3} = 2G_{H_2O_{(g)}} - G_{O_{2(g)}} - 4G_{(H^+ - e^-)} = -4.92eV \qquad \textbf{Equation 4.19}$$

$$\mathbf{G_{O_{2(g)}}} = \mathbf{4.92eV} \qquad \textbf{Equation 4.20}$$

6. The free energy of reaction at a given potential U and electron charge q, can be expressed as:

$$\Delta G_i(U) = \Delta G_i(U = 0) - Uq$$ **Equation 4.21**

4.3.3 Oxygen Reduction Reaction Modeling

4.3.3.1 ORR Reaction Mechanism

Tables 1.2 and 4.1 illustrate experimental and modeling results that corroborate the 4-electron reaction pathway mechanism on Fe-Porphyrin. The overall reaction is represented by:

$$O_{2(g)} + 4(H^+ + e^-) \leftrightharpoons 2H_2O_{(g)}$$ **Reaction 4.4**

The simplest 4-electron reaction mechanism was presented by Norskov and collaborators [24], where the ORR is described as four elementary steps, each with one electron transfer:

$$* + O_{2(g)} + (H^+ + e^-) \leftrightharpoons OOH^*$$ **Reaction 4.5**

$$OOH^* + (H^+ + e^-) \leftrightharpoons O^* + H_2O_{(g)}$$ **Reaction 4.6**

$$O^* + (H^+ + e^-) \leftrightharpoons OH^*$$ **Reaction 4.7**

$$OH^* + (H^+ + e^-) \leftrightharpoons H_2O_{(g)}$$ **Reaction 4.8**

The total Gibbs free energy of reaction is calculated as:

$$\Delta G_{rxn} = \sum_i \nu_i G_i$$ **Equation 4.22**

Where ν_i is the stoichiometry coefficient of the reaction positive for products and negative for reactants. G_i the Gibss free energy of the reactants and products. The equations are:

$$\Delta G_{rxn,4.4} = 2G_{H_2O_{(g)}} - G_{O_{2(g)}} - 4G_{(H^+ - e^-)} = 4.92eV$$ **Equation 4.23**

$$\Delta G_{rxn,4.5} = G_{OOH^*} - G_{O_{2(g)}} - G_{(H^+ - e^-)}$$ **Equation 4.24**

$$\Delta G_{rxn,4.6} = G_{O^*} + G_{H_2O_{(g)}} - G_{OOH^*} - G_{(H^+ - e^-)}$$ **Equation 4.25**

$$\Delta G_{rxn,4.7} = G_{OH^*} - G_{O^*} - G_{(H^+ - e^-)}$$ **Equation 4.26**

$$\Delta G_{rxn,4.8} = G_{H_2O_{(g)}} - G_{OH^*} - G_{(H^+ - e^-)}$$ **Equation 4.27**

4.3.3.2 Adsorption energies calculation

To solve equations 4.23 to 4.28 we need to calculate the Gibbs energies of each adsorbate. Reactions 4.8 to 4.10 are the simplest reactions to calculate O and OH adsorption energies as follow:

$$H_2O_{(g)} \leftrightharpoons OH^* + H^* \qquad \textbf{Reaction 4.9}$$

$$H_{2(g)} \leftrightharpoons 2H^* \qquad \textbf{Reaction 4.10}$$

$$OH^* \leftrightharpoons H^* + O^* \qquad \textbf{Reaction 4.11}$$

The reaction energies for reactions 4.9, 4.10 and 4.11 are:

$$\Delta E_{rxn,4.9} = E_{OH^*} + E_{H^*} - E_{H_2O} \qquad \textbf{Equation 4.28}$$

$$\Delta E_{rxn,4.10} = 2E_{H^*} - E_{H_2} \qquad \textbf{Equation 4.29}$$

$$\Delta E_{rxn,4.11} = E_{O^*} + E_{H^*} - E_{OH^*} \qquad \textbf{Equation 4.30}$$

From equation 4.29 and 4.12

$$E_{H^*} = \frac{\Delta E_{rxn,4.10}}{2} \quad \textbf{Equation 4.31}$$

Substituting equation 4.32, 4.28, and 4.10 into 4.28

$$E_{0H^*} = \Delta E_{rxn,4.9} - \frac{\Delta E_{rxn,4.10}}{2} \qquad \textbf{Equation 4.32}$$

Replacing equation 4.32 and 4.33 into 4.17

$$E_{0^*} = \Delta E_{rxn,4.11} - \Delta E_{rxn,4.10} + \Delta E_{rxn,4.9} \qquad \textbf{Equation 4.33}$$

4.3.3.3 Modeling System

Based on the assumptions, the adsorption energies calculation and the reaction energies for reactions 4.9 to 4.11 can be calculated as:

$$\Delta G_{rxn,4.5} = G_{OOH^*} - G_{O_{2(g)}} = (E_{0H^*} + 0.35 + 3.2) - 4.92 \qquad \textbf{Equation 4.34}$$

$$\Delta G_{rxn,4.6} = G_{O^*} - G_{OOH^*} = (E_{0^*} + 0.05) - (E_{0H^*} + 0.35 + 3.2) \qquad \textbf{Equation 4.35}$$

$$\Delta G_{rxn,4.7} = G_{OH^*} - G_{O^*} = (E_{0H^*} + 0.35) - (E_{0^*} + 0.05) \qquad \textbf{Equation 4.36}$$

$$\Delta G_{rxn,4.8} = - G_{OH^*} = -(E_{0H^*} + 0.35) \qquad \textbf{Equation 4.37}$$

Equations 4.35 to 4.38 represent our simulation system expressed in terms of reactions 4.9, 4.10, and 4.11. Table 4.2 presents the required NEB calculations to obtain the activation energies.

Table 4.2 Simulation plan for Iron, Porphyrin and Iron Prophyrin

Reaction	Structures		
	Fe(111)	Porphyrin (Pp)	Iron Porphyrin(FeP)
$H_2O_{(g)} \leftrightharpoons OH^* + H^*$	1	1	1
$H_{2(g)} \leftrightharpoons 2H^*$	1	1	1
$OH^* \leftrightharpoons H^* + O^*$	1	1	1
Total NEB Simulations	3	3	3

4.3.4 Sabatier Principle and volcano plots

A very useful analysis of catalytic reactions is provided for by the construction of so-called volcano plots. In a volcano plot, the catalytic rate of a reaction normalized per unit reactive surface area is plotted as a function of the adsorption energy of the reactant, product molecule, or reaction intermediates. A volcano plot correlates a kinetic parameter, such as the activation energy or reaction rate, with a thermodynamic parameter, such as the adsorption energy. The maximum in the volcano plot corresponds to the Sabatier principle maximum, where the rate of activation of reactant molecules and the desorption of product molecules balance[143].

The Sabatier principle states that in the best catalysts, the binding energy between atoms and molecules with catalysts should neither be too strong nor too weak. If the interaction is too weak, then there will be no reaction on the surface because it is difficult for the catalyst surface to bind the reactants. If the interaction is too strong, then the reaction reactant or product is difficult to desorb from the catalyst surface, which also lowers the activity as figure 4.6 illustrates. Figure 4.7 shows such a volcano plot, which was first introduced by Balandin in 1969[144]. The basic idea is that if plotting rate of chemical reaction on a heterogeneous catalyst versus some adsorption property, for instance adsorption enthalpy, then according to Sabatier's principle, the plot will have a maximum, showing a shape like a volcano for the relationship between activity and bond strength [143, 145]. Volcano plots has been a successful qualitative tool for understanding catalyst activity but it lacks predictive power, and it cannot be tested experimentally.

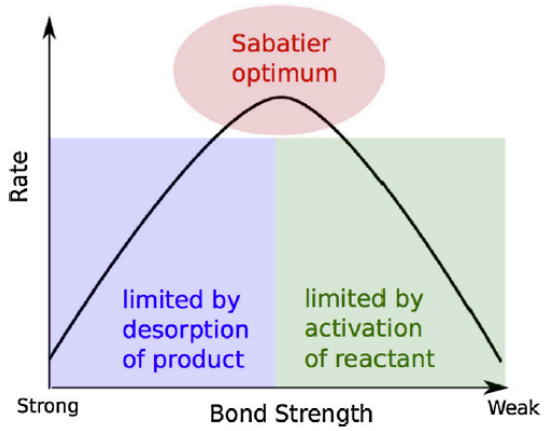


Figure 4.7 Schematic representation of Sabatier principle[145].

One of the key points building a volcano plot is to identify the quantity or "descriptor" used to characterize the "bond strength" between the relevant intermediate and the catalyst, or what value of the "bond strength" corresponds to the optimum catalyst. For ORR reactions it has been proven that the better descriptors are the O or OH adsorption and its dimensionality can be reduce by scaling relations [20, 33, 36, 92, 95, 145].

For electrocatalytic systems, the reactions are potential dependent. In other words, the adsorption energies change as the potential applied to the system, as follow:

$$E_a = \gamma \Delta E + \xi \qquad \textbf{Equation 4.38}$$

Where γ is the transfer coefficient, usually 0.5. ξ is a constant from the specific surface and ΔE is the reaction energy. The typical procedure to calculate the volcano plots implies the potential energy diagram calculation (free Gibbs energies vs. reaction coordinates), with the activation energies calculated relative to the ground state (U=0).

Then, the adsorption energies for the descriptors (usually the main atom vs. one intermediate) are plotted for different surfaces to find the correlation.

Finally, the relation obtained from the adsorbates allows reduction of variables and the volcano plot can be calculated as a function of one of the descriptors.

One of the common approaches for electrocatalysis is to plot against the overpotential for ORR which can be calculated as:

$$\eta(i) = \left| U(i) - U_{eq} \right| \qquad \textbf{Equation 4.39}$$

4.4 Results and discussion

The platinum system was chosen as a comparison point to understand the energetics of the Iron Porphyrin components for the ORR.

4.4.1 Lattice Parameter

For surface chemistry calculations we require the adequate crystal structure description by calculating the lattice parameters, crystal orientation and final structure to find the right Pseudo-Potentials and Exchange-Correlation functional. Finally, the kinetic energy cutoff and k-point parameters are obtained. Relaxation of the crystal structure, slabs and molecules with reactants and products are required before starting the NEB simulations. Table 4.3 summarizes information about the crystal structure of Pt and Fe as figure 4.8 illustrates. Both metals have cubic structures but with different atomic configurations.

4.4.2 Relaxation steps

I evaluated GGA (PBE, PW91) and LDA functionas to obtain the kinetic energy cutoff and used the Monkhorst-Pack mesh to run the simulations. Figure 4.9 evaluates the kinetic energy for Pt and Fe crystals. For Pt systems the kinetic energy cutoff is higher for the PBE and LDA functional while PW91 is higher for Fe. Moreover, the Monkhorst-Pack mesh behavior is similar for all the functionals in Pt as well as in Fe as figure 4.9 illustrates. These parameters are summarized in table 4.4. Figure 4.10 illustrates the potential energy curve for the functional and the calculated lattice parameter for Pt and Fe. For platinum, the lattice parameter error is 2% for GGA functionals and 0.45% for LDA. For iron, the lattice parameter is 4% for LDA, 2.5% for GGA-PW91 and 0.1% for GGA-PBE. Based on these results and the evidence shown in Table 4.1, I chose the PBE functional to carry on the rest of the simulations.

The second part of the simulations are for Pt(111), Fe(111) Porphyrin (Pp) and Iron Porphyrin (FePp) surfaces. The slabs for simulations were created using VESTA [146]. For Pt(111) a slab with 27 atoms and 3 layers was and for Fe(111) a slab with 18 atoms and 3 layers were created. Porphyrin and Iron porphyrin are evaluated as molecules from their xyz structures. Figures 4.12 and 4.13 illustrate the parameters for these structures. It is important to say that adding more atoms creates stronger interaction and as a consequence, the kinetic energy cutoff increases compared with the single crystal system. Moreover, the k-point calculations also need a finer mesh for the slabs.

Table 4.3 Crystal Structure information for Pt and Fe

	Pt		Fe	
Space group	Fm-3m		lm-3m	
Space group number	225		229	
Structure	ccp (cubic close-packed)		bcc (body-centered cubic)	
Cell parameters	a: 392.42 pm b: 392.42 pm c: 392.42 pm	α: 90.000° β: 90.000° γ: 90.000°	a: 286.65 pm b: 286.65 pm c: 286.65 pm	α: 90.000° β: 90.000° γ: 90.000°

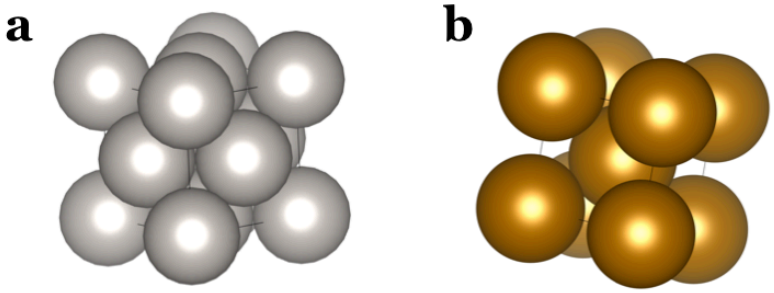


Figure 4.8 Crystal Structures a)Pt (ccp) b)Fe(bcc) Relaxation steps

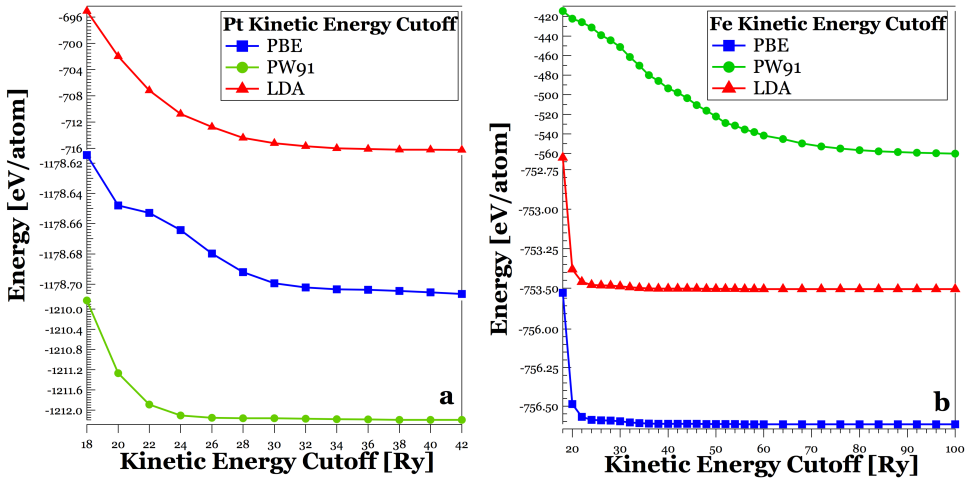


Figure 4.9 Kinetic Energy Cutoff. a) Pt b) Fe.

Table 4.4 Parameters for the Pt and Fe relaxation

	Pt Kinetic Energy [Ry]	k-points	Fe Kinetic Energy [Ry]	k-points
LDA	38	7x7x7	26	7x7x7
PBE	38	7x7x7	26	7x7x7
PW91	28	7x7x7	80	7x7x7

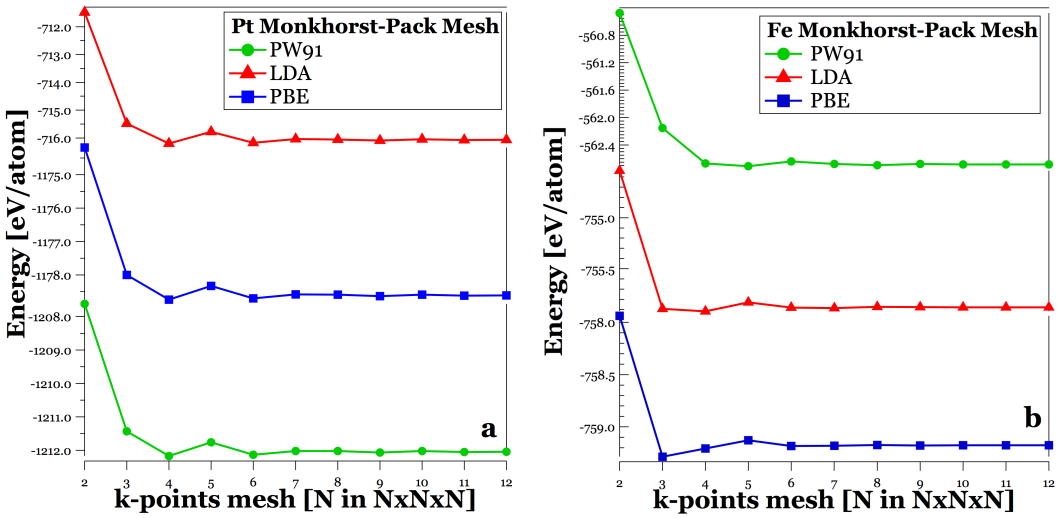


Figure 4.10 Monkhorst-Pack Mesh a) Pt b)Fe.

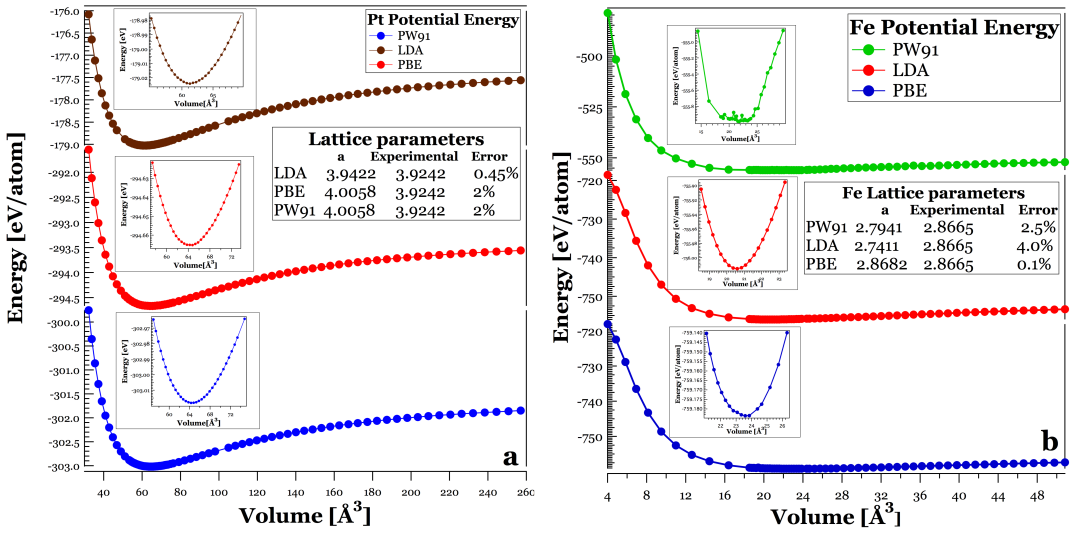


Figure 4.11 Potential Energy Curve to extract Lattice Parameters. a) Pt b) Fe.

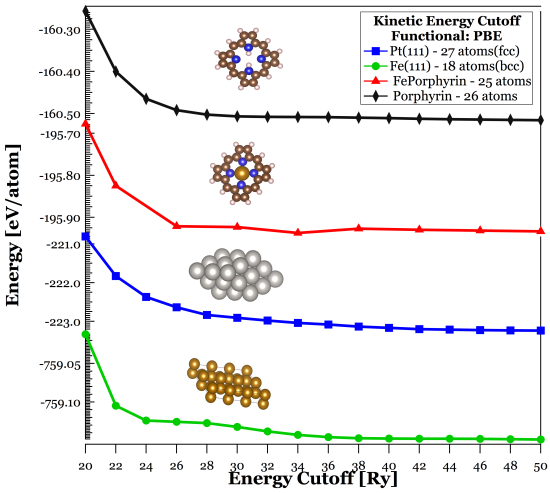


Figure 4.12 Kinetic Energy Cutoff for the simulation systems

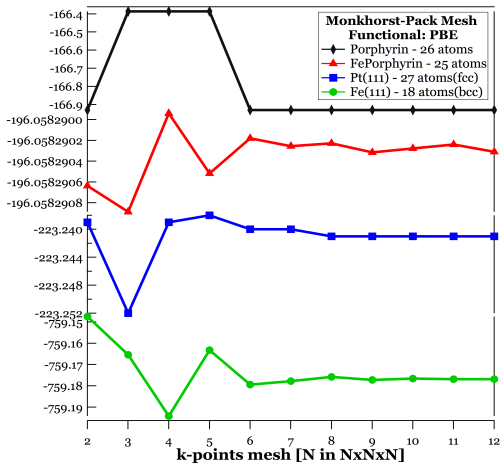


Figure 4.13 Monkhorst-Pack Mesh for the simulation systems

Table 4.5 Simulation parameters for all systems

	Pt	Fe	Porphyrin	Fe Porphyrin
Kinetic Energy Cutoff [Ry]	40	38	38	32
k-points	9x9x9	9x9x9	7x7x7	9x9x9

Table 4.5 summarizes the parameters used for the relaxation. The relaxation of these structures is made by using the relax feature of Quantum Espresso software. Once the structures are relaxed, I used Avogadro to draw the structures with O, H_2O, OH, O_2, H_2 and relax again to create the NEB input files. Appendix B shows a sample of these input files.

4.4.3 Activation Energies

The activation energy calculation requires equilibration steps for the initial and final images across the reaction pathway. Figures 4.14 to 4.16 illustrate the potential energy diagrams for reactions 4.9 to 4.10 (H_2O, H_2 and OH* dissociation) on Porphyrin and figures 4.17 to 4.29 for iron porphyrin. (Note that in all of these diagrams, the dashed lines are intended only to sketch plausible pathways based on the calculated values. They are not themselves calculated) For all of the reactions, the initial state is the adsorption step of the reactant and the final state was selected as the lowest energy point for different final state sites. The number of points for the path extrapolation was 5 and the convergence criteria were 0.1 eV. Figure 4.14 shows the calculated reaction path for water dissociation on Porphyrin. Oxygen adsorption occurs on N_β, which corresponds to the pyrrolic nitrogen. However, the oxygen bond to this nitrogen is weak, leading to H adsorption on N_β. Then, the H-O bond elongates and H* and OH* are adsorbed onto the N_β. Finally, the hydrogen is adsorbed onto the C_α. This potential energy diagram illustrates two intermediate states before breaking the OH – H bond. This result illustrates weak O-N interaction.

Figure 4.15 describes the reaction path for hydrogen dissociation on Porphyrin. Hydrogen is adsorbed on N_β, which corresponds to the pyrrolic nitrogen. The next two steps illustrate the bond elongation and breaking. Then, the hydrogen broken is adsorbed on the C_m to finally migrate to the C_α.

Figure 4.16 describes the reaction path for OH* dissociation on Porphyrin. The evolution from the OH* adsorbate to the O* and H* adsorbates is evident in this pathway. OH* is adsorbed on N_β, H is attracted by the N environment of the porphyrin center and reorganized to elongation and bond-breaking steps.

Figure 4.17 sketches the reaction path for water dissociation on Iron Porphyrin. Oxygen adsorbs on the N_β as in the Porphyrin. It is surprising to observe the weak O-Fe bond. Moreover, OH-H bond breaking occurs when H is adsorbed on top of the iron. Then, H* is adsorbed on the N_β. Finally, the OH* is re-absorbed into the Fe.

Figure 4.18 describes the reaction path for hydrogen dissociation on Iron Porphyrin. All the hydrogen bond breaking occurs on Fe. Once the bond is broken, one hydrogen migrates to N_β and the other one remains on the Fe. Figure 4.19 describes the reaction path for OH* dissociation on Iron Porphyrin. It shows the evolution from OH* adsorbate to O* and H*. As for Porphyrin, the H is attracted by N environment of the porphyrin center, forcing the OH* adsorbate to migrate until its final elongation and bond breaking. Both reaction pathways demonstrate the weak adsorption of oxygen in these molecules.

The reaction pathways obtained for Porphyrin and Fe-Porphyrin illustrated multiple saddle points and does not show the typical Gaussian shape for the activation energies. A closer look at the NEB method reveals the sensitivity of the method in terms of the path extrapolation for which the spring forces change drastically when we have strongly vibrating systems. To correct this problem, I ran CI-NEB simulations, which, as described in equation 4.9, modifies the tangential component of the force making the method less sensitive to the spring. Another feature of this method is the variable spring constant along the path with generates uneven path extrapolation but a better approximation to the saddle point. Figures 4.20 and 4.21 illustrate the corrected potential energies for the systems under study. The reaction mechanism has minor changes in comparison with the pure NEB method but the accuracy of the activation energies improved, as the shape of the curves for both systems illustrate. Table 4.6 condenses the adsorption and reaction energies obtained among with values for transition metals with 111 orientations. Porphyrin and Iron porphyrin values are higher than those for their metallic counterparts. However, those values are closer to those for Au, which indicates a weak oxygen adsorption. Porphyrin and Iron Porphyrin reaction energies are higher than for any of the metals, which is a reflection of the endothermic nature of reactions 4.6 and 4.7 for these material

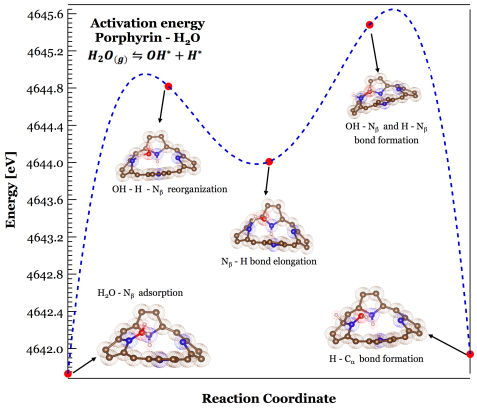


Figure 4.14 Activation energy diagram for H_2O dissociation on Porphyrin.

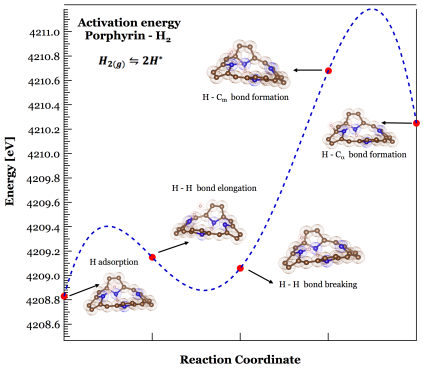


Figure 4.15 Activation energy diagram for H_2 dissociation.

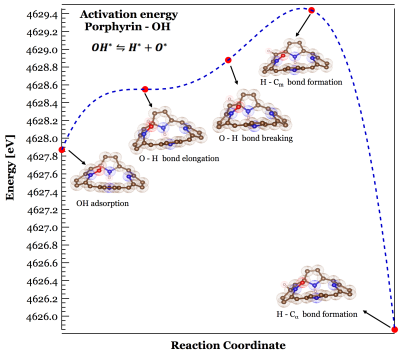


Figure 4.16 Activation Energy diagram for OH dissociation in Porphyrin.

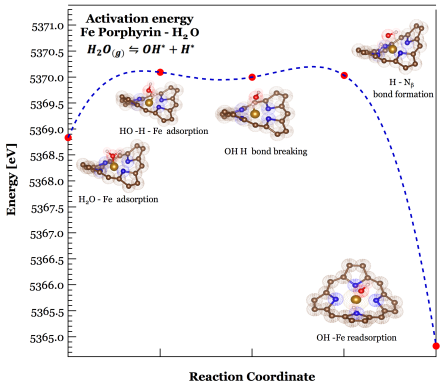


Figure 4.17 Activation energy diagram for H2O dissociation.

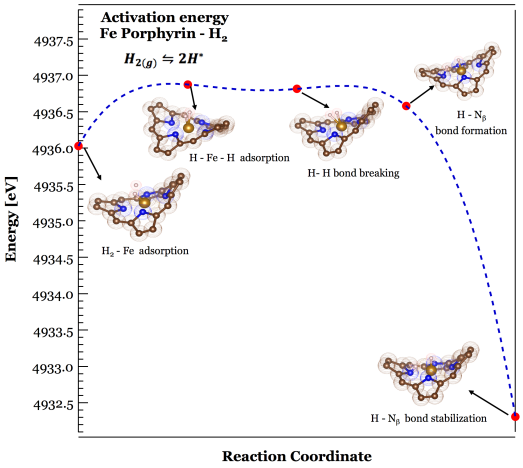


Figure 4.18 Activation energy diagram for H_2 dissociation.

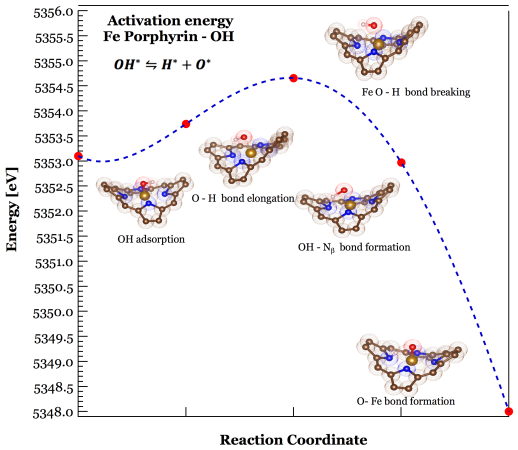


Figure 4.19 Activation energy diagram for OH dissociation.

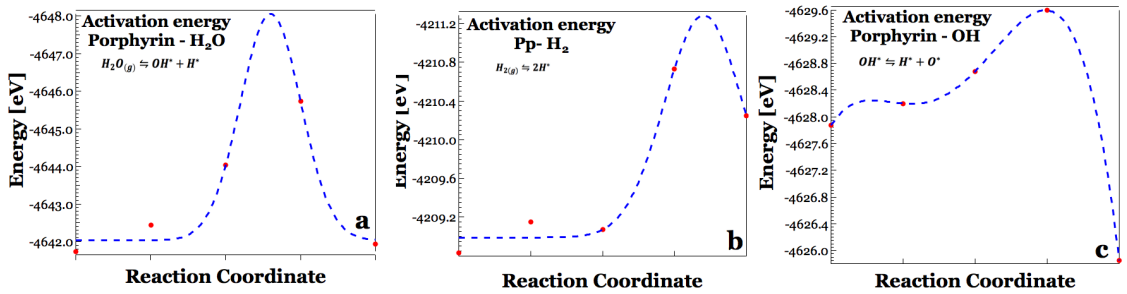


Figure 4.20 Porphyrin corrected activation energies with CI-NEB.

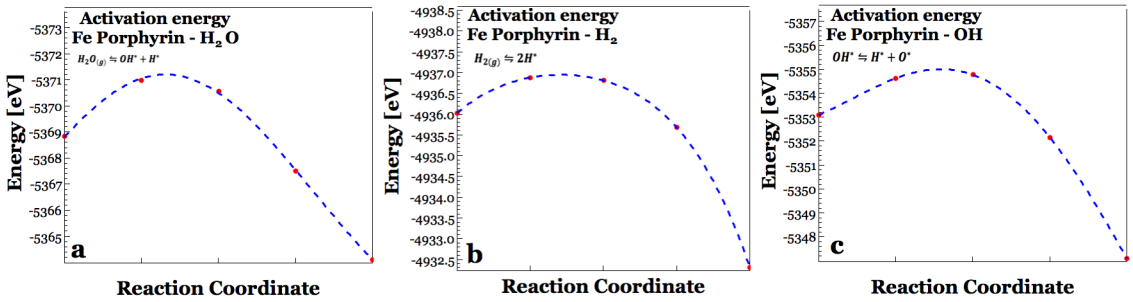


Figure 4.21 Fe-Porphyrin corrected activation energies with CI-NEB.

.

Table 4.6 Calculated reaction, adsorption, and free Gibbs energies. Metals (111) from CatApp. Porphyrin and Iron Porphyrin from this work.

	$\Delta E_{rxn,4}$	$\Delta E_{rxn,4.}$	$\Delta E_{rxn,4.1}$	E_{OH^*}	E_{O^*}	$\Delta G_{rxn,4.}$	$\Delta G_{rxn,4.}$	$\Delta G_{rxn,4.}$	$\Delta G_{rxn,4}$
Ru	-0.25	-1.000	-0.700	0.25	0.05	-1.720	-3.140	-0.06	0.00
Au	1.600	0.340	1.400	1.43	2.66	-0.540	-1.710	-1.490	-1.180
Pd	0.540	-0.790	0.220	0.94	1.55	-1.035	-2.325	-0.875	-0.685
Rh	0.110	-0.660	-0.200	0.44	0.57	-1.530	-2.810	-0.390	-0.190
Cu	0.210	-0.150	0.680	0.29	1.04	-1.685	-2.185	-1.015	-0.035
Pt	0.600	-0.700	0.310	0.95	1.61	-1.020	-2.280	-0.920	-0.700
Fe	0.651	0.240	0.769	0.53	1.18	-1.440	-2.291	-0.909	-0.281
Pp	-1.421	-0.209	2.019	2.73	3.23	1.359	-2.998	-0.202	-3.080
FePp	4.015	3.723	5.098	2.86	7.00	1.492	0.636	-3.836	-3.212

4.4.4 Gibbs energy graphs

Equations 4.35 to 4.38 represent the reaction energies for the 4-electron reactions mechanism study here. The procedure to calculate the Gibbs energies is:

1. Calculate the reaction energies for reactions 4.9 to 4.11 through CI-NEB calculation. Those values are extracted from figures 4.20 to 4.21. The results are summarized in table 4.6.
2. Calculate the Gibbs free energy at U=0 from equations 4.35 to 4.38.
3. Calculate the rate limiting potential as:

$$\boldsymbol{U_{lim} = -max\left(\Delta G^{U=0}_{rxn,4.5}, \Delta G^{U=0}_{xn,4.6}, \Delta G^{U=0}_{xn,4.7} \Delta G^{U=0}_{xn,4.8}\right)/|q|} \qquad \textbf{Equation 4.40}$$

4. Calculate the overpotential, η_{ORR} as:

$$\boldsymbol{\eta_{ORR} = OCV - U_{lim}} \qquad \textbf{Equation 4.41}$$

5. Calculate the Gibbs free energy as a function of the potential:

$$\boldsymbol{\Delta G_i(U) = \Delta G_i^{U=0} - U \times q} \qquad \textbf{Equation 4.42}$$

6. Plot $\boldsymbol{\Delta G_{rxn}}$ vs. reaction coordinates and at different potentials values.
7. Plot the adsorption energy of OH* vs. O* and obtain the scaling relations (figure 4.).

$$\boldsymbol{E_{OH^*} = 0.480 E_{O^*} + 0.117} \qquad \textbf{Equation 4.43}$$

8. Create a vector for $E_{O^*,s}$ that captures the adsorption energy for each material.
9. Recalculate $E_{OH^*,s}$ by using the scaling relation.
10. Recalculate $\eta_{ORR,s}$ for each E_{O^*} value.
11. Plot $\eta_{ORR,s}$ vs. $E_{O^*,s}$ and the original values of η_{ORR} vs. E_{O^*} for the different metals.

Figure 4.22 illustrates different behavior for each metal as a reflection of the

electronic environment of the metal. Moreover, the potential decreases the free energy in most of the cases. Ru, Cu and Rh have strong OH binding energies, which make it difficult to remove it from the surface. Au has great O_2 activation however, it has a weak surface oxygen bond which make difficult the OOH formation.

Figure 4.23 shows Fe, Porphyrin and Iron Porphyrin compared to Pt. Fe(111) has strong OH binding energies, which make the reduction steps difficult. In Porphyrin and Fe-Porphyrin, O_2 activation is not favorable and it is reflected in the upward steps in figures 4.23c and 4.23d. Porphyrin has a weak interaction with oxygen, which is reflected in the difficulty of O-O breaking compared with that on Pt, as figure 4.23c illustrates.

Table 4.5 summarizes the reaction energies, O* and OH* adsorption and free Gibbs energy for model reaction mechanism under study. The first step is the superoxide formation, which in the diagram in figure 4.24 is a 3 step process [147].

Analogous to the model mechanism on Pt, it has been found that metal macrocycle complexes undergo a mixed 2e- and 4e- mechanism. In rare cases, transition metal macrocyclic complexes can also catalyze a 1-electron O2 reduction, producing superoxide ions [29]. This assumption was indeed corroborated with our simple model. From figure 4.24 the superoxide step implies a positive free Gibbs energy leading to an unfavorable reaction step. The O interaction with Porphyrin and Fe Porphyrin interaction is weak and thus both tend towards the right side of the volcano plot.

For the reduction steps, both Porphyrin and Fe Porphyrin have a favorable Gibbs energy of reaction (taller steps, higher reaction energies). Thus those steps cannot be considered the rate limiting steps. One aspect that was not considered here was the coverage effect on the activity of the materials. Further studies must be done to be able to elucidate the nature of the double Tafel slope.

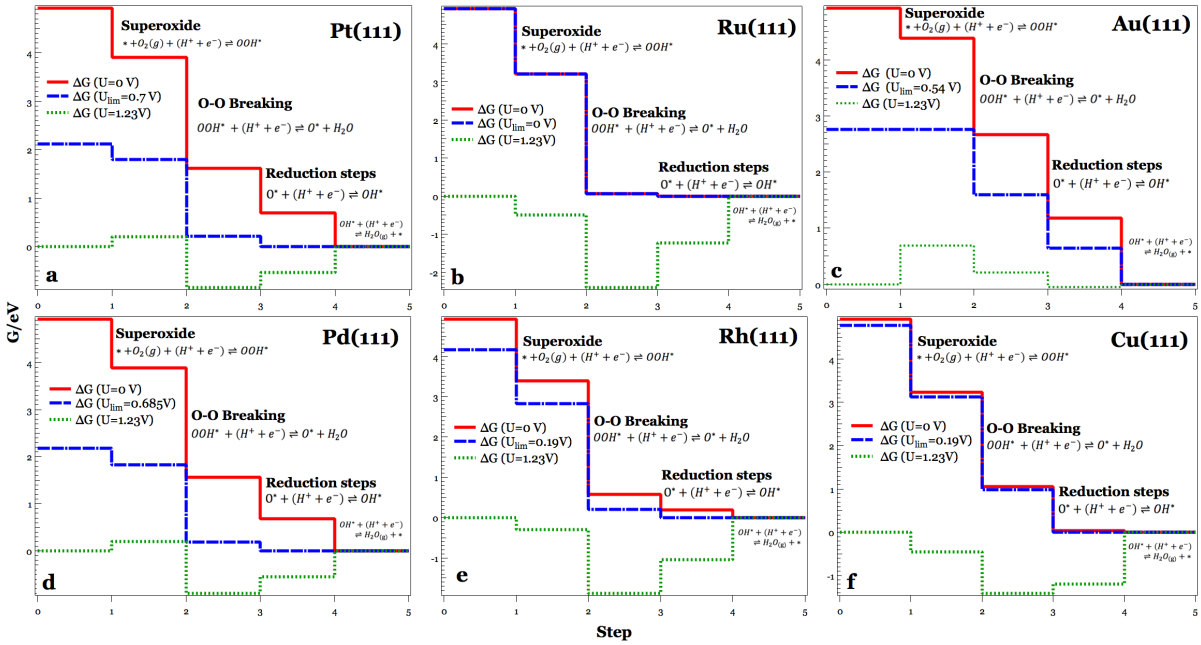


Figure 4.22 Free energy diagrams for different (111) Metals [35]. a) Pt b) Ru c) Au d) Pd e) Rh f) Cu.

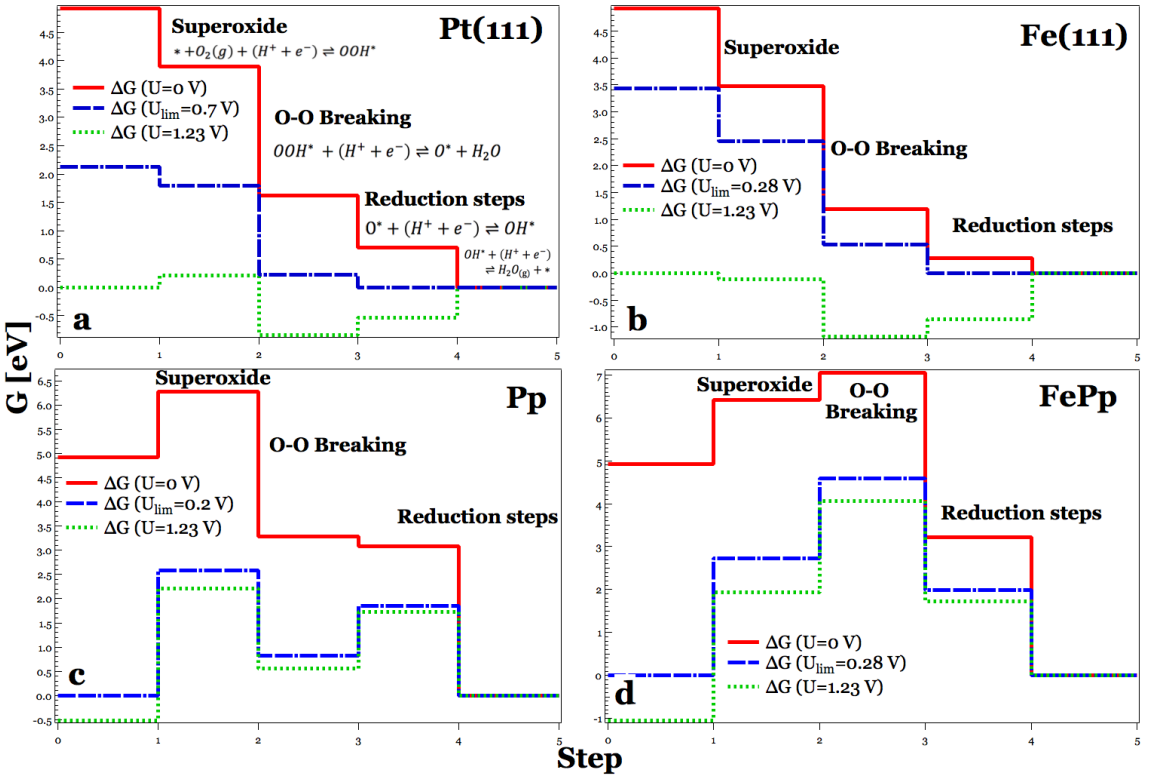


Figure 4.23 Gibbs Energy for Our simulation system. a) Pt b) Fe c) Porphyrin d) Fe Porphyrin.

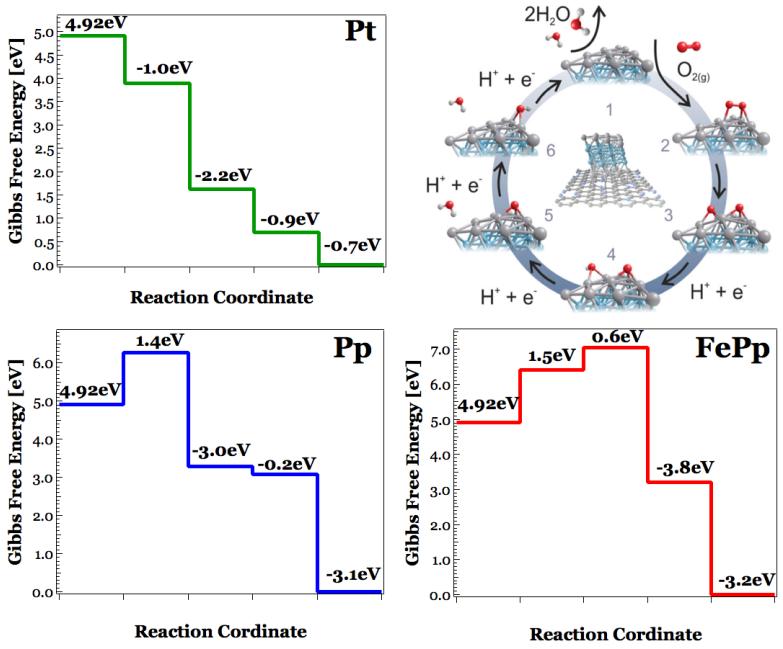


Figure 4.24 Gibbs energies for ORR model mechanism. Schematic representation of ORR on Pt-based catalyst [147].

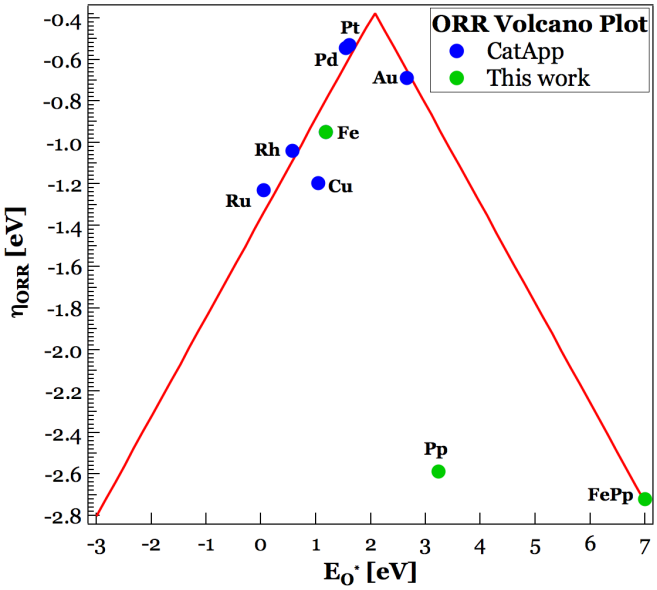


Figure 4.25 ORR Volcano Plot.

4.4.5 Volcano Plots

Figure 4.25 illustrates the relationship between the adsorption energy of the intermediates, known as the scaling relation. In order to improve catalyst performance we need to establish the most preferable surface that minimizes this relation, which means that the catalyst performance is tied to the behavior of the intermediates. One specific surface can be favorable for one of the intermediates but not for the other.

Figure 4.26 represents the volcano plot for the ORR, which illustrates that the best catalyst for this reaction should be in the top of the volcano according to the Sabatier principle. This figure also shows us that it is necessary to design better catalysts to enhance higher activities to move to the top of the volcano plot, modifying the binding of the ORR intermediates to get faster kinetics and decrease the overpotential related to the scaling relations.

From figure 4.26 we can infer that the activity of the Porphyrin is very low due to its weak oxygen bonding to the surface. Moreover, iron porphyrin mimics the porphyrin behavior and its catalytic activity is similar. This volcano plot corroborates our first assumptions during the calculation of the reaction energies, namely that oxygen binds poorly on porphyrin and iron porphyrin.

4.5 Conclusions

The macroscale model points to two important features in NPM Catalysts. Oxygen adsorption on the surface plays an important role in the reduction pathways. I was able to evaluate the Porphyrin and Iron Porphyrin activity compared to metal particles. It was evident that the oxygen activation in Fe porphyrin is not favorable and this material by itself presents similar activity to that of the Porphyrin, i.e. low activity. The presence of the metal center does not imply that the activity will follow the metal activity. Indeed, the case was quite the opposite and it opens a question about the role of the metal: is it useful as an actor in the pyrolysis process and for further active site formation.?What is clear from the activation energy diagrams for Fe Porphyrin is that the Fe-O bond is

weak and most of the bond breaking is actually facilitated by the N-H interaction.

The methodology presented in this chapter gives us important qualitative information about the possibility of N-coordinated active sites. The reason behind the poor activity of non-pyrolyzed materials might be related with poor oxygen activation on the catalytic surface. However, further coverage dependent studies must be carried on to develop an appropriate idea of the oxygen, Porphyrin and iron center interaction.

5 MESOSCALE MODELING: STEPS TOWARDS UNDERSTANDING THE ACTIVE SITE

Abstract

This chapter describes emerging studies and further directions to expand the description and understanding of NPMC active sites described in previous chapters. An approach to describe the real active site, from the modeling perspective, is provided along with some supporting experiments. Macroscale modeling of NPMC system directs our efforts towards catalysis behavior studies due to the large activation overpotentials. Microscale modeling corroborated the low activity of the non-pyrolyzed system towards ORR in during experiments due to the poor oxygen activation on the catalyst under study. This final chapter aims to suggest a modeling tool that provides information about the real active site configuration. From this perspective, single molecule behavior will not be enough to describe the real reaction environment. Here, we present an initial approach with molecular dynamics tools to understand the structure evolution and its radial distribution compared with the XRD experiments on the iron Porphyrin.

5.1 Introduction

The motivation for NPMC studies was related to previous research in our group. We were working with a copper triazole complex synthesized in a two-step process. In the first step, 1,2-benzenedinitrile was covalently anchored to the carbon support Black Pearls 2000 (BP2000) from Cabot Corp using diazonium-coupling chemistry. BP2000 carbon was modified and further dried overnight with heating. In the second step, the dried modified carbon was suspended in water and aqueous solutions of 3,5-diaminotriazole and Cu(OAc)2 were added. The resulting aqueous suspension was heated at 140◦C for 4 hours in a microwave reactor, to yield Cu-TriazoloPhthalocyanine (Cu-TrPc/C) supported on carbon. Figure 5.1 illustrates the synthesis process to obtain the Cu-TrPc/C catalyst [148]. Different pyrolysis conditions were applied and structural changes were followed by XRD experiments, as figure 5.2 illustrates. It can be seen that after pyrolysis at 600◦C and 700◦C very sharp CuO peaks are detected, indicating the formation of large Cu metal particles during pyrolysis. As the pyrolysis temperature increases above 800◦C a mixture of CuO and Cu_2O is detected. The XRD peak widths are rather narrow, approximately 0.19 degrees (FWHM) for the

Cu(111) peak and 0.34 degrees (FWHM) for the Cu_2O(111) peak in the sample pyrolyzed at 950◦C. These correspond to Scherer domain widths of 45 nm and 24 nm, respectively. These XRD results were qualitative evidence of the structural changes during pyrolysis. Figure 5.2 illustrates that the as-synthesized material does not exhibit any characteristic peaks for copper in any of its possible forms, as a metallic particle or as a copper oxide. As the treatment temperature is increased, these peaks started to appear and finally, we can see the formation of metallic particles and oxides. Our first question, based on literature evidence of multiple site formation was: Does this pyrolysis pattern follow the same trends for different structures?

A review of the literature on this specific question led to the work of Vallejos-Burgos and collaborators [149] in which they combined porosity experiments, XRD, Raman spectroscopy, EXAFS and XPS techniques to track the structural and coordination changes in pyrolyzed phthalocyanines. Figure 5.3 schematically represents their results. The porosity, especially in the micropores range, is developed only after the original phthalocyanine structure is destroyed, but this process occurs at different temperature ranges depending on the metal center. The metal-containing samples are the most refractory, which generates clear peaks for crystalline metallic forms, appear as result of structure reorganization. The details of pore size evolution also depend on the coordinating atom. They are especially sensitive to it in the case of H-Pc and Co-Pc, which both exhibit the highest microporosity development at intermediate temperature.

The metallic form of the metal centers was extracted from the XRD and EXAFS profiles. XPS confirms the presence of metallic particles in subsurface regions (approximate etched depths for C, Co and Cu are 1–2 nm, 13 nm and 20 nm, respectively). The differences in N/C atomic ratio between elemental analysis and XPS indicate a heterogeneous radial distribution in the particle. For most HTT analyzed, surface N/C is almost twice that of bulk. An exception is seen in the case of Co-Pc HT above 550 °C where total bulk N/C is very similar to the surface value. They also corroborate the presence of the various N coordination with the C support have been presented. All N types are found at the edge of graphene layers.

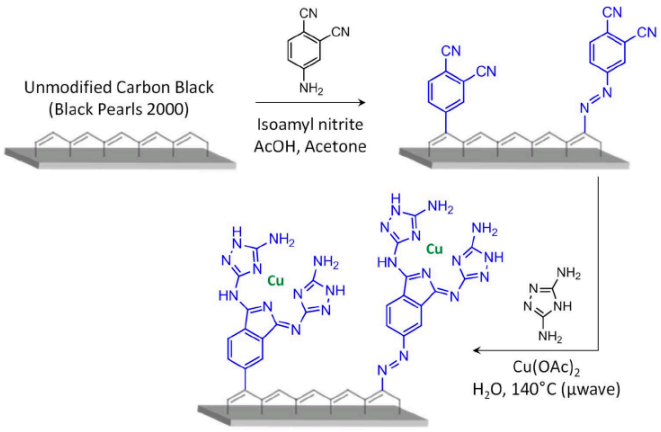


Figure 5.1 Synthesis scheme for Cu-TrPc/C complex covalently immobilized to BP2000 carbon support [148].

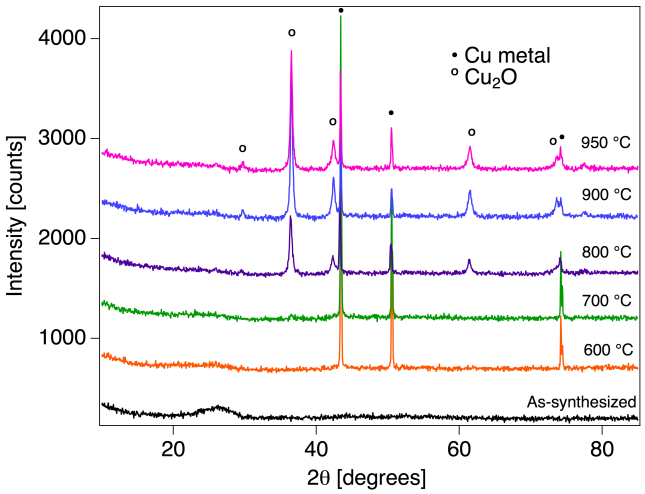


Figure 5.2 XRD pattern of Cu-TrPc catalyst before and after pyrolysis from 600◦C to 950◦C. [148].

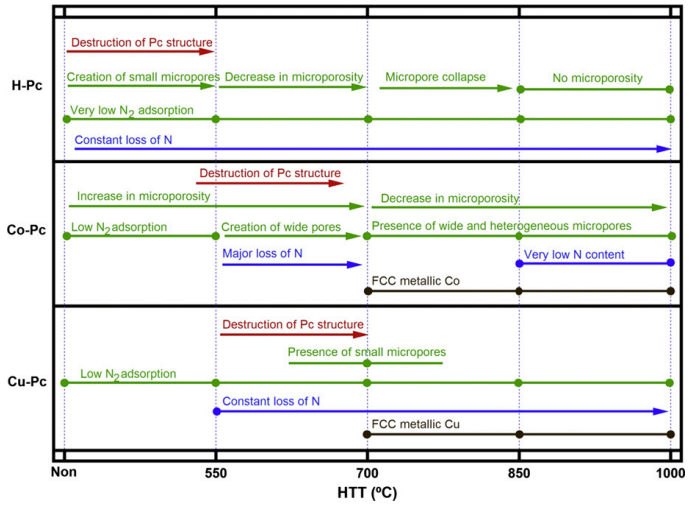


Figure 5.3 Schematic representation of main structural changes occurring during HT of all Pc samples [149].

This study reveals the organic frame destruction to create active sites, multiple sites formation, and the temperature associated with the structural changes. It provides an important insight for the effects of pyrolysis temperatures but raises the question about the microporosity formation and its relation with the nitrogen coordination.

Studies made by multiple laboratories were summarized by Jaouen and collaborators [58] for different catalyst types. From elemental surface analysis they found that the nitrogen is found in several characteristic structures. Pyridinic, nitrile, and pyrrolic N atoms are likely to be involved in the active sites. Also, they report that the mass activity of Co-based catalysts has been shown for one type of catalyst to be about 10 times lower than that of Fe. The amount of pores differs widely among the various NPMCs evaluated. The shapes of the isotherms are, however, grossly similar and typical of carbonaceous materials with a majority of mesopores present.

They found three important factors to explain the activity of NPMCS: the metal content, the N content, and the microporous area created during the heat treatment. For instance, activity increased linearly only up to a metal content of about 0.1 wt. %. Metal content higher than 0.1 wt. % led to the concomitant decrease of the microporous area of the catalysts, with less activity. In particular, Fe coordinated with proper organic structure and at the surface, might be an active site for the ORR. Other catalysts in this study show that increasing Fe content resulted in the activity declining.

A possible explanation is NH_3 decomposition into N_2 and H_2 during pyrolysis catalyzed by Fe. Hydrogen is less reactive than NH_3, and consequently both the microporous area and N content decreased with higher Fe content with negative effect on the activity. They proposed to avoid using carbon supports due to morphology dependence of the catalyst during the carbonization/graphitization process of precursor molecules. They enhanced metal content with this solution (up to 3% Fe). Moreover, the total surface content of N does not determine the activity even though N atoms are known to be present in the active sites. Finally, by increasing the microporous surface area, the activity increased for disordered carbonaceous materials. From this study they concluded that the pores hosting

active sites seem to be 5-20 Å wide. Pores <5 Å also may host a few active sites, but their accessibility to O_2 or H^+ is very low for NPMCs synthesized without a preexisting carbon support.

These studies elucidated important factors in the fabrication process of NPMCs in terms of the pyrolysis temperatures, metal content, carbon structures and microporosity. The questions to be answered are what is the relation between the metal content and the microstructure generation? How does the structure reorganize around N-coordinated and Fe-N coordinated sites?

This final chapter gives an initial approach to understanding the microstructure formation from the modeling perspective. To date, there are not modeling studies addressing this particular problem, mainly due to the lack of information on the metal/nitrogen, metal/carbon and nitrogen/carbon interactions during the pyrolysis process as well the formation of extended structures. These interactions imply changes in the oxidation states, bond breaking and bond formation as a function of the temperature.

DFT studies are limited by the number of atoms that can be studied, on one hand, and by the treatment temperature on the other. However, molecular dynamics per se, does not take into account the electronic interactions and would not be enough to describe the system under pyrolysis conditions.

I studied the Fe Porphyrin as whole entity, trying to recreate the molecule with the right parameters and finally, construct a catalyst layer that reproduces the Fe content found from SEM and BET studies and compare the initial results with the XRD experiments.

5.2 Experimental evidence

One of the main challenges in elucidating the active site is the necessity of high-end techniques that provide an in-situ chemical environment. Our approach was done with the techniques available and matched with the MD simulations. Further studies will be required to generate more high-quality structural data to validate our initial modeling results.

5.2.1 Perfusion Calorimetry

To perform the calorimetry experiments we used the TAM III multi-channel, microcalorimetric system from TA Instruments. TAM offers maximum sensitivity, flexibility, and performance. TAM III employs patented thermostat technology to precisely control the liquid bath temperature to within 0.0001 °C, and can be operated in isothermal, step-isothermal or temperature-scanning mode. Figure 5.4 depicts the experiment set up.

The main purpose of this experiment was to evaluate the adsorption energy of oxygen and reconstruct the copper triazole unit described in the introductory part of this chapter. The experiment carried out here was a modification of the original relative humidity perfusion experiment where the water was replaced by argon to remove water from the powders under study and the switched to oxygen.

The general procedure consists of loading a solid sample into an ampoule and lowering it into the calorimetric measuring unit. Argon is then passed over the solid in the ampoule. After stabilization, the sample is kept during 24 hours on argon then switched to oxygen and left 24 hours. These steps are repeated until no changes are present in the sample. The switching between gases is controlled by the action of two mass flow controllers, which are controlled by the TAM Assistant software and a shut down of the main gas line.

Argon enters the system through a Swagelock connection on the stainless steel tube configured as a spiral around the ampoule. The flow then passes into the flow divider and down the center of the perfusion shaft into the ampoule. The oxygen is connected to the second Swagelock where it will pass through two temperature-controlled humidifier chambers before it passes into the sample ampoule.

The temperature of the humidifier chambers is controlled by the precision thermostat. The outflow from the ampoule passes up the main tube along the outer surface of the perfusion shaft and out of the lower of the two Omnifit connectors.

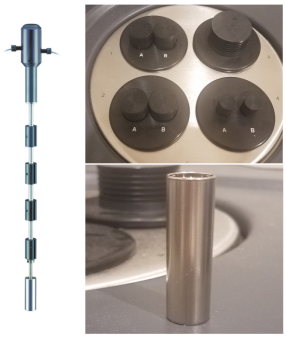


Figure 5.4 Perfusion experiment set up.

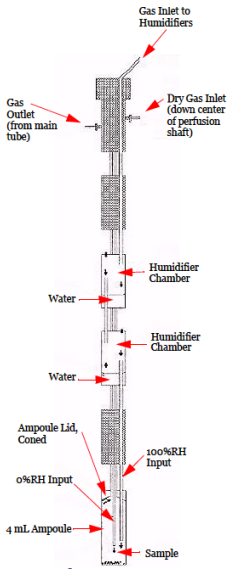


Figure 5.5 Schematic representation of the perfusion calorimeter parts.

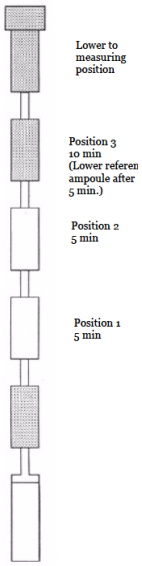


Figure 5.6 Calorimeter equilibration positions.

Table 5.1 Experimental conditions

Sample	Temperature [°C]	Weight [mg]	Mass Flow [mL/h]
Cu-TrPc (Heat Treatment)	45	48.32	200
Cu-TrPc	45	51.63	200
BP2000 Modified	45	51.58	200
BP2000	45	49.73	200

The recommended sample loading ranges between 50mg to 200mg. An empty ampoule must be used as reference point, equilibrated, and then, the ampoule with the sample must be introduced. Figure 5.6 illustrates the equilibration points and the time required for each one. This equilibration is particularly important for accuracy in the adsorption enthalpy calculation.

Table 5.1 summarizes the experimental details and samples evaluated with this procedure. The idea behind the experiment was to emulate the copper triazole (Cu-TrPc) synthesis process and analyze the structure evolution and the possible site or sites, if visible, present during the adsorption process. For this purpose, the carbon support (BP2000) with and without treatment was studied, then the as-synthesized catalyst and finally, the pyrolyzed sample.

5.2.2 XRD

The XRD patterns shown in Figure 5.2 were measured with a Bruker D2 Phaser diffractometer with Cu Kα radiation. For SEM imaging, a Hitachi S-4800 field emission scanning electron microscope was employed; this equipment features a resolution of 1.0 nm and a variable acceleration voltage of 0.5-30 kV. A 300 kV HF-3300 TEM/STEM, with a cold-field emission gun and 0.13 nm resolution was used to analyze the microstructure of the materials. The same methodology was employed to extract the XRD patterns for the Iron Porphyrin [121].

5.3 Mesoscale modeling

In this technique the atoms are the basic particle and it disregards nuclei and electrons. The system is described by Newton's equations of motion. To run MD simulations is necessary to get the potential from experimental data and thus, electronic and magnetic properties cannot be obtained. This method solves Newton's equation of motion to predict the motion of any particle-like object.

$$F = ma \qquad \textbf{Equation 5.1}$$

Where F is the force vector, m the atomic mass and a is the acceleration vector. MD simulations approximate atoms as spheres with points of mass at the

center. In this approximation the role of the electron is totally neglected, and the electronic wave function is assumed to instantaneously adapt to the current configuration of atoms. The MD simulations run in LAMMPS a classical molecular dynamics open source code, and an acronym for Large-scale Atomic/Molecular Massively Parallel Simulator. It is distributed by Sandia National Laboratories [150].

Figure 5.7 represents the general procedure to run MD simulations. During and after equilibration steps, the data are stored for each (or some) time steps like positions, momenta, energies, and forces. The properties of the system are calculated via statistical mechanical analysis. The main limitations for MD runs are the availability and accuracy potential, the length scale of just nanoseconds and no electromagnetic properties calculations.

5.3.1 MD Potentials

The potential well is a region surrounding a local minimum of potential energy (atoms near enough to feel attraction or repulsion – interatomic potential). This potential is generated empirically. The potential is calculated as the negative gradient of the potential energy with respect to the position and from the newton's equation of motion as:

$$\boldsymbol{F = ma = m\frac{dv}{dt} = m\frac{d^2r}{dt^2} = \frac{d}{dt}\left(m\frac{dr}{dt}\right) = \frac{d}{dt}(mv) = \frac{dp}{dt}} \qquad \textbf{Equation 5.2}$$

Where p is the momentum and m the mass. For MD calculations is true that the energy should be constant. Then, the force can be calculated as:

$$\boldsymbol{F = -\nabla U(r)} \qquad \textbf{Equation 5.3}$$

Where U is the potential energy and r is the interatomic distance. Atoms follow the line of minimum energy according with its potential. As consequence, they are specific for each system because they are calculated by fitting certain functions with parameters from experimental data or from first-principle methods.

5.3.1.1 MD Pair potentials

For a N-atom system (N: number of atoms), the i-atom interacts with another atom at the same time, so the potential energy can be calculated as:

$$\boldsymbol{U(r) = \sum_{i<j}^{N} U_2(r_i, r_j) + \sum_{i<j<k}^{N} U_3(r_i, r_j, r_k) + \cdots}$$ **Equation 5.4**

Where U_2 and U_3 are the two and three atoms potentials respectively. U_2 has (N-1) interactions per atom. Lennard-Jones potential is the most common pair potential and the number of pair is calculated as:

$N_{pair} = \frac{(N-1)N}{2}$, this pair potential scales as N^2. Then, the Lennard-Jones potential is calculated as:

$$\boldsymbol{U_{LJ} = 4\varepsilon\left[\left(\frac{\sigma}{r}\right)^{12} - \left(\frac{\sigma}{r}\right)^{6}\right]}$$ **Equation 5.5**

ε: lowest energy of the potential curve=cohesive energy

σ: interatomic potential at which $U_{LJ}=0$

In force form:

$$\boldsymbol{F_{LJ} = \frac{24\varepsilon}{\sigma}\left[2\left(\frac{\sigma}{r}\right)^{13} - \left(\frac{\sigma}{r}\right)^{7}\right]}$$ **Equation 5.6**

5.3.1.2 Embedded atom method potentials (EAM)

EAM is suitable for metals, transition metals, FCC metals atoms (or ions) located in the middle of the electron sea and mostly, coordinated with 8-12 other atoms. This method considers the long-range interactions (coulomb interactions) by calculating an effective electron density at a given atomic site as one parameter, capturing some effects with simple potential. The approach is similar to the mean-field approximation. Thus:

$$\boldsymbol{U_{EAM} = \sum_{i \neq j} U_{ij}(r_{ij}) + \sum_i F_i(\rho_i)}$$ **Equation 5.7**

Where $F_i(\rho_i)$ is the embedding energy function.

$$\boldsymbol{\rho_i = \frac{1}{2}\sum_{j \neq i} \rho_j(r_{ij})}$$ **Equation 5.8**

ρ_i: Electron density at site i as a linear superposition of valence electrons clouds from all other atoms. For calculations MD calculate first ρ_i, then the embedding energies and finally added the pair potentials. Not suitable for alloys.

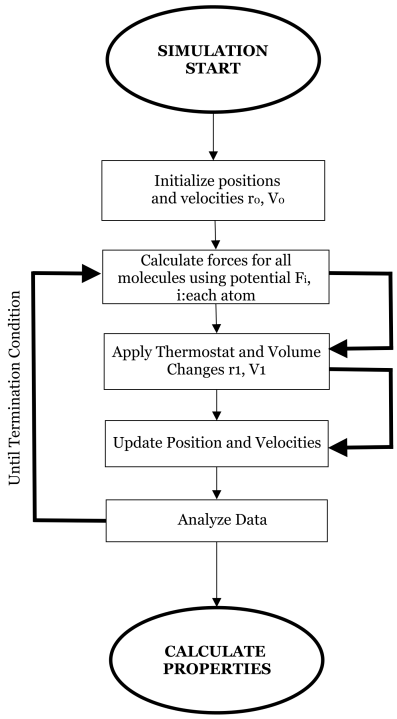


Figure 5.7 MD simulation scheme.

5.3.1.3 Tersoff potential

Tersoff potential is suitable for covalent solids with strong directional bonds of equivalent strength, sp3. Is suitable for SiC, Si, diamond, graphite (being careful of the layer to layer description out of range of this potential), amorphous carbon and hydrocarbons. The bond angle and bond order are the prime characteristics of these materials. The strength of the bond is a function of the local environment, coordination number and bond angle.

$$U_{Tersoff} = \frac{1}{2}\sum_{i \neq j} U_R(r_{ij}) + \frac{1}{2}\sum_{i \neq j} B_{ij} U_A(r_{ij}) \qquad \textbf{Equation 5.9}$$

U_R, U_A: repulsive and attractive potentials

B_{ij}: bond order between i and j atoms

$$B_{ij} \propto \frac{1}{\sqrt{N_{coor}}} \qquad \textbf{Equation 5.10}$$

5.3.2 Organic molecules potentials

To simulate organic molecules, the interaction potential is divided into intermolecular (between molecules) and intramolecular (within a molecule) components and can be described as[151]:

$$U_{total} = U_{inter} + U_{intra} \qquad \textbf{Equation 5.11}$$

5.3.2.1 Intermolecular (Non-bonded) Potentials

The intermolecular potential or non-bonded potential is often separated into a short-range interaction, such as Lennard-Jones, and a long-range interaction, usually Coulombic.

$$U_{inter} = U_{inter,SR} + U_{inter,LR} \qquad \textbf{Equation 5.12}$$

5.3.2.2 Short-range (Dispersive) Potentials

The total short-range interaction is often expressed as the sum of pairwise interactions between atoms located on different molecules. In the following notation *i* and *j* represent the molecule and *a* identify the atom type (C, H,N,O, and Fe for iron Porphyrin)

$$U_{inter,SR} = \frac{1}{2}\sum_{im=1}^{N_m}\sum_{jm=1}^{N_m}\sum_{ia=1}^{N_{a,t(im)}}\sum_{ja=1}^{N_{a,t(jm)}} 4\varepsilon_{t(ia)t(ja)}\left[\left(\frac{\sigma_{t(ia)t(ja)}}{r_{ia,im,ja,jm}}\right)^{12} - \left(\frac{\sigma_{t(ia)t(ja)}}{r_{ia,im,ja,jm}}\right)^{6}\right] \qquad \textbf{Equation 5.13}$$

In this expression N_m indicates the number of molecules in the system, $N_{a,t(jm)}$ the number of atoms in a molecule of type *im*. $\varepsilon_{t(ia)t(ja)}$ and $\sigma_{t(ia)t(ja)}$ are Lennard-Jones parameters as functions of the types of atoms *ia* and *ja*. The separation between particles, $r_{ia,im,ja,jm}$, is the distance between atom *ia* on molecule *im* and atom *ja* on molecule *jm*.

Equation 5.13 is equivalent to equation 5.5 for the Leonard-Jones pair potential with the addition of the molecule to molecule interaction. For iron porphyrin the interactions to include are C-C, H-H, N-N, Fe-Fe, C-H, C-N, C-Fe, Fe-N, N-H.

5.3.2.3 Long-range (Coulombic) Potentials

The long-range potential is referred to as the Coulombic potential.

$$U_{inter,LR} = \frac{1}{2}\sum_{im=1}^{N_m}\sum_{jm=1}^{N_m}\sum_{ia=1}^{N_{a,t(im)}}\sum_{ja=1}^{N_{a,t(jm)}} \frac{1}{4\pi\varepsilon_0}\frac{q_{ia,im}q_{ja,jm}}{r_{ia,im,ja,jm}} \qquad \textbf{Equation 5.14}$$

Where $q_{ia,im}$ is the charge on atom *ia* of molecule *im,* ε_o the permittivity of free space.

5.3.2.4 Intramolecular (Bonded) Potentials

Intramolecular potentials include bonded interactions for atoms whose relative interactions are dominated by the nature of local chemical bonds and non-bonded interactions for atoms, which are separated by many bonds.

$$U_{intra} = U_{intra,bonded} + U_{intra,non-bonded}$$ **Equation 5.15**

The intramolecular non-bonded interactions are the same as those for the intermolecular interactions described above. The intramolecular bonded potential energy is typically composed of four components; they are empirical in nature and are defined in order to reproduce known geometries of molecules.

$$U_{intra,bonded} = \sum_{im=1}^{N_m} \left(U_{bond} + U_{angle} + U_{dihedral} + U_{improper}\right)$$ **Equation 5.16**

5.3.2.5 Bond (Stretching) Term

This potential describes the interaction between two atoms connected by a chemical bond. Often, this interaction is described by a Hookean spring as follows:

$$U_{bond} = \sum_{bonds} \frac{k_{r,t(ia),t(ja)}}{2} \left(r_{ia,ja} - r_{eq,t(ia),t(ja)}\right)^2$$ **Equation 5.17**

Where the force constant and the equilibrium bond distance, $k_{r,t(ia),t(ja)}$ and $r_{eq,t(ia),t(ja)}$, are defined for a bond connecting atoms of type *ia* and type *ja*. Besides specifics of bond type, the only thing that matters in this bond is the distance between atoms, $r_{ia,ja}$. Therefore, this potential describes bond stretching between adjacent atoms.

5.3.2.6 Angle (Bending) Term

This potential describes the interaction between three atoms connected in sequence by two chemical bonds. Often, this interaction is described by a Hookean spring applied to the angle defined by the three atoms, $\theta_{ia,ja,ka}$, rather than distance between them.

$$U_{angle} = \sum_{angles} \frac{k_{\theta,t(ia),t(ja),t(ka)}}{2} \left(\theta_{ia,ja,ka} - \theta_{eq,t(ia),t(ja),t(ka)}\right)^2$$ **Equation 5.18**

Where the force constant and the equilibrium bond distance, $k_{\theta,t(ia),t(ja),t(ka)}$ and $\theta_{eq,t(ia),t(ja),t(ka)}$, are defined for an angle of a series of atoms of type *ia*, type *ja* and type *ka*. Besides type, the only thing that matters in this bond is the angle, $\theta_{ia,ja,ka}$, defined by the three atomic positions

$$\boldsymbol{cos(\theta_{ia,ja,ka})} = \frac{(\boldsymbol{r_{ia}-r_{ja}})\cdot(\boldsymbol{r_{ka}-r_{ja}})}{|\boldsymbol{r_{ia}-r_{ja}}||\boldsymbol{r_{ka}-r_{ja}}|} \qquad \textbf{Equation 5.19}$$

5.3.2.7 Dihedral (Torsion) Term

This potential describes the interaction between four atoms connected in sequence by three chemical bonds. Often, this interaction is described by a combination of trigonometric functions, based on the torsion angle, $\theta_{ia,ja,ka,la}$, defined by the positions of atoms, *ia*, *ja*, *ka* and *la*.

$$\boldsymbol{U_{angle}} = \sum_{\boldsymbol{dihedrals}} \left(\begin{matrix} \frac{\boldsymbol{V_1}}{\boldsymbol{2}}[\boldsymbol{1+cos(\phi-\phi_1)}] + \frac{\boldsymbol{V_2}}{\boldsymbol{2}}[\boldsymbol{1+cos(2\phi-\phi_2)}] \\ + \frac{\boldsymbol{V_3}}{\boldsymbol{2}}[\boldsymbol{1+cos(3\phi-\phi_3)}] + \frac{\boldsymbol{V_4}}{\boldsymbol{2}}[\boldsymbol{1+cos(4\phi-\phi_4)}] \end{matrix} \right) \qquad \textbf{Equation 5.20}$$

5.3.2.8 Improper (Torsion) Term

This potential describes the interaction between four atoms, in which atoms three of the four atoms are connected to the fourth three chemical bonds. This interaction potential is typically used to induce planarity in molecules. The improper torsion angle is defined as the angle between two planes. The first plane is defined by the i, j and k atoms and the second plane is defined by the j, k and l atoms. One example of a corresponding functional form for the improper torsion is

$$\boldsymbol{U_{improper}} = \sum_{\boldsymbol{improper}} (\boldsymbol{K}[\boldsymbol{1+d\ cos(n\phi)}]) \qquad \textbf{Equation 5.21}$$

This form looks like one term of the dihedral potential in which the equilibrium angle is set to zero.

5.3.2.9 Intramolecular Non-bonded Term

As noted above, the intramolecular non-bonded term has the same functional form as the intermolecular non-bonded term.

$$U_{intra,non-bond,SR}$$

$$= \frac{1}{2}\sum_{im=1}^{N_m}\sum_{ia=1}^{N_{a,t(im)}}\sum_{ja*}^{N_{a,t(im)}} 4\varepsilon_{t(ia)t(ja)}\left[\left(\frac{\sigma_{t(ia)t(ja)}}{r_{ia,im,ja,jm}}\right)^{12} - \left(\frac{\sigma_{t(ia)t(ja)}}{r_{ia,im,ja,im}}\right)^{6}\right] \quad \textbf{Equation 5.22}$$

$$U_{intra,non-bond,LR}$$

$$= \frac{1}{2}\sum_{im=1}^{N_m}\sum_{ia=1}^{N_{a,t(im)}}\sum_{ja*}^{N_{a,t(im)}} \frac{1}{4\pi\varepsilon_0}\frac{q_{ia,im}q_{ja,jm}}{r_{ia,im,ja,im}} \quad \textbf{Equation 5.23}$$

5.3.2.10 Intramolecular potentials

Some of the commonly used intramolecular potentials are: OPLS-aa (all atom)[152], OPLS-ua (united atom) [153], TraPPE (united atom) [154], TraPPE (all atom) [155], CHARMM [156], UFF: Universal Force Field [157].

5.3.3 Ensembles

MD simulations make a large set of atomic configurations (ensembles) with certain constraints (temperature, pressure, volume and chemical potential) to obtain a set of properties. We can obtain entropies, Helmholtz and Gibbs free energies, diffusion coefficients, and many other structural properties. Table 5.2 illustrates the types of ensembles and the fixed variables. Ω is the partition function and it represents all the accessible phase-space volume.

In MD simulations, the total energy E is a constant of motion. If we assume that the time averages are equivalent to ensemble averages, then the time averages obtain in a conventional MD simulation are equivalent to the ensemble averages in the micro canonical ensemble [158].

The treatment of temperature, volume, and pressure in term of the momenta is describe as follow:

- Pressure (F is treated as pairwise potential function)

$$P = \frac{1}{V}\left[\frac{1}{3}\sum_i^N\left(\sum_{j>i}^N F_{ij}\left|q_i - q_j\right| + \frac{|p_i|}{m_i}\right)\right] \quad \textbf{Equation 5.24}$$

- Temperature

$$\boldsymbol{T = \frac{1}{3Nk_B}\sum_i^N \frac{|p_i|^2}{m_i}}$$ **Equation 5.25**

- Volume: calculated from the unit cell parameters and obtain as the molecules densities divided by the number of molecules of the system

$$\boldsymbol{V = \frac{N}{\rho_{molecules}}}$$ **Equation 5.26**

$$\boldsymbol{\rho_{molecules} = \rho_{bulk} * N_A}$$ **Equation 5.27**

Ensembles at constant temperature (NVT) are used to obtain volume or pressure changes in the system and at constant pressure (NPT) to obtain volume or temperature changes of the system. The way to control pressure or temperatures include four type of approaches: stochastic methods by constraining the system to preset distribution function, strong-coupling methods by scaling system variables to give exact preset derived value, weak-coupling methods by scaling system variable in the direction of the desired value or extended dynamics it is based on a reformulation of the Lagrangian equations of motion of the system In particular, the extended Lagrangian method, first introduced by Andersen in the context of constant pressure MD simulations [104], has become one of the most important tricks to extend the applicability of MD simulations [158].

Table 5.2 Ensembles used in MD and MC simulations

Ensembles	Fixed Variables	Remarks
Microcanonical	N, V, E	Isolated system. Very common in MD $S=k\ln\Omega_{NVE}$
Canonical	N, V, T	Very common in MC. Common in MD $F=-kT\ln\Omega_{NVT}$
Isobaric-isothermal	N, P, T	$G=-kT\Omega_{NPT}$
Grand canonical	μ, V, T	Rarely in MD, more in MC. $\mu=-kT\Omega_{NPT}$

5.3.3.1 Thermostats

5.3.3.1.1 Stochastic Langevin

This thermostat applies friction and random force to momenta. Andersen thermostat is one to most common ones where the system is coupled to a heat bath that imposes the desired temperature. Stochastic impulsive forces that act occasionally on randomly selected particles represent the coupling to a heat bath [158, 159].

$$\frac{dp_i}{dt} = \sum_j^N \left(F_{ij}\left|q_i - q_j\right|\right) + \gamma p_i + R_i(t) \qquad \textbf{Equation 5.28}$$

5.3.3.1.2 Strong coupling

This is a isokinetic/Gaussian thermostat that scales velocity

$$\frac{dp_i}{dt} = \sum_j^N \left(F_{ij}\left|q_i - q_j\right|\right) + \alpha p_i \qquad \textbf{Equation 5.29}$$

5.3.3.1.3 Weak coupling

Also known as Berendsen bath, where the unit cell is immersed in surrounding bath at T_0 and with a relaxation constant, τ[160].

$$\frac{dp_i}{dt} = \sum_j^N \left(F_{ij}\left|q_i - q_j\right|\right) + \frac{p_i}{\tau_T}\left[\frac{T_0}{T} - 1\right] \qquad \textbf{Equation 5.30}$$

5.3.3.1.4 Nose-Hoover thermostat

Nose's approach use an extended Lagrangian; that is, a Lagrangian that contains additional, artificial coordinates and velocities. Extended Lagrangian methods are widely used not only for simulations in ensembles other than constant NVE, but also as a stable and efficient approach to perform simulations in which an expensive optimization has to be carried out at each time step [161].

$$\frac{dp}{dt} = \sum_i^N \sum_{j>i}^N \left(F_{ij}\left|q_i - q_j\right|\right) + \frac{p_\eta}{Q} p \qquad \textbf{Equation 5.31}$$

$$\frac{dp_\eta}{dt} = \sum_{ji}^N \frac{|p_i|^2}{2m_i} - \frac{3}{2} n k_B T \qquad \textbf{Equation 5.32}$$

Where Q is a "heat bath mass" and the suggested value is $6nk_BT$.

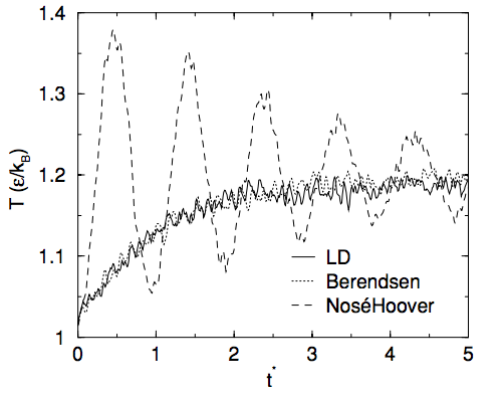


Figure 5.8 Thermostat comparison [159].

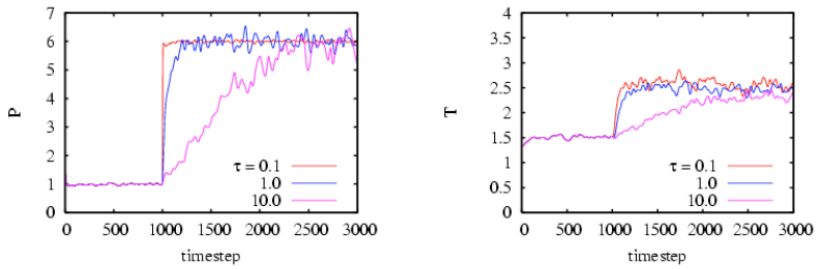


Figure 5.9 Berendsen barostat and thermostat for different relaxation constants [159].

5.3.3.2 Barostats

Most experiments are performed at constant pressure instead of constant volume. If one is interested in simulating the effect of, for example, the composition of the solvent on the properties of a system one has to adjust the volume of an NVT simulation to ensure that the pressure remains constant. For such a system it is therefore much more convenient to simulate at constant pressure. To simulate at constant pressure in a MD simulation the volume is considered as a dynamical variable that changes during the simulation.

5.3.3.2.1 Weak coupling Berendsen bath

The barostat scales each dimension by μ: where β is isothermal compressibility with τ as relaxation constant [160].

$$\boldsymbol{\mu = \left[1 - \frac{\beta \partial t}{\tau}(P_0 - P)\right]^{1/3}} \qquad \textbf{Equation 5.33}$$

Together with the Berendsen thermostat they provide the realistic fluctuations of temperature and pressure.

5.3.3.2.2 Other Barostats

The extended dimension of Nosé-Hoover thermostat can be applied to pressure to give a Nosé-Hoover barostat [162, 163]. The Parrinello-Rahman barostat[164] extended this further by making each unit vector of the unit-cell independent so that as with Nosé-Hoover the volume is a variable in the simulation. Additionally, allows dynamic shape change (gives control of stress as well as pressure).

5.3.4 General procedure for MD molecules modeling

To build a molecule or molecule system in MD is necessary to follow a specific order to be able to capture all the molecular inter and intra molecular interactions [151]. The steps are as follows:

1. Find or build a reasonable model of the isolated molecule: common molecules can be found in The NIST Chemistry webbook for tens of thousands of common compounds (http://webbook.nist.gov/chemistry/). If the molecule is not found, software like Avogadro can be used to build the molecule. In

general, pdb format files are preferable because they contain the bond information.

2. Build a complete input configuration for the isolated molecule: this step requires information on the connectivity between atoms. This step will allow us to identify the pair interactions, improper, dihedral, and angle terms. For this purpose, if more than one atom has different coordination, they must be identified as separate types of atoms. For instance, for the iron Porphyrin we have three distinctive carbons and two nitrogen as figure 5.10 illustrates.
3. Build a LAMMPS input configuration for the isolated molecule; two important files are required for the LAMMPS run. The first is a configuration file, which contains all of the necessary information including all intramolecular modes for the molecule to be simulated.

   The second file provides the essential information needed to build the potential. Importantly, this file identifies the number and type of each mode. It should include types of atoms (C, H, N, Fe), types of non-bonded interactions (C_β-C_β, C_α-N_α, Fe-N_α, etc), types of stretching (bond) interactions (C_α-C_β, C_β-H, etc), types of bending (angles) interactions (C_α-C_β-N_α, C_β-C_α-N_α, etc), and types of dihedral torsion interaction (Fe-N_α-C_α-C_β, Fe-N_β-C_m-C_α).

   Potential parameters for each one of these modes must be provided in the LAMMPS input file. Therefore this file is crucial to the next step of the procedure.
4. Build a LAMMPS input file with the appropriate potential: it is important to observe how the potential is described in the input file. In our application we used the OPLS-aa potential with some modification that will be explained later. Numerical values of the parameters for the OPLS-aa potential are inserted into the input file. It is important to look for the right carbon configuration. For instance, CT is tetrahedral (sp^3) carbon and HC is hydrogen bound to this type of carbon.
5. Build a LAMMPS input file for a system of molecules: once the right molecule is built and simulated successfully, a system of molecules can be built. For dilute systems (a gas), the molecules are spaced far enough apart that we have no overlap between atoms. However, for condensed phases the molecules are

not space far enough apart to avoid overlap and if the simulation is started using this initial configuration, it will immediately blow up.

To generate stable initial configurations of our Porphyrin system we can either start as a dilute system or use a barostat to drive the system to the desired density. The practical problem with this approach is that it usually takes too long for the barostat to work. To overcome this problem, we can use the "energy minimization feature of LAMMPS to push the molecules away from their overlapping configurations". Another way is to recognize the source of the instability, which is the repulsive component of the Lennard-Jones interaction. By shrinking the size of the sigma, then the instability will vanish. Then, one simply artificially "grows" the size of the atoms in a gradual way until they are the appropriate size. At that point, you have a stable state at the proper density.

6. Run LAMMPS simulation: the key part in this step is to generate a stable initial configuration of the disordered solid phase as mentioned in the previous numeral. Once the configuration is stable, the simulation can proceed.

5.3.5 Intramolecular potential parameters

To simulate the iron Porphyrin we used the OPLSAA potential. The parameters for this potential can be found in the article by Jorgensen et al. [152]. It was developed initially for organic liquids but it has been extended to other organic molecules. The analysis for iron Porphyrin leads to the next configuration: Iron Porphyrin molecule contains 25 atoms, 32 bonds, 54 angles (three atoms interactions), 92 dihedrals (four atoms interactions), 0 impropers. The molecule components are summarized in table 5.3.

All of these parameters need to be specified in the input file. Originally, the Fe-N and N-C interactions were not present in the OPLS-aa parameters. Since its publication two decades ago, OPLS force field for organic and biomolecular systems have emphasized the importance of conformational energetics, basic intermolecular energetics in the gas phase, and the value of testing the force field on thermodynamic properties of pure organic liquids, especially heats of

vaporization, densities, and hydration free energies. Correct representation of the latter properties gives confidence in the description of non-bonded interactions including hydrogen bonding and in the size of molecules.

The parameter selection is based on the chemistry environment surrounding the molecules. The notation employ for individual atoms, depend on the hybrid state of the atom to select the proper values. Where, C represents the carbon hybrid state in carbonyl bonds, CT hybrid state in alkanes, CM hybrid state alkene C. The complete list of notation and parameter values can be found in the supplementary information from Jorgensen et al. work [152].

The carbon types and parameters were found in this potential but the bond, angles and dihedral types that include Fe were not described by these parameters. My first approximation was to use N-C interactions as Fe-C interactions. However, the representation of the single molecule was not successful and the final structure was separated (Figure 5.13). Further reading allow me to find the rest of parameters from the molecular mechanics force field studied of iron Porphyrin made by Marques and collaborators [165]. The parameters were obtained with a similar approach as for the OPLS-aa potential. Some adjustment to the bond stretching and angle bending parameters was required to use it as OPLS-aa input in LAMMPS. Tables 5.4 to 5.7 summarize the parameters used in this work.

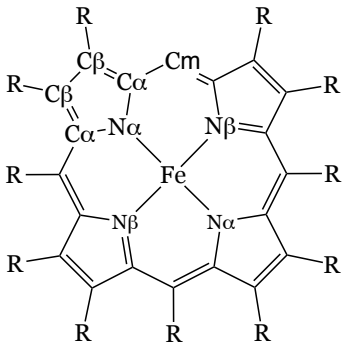


Figure 5.10 Fe Porphyrin bond types

Table 5.3 Iron Porphyrin molecule components

Component	Number	List
Atoms types	6	Fe, N_α, N_β, C_α, C_β, and C_m
Bond types	7	Fe -N_α, Fe-N_β, N_α -C_α, N_β -C_β, C_α- C_β, C_β- C_β, and C_α - C_m
Angle types	14	C_m – C_α – C_β, C_m – C_α – N_β, C_m – C_α – N_α, C_α – C_m – C_α, C_α – C_β – C_β, C_α – N_α – C_α, C_α – N_α – Fe, C_α – N_β – C_α, C_α – N_β – Fe, C_β – C_α – N_α, C_β – C_α – N_β, N_α – Fe– N_α, N_α – Fe– N_β, and N_β – Fe– N_β.
Dihedral types	19	C_m – C_α – C_β– C_β, C_m – C_α – N_α – C_α, C_m – C_α – N_α – Fe, C_m – C_α – N_β – C_α, C_m – C_α – N_β – Fe, C_α – C_m – C_α – C_β, C_α – C_m – C_α – N_α, C_α – C_m – C_α – N_β, C_α – C_β – C_β– C_α, C_α – N_α – C_α– C_β, C_α – N_α – Fe – N_α, C_α – N_α – Fe – N_β, C_α – N_β – C_α – C_β, C_α – N_β – Fe– N_α, C_α – N_β – Fe – N_β, C_β – C_α – N_α – Fe, C_β – C_α – N_β– Fe, C_β – C_β – C_α – N_α, and C_β – C_α – C_α – N_β.
Improper	0	

Table 5.4 OPLS-AA Non-Bonded Pairwise interactions

Pair	ε [kcal/mol]	σ [Å]
C_m - C_m	0.044	1.940
C_α - C_α	0.044	1.940
C_β- C_β	0.044	1.040
Fe - Fe	0.090	2.070
N_α - N_α	0.055	1.820
N_β - N_β	0.044	1.040

Table 5.5 Bond Stretching Parameters

Bond type	k_r [kcal/mol-Å²]	r_{eq}[Å]
C_m - C_α	690.34	1.389
C_β - C_α	345.17	1.439
C_α - N_α	797.48	1.380
C_α - N_β	797.48	1.380
C_β - C_β	755.06	1.350
Fe - N_α	215.73	2.066
Fe - N_β	215.73	2.066

Table 5.6 Angle Bending Parameters

Angle type	k_θ [kcal/mol-Å2-degree]	θ_{eq} [degree]
C_m – C_α – C_β	287.82	124.7
C_m – C_α – N_β	172.69	125.4
C_m – C_α – N_α	172.69	125.4
C_α – C_m – C_α	143.91	124.6
C_α – C_β – C_β	338.19	107.3
C_α – N_α – C_α	431.73	105.8
C_α – N_α – Fe	503.69	126.8
C_α – N_β – C_α	431.73	105.8
C_α – N_β – Fe	503.69	126.8
C_β – C_α – N_α	215.87	109.9
C_β – C_α – N_β	215.87	109.9
N_α – Fe– N_α	3.5978	154.0
N_α – Fe– N_β	143.91	90.0
N_β – Fe– N_β	3.5978	154.0

Table 5.7 OPLS-AA Fourier Coefficients (kcal/mol) for Torsional Energy Functions

Dihedral	V_1	V_2	V_3	V_4
$C_m - C_\alpha - C_\beta - C_\beta$	0.0000	5.3000	0.0000	0.0000
$C_m - C_\alpha - N_\alpha - C_\alpha$	0.0000	7.2000	0.0000	0.0000
$C_m - C_\alpha - N_\alpha - Fe$	0.0000	0.2400	0.0000	0.0000
$C_m - C_\alpha - N_\beta - C_\alpha$	0.0000	7.2000	0.0000	0.0000
$C_m - C_\alpha - N_\beta - Fe$	0.0000	0.2400	0.0000	0.0000
$C_\alpha - C_m - C_\alpha - C_\beta$	0.1700	1.4500	0.0000	0.0000
$C_\alpha - C_m - C_\alpha - N_\alpha$	0.0000	1.6000	0.0000	0.0000
$C_\alpha - C_m - C_\alpha - N_\beta$	0.0000	1.6000	0.0000	0.0000
$C_\alpha - C_\beta - C_\beta - C_\alpha$	0.0000	5.6000	0.0000	0.0000
$C_\alpha - N_\alpha - C_\alpha - C_\beta$	0.0000	12.000	0.0000	0.0000
$C_\alpha - N_\alpha - Fe - N_\alpha$	0.0000	0.0000	0.0000	0.0000
$C_\alpha - N_\alpha - Fe - N_\beta$	0.0000	0.2000	0.0000	0.0000
$C_\alpha - N_\beta - C_\alpha - C_\beta$	0.0000	12.000	0.0000	0.0000
$C_\alpha - N_\beta - Fe - N_\alpha$	0.0000	0.2000	0.0000	0.0000
$C_\alpha - N_\beta - Fe - N_\beta$	0.0000	0.0000	0.0000	0.0000
$C_\beta - C_\alpha - N_\alpha - Fe$	0.0000	0.1700	0.0000	0.0000
$C_\beta - C_\alpha - N_\beta - Fe$	0.0000	0.1700	0.0000	0.0000
$C_\beta - C_\beta - C_\alpha - N_\alpha$	0.0000	9.1000	0.0000	0.0000
$C_\beta - C_\alpha - C_\alpha - N_\beta$	0.0000	9.1000	0.0000	0.0000

5.4 Results

5.4.1 Calorimetry

Figure 5.8 illustrates the results obtained from the Calorimetry experiment. As explained in the experimental section, during the first 24 hours of the experiment the samples were run under argon desorb water and other adsorbed materials from the surface under study. The first peaks represent the water desorption for all materials.

All samples present two water adsorption sites. Desorption processes are exothermic, which is indicated by the negative power values (by integrating with mass and over the temperature range we will obtain the enthalpy change). The only difference in behavior is observed when the Cu-TrPc is attached to the surface. However, water was not the focus of study here. Our interest was in understanding the oxygen behavior in these materials. In general, all samples present two-adsorption sites, one endothermic and one exothermic. Both sites are noticeable in the Cu-TrPc without pyrolysis sample (light blue). However, the catalyst after pyrolysis (dark blue) has the lowest adsorption energies.

The exothermic sites take more than four hours to return to the initial stabilization points, which might indicate a higher population of these sites and lower porosity and difficult oxygen access. The endothermic sites take roughly two hours before switching to the exothermic ones, which might be related with higher porosity and faster transport of oxygen. Important conclusions from these experiments are that the presence of multiple sites and that the final pyrolyzed sample seems to share the main characteristics of the carbon support. This differential approach to understanding the catalyst evolution from synthesized to pyrolyzed catalyst was not applied to Fe Porphyrin but it can be useful to compare the presence of both exothermic and endothermic peaks. Nonetheless, if this can be expanded to reveal energetics of binding at various sites this will be a helpful tool for mechanistic understanding.

Calorimetry studies provided thermodynamic information regarding bonding energies, reaction enthalpies, thermal desorption but it needs to be combined with experiments that can provided complementary information about the

desorption species. For instance, a mass-spectrometer combined with UHV systems, to measure the partial pressure of the desorbing species would be useful.

Moreover, these measurements are also a convenient means to compare, contrast and combine the results of calorimetric measurements with data obtained in adsorption experiments using the methods used to study other kinds of systems, e.g. all-metal systems, such as surface potential measurements, ellipsometric studies, measurements of low energy diffraction, X-ray diffraction or Auger electron spectroscopy, and XPS[166].

5.4.2 XRD

We tried to understand the system evolution of the iron Porphyrin through XRD. XRD patterns corresponding to the as-synthesized and pyrolyzed (before and after the acid treatment) samples are presented in Figure 5.9. The synthesized material does not exhibit any particular feature that allows us to identify a specific structure. After heat treatment, the presence of graphitic carbon ($2\theta=26°$) and metallic Fe (110) ($2\theta=45°$) can be appreciated in both pyrolyzed samples (before and after acid treatment), in agreement with the observations made from TEM and SEM images [121] as shown in chapter 3.

The presence of Fe(110) can give us an idea of the Fe distances and we can transform the XRD patterns to generate a radial distribution of the atoms for further analysis with the MD results.

5.4.3 MD Modeling results

The results here follow the sequential steps from 5.3.4 made from the single molecule simulation to its solid form.

5.4.3.1 Single molecule modeling

Figures 5.10 and 5.11 illustrate the single molecule simulation. Figure 5.10 represents the molecule with the OPLS-aa parameters and taking the Fe-N as N-C interactions. It is evident that the pair interactions, the angles and torsion will be different from and sp2 C-N interaction. As a result, I was not able to get a correct structure; the bond lengths and angles found in literature for iron Porphyrin were not consistent. Accordingly, this approach was discarded.

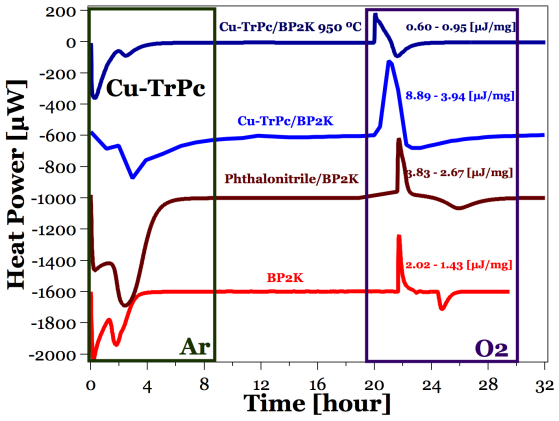


Figure 5.11 Calorimetry results for copper triazole catalyst (Cu-TrPc)

.

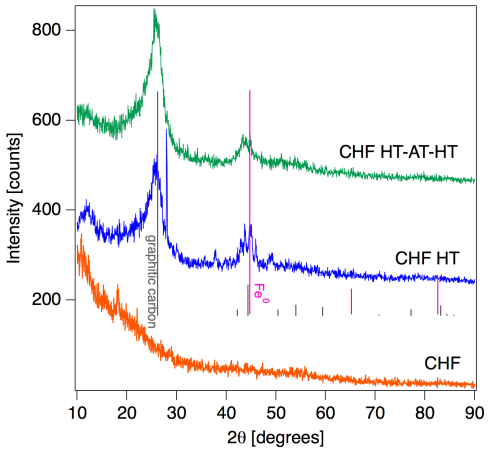


Figure 5.12 Cu Kα x-ray diffraction patterns for the as-prepared catalyst (CHF-1), the catalyst after 700°C heat treatment (HT), and the catalyst after 700°C heat treatment followed by acid treatment and final 700°C heat treatment (HT+AT+HT)[121].

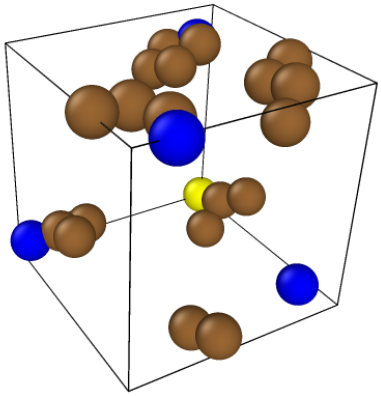


Figure 5.13 Iron Porphyrin single molecule with wrong OPLS-aa parameters.

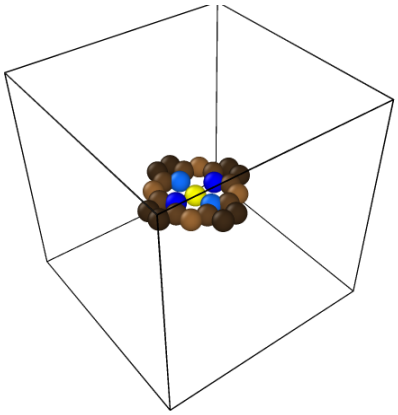


Figure 5.14 Iron Porphyrin with the MM2 parameters from Marques work [165].

Figure 5.11 represents the simulation with the MM2 potential generated by Marques for Iron Porphyrin[165]. The development of this potential was validated with crystallographic experimental results. The coordination numbers spin states and number of structures obtained was summarized in tables 5.4 to 5.7 of this work. Bond angles and length were extracted from table 2. The original torsional parameters from Marques were divided by half to correspond with the OPLS-aa potential. The V_4 term in equation 5.20 is zero for the MM2 potential. Bond stretching parameters were transformed in units from mdyn/Å to kcal/(mol-Å^2). Angle bending constant from mdyn/Å-rad to kcal/(mol-Å2-degree). From the single molecule-modeling figure 5.11, we were capable to represent the three types of carbon, two nitrogens and the iron in the Iron Porphyrin. This allows us to move forward in the system of molecules simulation. The input file for the Iron Porphyrin and LAMMPS input files are described in the appendix.

5.4.3.2 System of molecules modeling

In order to calculate the system size for modeling, extra experimental data is required. We need the bulk density and the solid density. The solid density was assumed to be the same as that for amorphous carbon and was extracted from literature. The solid density was calculated from the porosity values measured with BET [121]. Additionally, the radii was calculated from XRD distances, assuming Fe(110) as is calculated from:

$$\frac{1}{d^2} = \frac{1}{a^2}(h^2 + k^2 + l^2) \qquad \textbf{Equation 5.34}$$

Where d is the atomic diameter, a is the lattice parameter and h, k, l are the indices. The simulated system includes 125 molecules, 3125 atoms, 4000 bonds, 6750 angles and 11500 dihedral interactions. The number of molecules was chosen from the solid density show in table 5.8 by assuring the minimum image convention, which implies that the periodic images of the atom should not see each other. Then, the periodic images of the particle should be at least half of the simulation box and much larger than the cutoff distance for non-bonded interactions.

Table 5.8 MD System simulation data

Required data	Value
ρ_{bulk}	2.009 g/cm^3
$\rho_{solid,exp}$	1.1210 g/cm^3
Porosity, ε	0.44
Fe content	5%
r_o	2.84 Å
Number of molecules	125
Number of atoms	3125

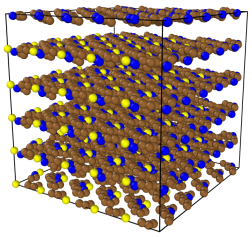


Figure 5.15 Iron Porphyrin initial point

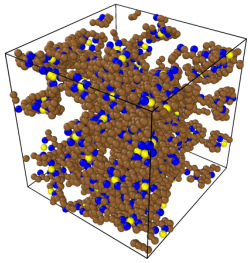


Figure 5.16 Iron Porphyrin final configuration

Figures 5.12 and 5.13 represent the initial and final configuration for the simulation. Figure 5.12 is an organized layered structure while the final configuration represents a disordered and amorphous configuration.

After equilibration, it is necessary to confirm the validity of the simulation run. In this sense, it is necessary to check conservation of total energy (kinetic and potential). The fluctuation should be less than 10^{-4} and is caused by instabilities within the system, an incorrect Δt or the integration algorithm. To deal with this problem, it is possible to make Δt smaller, run for a longer time or increase the system size. To prevent the cell from moving the total linear momentum should be zero.

$$\boldsymbol{p = \sum_i m_i v_i = 0} \quad \textbf{Equation 5.35}$$

Figure 5.17 illustrates the energy conservation of our system. After the stabilization steps (20000 fs), the energy is conserved. This result suggests that our simulations are conducted in a regime in which energy is conserved. The oscillations in this figure are a consequence of the Nose-Hoose barostat function.

Post-processing of the data results allows us to calculate the radial distribution function. This calculation is analogous to XRD and it shows how the atoms are distributed around certain atom, g(r).

$$\boldsymbol{g(r) = \frac{dN/N}{dV/V} = \frac{V}{N}\frac{\langle N(r,\Delta r)\rangle}{4\pi r^2 \Delta r} = \frac{1}{4\pi r^2}\frac{1}{N\rho}\sum_{i=1}^{N}\sum_{j\neq i}^{N}\langle \delta(r - |r_j - r_i|)\rangle} \quad \textbf{Equation 5.36}$$

$\langle N(r,\Delta r)\rangle$: Number of atoms in the shell

$4\pi r^2 \Delta r$: Shell volume between r and Δr.

Figure 5.18 illustrates an example for Si and the differences between crystal, liquid and amorphous structure based on the radial distance. The first peak corresponds to the averaged nearest neighbor (atomic packing and bonding). Broadened peaks indicates amorphous structures. Coordination numbers can be obtained as equation 5.16 shows.

$$\boldsymbol{N_{coor} = \rho \int_{r_1}^{r_2} g(r) 4\pi r^2 dr} \quad \textbf{Equation 5.37}$$

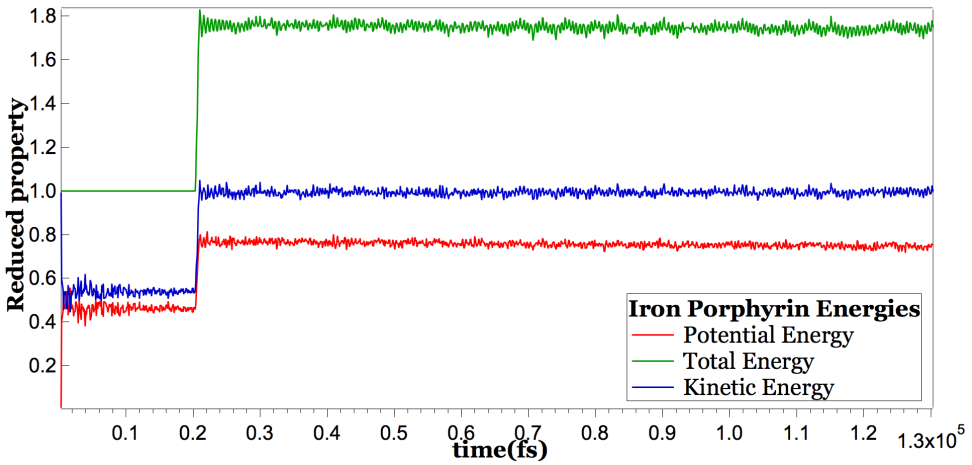


Figure 5.17 Total, Potential and Kinetic energy for the system

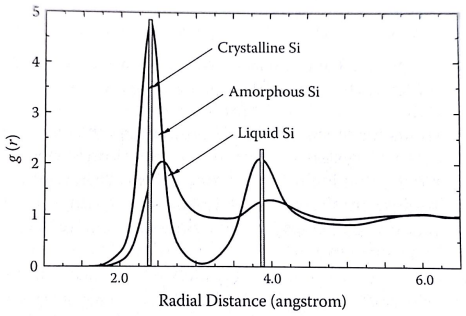


Figure 5.18. Typical radial distribution functions for Si in various forms: amorphous and liquid [167].

Figure 5.16 shows the calculated distribution of atoms around Fe. These results are then compared with the XRD results transformed from Figure 5.9. One important result from these calculations is the ability to reproduce the Fe-C distances, which is represented by distances of about 1-1.5 Å. The Fe(110) was not captured by our simulation and it seems to be shifted compared with the experimental results. The main explanation from this approach is the lack of bond representation in the structure. The individual molecules are moved as an entity and the structural changes cannot be represented due to the incapacity to study bond breaking and reorganization.

To capture the Fe(110) peaks from the XRD results it is necessary to carry on simulations where the bonds are allowed to break and reorganize, as well as, capture the molecules evolution with temperature. The direction to follow is run a reactive MD simulation, by using reaction force field (ReaxFF) [168] as potential.

This method employs a smooth transition from non-bonded to single, double, and triple bonded systems by employing a bond length / bond order relationship. Bond orders updated per iteration. Moreover, the connectivity interactions (valence and torsion angles) are dependent on bond-order, such that energy contributions disappear upon bond dissociation.

Non-bonded interactions (van der Waals, Coulomb) are calculated between every atom pair. Excessive close-range non-bonded interactions are avoided by shielding. Geometry-dependent charge calculation scheme that accounts for polarization effects [168].

The current development of the ReaxFF does not include Fe interactions. To be able to use this potential is necessary to obtain the Fe interactions from first principle calculations, which is beyond the scope of this research.

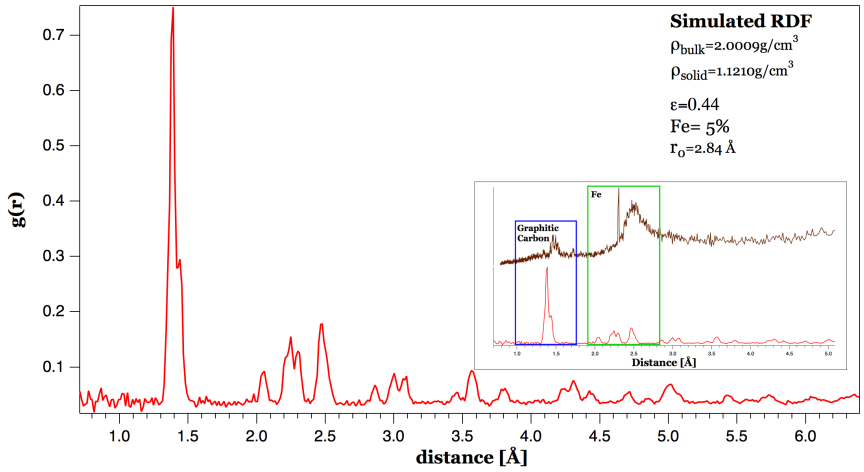


Figure 5.19 Radial distribution of the final configuration.

5.5 Conclusions

Preliminary results were presented using several complementary methods of study of active sites. Mesoscale modeling combined with experimental results showed evidence of both porosity formation and multiple active sites. From the calorimetry results, we revealed the presence of at least two types of adsorption sites. One of these is exothermic and one is endothermic towards oxygen adsorption. XRD results also showed the creation of metal particles and metal oxides for both catalyst studies in this section.

In computational studies, we were capable of representing the iron Porphyrin as a single molecule and as a system. To do it we modify the MM2 parameters presented by Marques for iron Porphyrin and then, extrapolate them to the OPLS-aa force field.

The final density reaches the experimental value as design by the experiment and I was able to reproduce the Fe-C distances with great accuracy. However, the presence of Fe (110) was not accurate and this is likely a result of the potential employed in this approach. Further studies to find reactive potentials (ReaxFF) are necessary to elucidate and validate the radial distribution functions obtained in this study.

GENERAL CONCLUSIONS

At the beginning, I never imagined the challenges that electrocatalysis still presents even for Pt-based systems, where all the electrochemical and characterization evidence has allowed the identification of Pt and Pt-alloy nanoparticles. For platinum systems we can easily test and characterize our possible active sites. Nowadays, multi-dimensional nanoparticle structures are possible and these have shown high activity as the work by Stamenkovic and collaborators at Argonne had shown.

In terms of fundamental theory, the contributions made by Nørskov and Anderson groups allowed us to study activity on catalytic materials based on surface and reactants interactions. Thanks to these works, we know understand the strong correlation between O* and OH* adsorbates on multiple metallic surfaces. CatApp, the catalysis database, created by Nørskov and collaborators, allow us to compare our simulation results and create our own scaling relations for our catalytic materials. Overall, the theory for metallic systems is complex but easily to apply for those systems.

NPMC modeling was another story. The majority of the work in the area has been concentrated in the experimental development of more active and stable materials. Dodelet's and Zelenay's contribution towards synthesis methodologies and characterization techniques has allow the identification of multiple sites. Mossbauer spectroscopy seems to be the most used technique to identify the iron materials and the amount of active sites proposed from these spectra lead to the implementation of microscopic modeling techniques to study ORR and NPMCs.

To date, more than five possible active sites have been proposed. However, most literature reports do not cover the classification based on activity and to date, no micro-kinetic studies have been reported to generate the kinetic volcano plots. Just one macroscopic model has been used by Jaouen to describe NPMCs but it does not relate performance with losses.

Calculating the overpotential losses is the first step to select the proper technique or to recommend a strategy to improve performance when our catalytic material is poorly characterized. For instance, in SAFCs the overpotential

analysis led us to identify clearly the dominance of mass transport effects as the source of losses. For SAFCs, further work on MEA and catalyst ensemble fabrication must be the focus to increase performance.

For NPMCs the results were as expected: the overpotential analysis shows poor activity when compared with Pt. The activation losses were two times larger than for Pt. Our hypothesis based on this analysis led us to think that the dual Tafel slopes may be related with the oxygen adsorption on the active site and will be a function of the surface coverage.

With those two ideas in mind, I decomposed the catalytic material into its more basic components: the Porphyrin, Fe and Fe Porphyrin. My idea was to understand each element's contribution to the activity and corroborate if the final site inherits its behavior from the Porphyrin or from the metallic center. To my surprise, the Fe Porphyrin derives its catalytic behavior from the Porphyrin, showing poor oxygen activation and highlighting the N-H affinity during the ORR process.

Magnetic materials simulations require bigger computational times and represent one of the limitations to expand the simulations results to include water layers as well as oxygen coverage dependence studies. However, I was able to show for the first time why the non-pyrolyzed Fe-porphyrin is not a good catalyst. Therefore, more detailed studies of elements of the reaction mechanism, such as the coverage influence on the oxygen stabilization, are required to confirm these initial findings.

Mesoscale modeling combined with experimental results showed evidence of both porosity formation and multiple active sites. Both techniques illustrate the presence of multiple sites. From the calorimetry results, we revealed the presence of at least two types of adsorption sites. One of these is exothermic and one is endothermic towards oxygen adsorption. XRD results also showed the creation of metal particles and metal oxides for both catalyst studies in this section.

In computational studies, we were capable of representing the iron Porphyrin as a single molecule and as a system. The final density reaches the experimental value and the Fe-C distances are reproduced with great accuracy. However, the presence of Fe(110) was not accurate and this is likely a result of the potential

employed in this approach. Further studies to find reactive potentials (ReaxFF) are necessary to elucidate and validate the radial distribution functions obtained in this study.

REFERENCES

[1] I.E.L. Stephens, A.S. Bondarenko, U. Gronbjerg, J. Rossmeisl, I. Chorkendorff, Understanding the electrocatalysis of oxygen reduction on platinum and its alloys, Energy & Environmental Science, 5 (2012) 6744-6762.

[2] D. van der Vliet, C. Wang, M. Debe, R. Atanasoski, N.M. Markovic, V.R. Stamenkovic, Platinum-alloy nanostructured thin film catalysts for the oxygen reduction reaction, Electrochimica Acta, 56 (2011) 8695-8699.

[3] H.A. Gasteiger, S.S. Kocha, B. Sompalli, F.T. Wagner, Activity benchmarks and requirements for Pt, Pt-alloy, and non-Pt oxygen reduction catalysts for PEMFCs, Applied Catalysis B: Environmental, 56 (2005) 9-35.

[4] S. Mukerjee, S. Srinivasan, M.P. Soriaga, J. McBreen, Role of Structural and Electronic Properties of Pt and Pt Alloys on Electrocatalysis of Oxygen Reduction: An In Situ XANES and EXAFS Investigation, Journal of The Electrochemical Society, 142 (1995) 1409-1422.

[5] C.M. Pedersen, M. Escudero-Escribano, A. Velázquez-Palenzuela, L.H. Christensen, I. Chorkendorff, I.E.L. Stephens, Benchmarking Pt-based electrocatalysts for low temperature fuel cell reactions with the rotating disk electrode: oxygen reduction and hydrogen oxidation in the presence of CO (review article), Electrochimica Acta, 179 (2015) 647-657.

[6] C. Chen, Y. Kang, Z. Huo, Z. Zhu, W. Huang, H.L. Xin, J.D. Snyder, D. Li, J.A. Herron, M. Mavrikakis, M. Chi, K.L. More, Y. Li, N.M. Markovic, G.A. Somorjai, P. Yang, V.R. Stamenkovic, Highly Crystalline Multimetallic Nanoframes with Three-Dimensional Electrocatalytic Surfaces, Science, 343 (2014) 1339-1343.

[7] F. Jaouen, E. Proietti, M. Lefevre, R. Chenitz, J.-P. Dodelet, G. Wu, H.T. Chung, C.M. Johnston, P. Zelenay, Recent advances in non-precious metal catalysis for oxygen-reduction reaction in polymer electrolyte fuel cells, Energy & Environmental Science, 4 (2011) 114-130.

[8] S. Yuan, G. Goenaga, L. Grabstanowicz, J. Shui, C. Chen, S. Commet, B. Reprogle, D.-J. Liu, New Approach to High-Efficiency Non-PGM Catalysts Using Rationally Designed Porous Organic Polymers, ECS Transactions, 58 (2013) 1671-1680.

[9] S. Ma, G.A. Goenaga, A.V. Call, D.-J. Liu, Cobalt Imidazolate Framework as Precursor for Oxygen Reduction Reaction Electrocatalysts, Chemistry – A European Journal, 17 (2011) 2063-2067.

[10] D.-J. Liu, G. Goenaga, S. Ma, S. Yuan, J. Shui, New Approaches to Non-PGM Catalysts through Rational Design, ECS Transactions, 30 (2011) 97-104.

[11] G.A. Goenaga, J. Brooksbank, C. Dabke, A. Belapure, A. Papandrew, S. Foister, T.A. Zawodzinski, Synthesis and Electrochemical Characterization of Co, Cu, Fe, Ni and Mn-Based Catalysts for ORR in PEM Fuel Cells, ECS Transactions, 50 (2013) 1749-1757.

[12] E. Proietti, F. Jaouen, M. Lefèvre, N. Larouche, J. Tian, J. Herranz, J.-P. Dodelet, Iron-based cathode catalyst with enhanced power density in polymer electrolyte membrane fuel cells, Nat Commun, 2 (2011) 416.

[13] A. Morozan, F. Jaouen, Metal organic frameworks for electrochemical applications, Energy & Environmental Science, 5 (2012) 9269-9290.
[14] G. Liu, X. Li, P. Ganesan, B.N. Popov, Development of non-precious metal oxygen-reduction catalysts for PEM fuel cells based on N-doped ordered porous carbon, Applied Catalysis B: Environmental, 93 (2009) 156-165.
[15] M. Lefèvre, E. Proietti, F. Jaouen, J.-P. Dodelet, Iron-Based Catalysts with Improved Oxygen Reduction Activity in Polymer Electrolyte Fuel Cells, Science, 324 (2009) 71-74.
[16] W. Seeliger, A. Hamnett, Novel electrocatalysts for oxygen reduction, Electrochimica Acta, 37 (1992) 763-765.
[17] R. Jasinski, A New Fuel Cell Cathode Catalyst, Nature, 201 (1964) 1212-1213.
[18] P. Ross, F. Watner, Prospects for the development of non-noble metal catalysts for hydrogen-air fuel cells, in, Lawrence Berkeley Laboratory, 1982.
[19] F. Jaouen, J. Herranz, M. Lefèvre, J.-P. Dodelet, U.I. Kramm, I. Herrmann, P. Bogdanoff, J. Maruyama, T. Nagaoka, A. Garsuch, J.R. Dahn, T. Olson, S. Pylypenko, P. Atanassov, E.A. Ustinov, Cross-Laboratory Experimental Study of Non-Noble-Metal Electrocatalysts for the Oxygen Reduction Reaction, ACS Applied Materials & Interfaces, 1 (2009) 1623-1639.
[20] M. Ferrandon, X. Wang, A.J. Kropf, D.J. Myers, G. Wu, C.M. Johnston, P. Zelenay, Stability of iron species in heat-treated polyaniline–iron–carbon polymer electrolyte fuel cell cathode catalysts, Electrochimica Acta, 110 (2013) 282-291.
[21] M. Yuasa, A. Yamaguchi, H. Itsuki, K. Tanaka, M. Yamamoto, K. Oyaizu, Modifying Carbon Particles with Polypyrrole for Adsorption of Cobalt Ions as Electrocatatytic Site for Oxygen Reduction, Chemistry of Materials, 17 (2005) 4278-4281.
[22] W.M. Millán, M.A. Smit, Study of electrocatalysts for oxygen reduction based on electroconducting polymer and nickel, Journal of Applied Polymer Science, 112 (2009) 2959-2967.
[23] R. Bashyam, P. Zelenay, A class of non-precious metal composite catalysts for fuel cells, Nature, 443 (2006) 63-66.
[24] G. Wu, K.L. More, C.M. Johnston, P. Zelenay, High-Performance Electrocatalysts for Oxygen Reduction Derived from Polyaniline, Iron, and Cobalt, Science, 332 (2011) 443-447.
[25] M. Ferrandon, A.J. Kropf, D.J. Myers, K. Artyushkova, U. Kramm, P. Bogdanoff, G. Wu, C.M. Johnston, P. Zelenay, Multitechnique Characterization of a Polyaniline–Iron–Carbon Oxygen Reduction Catalyst, The Journal of Physical Chemistry C, 116 (2012) 16001-16013.
[26] C.W.B. Bezerra, L. Zhang, K. Lee, H. Liu, A.L.B. Marques, E.P. Marques, H. Wang, J. Zhang, A review of Fe–N/C and Co–N/C catalysts for the oxygen reduction reaction, Electrochimica Acta, 53 (2008) 4937-4951.
[27] F. Jaouen, M. Lefèvre, J.-P. Dodelet, M. Cai, Heat-Treated Fe/N/C Catalysts for O2 Electroreduction: Are Active Sites Hosted in Micropores?, The Journal of Physical Chemistry B, 110 (2006) 5553-5558.
[28] T.E. Springer, T.A. Zawodzinski, S. Gottesfeld, Polymer Electrolyte Fuel Cell Model, Journal of The Electrochemical Society, 138 (1991) 2334-2342.

[29] C. Song, J. Zhang, Electrocatalytic Oxygen Reduction Reaction, in: J. Zhang (Ed.) PEM Fuel Cell Electrocatalysts and Catalyst Layers, Springer London, 2008, pp. 89-134.
[30] T.E. Springer, M.S. Wilson, S. Gottesfeld, Modeling and Experimental Diagnostics in Polymer Electrolyte Fuel Cells, Journal of The Electrochemical Society, 140 (1993) 3513-3526.
[31] X.-S. Wang, M. Chrzanowski, D. Yuan, B.S. Sweeting, S. Ma, Covalent Heme Framework as a Highly Active Heterogeneous Biomimetic Oxidation Catalyst, Chemistry of Materials, 26 (2014) 1639-1644.
[32] J.G. Lee, Computational Materials Science An Introduction, in: T.F. Group (Ed.) Computational Materials Science An Introduction, CRC Press, 2012, pp. 1-8.
[33] J.G. Lee, Computational Materials Science An Introduction, in: T.F. Group (Ed.) Computational Materials Science An Introduction, CRC Press, 2012, pp. 109-144.
[34] J.K. Nørskov, F. Studt, F. Abild-Pedersen, T. Bligaard, Surface Electrocatalysis, in: Fundamental Concepts in Heterogeneous Catalysis, John Wiley & Sons, Inc, 2014, pp. 155-174.
[35] J.K. Nørskov, F. Studt, F. Abild-Pedersen, T. Bligaard, The Potential Energy Diagram, in: Fundamental Concepts in Heterogeneous Catalysis, John Wiley & Sons, Inc, 2014, pp. 6-25.
[36] J.K. Nørskov, F. Studt, F. Abild-Pedersen, T. Bligaard, Activity and Selectivity Maps, in: Fundamental Concepts in Heterogeneous Catalysis, John Wiley & Sons, Inc, 2014, pp. 97-113.
[37] G. Mills, H. Jónsson, G.K. Schenter, Reversible work transition state theory: application to dissociative adsorption of hydrogen, Surface Science, 324 (1995) 305-337.
[38] G. Henkelman, B.P. Uberuaga, H. Jónsson, A climbing image nudged elastic band method for finding saddle points and minimum energy paths, The Journal of Chemical Physics, 113 (2000) 9901-9904.
[39] Y. Kanai, A. Tilocca, A. Selloni, R. Car, First-principles string molecular dynamics: An efficient approach for finding chemical reaction pathways, The Journal of Chemical Physics, 121 (2004) 3359-3367.
[40] D. Sheppard, R. Terrell, G. Henkelman, Optimization methods for finding minimum energy paths, The Journal of Chemical Physics, 128 (2008) 134106.
[1] F. Jaouen, E. Proietti, M. Lefevre, R. Chenitz, J.-P. Dodelet, G. Wu, H.T. Chung, C.M. Johnston, P. Zelenay, Recent advances in non-precious metal catalysis for oxygen-reduction reaction in polymer electrolyte fuel cells, Energy & Environmental Science, 4 (2011) 114-130.
[2] F. Charreteur, F. Jaouen, S. Ruggeri, J.-P. Dodelet, Fe/N/C non-precious catalysts for PEM fuel cells: Influence of the structural parameters of pristine commercial carbon blacks on their activity for oxygen reduction, Electrochimica Acta, 53 (2008) 2925-2938.
[3] G. Wu, Z. Chen, K. Artyushkova, F.H. Garzon, P. Zelenay, Polyaniline-derived Non-Precious Catalyst for the Polymer Electrolyte Fuel Cell Cathode, ECS Transactions, 16 (2008) 159-170.

[4] G.A. Goenaga, J. Brooksbank, C. Dabke, A. Belapure, A. Papandrew, S. Foister, T.A. Zawodzinski, Synthesis and Electrochemical Characterization of Co, Cu, Fe, Ni and Mn-Based Catalysts for ORR in PEM Fuel Cells, ECS Transactions, 50 (2013) 1749-1757.
[5] M. Ferrandon, X. Wang, A.J. Kropf, D.J. Myers, G. Wu, C.M. Johnston, P. Zelenay, Stability of iron species in heat-treated polyaniline–iron–carbon polymer electrolyte fuel cell cathode catalysts, Electrochimica Acta, 110 (2013) 282-291.
[6] F. Jaouen, V. Goellner, M. Lefèvre, J. Herranz, E. Proietti, J.P. Dodelet, Oxygen reduction activities compared in rotating-disk electrode and proton exchange membrane fuel cells for highly active FeNC catalysts, Electrochimica Acta, 87 (2013) 619-628.
[7] D. van der Vliet, C. Wang, M. Debe, R. Atanasoski, N.M. Markovic, V.R. Stamenkovic, Platinum-alloy nanostructured thin film catalysts for the oxygen reduction reaction, Electrochimica Acta, 56 (2011) 8695-8699.
[8] J. Larminie, A. Dicks, Fuel Cell Systems Explained, in, John Wiley & Sons Ltd, 2003.
[9] A.Z. Weber, J. Newman, Modeling Transport in Polymer-Electrolyte Fuel Cells, Chemical Reviews, 104 (2004) 4679-4726.
[10] U. Tylus, Q. Jia, K. Strickland, N. Ramaswamy, A. Serov, P. Atanassov, S. Mukerjee, Elucidating Oxygen Reduction Active Sites in Pyrolyzed Metal–Nitrogen Coordinated Non-Precious-Metal Electrocatalyst Systems, The Journal of Physical Chemistry C, 118 (2014) 8999-9008.
[11] E. Yeager, Electrocatalysts for O2 reduction, Electrochimica Acta, 29 (1984) 1527-1537.
[12] R.R. Adžić, J.X. Wang, Configuration and Site of O2 Adsorption on the Pt(111) Electrode Surface, The Journal of Physical Chemistry B, 102 (1998) 8988-8993.
[13] H.S. Wroblowa, P. Yen Chi, G. Razumney, Electroreduction of oxygen, Journal of Electroanalytical Chemistry and Interfacial Electrochemistry, 69 (1976) 195-201.
[14] E. Yeager, Dioxygen electrocatalysis: mechanisms in relation to catalyst structure, Journal of Molecular Catalysis, 38 (1986) 5-25.
[15] A. Damjanovic, V. Brusic, Electrode kinetics of oxygen reduction on oxide-free platinum electrodes, Electrochimica Acta, 12 (1967) 615-628.
[16] X. Chen, D. Xia, Z. Shi, J. Zhang, Theoretical Study of Oxygen Reduction Reaction Catalysts: From Pt to Non-precious Metal Catalysts, in: M. Shao (Ed.) Electrocatalysis in Fuel Cells: A Non- and Low- Platinum Approach, Springer London, London, 2013, pp. 339-373.
[17] A.B. Anderson, T.V. Albu, Catalytic Effect of Platinum on Oxygen Reduction An Ab Initio Model Including Electrode Potential Dependence, Journal of The Electrochemical Society, 147 (2000) 4229-4238.
[18] A.B. Anderson, O2 reduction and CO oxidation at the Pt-electrolyte interface. The role of H2O and OH adsorption bond strengths, Electrochimica Acta, 47 (2002) 3759-3763.

[19] R.A. Sidik, A.B. Anderson, Density functional theory study of O2 electroreduction when bonded to a Pt dual site, Journal of Electroanalytical Chemistry, 528 (2002) 69-76.
[20] A.B. Anderson, Theory at the electrochemical interface: reversible potentials and potential-dependent activation energies, Electrochimica Acta, 48 (2003) 3743-3749.
[21] A.B. Anderson, J. Roques, S. Mukerjee, V.S. Murthi, N.M. Markovic, V. Stamenkovic, Activation Energies for Oxygen Reduction on Platinum Alloys: Theory and Experiment, The Journal of Physical Chemistry B, 109 (2005) 1198-1203.
[22] A.B. Anderson, Y. Cai, R.A. Sidik, D.B. Kang, Advancements in the local reaction center electron transfer theory and the transition state structure in the first step of oxygen reduction over platinum, Journal of Electroanalytical Chemistry, 580 (2005) 17-22.
[23] A.B. Anderson, Insights into electrocatalysis, Physical Chemistry Chemical Physics, 14 (2012) 1330-1338.
[24] J.K. Nørskov, J. Rossmeisl, A. Logadottir, L. Lindqvist, J.R. Kitchin, T. Bligaard, H. Jónsson, Origin of the Overpotential for Oxygen Reduction at a Fuel-Cell Cathode, The Journal of Physical Chemistry B, 108 (2004) 17886-17892.
[25] M.T.M. Koper, Thermodynamic theory of multi-electron transfer reactions: Implications for electrocatalysis, Journal of Electroanalytical Chemistry, 660 (2011) 254-260.
[26] J. Rossmeisl, A. Logadottir, J.K. Nørskov, Electrolysis of water on (oxidized) metal surfaces, Chemical Physics, 319 (2005) 178-184.
[27] F. Abild-Pedersen, J. Greeley, F. Studt, J. Rossmeisl, T.R. Munter, P.G. Moses, E. Skúlason, T. Bligaard, J.K. Nørskov, Scaling Properties of Adsorption Energies for Hydrogen-Containing Molecules on Transition-Metal Surfaces, Physical Review Letters, 99 (2007) 016105.
[28] A.J. Bard, L.R. Faulkner, Electrochemical Methods: fundamentals and applications, Second ed., John Wiley & Sons, Inc, 2001.
[29] C. Song, J. Zhang, Electrocatalytic Oxygen Reduction Reaction, in: J. Zhang (Ed.) PEM Fuel Cell Electrocatalysts and Catalyst Layers, Springer London, 2008, pp. 89-134.
[30] J.X. Wang, F.A. Uribe, T.E. Springer, J. Zhang, R.R. Adzic, Intrinsic kinetic equation for oxygen reduction reaction in acidic media: the double Tafel slope and fuel cell applications, Faraday Discussions, 140 (2009) 347-362.
[31] A. Holewinski, S. Linic, Elementary Mechanisms in Electrocatalysis: Revisiting the ORR Tafel Slope, Journal of The Electrochemical Society, 159 (2012) H864-H870.
[32] C. Song, Y. Tang, J.L. Zhang, J. Zhang, H. Wang, J. Shen, S. McDermid, J. Li, P. Kozak, PEM fuel cell reaction kinetics in the temperature range of 23–120°C, Electrochimica Acta, 52 (2007) 2552-2561.
[33] I.E.L. Stephens, A.S. Bondarenko, U. Gronbjerg, J. Rossmeisl, I. Chorkendorff, Understanding the electrocatalysis of oxygen reduction on platinum and its alloys, Energy & Environmental Science, 5 (2012) 6744-6762.
[34] A. Wieckowski, M. Neurock, Contrast and Synergy between Electrocatalysis and Heterogeneous Catalysis, Advances in Physical Chemistry, (2011).

[35] S. Wang, V. Petzold, V. Tripkovic, J. Kleis, J.G. Howalt, E. Skulason, E.M. Fernandez, B. Hvolbaek, G. Jones, A. Toftelund, H. Falsig, M. Bjorketun, F. Studt, F. Abild-Pedersen, J. Rossmeisl, J.K. Norskov, T. Bligaard, Universal transition state scaling relations for (de)hydrogenation over transition metals, Physical Chemistry Chemical Physics, 13 (2011) 20760-20765.
[36] V. Viswanathan, H.A. Hansen, J. Rossmeisl, J.K. Nørskov, Universality in Oxygen Reduction Electrocatalysis on Metal Surfaces, ACS Catalysis, 2 (2012) 1654-1660.
[37] H.A. Gasteiger, S.S. Kocha, B. Sompalli, F.T. Wagner, Activity benchmarks and requirements for Pt, Pt-alloy, and non-Pt oxygen reduction catalysts for PEMFCs, Applied Catalysis B: Environmental, 56 (2005) 9-35.
[38] S. Mukerjee, S. Srinivasan, M.P. Soriaga, J. McBreen, Role of Structural and Electronic Properties of Pt and Pt Alloys on Electrocatalysis of Oxygen Reduction: An In Situ XANES and EXAFS Investigation, Journal of The Electrochemical Society, 142 (1995) 1409-1422.
[39] C.M. Pedersen, M. Escudero-Escribano, A. Velázquez-Palenzuela, L.H. Christensen, I. Chorkendorff, I.E.L. Stephens, Benchmarking Pt-based electrocatalysts for low temperature fuel cell reactions with the rotating disk electrode: oxygen reduction and hydrogen oxidation in the presence of CO (review article), Electrochimica Acta, 179 (2015) 647-657.
[40] C. Chen, Y. Kang, Z. Huo, Z. Zhu, W. Huang, H.L. Xin, J.D. Snyder, D. Li, J.A. Herron, M. Mavrikakis, M. Chi, K.L. More, Y. Li, N.M. Markovic, G.A. Somorjai, P. Yang, V.R. Stamenkovic, Highly Crystalline Multimetallic Nanoframes with Three-Dimensional Electrocatalytic Surfaces, Science, 343 (2014) 1339-1343.
[41] S. Yuan, G. Goenaga, L. Grabstanowicz, J. Shui, C. Chen, S. Commet, B. Reprogle, D.-J. Liu, New Approach to High-Efficiency Non-PGM Catalysts Using Rationally Designed Porous Organic Polymers, ECS Transactions, 58 (2013) 1671-1680.
[42] S. Ma, G.A. Goenaga, A.V. Call, D.-J. Liu, Cobalt Imidazolate Framework as Precursor for Oxygen Reduction Reaction Electrocatalysts, Chemistry – A European Journal, 17 (2011) 2063-2067.
[43] D.-J. Liu, G. Goenaga, S. Ma, S. Yuan, J. Shui, New Approaches to Non-PGM Catalysts through Rational Design, ECS Transactions, 30 (2011) 97-104.
[44] E. Proietti, F. Jaouen, M. Lefèvre, N. Larouche, J. Tian, J. Herranz, J.-P. Dodelet, Iron-based cathode catalyst with enhanced power density in polymer electrolyte membrane fuel cells, Nat Commun, 2 (2011) 416.
[45] A. Morozan, F. Jaouen, Metal organic frameworks for electrochemical applications, Energy & Environmental Science, 5 (2012) 9269-9290.
[46] G. Liu, X. Li, P. Ganesan, B.N. Popov, Development of non-precious metal oxygen-reduction catalysts for PEM fuel cells based on N-doped ordered porous carbon, Applied Catalysis B: Environmental, 93 (2009) 156-165.
[47] M. Lefèvre, E. Proietti, F. Jaouen, J.-P. Dodelet, Iron-Based Catalysts with Improved Oxygen Reduction Activity in Polymer Electrolyte Fuel Cells, Science, 324 (2009) 71-74.
[48] W. Seeliger, A. Hamnett, Novel electrocatalysts for oxygen reduction, Electrochimica Acta, 37 (1992) 763-765.

[49] T. Li, P.B. Balbuena, Computational Studies of the Interactions of Oxygen with Platinum Clusters, The Journal of Physical Chemistry B, 105 (2001) 9943-9952.
[50] B.C. Han, C.R. Miranda, G. Ceder, Effect of particle size and surface structure on adsorption of O and OH on platinum nanoparticles: A first-principles study, Physical Review B, 77 (2008) 075410.
[51] Y. Xu, A.V. Ruban, M. Mavrikakis, Adsorption and Dissociation of O2 on Pt–Co and Pt–Fe Alloys, Journal of the American Chemical Society, 126 (2004) 4717-4725.
[52] T. Bligaard, J.K. Nørskov, Ligand effects in heterogeneous catalysis and electrochemistry, Electrochimica Acta, 52 (2007) 5512-5516.
[53] H.A. Hansen, V. Viswanathan, J.K. Nørskov, Unifying Kinetic and Thermodynamic Analysis of 2 e– and 4 e– Reduction of Oxygen on Metal Surfaces, The Journal of Physical Chemistry C, 118 (2014) 6706-6718.
[54] J. Greeley, T.F. Jaramillo, J. Bonde, I. Chorkendorff, J.K. Norskov, Computational high-throughput screening of electrocatalytic materials for hydrogen evolution, Nat Mater, 5 (2006) 909-913.
[55] V.R. Stamenkovic, B. Fowler, B.S. Mun, G. Wang, P.N. Ross, C.A. Lucas, N.M. Marković, Improved Oxygen Reduction Activity on Pt₃Ni(111) via Increased Surface Site Availability, Science, 315 (2007) 493-497.
[56] R. Jasinski, A New Fuel Cell Cathode Catalyst, Nature, 201 (1964) 1212-1213.
[57] P. Ross, F. Watner, Prospects for the development of non-noble metal catalysts for hydrogen-air fuel cells, in, Lawrence Berkeley Laboratory, 1982.
[58] F. Jaouen, J. Herranz, M. Lefèvre, J.-P. Dodelet, U.I. Kramm, I. Herrmann, P. Bogdanoff, J. Maruyama, T. Nagaoka, A. Garsuch, J.R. Dahn, T. Olson, S. Pylypenko, P. Atanassov, E.A. Ustinov, Cross-Laboratory Experimental Study of Non-Noble-Metal Electrocatalysts for the Oxygen Reduction Reaction, ACS Applied Materials & Interfaces, 1 (2009) 1623-1639.
[59] M. Yuasa, A. Yamaguchi, H. Itsuki, K. Tanaka, M. Yamamoto, K. Oyaizu, Modifying Carbon Particles with Polypyrrole for Adsorption of Cobalt Ions as Electrocatatytic Site for Oxygen Reduction, Chemistry of Materials, 17 (2005) 4278-4281.
[60] W.M. Millán, M.A. Smit, Study of electrocatalysts for oxygen reduction based on electroconducting polymer and nickel, Journal of Applied Polymer Science, 112 (2009) 2959-2967.
[61] R. Bashyam, P. Zelenay, A class of non-precious metal composite catalysts for fuel cells, Nature, 443 (2006) 63-66.
[62] G. Wu, K.L. More, C.M. Johnston, P. Zelenay, High-Performance Electrocatalysts for Oxygen Reduction Derived from Polyaniline, Iron, and Cobalt, Science, 332 (2011) 443-447.
[63] M. Ferrandon, A.J. Kropf, D.J. Myers, K. Artyushkova, U. Kramm, P. Bogdanoff, G. Wu, C.M. Johnston, P. Zelenay, Multitechnique Characterization of a Polyaniline–Iron–Carbon Oxygen Reduction Catalyst, The Journal of Physical Chemistry C, 116 (2012) 16001-16013.
[64] C.W.B. Bezerra, L. Zhang, K. Lee, H. Liu, A.L.B. Marques, E.P. Marques, H. Wang, J. Zhang, A review of Fe–N/C and Co–N/C catalysts for the oxygen reduction reaction, Electrochimica Acta, 53 (2008) 4937-4951.

[65] F. Jaouen, M. Lefèvre, J.-P. Dodelet, M. Cai, Heat-Treated Fe/N/C Catalysts for O2 Electroreduction: Are Active Sites Hosted in Micropores?, The Journal of Physical Chemistry B, 110 (2006) 5553-5558.
[66] F. Jaouen, J.-P. Dodelet, Non-Noble Electrocatalysts for O2 Reduction: How Does Heat Treatment Affect Their Activity and Structure? Part I. Model for Carbon Black Gasification by NH3: Parametric Calibration and Electrochemical Validation, The Journal of Physical Chemistry C, 111 (2007) 5963-5970.
[67] F. Jaouen, A.M. Serventi, M. Lefèvre, J.-P. Dodelet, P. Bertrand, Non-Noble Electrocatalysts for O2 Reduction: How Does Heat Treatment Affect Their Activity and Structure? Part II. Structural Changes Observed by Electron Microscopy, Raman, and Mass Spectroscopy, The Journal of Physical Chemistry C, 111 (2007) 5971-5976.
[68] L. Wu, Y. Nabae, S. Moriya, K. Matsubayashi, N.M. Islam, S. Kuroki, M.-a. Kakimoto, J.-i. Ozaki, S. Miyata, Retracted article: Pt-free cathode catalysts prepared via multi-step pyrolysis of Fe phthalocyanine and phenolic resin for fuel cells, Chemical Communications, 46 (2010) 6377-6379.
[69] H. Lv, D. Li, D. Strmcnik, A.P. Paulikas, N.M. Markovic, V.R. Stamenkovic, Recent advances in the design of tailored nanomaterials for efficient oxygen reduction reaction, Nano Energy, 29 (2016) 149-165.
[70] S. Kattel, P. Atanassov, B. Kiefer, A density functional theory study of oxygen reduction reaction on non-PGM Fe-Nx-C electrocatalysts, Physical Chemistry Chemical Physics, 16 (2014) 13800-13806.
[71] U.I. Kramm, J. Herranz, N. Larouche, T.M. Arruda, M. Lefevre, F. Jaouen, P. Bogdanoff, S. Fiechter, I. Abs-Wurmbach, S. Mukerjee, J.-P. Dodelet, Structure of the catalytic sites in Fe/N/C-catalysts for O2-reduction in PEM fuel cells, Physical Chemistry Chemical Physics, 14 (2012) 11673-11688.
[72] U.I. Kramm, I. Abs-Wurmbach, I. Herrmann-Geppert, J. Radnik, S. Fiechter, P. Bogdanoff, Influence of the Electron-Density of FeN4-Centers Towards the Catalytic Activity of Pyrolyzed FeTMPPCl-Based ORR-Electrocatalysts, Journal of The Electrochemical Society, 158 (2011) B69-B78.
[73] H. Tributsch, U.I. Koslowski, I. Dorbandt, Experimental and theoretical modeling of Fe-, Co-, Cu-, Mn-based electrocatalysts for oxygen reduction, Electrochimica Acta, 53 (2008) 2198-2209.
[74] A.L. Bouwkamp-Wijnoltz, W. Visscher, J.A.R. van Veen, E. Boellaard, A.M. van der Kraan, S.C. Tang, On Active-Site Heterogeneity in Pyrolyzed Carbon-Supported Iron Porphyrin Catalysts for the Electrochemical Reduction of Oxygen: An In Situ Mössbauer Study, The Journal of Physical Chemistry B, 106 (2002) 12993-13001.
[75] R. Baker, D.P. Wilkinson, J. Zhang, Electrocatalytic activity and stability of substituted iron phthalocyanines towards oxygen reduction evaluated at different temperatures, Electrochimica Acta, 53 (2008) 6906-6919.
[76] J.H. Zagal, Metallophthalocyanines as catalysts in electrochemical reactions, Coordination Chemistry Reviews, 119 (1992) 89-136.
[77] H.-W. Wu, A review of recent development: Transport and performance modeling of PEM fuel cells, Applied Energy, 165 (2016) 81-106.
[78] D.M. Fadzillah, M.I. Rosli, M.Z.M. Talib, S.K. Kamarudin, W.R.W. Daud, Review on microstructure modelling of a gas diffusion layer for proton exchange

membrane fuel cells, Renewable and Sustainable Energy Reviews, 77 (2017) 1001-1009.
[79] T.E. Springer, T.A. Zawodzinski, S. Gottesfeld, Polymer Electrolyte Fuel Cell Model, Journal of The Electrochemical Society, 138 (1991) 2334-2342.
[80] D.M. Bernardi, M.W. Verbrugge, A Mathematical Model of the Solid-Polymer-Electrolyte Fuel Cell, Journal of The Electrochemical Society, 139 (1992) 2477-2491.
[81] T.F. Fuller, J. Newman, Water and Thermal Management in Solid-Polymer-Electrolyte Fuel Cells, Journal of The Electrochemical Society, 140 (1993) 1218-1225.
[82] T.V. Nguyen, R.E. White, A Water and Heat Management Model for Proton-Exchange-Membrane Fuel Cells, Journal of The Electrochemical Society, 140 (1993) 2178-2186.
[83] L. Xu, C. Fang, J. Hu, S. Cheng, J. Li, M. Ouyang, W. Lehnert, Parameter extraction and uncertainty analysis of a proton exchange membrane fuel cell system based on Monte Carlo simulation, International Journal of Hydrogen Energy, 42 (2017) 2309-2326.
[84] Y. Kawagoe, T. Oshima, K. Tomarikawa, T. Tokumasu, T. Koido, S. Yonemura, A study on pressure-driven gas transport in porous media: from nanoscale to microscale, Microfluidics and Nanofluidics, 20 (2016) 162.
[85] C.H. Park, C.H. Lee, M.D. Guiver, Y.M. Lee, Sulfonated hydrocarbon membranes for medium-temperature and low-humidity proton exchange membrane fuel cells (PEMFCs), Progress in Polymer Science, 36 (2011) 1443-1498.
[86] K.-D. Kreuer, S.J. Paddison, E. Spohr, M. Schuster, Transport in Proton Conductors for Fuel-Cell Applications: Simulations, Elementary Reactions, and Phenomenology, Chemical Reviews, 104 (2004) 4637-4678.
[87] C. Wei, Z. Zhao, A. Fisher, J. Zhu, D. Cheng, Theoretical Study on the Structures and Thermal Properties of Ag–Pt–Ni Trimetallic Clusters, Journal of Cluster Science, 27 (2016) 1849-1861.
[88] S. Shin, A.-R. Kim, S. Um, Statistical prediction of fuel cell catalyst effectiveness: Quasi-random nano-structural analysis of carbon sphere-supported platinum catalysts, International Journal of Hydrogen Energy, 41 (2016) 9507-9520.
[89] Y. Kanai, A. Tilocca, A. Selloni, R. Car, First-principles string molecular dynamics: An efficient approach for finding chemical reaction pathways, The Journal of Chemical Physics, 121 (2004) 3359-3367.
[90] M.T.M. Koper, Molecular-Level Modeling of Anode and Cathode Electrocatalysis for PEM Fuel Cells, in: S.J. Paddison, K.S. Promislow (Eds.) Device and Materials Modeling in PEM Fuel Cells, Springer New York, New York, NY, 2009, pp. 485-508.
[91] A. Wieckowski, M. Neurock, Contrast and Synergy between Electrocatalysis and Heterogeneous Catalysis, Advances in Physical Chemistry, 2011 (2011) 18.
[92] J. Rossmeisl, E. Skúlason, M.E. Björketun, V. Tripkovic, J.K. Nørskov, Modeling the electrified solid–liquid interface, Chemical Physics Letters, 466 (2008) 68-71.

[93] D. Cao, G.Q. Lu, A. Wieckowski, S.A. Wasileski, M. Neurock, Mechanisms of Methanol Decomposition on Platinum: A Combined Experimental and ab Initio Approach, The Journal of Physical Chemistry B, 109 (2005) 11622-11633.
[94] R.A. van Santen, M. Neurock, Mechanisms for Aqueous Phase Heterogeneous Catalysis and Electrocatalysis; A Comparison with Heterogeneous Catalytic Reactions, in: Molecular Heterogeneous Catalysis, Wiley-VCH Verlag GmbH & Co. KGaA, 2007, pp. 267-312.
[95] J.K. Nørskov, F. Studt, F. Abild-Pedersen, T. Bligaard, Surface Electrocatalysis, in: Fundamental Concepts in Heterogeneous Catalysis, John Wiley & Sons, Inc, 2014, pp. 155-174.
[96] A. Vojvodic, J.K. Nørskov, New design paradigm for heterogeneous catalysts, National Science Review, 2 (2015) 140-143.
[97] S.M. Haile, C.R.I. Chisholm, K. Sasaki, D.A. Boysen, T. Uda, Solid acid proton conductors: from laboratory curiosities to fuel cell electrolytes, Faraday Discussions, 134 (2007) 17-39.
[98] A.B. Papandrew, R.W. Atkinson Iii, R.R. Unocic, T.A. Zawodzinski, Ruthenium as a CO-tolerant hydrogen oxidation catalyst for solid acid fuel cells, Journal of Materials Chemistry A, 3 (2015) 3984-3987.
[99] A.B. Papandrew, D.L. Wilson, N. M. Cantillo, S. Hawks, R.W. Atkinson, G.A. Goenaga, T.A. Zawodzinski, Electrochemical Hydrogen Separation via Solid Acid Membranes, Journal of The Electrochemical Society, 161 (2014) F679-F685.
[100] D.B. C.RI Chisholm, AB Papandrew, SK Zecevic, SY Cha, KA Sasaki, A Varga, KP Glapis, SM Haile, From Laboratory Breakthrough to Technological Realization: The Development Path for Solid Acid Fuel Cells, The Electrochemical Society interface, 18 (2009) 53 - 59.
[101] T.E. Springer, M.S. Wilson, S. Gottesfeld, Modeling and Experimental Diagnostics in Polymer Electrolyte Fuel Cells, Journal of The Electrochemical Society, 140 (1993) 3513-3526.
[102] A. Ikeda, S.M. Haile, The thermodynamics and kinetics of the dehydration of CsH_2PO_4 studied in the presence of SiO_2, Solid State Ionics, 213 (2012) 63-71.
[103] J. Bear, Y. Bachmat, Transport Phenomena in Porous Media — Basic Equations, in: J. Bear, M.Y. Corapcioglu (Eds.) Fundamentals of Transport Phenomena in Porous Media, Springer Netherlands, Dordrecht, 1984, pp. 3-61.
[104] T.C. Choy, Chapter 1. Essentials, in: Effective Medium Theory : Principles and Applications, Oxford Science Publications, 1999, pp. 10-23.
[105] H.B. Mann, D.R. Whitney, On a Test of Whether one of Two Random Variables is Stochastically Larger than the Other, The Annals of Mathematical Statistics, 18 (1947) 50-60.
[106] J.W. Pratt, Concepts of Nonparametric Theory, in: J.D. Gibbons, SpringerLink (Eds.), New York, NY : Springer New York, 1981, pp. 318-336.
[107] A.B. Papandrew, C.R.I. Chisholm, S.K. Zecevic, G.M. Veith, T.A. Zawodzinski, Activity and Evolution of Vapor Deposited Pt-Pd Oxygen Reduction Catalysts for Solid Acid Fuel Cells, Journal of The Electrochemical Society, 160 (2013) F175-F182.
[108] A.B. Papandrew, C.R.I. Chisholm, R.A. Elgammal, M.M. Özer, S.K. Zecevic, Advanced Electrodes for Solid Acid Fuel Cells by Platinum Deposition on CsH_2PO_4, Chemistry of Materials, 23 (2011) 1659-1667.

[109] A.B. Papandrew, S.S. John, R.A. Elgammal, D.L. Wilson, R.W. Atkinson, J.S. Lawton, T.M. Arruda, T.A. Zawodzinski, Vapor-Deposited Pt and Pd-Pt Catalysts for Solid Acid Fuel Cells: Short Range Structure and Interactions with the CsH2PO4 Electrolyte, Journal of The Electrochemical Society, 163 (2016) F464-F469.
[110] S. Arisetty, X. Wang, R. Ahluwalia, R. Mukundan, R. Borup, J. Davey, D. Langlois, F. Gambini, O.Y. Polevaya, S. Blanchet, Effect of Platinum Loading on Catalyst Stability under Cyclic Potentials, ECS Transactions, 41 (2011) 797-809.
[111] J.A.R. van Veen, H.A. Colijn, J.F. van Baar, On the effect of a heat treatment on the structure of carbon-supported metalloporphyrins and phthalocyanines, Electrochimica Acta, 33 (1988) 801-804.
[112] K. Wiesener, N4-chelates as electrocatalyst for cathodic oxygen reduction, Electrochimica Acta, 31 (1986) 1073-1078.
[113] J.-P. Dodelet, The Controversial Role of the Metal in Fe- or Co-Based Electrocatalysts for the Oxygen Reduction Reaction in Acid Medium, in: M. Shao (Ed.) Electrocatalysis in Fuel Cells: A Non- and Low- Platinum Approach, Springer London, London, 2013, pp. 271-338.
[114] B. van Wingerden, J.A.R. van Veen, C.T.J. Mensch, An extended X-ray absorption fine structure study of heat-treated cobalt porphyrin catalysts supported on active carbon, Journal of the Chemical Society, Faraday Transactions 1: Physical Chemistry in Condensed Phases, 84 (1988) 65-74.
[115] D. Scherson, A.A. Tanaka, S.L. Gupta, D. Tryk, C. Fierro, R. Holze, E.B. Yeager, R.P. Lattimer, Transition metal macrocycles supported on high area carbon: Pyrolysis—mass spectrometry studies, Electrochimica Acta, 31 (1986) 1247-1258.
[116] S. Gupta, D. Tryk, I. Bae, W. Aldred, E. Yeager, Heat-treated polyacrylonitrile-based catalysts for oxygen electroreduction, J Appl Electrochem, 19 (1989) 19-27.
[117] B. Nikolic, R.R. Adzic, E.B. Yeager, Reflectance spectra of monolayers of tetrasulfonated transition metal phthalocyanines adsorbed on electrode surfaces, Journal of Electroanalytical Chemistry and Interfacial Electrochemistry, 103 (1979) 281-287.
[118] A. Fuhrmann, K. Wiesener, I. Iliev, S. Gamburzev, A. Kaisheva, A contribution to the characterization of heat-treated electrocatalytically active tetramethoxy-phenylporphyrinato-cobalt-II, Journal of Power Sources, 6 (1981) 69-81.
[119] K.-D. Kreuer, Fuel Cells: Selected Entries from the Encyclopedia of Sustainability Science and Technology, Springer, Sttutgart, Germany, 2013.
[120] X.-S. Wang, M. Chrzanowski, D. Yuan, B.S. Sweeting, S. Ma, Covalent Heme Framework as a Highly Active Heterogeneous Biomimetic Oxidation Catalyst, Chemistry of Materials, 26 (2014) 1639-1644.
[121] N.M. Cantillo, G.A. Goenaga, W. Gao, K. Williams, C.A. Neal, S. Ma, K.L. More, T.A. Zawodzinski, Investigation of a microporous iron(iii) porphyrin framework derived cathode catalyst in PEM fuel cells, Journal of Materials Chemistry A, 4 (2016) 15621-15630.

[122] J. Zhang, Y. Tang, C. Song, J. Zhang, H. Wang, PEM fuel cell open circuit voltage (OCV) in the temperature range of 23°C to 120°C, Journal of Power Sources, 163 (2006) 532-537.
[123] L. Zhang, C. Ma, S. Mukerjee, Oxygen permeation studies on alternative proton exchange membranes designed for elevated temperature operation, Electrochimica Acta, 48 (2003) 1845-1859.
[124] D.E. Bikiel, L. Boechi, L. Capece, A. Crespo, P.M. De Biase, S. Di Lella, M.C. Gonzalez Lebrero, M.A. Marti, A.D. Nadra, L.L. Perissinotti, D.A. Scherlis, D.A. Estrin, Modeling heme proteins using atomistic simulations, Physical Chemistry Chemical Physics, 8 (2006) 5611-5628.
[125] S. Kabir, K. Artyushkova, B. Kiefer, P. Atanassov, Computational and experimental evidence for a new TM-N3/C moiety family in non-PGM electrocatalysts, Physical Chemistry Chemical Physics, 17 (2015) 17785-17789.
[126] C.E. Szakacs, M. Lefevre, U.I. Kramm, J.-P. Dodelet, F. Vidal, A density functional theory study of catalytic sites for oxygen reduction in Fe/N/C catalysts used in H2/O2 fuel cells, Physical Chemistry Chemical Physics, 16 (2014) 13654-13661.
[127] G. Paolo, B. Stefano, B. Nicola, C. Matteo, C. Roberto, C. Carlo, C. Davide, L.C. Guido, C. Matteo, D. Ismaila, C. Andrea Dal, G. Stefano de, F. Stefano, F. Guido, G. Ralph, G. Uwe, G. Christos, K. Anton, L. Michele, M.-S. Layla, M. Nicola, M. Francesco, M. Riccardo, P. Stefano, P. Alfredo, P. Lorenzo, S. Carlo, S. Sandro, S. Gabriele, P.S. Ari, S. Alexander, U. Paolo, M.W. Renata, QUANTUM ESPRESSO: a modular and open-source software project for quantum simulations of materials, Journal of Physics: Condensed Matter, 21 (2009) 395502.
[128] G. Henkelman, B.P. Uberuaga, H. Jónsson, A climbing image nudged elastic band method for finding saddle points and minimum energy paths, The Journal of Chemical Physics, 113 (2000) 9901-9904.
[129] G. Henkelman, H. Jónsson, Improved tangent estimate in the nudged elastic band method for finding minimum energy paths and saddle points, The Journal of Chemical Physics, 113 (2000) 9978-9985.
[130] J.G. Lee, Computational Materials Science An Introduction, in: T.F. Group (Ed.) Computational Materials Science An Introduction, CRC Press, 2012, pp. 109-144.
[131] R. Chen, H. Li, D. Chu, G. Wang, Unraveling Oxygen Reduction Reaction Mechanisms on Carbon-Supported Fe-Phthalocyanine and Co-Phthalocyanine Catalysts in Alkaline Solutions, The Journal of Physical Chemistry C, 113 (2009) 20689-20697.
[132] S.-F. Huang, K. Terakura, T. Ozaki, T. Ikeda, M. Boero, M. Oshima, J.-i. Ozaki, S. Miyata, First-principles calculation of the electronic properties of graphene clusters doped with nitrogen and boron: Analysis of catalytic activity for the oxygen reduction reaction, Physical Review B, 80 (2009) 235410.
[133] X. Chen, F. Li, N. Zhang, L. An, D. Xia, Mechanism of oxygen reduction reaction catalyzed by Fe(Co)-Nx/C, Physical Chemistry Chemical Physics, 15 (2013) 19330-19336.

[134] L. Zhang, Z. Xia, Mechanisms of Oxygen Reduction Reaction on Nitrogen-Doped Graphene for Fuel Cells, The Journal of Physical Chemistry C, 115 (2011) 11170-11176.
[135] X. Bao, X. Nie, D. von Deak, E.J. Biddinger, W. Luo, A. Asthagiri, U.S. Ozkan, C.M. Hadad, A First-Principles Study of the Role of Quaternary-N Doping on the Oxygen Reduction Reaction Activity and Selectivity of Graphene Edge Sites, Topics in Catalysis, 56 (2013) 1623-1633.
[136] S. Kattel, P. Atanassov, B. Kiefer, Catalytic activity of Co-Nx/C electrocatalysts for oxygen reduction reaction: a density functional theory study, Physical Chemistry Chemical Physics, 15 (2013) 148-153.
[137] Y. Zheng, W. Xiao, M. Cho, K. Cho, Density functional theory calculations for the oxygen dissociation on nitrogen and transition metal doped graphenes, Chemical Physics Letters, 586 (2013) 104-107.
[138] C. Linares-Flores, J. Espinoza-Vergara, J.H. Zagal, R. Arratia-Perez, Reactivity trends of Fe phthalocyanines confined on graphite electrodes in terms of donor–acceptor intermolecular hardness: Linear versus volcano correlations, Chemical Physics Letters, 614 (2014) 176-180.
[139] Y. Chen, X. Hua, S. Chen, Theoretical study of stability of metal-N4 macrocyclic compounds in acidic media, Chinese Journal of Catalysis, 37 (2016) 1166-1171.
[140] G. Mills, H. Jónsson, G.K. Schenter, Reversible work transition state theory: application to dissociative adsorption of hydrogen, Surface Science, 324 (1995) 305-337.
[141] D. Sheppard, R. Terrell, G. Henkelman, Optimization methods for finding minimum energy paths, The Journal of Chemical Physics, 128 (2008) 134106.
[142] F. Calle-Vallejo, J.I. Martinez, J. Rossmeisl, Density functional studies of functionalized graphitic materials with late transition metals for oxygen reduction reactions, Physical Chemistry Chemical Physics, 13 (2011) 15639-15643.
[143] R.A. van Santen, Molecular Catalytic Kinetics Concepts, in: Novel Concepts in Catalysis and Chemical Reactors, Wiley-VCH Verlag GmbH & Co. KGaA, 2010, pp. 1-30.
[144] A.A. Balandin, Modern State of the Multiplet Theor of Heterogeneous Catalysis1*The paper was prepared for publication by E.I. Klabunovskii, Advances in Catalysis, 19 (1969) 1-210.
[145] A.J. Medford, A. Vojvodic, J.S. Hummelshøj, J. Voss, F. Abild-Pedersen, F. Studt, T. Bligaard, A. Nilsson, J.K. Nørskov, From the Sabatier principle to a predictive theory of transition-metal heterogeneous catalysis, Journal of Catalysis, 328 (2015) 36-42.
[146] K. Momma, F. Izumi, VESTA: a three-dimensional visualization system for electronic and structural analysis, Journal of Applied Crystallography, 41 (2008) 653-658.
[147] E. Gracia-Espino, X. Jia, T. Wågberg, Improved Oxygen Reduction Performance of Pt–Ni Nanoparticles by Adhesion on Nitrogen-Doped Graphene, The Journal of Physical Chemistry C, 118 (2014) 2804-2811.
[148] G.A. Goenaga, S. Foister, A. Belapure, K. Byrne, S. Hawks, A.B. Papandrew, T. Zawodzinski, Pyrolyzed Copper-Based Catalyst with High Oxygen Reduction

Activity for PEM Fuel Cell Applications, ECS Electrochemistry Letters, 3 (2014) F68-F71.
[149] F. Vallejos-Burgos, S. Utsumi, Y. Hattori, X. García, A.L. Gordon, H. Kanoh, K. Kaneko, L.R. Radovic, Pyrolyzed phthalocyanines as surrogate carbon catalysts: Initial insights into oxygen-transfer mechanisms, Fuel, 99 (2012) 106-117.
[150] S. Plimpton, Fast Parallel Algorithms for Short-Range Molecular Dynamics, Journal of Computational Physics, 117 (1995) 1-19.
[151] D. Keffer, Simulation of Molecules, in, Universiyt of Tennesse, 2016, pp. MSE 614 Course Website.
[152] W.L. Jorgensen, D.S. Maxwell, J. Tirado-Rives, Development and Testing of the OPLS All-Atom Force Field on Conformational Energetics and Properties of Organic Liquids, Journal of the American Chemical Society, 118 (1996) 11225-11236.
[153] W.L. Jorgensen, J. Tirado-Rives, The OPLS [optimized potentials for liquid simulations] potential functions for proteins, energy minimizations for crystals of cyclic peptides and crambin, Journal of the American Chemical Society, 110 (1988) 1657-1666.
[154] M.G. Martin, J.I. Siepmann, Transferable Potentials for Phase Equilibria. 1. United-Atom Description of n-Alkanes, The Journal of Physical Chemistry B, 102 (1998) 2569-2577.
[155] B. Chen, J.I. Siepmann, Transferable Potentials for Phase Equilibria. 3. Explicit-Hydrogen Description of Normal Alkanes, The Journal of Physical Chemistry B, 103 (1999) 5370-5379.
[156] D. Yin, A.D. MacKerell, Combined ab initio/empirical approach for optimization of Lennard–Jones parameters, Journal of Computational Chemistry, 19 (1998) 334-348.
[157] A.K. Rappe, C.J. Casewit, K.S. Colwell, W.A. Goddard, W.M. Skiff, UFF, a full periodic table force field for molecular mechanics and molecular dynamics simulations, Journal of the American Chemical Society, 114 (1992) 10024-10035.
[158] D. Frenkel, B. Smit, Chapter 6 - Molecular Dynamics in Various Ensembles, in: Understanding Molecular Simulation (Second Edition), Academic Press, San Diego, 2002, pp. 139-163.
[159] J. Finnerty, German Research School for Simulation Sciences, in: Molecular Dynamics meets the physical world: Thermostats and barostats, 2011.
[160] H.J.C. Berendsen, J.P.M. Postma, W.F. van Gunsteren, A. DiNola, J.R. Haak, Molecular dynamics with coupling to an external bath, The Journal of Chemical Physics, 81 (1984) 3684-3690.
[161] W.G. Hoover, Canonical dynamics: Equilibrium phase-space distributions, Physical Review A, 31 (1985) 1695-1697.
[162] D.J. Keffer, C. Baig, P. Adhangale, B.J. Edwards, A generalized Hamiltonian-based algorithm for rigorous equilibrium molecular dynamics simulation in the canonical ensemble, Journal of Non-Newtonian Fluid Mechanics, 152 (2008) 129-139.
[163] D.J. Keffer, C. Baig, P. Adhangale, B.J. Edwards, A generalized Hamiltonian-based algorithm for rigorous equilibrium molecular dynamics

simulation in the isobaric–isothermal ensemble, Molecular Simulation, 32 (2006) 345-356.
[164] M. Parrinello, A. Rahman, Polymorphic transitions in single crystals: A new molecular dynamics method, Journal of Applied Physics, 52 (1981) 7182-7190.
[165] H.M. Marques, O.Q. Munro, N.E. Grimmer, D.C. Levendis, F. Marsicano, G. Pattrick, T. Markoulides, A force field for molecular mechanics studies of iron porphyrins, Journal of the Chemical Society, Faraday Transactions, 91 (1995) 1741-1749.
[166] G. Wedler, The role of adsorption calorimetry in the study of surface phenomena, Journal of thermal analysis, 14 (1978) 15-26.
[167] J.G. Lee, Computational Materials Science: An Introduction, Taylor & Francis, 2011.
[168] A.C.T. van Duin, S. Dasgupta, F. Lorant, W.A. Goddard, ReaxFF: A Reactive Force Field for Hydrocarbons, The Journal of Physical Chemistry A, 105 (2001) 9396-9409.
[169] M. Thompson, Notes on Statistics and Data Quality for Analytical Chemists, World Scientific & Imperial College Press, River Edge, NJ, USA, 2011.
[170] IBM, IBM SPSS STATISTICS 19 Algorithms, in: Nonparametric Test Algorithms, 2010, pp. 649-653.

APPENDIX

Statistical test

Mann-Whitney U and Kolmogorov-Smirnov (Two-samples) are the most common nonparametric tests to evaluate goodness of fit. These tests are based on rank calculations rather than parametric parameters based on distributions [169, 170].

Mann-Whitney U

For two independent and continuous samples, this tests evaluates:

H_o: $F_1(x) = F_2(x)$ $\forall x$ (A1)

H_A: $F_1(x) \geq F_2(x)$ For some x (A2)

$H_{A'}$: $F_1(x) \leq F_2(x)$ For some x (A3)

$p_1 = \min[P(Z \leq T_1), P(Z \geq T_1)]$ (A4)

$p\text{-}value = 2p_1$ (A5)

T_1 is the Mann-Whitney U test statistic calculated as:

$$T_1 = \frac{T - n\left(\frac{N+1}{2}\right) - \frac{1}{2}}{\sqrt{\frac{nm}{N(N-1)}\sum_{i+1}^{N} R_i^2 - \frac{nm(N+1)^2}{4(N-1)}}} \quad \text{(A6)}$$

$$T = \sum_{i=1}^{n} R(x_i) \quad \text{(A7)}$$

Where n and m are the size of the samples, $N=n+m$, and R is the rank of the observations. If $p_1<\alpha$ (α: significance) we reject the null hypothesis for $T<0$ in favor of $H_{A'}$ otherwise ($T>0$) in favor of H_A. If p-value<0 we reject null hypothesis in favor or either $H_{A'}$ or $H_{A'}$.

Two-samples Kolmogorov-Smirnov

$$D_{nm} = \left(\frac{nm}{m+n}\right)^{1/2} \sup_x |S_{1,n}(x) - S_{2,m}(x)| \quad \text{(A8)}$$

H_o: $F_1(x) = F_2(x)$ $\forall x$ within the samples (A9)

H_A: $F_1(x) \neq F_2(x)$ for some x.

(A10)

$$p-value=\begin{cases}1 & 0\le Z<0.27\\ 1-\frac{\sqrt{2\pi}}{Z}(Q+Q^9+Q^{25}),\quad Q=e^{-\frac{\pi^2}{8Z^2}} & 0.27\le Z<1\\ 2(Q-Q^4+Q^9-Q^{16}),\quad Q=e^{-2Z^2} & 1\le Z<3.1\\ 0 & Z\ge 3.1\end{cases} \quad \text{(A11)}$$

Where n and m are the size of the samples, D_{nm} is the KS test statistic, $Z=f(D_{nm})$, and $S_{i,n}$ are the empirical distribution functions.

If $D_{nm} > c(\alpha)\left(\frac{nm}{m+n}\right)^{1/2}$, the null hypothesis is rejected with α significance or if p-value>α we reject the null hypothesis.

LAMMPS Fe Porphyrin Configuration File

25 atoms
32 bonds
54 angles
92 dihedrals
0 impropers
6 atom types
7 bond types
14 angle types
19 dihedral types
0 improper types
-0.100000000000000E+02 0.100000000000000E+02 xlo xhi
-0.100000000000000E+02 0.100000000000000E+02 ylo yhi
-0.100000000000000E+02 0.100000000000000E+02 zlo zhi

Masses

1 0.120107000000000E+02
2 0.120107000000000E+02
3 0.120107000000000E+02
4 0.528450000000000E+02
5 0.140070000000000E+02
6 0.140070000000000E+02

Atoms

1 1 4 0.000000000000000E+00 -0.100000000000000E-02 0.100000000000000E-02 0.980000000000000E-01 # Fe
2 1 1 0.000000000000000E+00 0.248300000000000E+01 -0.226800000000000E+01 -0.920000000000000E-01 # C1
3 1 1 0.000000000000000E+00 -0.231900000000000E+01 -0.244200000000000E+01 -0.980000000000000E-01 # C1
4 1 1 0.000000000000000E+00 -0.248900000000000E+01 0.227300000000000E+01 -0.930000000000000E-01 # C1
5 1 1 0.000000000000000E+00 0.231400000000000E+01 0.244000000000000E+01 -0.820000000000000E-01 # C1
6 1 5 0.000000000000000E+00 0.630000000000000E-01 -0.182600000000000E+01 -0.275000000000000E+00 # N1
7 1 2 0.000000000000000E+00 0.116800000000000E+01 -0.261200000000000E+01 -0.411000000000000E+00 # C2
8 1 3 0.000000000000000E+00 0.815000000000000E+00 -0.391500000000000E+01 -0.894000000000000E+00 # C3
9 1 3 0.000000000000000E+00 -0.531000000000000E+00 -0.396400000000000E+01 -0.894000000000000E+00 # C3
10 1 2 0.000000000000000E+00 -0.983000000000000E+00 -0.269300000000000E+01 -0.412000000000000E+00 # C2
11 1 6 0.000000000000000E+00 -0.187900000000000E+01 -0.660000000000000E-01 0.259000000000000E+00 # N2
12 1 2 0.000000000000000E+00 -0.266400000000000E+01 -0.116800000000000E+01 0.329000000000000E+00 # C2
13 1 3 0.000000000000000E+00 -0.390600000000000E+01 -0.815000000000000E+00 0.958000000000000E+00 # C3
14 1 3 0.000000000000000E+00 -0.395700000000000E+01 0.538000000000000E+00 0.956000000000000E+00 # C3
15 1 2 0.000000000000000E+00 -0.273600000000000E+01 0.978000000000000E+00 0.340000000000000E+00 # C2
16 1 5 0.000000000000000E+00 -0.670000000000000E-01 0.182800000000000E+01 -0.269000000000000E+00 # N1
17 1 2 0.000000000000000E+00 -0.117200000000000E+01 0.261800000000000E+01 -0.401000000000000E+00 # C2
18 1 3 0.000000000000000E+00 -0.813000000000000E+00 0.391400000000000E+01 -0.900000000000000E+00 # C3
19 1 3 0.000000000000000E+00 0.532000000000000E+00 0.396100000000000E+01 -0.900000000000000E+00 # C3
20 1 2 0.000000000000000E+00 0.981000000000000E+00 0.269200000000000E+01 -0.408000000000000E+00 # C2
21 1 6 0.000000000000000E+00 0.187600000000000E+01 0.630000000000000E-01 0.272000000000000E+00 # N2
22 1 2 0.000000000000000E+00 0.266100000000000E+01 0.116700000000000E+01 0.342000000000000E+00 # C2
23 1 3 0.000000000000000E+00 0.392400000000000E+01 0.813000000000000E+00 0.930000000000000E+00 # C3

24 1 3 0.000000000000000E+00 0.397000000000000E+01 -0.540000000000000E+00 0.939000000000000E+00 # C3
25 1 2 0.000000000000000E+00 0.273200000000000E+01 -0.980000000000000E+00 0.371000000000000E+00 # C2

Bonds

1	6	1	6
2	7	1	11
3	6	1	16
4	7	1	21
5	1	2	7
6	1	2	25
7	1	3	10
8	1	3	12
9	1	4	15
10	1	4	17
11	1	5	20
12	1	5	22
13	3	6	7
14	3	6	10
15	2	7	8
16	5	8	9
17	2	9	10
18	4	11	12
19	4	11	15
20	2	12	13
21	5	13	14
22	2	14	15
23	3	16	17
24	3	16	20
25	2	17	18
26	5	18	19
27	2	19	20
28	4	21	22
29	4	21	25
30	2	22	23
31	5	23	24
32	2	24	25

Angles

1	13	6	1	11
2	12	6	1	16
3	13	6	1	21
4	7	1	6	7
5	7	1	6	10

6	13	11	1	16
7	14	11	1	21
8	9	1	11	12
9	9	1	11	15
10	13	16	1	21
11	7	1	16	17
12	7	1	16	20
13	9	1	21	22
14	9	1	21	25
15	4	7	2	25
16	2	2	7	6
17	1	2	7	8
18	3	2	25	21
19	1	2	25	24
20	4	10	3	12
21	2	3	10	6
22	1	3	10	9
23	3	3	12	11
24	1	3	12	13
25	4	15	4	17
26	3	4	15	11
27	1	4	15	14
28	2	4	17	16
29	1	4	17	18
30	4	20	5	22
31	2	5	20	16
32	1	5	20	19
33	3	5	22	21
34	1	5	22	23
35	6	7	6	10
36	10	6	7	8
37	10	6	10	9
38	5	7	8	9
39	5	8	9	10
40	8	12	11	15
41	11	11	12	13
42	11	11	15	14
43	5	12	13	14
44	5	13	14	15
45	6	17	16	20
46	10	16	17	18
47	10	16	20	19
48	5	17	18	19
49	5	18	19	20
50	8	22	21	25
51	11	21	22	23
52	11	21	25	24

53	5	22	23	24
54	5	23	24	25

Dihedrals

1	12	7	6	1	11
2	12	10	6	1	11
3	14	6	1	11	12
4	14	6	1	11	15
5	11	7	6	1	16
6	11	10	6	1	16
7	11	6	1	16	17
8	11	6	1	16	20
9	12	7	6	1	21
10	12	10	6	1	21
11	14	6	1	21	22
12	14	6	1	21	25
13	3	1	6	7	2
14	16	1	6	7	8
15	3	1	6	10	3
16	16	1	6	10	9
17	14	12	11	1	16
18	14	15	11	1	16
19	12	11	1	16	17
20	12	11	1	16	20
21	15	12	11	1	21
22	15	15	11	1	21
23	15	11	1	21	22
24	15	11	1	21	25
25	5	1	11	12	3
26	17	1	11	12	13
27	5	1	11	15	4
28	17	1	11	15	14
29	12	17	16	1	21
30	12	20	16	1	21
31	14	16	1	21	22
32	14	16	1	21	25
33	3	1	16	17	4
34	16	1	16	17	18
35	3	1	16	20	5
36	16	1	16	20	19
37	5	1	21	22	5
38	17	1	21	22	23
39	5	1	21	25	2
40	17	1	21	25	24
41	7	6	7	2	25
42	6	8	7	2	25

43	8	7	2	25	21
44	6	7	2	25	24
45	2	2	7	6	10
46	1	2	7	8	9
47	4	2	25	21	22
48	1	2	25	24	23
49	7	6	10	3	12
50	6	9	10	3	12
51	8	10	3	12	11
52	6	10	3	12	13
53	2	3	10	6	7
54	1	3	10	9	8
55	4	3	12	11	15
56	1	3	12	13	14
57	8	11	15	4	17
58	6	14	15	4	17
59	7	15	4	17	16
60	6	15	4	17	18
61	4	4	15	11	12
62	1	4	15	14	13
63	2	4	17	16	20
64	1	4	17	18	19
65	7	16	20	5	22
66	6	19	20	5	22
67	8	20	5	22	21
68	6	20	5	22	23
69	2	5	20	16	17
70	1	5	20	19	18
71	4	5	22	21	25
72	1	5	22	23	24
73	10	8	7	6	10
74	10	7	6	10	9
75	18	6	7	8	9
76	18	6	10	9	8
77	9	7	8	9	10
78	13	13	12	11	15
79	13	12	11	15	14
80	19	11	12	13	14
81	19	11	15	14	13
82	9	12	13	14	15
83	10	18	17	16	20
84	10	17	16	20	19
85	18	16	17	18	19
86	18	16	20	19	18
87	9	17	18	19	20
88	13	23	22	21	25
89	13	22	21	25	24

```
90     19     21     22     23     24
91     19     21     25     24     23
92      9     22     23     24     25
```

LAMMPS INPUT FILE FOR Fe Porphyrin

```
#
units real
boundary p p p
atom_style full

read_data config_fepor.txt



# interaction styles
pair_style lj/cut/coul/cut 12.0
bond_style harmonic
angle_style harmonic
dihedral_style opls
pair_modify mix geometric tail yes


# OPLS considers 1-4 interactions with 50%.

special_bonds lj/coul 0.0 0.0 0.5


# force field parameters

# missing nonbonded parameters are inferred from mixing.

pair_coeff   1 1  0.044 1.940   # C1-C1(M)
pair_coeff   2 2  0.044 1.940        # C2-C2(A)
pair_coeff   3 3  0.044 1.040        # C3-C3(B)
pair_coeff   4 4  0.090 2.070        # Fe-Fe
pair_coeff   5 5  0.055 1.820        # N1-N1(A)
pair_coeff   6 6  0.044 1.040        # N2-N2(B)


bond_coeff   1   690.34 1.389    # CM-CA
bond_coeff   2   345.17 1.439    # CA-CB
bond_coeff   3   797.48 1.380    # CA-NA
bond_coeff   4   797.48 1.380    # CA-NB
bond_coeff   5   755.06 1.350    # CB-CB
bond_coeff   6   215.73 2.066    # Fe-NA
bond_coeff   7   215.73 2.066    # Fe-NB
```

```
angle_coeff  1    287.82 124.7    # CM-CA-CB
angle_coeff  2    172.69 125.4    # CM-CA-NA
angle_coeff  3    172.69 125.4    # CM-CA-NA
angle_coeff  4    143.91 124.6    # CA-CM-CA
angle_coeff  5    338.19 107.3    # CA-CB-CB
angle_coeff  6    431.73 105.8    # CA-NA-CA
angle_coeff  7    503.69 126.8    # CA-NA-Fe
angle_coeff  8    431.73 105.8    # CA-NB-CA
angle_coeff  9    503.69 126.8    # CA-NB-Fe
angle_coeff  10   215.87 109.9    # CB-CA-NA
angle_coeff  11   215.87 109.9    # CB-CA-NB
angle_coeff  12   3.5978 154.0    # NA-Fe-NA
angle_coeff  13   143.91  90.0    # NA-Fe-NB
angle_coeff  14   3.5978 154.0    # NB-Fe-NB


dihedral_coeff 1  0.0000 5.3000 0.0000 0.0000  # CM-CA-CB-CB
dihedral_coeff 2  0.0000 7.2000 0.0000 0.0000  # CM-CA-NA-CA
dihedral_coeff 3  0.0000 0.2400 0.0000 0.0000  # CM-CA-NA-Fe
dihedral_coeff 4  0.0000 7.2000 0.0000 0.0000  # CM-CA-NB-CA
dihedral_coeff 5  0.0000 0.2400 0.0000 0.0000  # CM-CA-NB-Fe
dihedral_coeff 6  0.1700 1.4500 0.0000 0.0000  # CA-CM-CA-CB
dihedral_coeff 7  0.0000 1.6000 0.0000 0.0000  # CA-CM-CA-NA
dihedral_coeff 8  0.0000 1.6000 0.0000 0.0000  # CA-CM-CA-NB
dihedral_coeff 9  0.0000 5.6000 0.0000 0.0000  # CA-CB-CB-CA
dihedral_coeff 10 0.0000 12.000 0.0000 0.0000  # CA-NA-CA-CB
dihedral_coeff 11 0.0000 0.0000 0.0000 0.0000  # CA-NA-Fe-NA
dihedral_coeff 12 0.0000 0.2000 0.0000 0.0000  # CA-NA-Fe-NB
dihedral_coeff 13 0.0000 12.000 0.0000 0.0000  # CA-NB-CA-CB
dihedral_coeff 14 0.0000 0.2000 0.0000 0.0000  # CA-NB-Fe-NA
dihedral_coeff 15 0.0000 0.0000 0.0000 0.0000  # CA-NB-Fe-NB
dihedral_coeff 16 0.0000 0.1700 0.0000 0.0000  # CB-CA-NA-Fe
dihedral_coeff 17 0.0000 0.1700 0.0000 0.0000  # CB-CA-NB-Fe
dihedral_coeff 18 0.0000 9.1000 0.0000 0.0000  # CB-CB-CA-NA
dihedral_coeff 19 0.0000 9.1000 0.0000 0.0000  # CB-CB-CA-NB

# initialize random velocities and run a few steps

# of MD to break symmetries.

velocity all create 100.0 53244 dist gaussian mom no rot no
fix 1 all nve
run 100

# and minimize for a bit to get a near 0K structure
```

```
minimize 1.0e-4 1.0e-6 100 1000

# write out restart for starting a new calculation
# or to convert it back into a data file.

write_restart stepr2b-min.restart

# equilibration. real ethane freezes at 89K and boils at 184K
# so we hope the force field has it as a liquid at 120K.

timestep 0.25
reset_timestep 0
neigh_modify every 10 delay 20 check yes
thermo 400
thermo_style multi

# rescale velocities to target temperature

velocity all scale 120.0

# and add a langevin thermostat to dissipate "hot spots".

fix 2 all langevin 120.0 120.0 50.0 6243


# equilibration trajectory
dump 1 all dcd 400 48xfepor-eq.dcd
dump_modify 1 unwrap yes
dump 2 all atom 400 dump.lammpstrj

# 20.0ps

run 80000

# keep a restart of this, too.
write_restart stepr2b-eq.restart
```

VITA

Diana Constanza Orozco-Gallo was boron in Bogota, Colombia. She completed her undergraduated and master degree at the National University of Colombia, Medellin Campus. In 2012, she started her PhD studies under the supervision of Dr. Thomas A. Zawodzinski. Her main focus of studies has been Fuel Cells modeling. During her master program she developed Computational Fluid Dynamics models implemented in COMSOL to design bipolar plates for PEM Fuel Cells. Moreover, her work was presented at SIBAE and ECS Meetings.

During her PhD studies she tried to solve the questions arised during her master degree about how to obtain better experimental parameters to improve Macroscale modeling and understand the phenomena related with electrocatalysis. As result, she developed the methodology presented in this work, it was implemented using different software tools such as Matlab and with open source code such as Quantum Espresso, LAMMPS, VESTA, Avogadro.

She is part of the Electrochemical Society (ECS) and Materials Research Society(MRS). She has participated in the ECS Meetings 225th and 230th presenting different talks: "*1D PEM Fuel Cell Model for Non-Precious Metal Catalyst Laye*r in Orlando,FL in 2014. "*A Multi-Scale Modeling Approach to Study and Design PEM Fuel Cells Catalyst Layers with Non-Precious Metals"* in Honolulu, HI in 2016.

She also participated in the MRS Meeting presenting: "*Beyond Pure Oxygen: PEM Fuel Cell Behavior of Non-Precious Metal-Based Air Electrodes Probed by Linked Experiments and Modeling*" in San Francisco, CA in 2015. She was also contributed to the research presented by Dr Papandrew at the 229th ECS Meeting: "*Understanding Cathodes for Solid Acid Fuel Cells By Coupling FIB-SEM 3D Reconstruction with Mathematical Modeling*" in San Diego, CA in 2016.